

INFORMATION TO USERS

This manuscript has been reproduced from the microfilm master. UMI films the text directly from the original or copy submitted. Thus, some thesis and dissertation copies are in typewriter face, while others may be from any type of computer printer.

The quality of this reproduction is dependent upon the quality of the copy submitted. Broken or indistinct print, colored or poor quality illustrations and photographs, print bleedthrough, substandard margins, and improper alignment can adversely affect reproduction.

In the unlikely event that the author did not send UMI a complete manuscript and there are missing pages, these will be noted. Also, if unauthorized copyright material had to be removed, a note will indicate the deletion.

Oversize materials (e.g., maps, drawings, charts) are reproduced by sectioning the original, beginning at the upper left-hand corner and continuing from left to right in equal sections with small overlaps.

Photographs included in the original manuscript have been reproduced xerographically in this copy. Higher quality 6" x 9" black and white photographic prints are available for any photographs or illustrations appearing in this copy for an additional charge. Contact UMI directly to order.

ProQuest Information and Learning
300 North Zeeb Road, Ann Arbor, MI 48106-1346 USA
800-521-0600

UMI[®]

University of Alberta

Modeling Transition Metal Compounds: Testing, Development, and Applications

by

Stephen Andrew Decker



A thesis submitted to the Faculty of Graduate Studies and Research in partial fulfillment of
the requirements for the degree of Doctor of Philosophy

Department of Chemistry

Edmonton, Alberta

Spring 2000



National Library
of Canada

Acquisitions and
Bibliographic Services

395 Wellington Street
Ottawa ON K1A 0N4
Canada

Bibliothèque nationale
du Canada

Acquisitions et
services bibliographiques

395, rue Wellington
Ottawa ON K1A 0N4
Canada

Your file Votre référence

Our file Notre référence

The author has granted a non-exclusive licence allowing the National Library of Canada to reproduce, loan, distribute or sell copies of this thesis in microform, paper or electronic formats.

The author retains ownership of the copyright in this thesis. Neither the thesis nor substantial extracts from it may be printed or otherwise reproduced without the author's permission.

L'auteur a accordé une licence non exclusive permettant à la Bibliothèque nationale du Canada de reproduire, prêter, distribuer ou vendre des copies de cette thèse sous la forme de microfiche/film, de reproduction sur papier ou sur format électronique.

L'auteur conserve la propriété du droit d'auteur qui protège cette thèse. Ni la thèse ni des extraits substantiels de celle-ci ne doivent être imprimés ou autrement reproduits sans son autorisation.

0-612-59947-7

Canada

University of Alberta

Library Release Form

Name of Author: Stephen Andrew Decker

Title of Thesis: Modeling Transition Metal Compounds: Testing, Development, and Applications

Degree: Doctor of Philosophy

Year this Degree Granted: 2000

Permission is hereby granted to the University of Alberta Library to reproduce single copies of this thesis and to lend or sell such copies for private, scholarly or scientific research purposes only.

The author reserves all other publication and other rights in association with the copyright in the thesis, and except as herein before provided, neither the thesis nor any substantial portion thereof may be printed or otherwise reproduced in any material form whatever without the author's prior written permission.



Stephen Andrew Decker
5470 North Drive
Manotick, Ontario
K4M 1G7

November 30, 1999

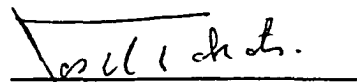
University of Alberta

Faculty of Graduate Studies and Research

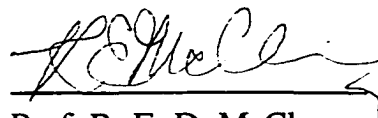
The undersigned certify that they have read, and recommend to the Faculty of Graduate Studies and Research for acceptance, a thesis entitled *Modeling Transition Metal Compounds: Testing, Development, and Applications* submitted by Stephen Andrew Decker in partial fulfillment of the requirements for the degree of Doctor of Philosophy.



Prof. M. Klobukowski



Prof. J. Takats



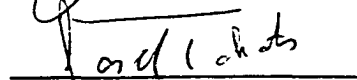
Prof. R. E. D. McClung



Prof. W. Jaeger



Prof. J. A. Tuszynski



Prof. M. C. Zerner

November 26, 1999

to my wife Wendy and my little girl Hannah

Abstract

Advances in computer technology and computational chemistry software have enabled researchers to model large chemical systems, including transition metal compounds. The work in the current thesis focuses on the testing, development, and application of modern computational chemistry methods for modeling transition metal compounds.

The reliability of the model core potential (MCP) formalism, which reduces the number of electrons treated in the calculation, was tested in a systematic study involving small main group molecules and the tetrahalogen complexes of the Group 4 metals. The MCP geometric parameters were found to be in good agreement with experimental values, provided the penultimate $(n-1)p$ atomic shell of the metal was included in the calculation. The computational efficiency of the MCP formalism was improved further by redesigning the valence basis sets to incorporate L-shell structure. Results from atomic and molecular test calculations indicate no significant differences between values computed using the new L-shell basis sets and the conventional ones.

Carbonyl fluxionality in $\text{Mn}_2(\text{CO})_{10}$ and $\text{Mn}_2(\text{CO})_6(\text{H}_2\text{PCH}_2\text{PH}_2)_2$, serving as a model of $\text{Mn}_2(\text{CO})_6(\text{Ph}_2\text{CH}_2\text{Ph}_2)_2$, was studied at the density functional theory and PM3(tm) levels. The DFT approach was the most fruitful, predicting a barrier of 19 - 21 kcal/mol for carbonyl migration in $\text{Mn}_2(\text{CO})_{10}$, slightly below the upper limit for fluxional processes to be detected by NMR, in contrast to its observed rigidity. DFT calculations predicted a barrier of 13 kcal/mol for carbonyl migration in the model $\text{Mn}_2(\text{CO})_6(\text{H}_2\text{PCH}_2\text{PH}_2)_2$ system, only 3 kcal/mol higher than the experimental estimate. The PM3(tm) semiempirical method predicted accurate molecular structures, but was less successful in computing the energy barrier. A hybrid DFT//PM3(tm) method, utilizing the energies from DFT calculations and the structures from PM3(tm) calculations, corrected the energy barriers.

The origin of the increased reactivity of the alkyne complexes of the Group 8 metals, $M(\text{CO})_4(\text{C}_2\text{R}_2)$, with respect to their parent carbonyl complexes, $M(\text{CO})_5$, was investigated at the DFT level. Calculated structures agreed well with experiment and the computed CO bond dissociation energy trends mirrored those found experimentally. Analysis of the metal-alkyne interaction revealed that the alkyne acts as a four-electron donor to stabilize the unsaturated $M(\text{CO})_3(\text{C}_2\text{R}_2)$ dissociation product, resulting in the increased reactivity.

Acknowledgements

I would first like to thank my supervisor Mariusz Klobukowski for his assistance over the past five years. I don't think I could have chosen a better Ph.D. supervisor. He let me pursue my own interests right from the start and was always willing to help with all sorts of problems ranging from computer glitches to colicky babies. I feel privileged to have worked with Mariusz and have the utmost respect for him as a scientist and as a person.

Over the years I have had the pleasure of working alongside a number of great graduate students in the Klobukowski group including: Dietmar Krause, Joanne Gainsforth, Chris Lovallo, and Jonathan Mane. I've enjoyed their companionship and thank them for listening to me, whether I was in a good mood or not.

I am thankful to have had the opportunity to work with Prof. Joe Takats and Prof. Robert Jordan in a very fruitful collaboration looking at the Group 8 metal-alkyne complexes (Chapter 5). They were great to work with and gave me a lot of insight into the problem from an experimental point of view. I would also like to thank the members of the Takats and Jordan research groups involved in this collaborative project, as either an active researcher or as an observer: Jason Cooke, Jean Pearson, John Washington, Tianfu Mao, and Greg Ferrence.

Along with the people I've collaborated with here at the University of Alberta many people have helped me immensely in carrying out my research and in preparing my thesis. The members of the chemistry department Computer and Network Services group: Ron Gardner, Scott Delinger, and Larry Coulson have been a great help to me over the years. The University of Alberta Computer and Network Services department has provided me with accounts on all of their research computers and enough disk space and CPU time to carry out the research contained in this thesis. I'd like to thank Christine Otter for the use of her laser printer during the preparation of this thesis. I am also grateful for the time and effort displayed by my committee members over the years.

The many friends I've made at the U of A has made graduate school life much more enjoyable and has helped to ease the stress on many occasions, and for this I am grateful. One of the first people I met at the U of A was Chris Daley and since then we've done lots together from playing and coaching hockey in the winter to hitting the links for a round of golf in the summer. The many squash matches Nghia Chiem and I have had over the years enabled us both to vent our frustrations and keep our sanity. Other colleagues who've

made life more enjoyable include: Mike Finot, Mike Ferguson, Jason Wiles and Chris Lee. I'd like to thank Dean and Ange Zaragoza for being great friends.

Of course, I could not have made it this far without the support of my family. I'm grateful that my parents and my in-laws believed in me and were able to make the trip to Edmonton on a number of occasions making us feel less isolated. Finally, I owe the biggest thank you of all to my beautiful wife Wendy, without whom I could not have done this. You have always been there for me and have supported me every step of the way, with your constant love, encouragement and support. You always have a smile and are able to pick me up when I'm feeling down. Thank you for understanding when I was working late finishing my thesis, instead of being at home helping to take care of Hannah. And the last person I'd like to thank is my sweet little daughter Hannah for just being you, crying and all!

Table of Contents

Chapter 1: Introduction

1.1 The Hartree-Fock Model	3
1.2 Post Hartree-Fock Methods.....	8
1.3 Density Functional Theory.....	11
1.4 Semiempirical Methods.....	14
1.5 Basis Sets	16
1.6 Pseudopotential Methods.....	20
1.6.1 Model Core Potentials.....	21
1.6.2 Effective Core Potentials	22
1.6.3 Quasi-Relativistic Pseudopotentials	23
1.6.4 Comparison of MCPs and ECPs	24
1.7 Interpreting the Energy and Wavefunction.....	25
1.8 Scope of the Thesis	28
1.9 References	29

Chapter 2: Benchmarking of Model Core Potentials: Application to Small Molecules and the Group 4 Metal Halogen Complexes (MX₄: M = Ti, Zr, Hf and X = F, Cl, Br, I)

2.1 Introduction.....	38
2.2 Computational Methods	40
2.2.1 Small Molecules	40
2.2.2 MX ₄ Molecules	41
2.3 Results and Discussion.....	43
2.3.1 Small Molecules	44
2.3.2 MX ₄ Molecules	57
2.4 Conclusions.....	64
2.5 References	66

Chapter 3: Incorporation of L-Shell Structure into the Model Core Potential Valence Basis Sets for the Main Group Elements

3.1 Introduction.....	70
3.2 Computational Methodologies.....	74

3.2.1 Fitting Procedures.....	74
3.2.2 Atomic Calculations.....	76
3.2.3 Molecular Calculations.....	77
3.3 Results and Discussion.....	79
3.3.1 L-Shell Fitting	79
3.3.2 Atomic Calculations.....	85
3.3.3 Molecular Calculations.....	90
3.3.4 Timings.....	96
3.4 Conclusions.....	98
3.5 References	99

Chapter 4: An Investigation into the Carbonyl Fluxionality of $\text{Mn}_2(\text{CO})_{10}$ and $\text{Mn}_2(\text{CO})_6(\text{H}_2\text{PCH}_2\text{PH}_2)_2$

4.1 Introduction.....	103
4.2 Computational Methods.....	105
4.2.1 $\text{Mn}_2(\text{CO})_{10}$	105
4.2.2 $\text{Mn}_2(\text{CO})_6(\text{dhpm})_2$	106
4.3 Results and Discussion.....	107
4.3.1 $\text{Mn}_2(\text{CO})_{10}$	107
4.3.2 $\text{Mn}_2(\text{CO})_6(\text{dhpm})_2$	116
4.4 Conclusions.....	123
4.5 References	125

Chapter 5: The First Carbonyl Bond Dissociation Energies of $\text{M}(\text{CO})_5$ and $\text{M}(\text{CO})_4(\text{C}_2\text{H}_2)$ (M = Fe, Ru, Os): The Role of the Acetylene Ligand from a Density Functional Perspective

5.1 Introduction.....	128
5.2 Computational Methods.....	130
5.3 Results and Discussion.....	132
5.3.1 Structures of the Carbonyl Complexes	132
5.3.2 Structures of the Alkyne Complexes.....	138
5.3.3 Carbonyl Bond Dissociation Energies	144
5.3.4 Reaction Profiles for CO Dissociation from $\text{M}(\text{CO})_5$ and $\text{M}(\text{CO})_4(\text{C}_2\text{H}_2)$..	149
5.3.5 The Role of the Acetylene Ligand	155
5.3.5.1 CDA Results	156
5.3.5.2 AIM Results.....	159

5.3.6 Dependence of the CO BDEs on the Metal Atom.....	165
5.4 Conclusions.....	166
5.5 References	168
Chapter 6: Final Conclusions	
6.1 Further Work.....	175
6.2 Final Comments.....	176
6.3 References	176
Appendix A: Supplementary Material for Chapter 2	178
Appendix B: Supplementary Material for Chapter 3	193
Appendix C: Supplementary Material for Chapter 5	215

List of Tables

Table 2.1: Summary of the Metal Atom Pseudopotential Valence Basis Sets Employed in Calculations of the MX_4 Complexes.....	42
Table 2.2: Summary of the Harmonic Vibrational Frequencies of Selected Diatomic Molecules.....	46
Table 2.3: Calculated (MCP) and Experimental Structural Parameters for the Tetraatomic Molecules Studied.....	53
Table 2.4: Calculated (MCP) and Experimental Structural Parameters for the Hydrocarbons Studied.....	54
Table 2.5: Valence Electron Correlation Energies of Selected Diatomic Molecules.....	55
Table 2.6: Valence Electron Correlation Energies of the Heavy Atom Hydride Polyatomic Molecules.....	56
Table 2.7: Summary of the Deviations between the Calculated and Experimental M-X Distances Averaged over all Twelve MX_4 Complexes.....	61
Table 2.8: Summary of the Computed ΔE_{rxn} Values for the Dihalogen Substitution Reactions of MX_4	63
Table 3.1: Sample MCP Valence Basis Set for Carbon.....	72
Table 3.2: MCP Valence Basis Set Contractions Employed for the Central Atoms of SF_6 , SeF_6 , and TeF_6	78
Table 3.3: A Representative Sample of the Optimum MCP-SP L-Shell Valence Basis Sets.....	80
Table 3.4: A Representative Sample of the Optimum MCP-DSP L-Shell Valence Basis Sets.....	83
Table 3.5: Summary of the Optimized A-F Distances in AF_6 (A = S, Se, Te).....	91
Table 3.6: Summary of the AF_6 Harmonic Vibrational Frequencies Computed using the MCP-SP Basis Sets.....	93
Table 3.7: Summary of the SeF_6 and TeF_6 Harmonic Vibrational Frequencies Computed using the MCP-DSP Basis Sets at the RHF Level of Theory.....	95
Table 3.8: Summary of the MCP-SP SCF, Geometry Optimization, and Hessian Timings for SeF_6	97
Table 4.1: Predicted Geometrical Parameters for the Three Conformers of	

$\text{Mn}_2(\text{CO})_{10}$	109
Table 4.2: Relative Energies of the $\text{Mn}_2(\text{CO})_{10}$ Conformers.....	113
Table 4.3: Structural Parameters of the $\text{Mn}_2(\text{CO})_n(\text{dhpm})_2$ Conformers ($n = 6, 5$)	117
Table 4.4: Relative Energies of the $\text{Mn}_2(\text{CO})_6(\text{dhpm})_2$ Conformers	122
Table 5.1: Geometric Parameters of $\text{M}(\text{CO})_5$ (D_{3h})	133
Table 5.2: Geometric Parameters of $\text{M}(\text{CO})_4$ (C_{2v}).....	137
Table 5.3: Selected Geometric Parameters of $\text{M}(\text{CO})_4(\text{C}_2\text{H}_2)$ (C_{2v}).....	140
Table 5.4: Selected Geometric Parameters of $\text{M}(\text{CO})_3(\text{C}_2\text{H}_2)$ (C_s).....	143
Table 5.5: First Carbonyl Bond Dissociation Energies of $\text{M}(\text{CO})_5$ and $\text{M}(\text{CO})_4(\text{C}_2\text{H}_2)$	145
Table 5.6: Singlet-Triplet Spacings of $\text{Fe}(\text{CO})_4$	150
Table 5.7: Summary of Charge Decomposition Analysis	158
Table 5.8: Charge Decomposition Analysis of Metal-Acetylene Bonding in $\text{M}(\text{CO})_4(\text{C}_2\text{H}_2)$ and $\text{M}(\text{CO})_3(\text{C}_2\text{H}_2)$	162
Table 5.9: Topological Properties at the Bond Critical Points of $\text{M}(\text{CO})_5$ and $\text{M}(\text{CO})_4(\text{C}_2\text{H}_2)$ and their CO Dissociated Products	164
Table A.1: Valence Electron Correlation Energies of the Homonuclear Diatomic Molecules	179
Table A.2: Valence Electron Correlation Energies of the Heteronuclear Diatomic Molecules	180
Table A.3: Summary of the Ti-X Distances and Total Energies for TiX_4	182
Table A.4: Summary of the Zr-X Distances and Total Energies for ZrX_4	184
Table A.5: Summary of the Hf-X Distances and Total Energies for HfX_4	187
Table A.6: Summary of the Computed Geometric Parameters for MX_2Y_2	190
Table A.7: Summary of the X-X Bond Distances of the Dihalides	192
Table B.1: Optimum MCP-SP L-Shell Basis Sets for the First Row Main Group Elements.....	194
Table B.2: Optimum MCP-SP L-Shell Basis Sets for the Second Row Main Group Elements.....	196
Table B.3: Optimum MCP-SP L-Shell Basis Sets for the Third Row Main Group Elements.....	198
Table B.4: Optimum MCP-SP L-Shell Basis Sets for the Fourth Row Main Group Elements.....	200

Table B.5: Optimum MCP-SP L-Shell Basis Sets for the Fifth Row Main Group Elements.....	202
Table B.6: Optimum MCP-DSP L-Shell Basis Sets for the Third Row Main Group Elements.....	204
Table B.7: Optimum MCP-DSP L-Shell Basis Sets for the Fourth Row Main Group Elements.....	207
Table B.8: Optimum MCP-DSP L-Shell Basis Sets for the Fifth Row Main Group Elements.....	211

List of Figures

Figure 1.1: Schematic to illustrate how excited configurations are generated in a CISD calculation	9
Figure 1.2: Schematic to illustrate basis set effects	18
Figure 1.3: An example of a potential energy hypersurface for a chemical reaction	27
Figure 2.1: Comparison of calculated and experimental bond lengths for the homonuclear diatomic molecules	45
Figure 2.2: Comparison of calculated and experimental bond lengths for the heteronuclear diatomic chalcogenides of the Group 14 elements	47
Figure 2.3: Comparison of calculated and experimental bond lengths for the mixed halogen diatomic molecules	49
Figure 2.4: Comparison of calculated and experimental bond lengths for the heteronuclear diatomic ions	50
Figure 2.5: Comparison of calculated and experimental bond lengths for the triatomic molecules	51
Figure 2.6: Comparison of calculated and experimental bond angles for the triatomic molecules	52
Figure 2.7: Magnitudes of the experimental M-X deviations averaged over the four halogen complexes of TiX_4 , plotted as a function of the metal atom valence basis set	58
Figure 2.8: Magnitudes of the experimental M-X deviations averaged over the four halogen complexes of ZrX_4 , plotted as a function of the metal atom valence basis set	59
Figure 2.9: Magnitudes of the experimental M-X deviations averaged over the four halogen complexes of HfX_4 , plotted as a function of the metal atom valence basis set	60
Figure 3.1: Plots of the deviation between the ns atomic orbital energies computed using the MCP-SP L-shell and conventional basis sets at the ROHF level	86
Figure 3.2: Plots of the deviation between the np atomic orbital energies computed using the MCP-SP L-shell and conventional basis sets at the ROHF level	87
Figure 3.3: Plots of the deviation between the ns atomic orbital energies computed using	

the MCP-DSP L-shell and conventional basis sets at the ROHF level.....	88
Figure 3.4: Plots of the deviation between the np atomic orbital energies computed using the MCP-DSP L-shell and conventional basis sets at the ROHF level.....	89
Figure 4.1: The three conformers of $Mn_2(CO)_{10}$ studied.....	108
Figure 4.2: Motions of the nuclei in the harmonic vibrational mode corresponding to the single negative curvature of the HF and DFT potential energy surfaces in the eclipsed (D_{4h}) transition state	114
Figure 4.3: Motions of the nuclei in the harmonic vibrational mode connecting the bridged (D_{2h}) and eclipsed (D_{4h}) conformers.....	115
Figure 4.4: The conformers of $Mn_2(CO)_6(dhpm)_2$ and $Mn_2(CO)_5(dhpm)_2$ studied.....	118
Figure 5.1: Structure of $Ru(CO)_4$	136
Figure 5.2: Structure of $Ru(CO)_4(C_2H_2)$	139
Figure 5.3: Structure of $Ru(CO)_3(C_2H_2)$	142
Figure 5.4: First CO bond dissociation energies of $M(CO)_5$ and $M(CO)_4(C_2H_2)$	148
Figure 5.5: CO dissociation trajectories for $Ru(CO)_5$ and $Os(CO)_5$	151
Figure 5.6: CO dissociation trajectory for $Fe(CO)_5$	153
Figure 5.7: CO dissociation trajectories for $Ru(CO)_4(C_2H_2)$	154
Figure 5.8: The four Dewar-Chatt-Duncanson type metal-acetylene MO interactions of the saturated $M(CO)_4(C_2H_2)$ complexes.....	160
Figure 5.9: The four Dewar-Chatt-Duncanson type metal-acetylene MO interactions of the unsaturated $M(CO)_3(C_2H_2)$ complexes.....	161
Figure 5.10: The metal-dependence of the C_2H_2 -M π_{\perp} - π_d energy gap in $M(CO)_3(C_2H_2)$	167
Figure C.1: The MO components of the $C_2H_2 \rightarrow M \pi_{\perp}$ - π_d interaction in $M(CO)_3(C_2H_2)$	216

List of Abbreviations

ac	acetylene
AIM	atoms in molecules
AMI	Austin model 1
Avg	average
ax	axial
BCP	bond critical point
BDE	bond dissociation energy
BLYP	an approximate density function comprised of Becke's gradient-corrected exchange functional and the gradient-corrected correlation functional of Lee, Yang, and Parr
BP86	an approximate density function comprised of Becke's gradient-corrected exchange functional and the gradient-corrected correlation functional of Perdew
br	bridged
BVWN	an approximate density function comprised of Becke's gradient-corrected exchange functional and the local correlation functional of Vosko, Wilk, and Nusair
B3LYP	an approximate density function comprised of Becke's three-parameter gradient-corrected hybrid exchange functional and the gradient-corrected correlation functional of Lee, Yang, and Parr
B3PW91	an approximate density function comprised of Becke's three-parameter gradient-corrected hybrid exchange functional and the gradient-corrected correlation functional of Perdew and Wang
CAS-SCF	complete active space self consistent field
CDA	charge decomposition analysis
CCSD(T)	coupled clusters with single and double substitutions including non-iterative triple contributions
CCSD(TQ)	coupled clusters with single and double substitutions including non-iterative triple and quadruple contributions
CGTF	contracted gaussian type function

CI	configuration interaction
CISD	configuration interaction including single and double excitations
CISDTQ	configuration interaction including single, double, triple, and quadruple excitations
CO BDE	carbonyl bond dissociation energy
DFT	density functional theory
dhpm	bis-(dihydrophosphino)-methane, $\text{H}_2\text{PCH}_2\text{PH}_2$
dissoc.	dissociation
dppm	bis-(diphenylphosphino)-methane, $(\text{C}_6\text{H}_5)_2\text{PCH}_2\text{P}(\text{C}_6\text{H}_5)_2$
DZ	double-zeta
ECP	effective core potential
E_h	Hartree, unit of energy in atomic units: $1E_h = 627.50659 \text{ kcal/mol}$ $= 27.211607 \text{ eV/particle}$
eq	equatorial
Expt.	experiment
GTF	gaussian type function
HF	Hartree-Fock
HFB	hexafluorobut-2-yne, $\text{C}_2(\text{CF}_3)_2$
ⁱ Pr	isopropyl, $(\text{CH}_3)_2\text{CH}$
KS	Kohn-Sham
MCP	model core potential
MCPF	modified coupled-pair functional
MC-SCF	multiconfiguration self consistent field
mE_h	milliHartree: $1mE_h = 0.62750659 \text{ kcal/mol} = 0.027211607 \text{ eV/particle}$
MM	molecular mechanics
MNDO	modified neglect of diatomic overlap
MO	molecular orbital
MP2	second-order Møller-Plesset perturbation theory
MR-CI	multi-reference configuration interaction

NBO	natural bond orbital
perp	perpendicular
PGTF	primitive gaussian type function
Ph	phenyl, C ₆ H ₅
PM3	parameterized method 3
PM3(tm)	parameterized method 3 extended to the transition metal elements
QRHF	quasi-relativistic Hartree-Fock
RCP	ring critical point
RHF	restricted Hartree-Fock
ROHF	restricted open-shell Hartree-Fock
S	singlet
SCF	self consistent field
STO	Slater type orbital
SVWN	an approximate density function comprised of Slater's local exchange functional and the local correlation functional of Vosko, Wilk, and Nusair
T	triplet
term	terminal
TZ	triple-zeta
UHF	unrestricted Hartree-Fock
vs.	versus
XC	exchange-correlation
ZINDO	Zerner's INDO (intermediate neglect of diatomic overlap)

Computational Method Notation

Method1/BS1 calculation performed at the Method1 level of theory employing basis set BS1 (e.g. CISD/TZ2d refers to a CISD calculation employing the basis set denoted TZ2d)

Method1/BS1//Method2/BS2 calculation of the total energy at the Method 1/BS1 level at the corresponding molecular geometry optimized at the Method2/BS2 level. (e.g. B3LYP/BS1//BLYP/BS1 refers to a calculation of the energy of a molecule at the DFT-B3LYP level employing basis set BS1, at the corresponding molecular geometry optimized at the DFT-BLYP level employing basis set BS1)

Chapter 1

Introduction

The astounding growth of computer technology over the last few decades has fueled tremendous advances in the field of computational chemistry. The computational chemist of today typically has access to computing resources powerful enough to enable them to study “real” chemical systems instead of very small diatomic and triatomic models of the molecule of interest. More chemists are turning to computers as an aid to understanding chemical problems than ever before and the acceptance of computational chemistry amongst the chemical community has mirrored this. The results of theoretical studies appear regularly in the mainstream organic and inorganic chemistry journals and are no longer confined to specialized journals read only by theoreticians. Computational chemistry has proven to be a beneficial tool for the pharmaceutical industry^{1,2}, and its importance to other industries has recently grown as well.³ Perhaps the best reflection of the growing role of computational chemistry was the 1998 Nobel prize in chemistry awarded jointly to John Pople, “for his development of computational methods in quantum chemistry”, and Walter Kohn, “for his development of density functional theory”.⁴

The chemistry of the transition metals has recently garnered a lot of attention from computational chemists.⁵⁻⁹ Transition metal complexes play an important role in a number of diverse fields ranging from biology to medicine to catalysis. The resourcefulness of the transition metal elements may be attributed to their ability to coordinate a variety of different ligands, in a number of molecular geometries, and to stabilize various oxidation and spin states.¹⁰ The metalloenzymes are an important class of enzymes in which the metal is the active site and the surrounding ligands act to bring the reactants together.^{11,12} Metallopharmaceuticals, such as the anti-cancer cis-platin drugs^{13,14}, $\text{cis-PtCl}_2(\text{NH}_3)_2$, and the technetium radiopharmaceuticals¹⁵ employed in medical imaging, play a significant part in the diagnosis and treatment of illness. Perhaps the most beneficial use of transition metal compounds, certainly in terms of economic impact, lies in the area of catalysis. A variety of transition metal heterogeneous and homogeneous catalysts are currently employed in important industrial processes including the polymerization of olefins, the hydrogenation of unsaturated hydrocarbons, and the Fischer-Tropsch reaction.^{11,16,17}

Until now, theoretical studies focusing on the chemistry of organic compounds has been more prevalent than those dealing with the chemistry of the transition metal elements. The wealth of information gained in these theoretical organic investigations has shown that modern computational chemistry techniques, if used correctly, are able to provide quantitative predictions of molecular geometries, reaction enthalpies, activation barriers and bond energies.¹⁸ Routine theoretical analyses of organic compounds can now be performed using well benchmarked techniques implemented in a number of very user-friendly programs.¹⁹

Unfortunately, the progress has been slower for the theoretical modeling of species containing transition metals. Methods which have proven to yield highly accurate results for organic molecules are often inadequate for treating transition metal systems since they must accurately describe the various chemical environments of the metal atom.^{6,9,20} The computational chemistry methods currently used in modeling transition metal compounds encompass all levels of sophistication from the most accurate quantum chemical *ab initio* and density functional theory methods, to the semiempirical and classical molecular mechanics schemes. Generally, the more comprehensive the method (i.e. fewest approximations), the more computationally demanding the calculations.

One of the primary problems encountered in modeling transition metal compounds is their large size, both in terms of the number of atoms and the number of electrons, which quickly drains computing resources. Open-shell systems, with unpaired electrons, which are quite common amongst transition metal compounds, require the use of more complex theoretical methods for proper treatment. Furthermore, the nature of the d electrons introduces a number of difficulties for the computational chemist interested in transition metal chemistry. The partially filled d shell of the metal atom usually leads to low lying electronic states upon formation of a complex, again requiring the use of more sophisticated methods.^{9,10} Relativistic effects become increasingly important as one descends the periodic table, and cannot be ignored when modeling the heavier transition elements.²¹

One approach which has been particularly beneficial in theoretical investigations of the chemistry of the transition metals is the pseudopotential formalism. Details of the pseudopotential methods along with a brief overview of the computational chemistry methodologies employed in this thesis; the Hartree-Fock (HF) and post-Hartree-Fock methods, the density functional theory (DFT) approach, and the semiempirical methods are provided in the following sections.

1.1 The Hartree-Fock Method

The following material provides a simple description of the Hartree-Fock approach, and is based on the detailed accounts found in Szabo and Ostlund²², McQuarrie and Simon²³, and Levine²⁴. The time-independent, nonrelativistic Schrödinger equation for a closed shell molecule with n electrons and N nuclei is given by:

$$\hat{H}\Psi(r_1, r_2, \dots, r_n; R_1, R_2, \dots, R_N) = E\Psi(r_1, r_2, \dots, r_n; R_1, R_2, \dots, R_N). \quad (1.1)$$

The Hamiltonian operator is defined as:

$$\hat{H} = -\frac{\hbar^2}{2} \sum_{A=1}^N \frac{1}{M_A} \nabla_A^2 - \frac{\hbar^2}{2m_e} \sum_i^n \nabla_i^2 + \sum_{A=1}^N \sum_{B>A}^N \frac{Z_A Z_B}{R_{AB}} - \sum_{i=1}^n \sum_{A=1}^N \frac{Z_A e^2}{r_{iA}} + \sum_{i=1}^n \sum_{j>i}^n \frac{e^2}{r_{ij}} \quad (1.2)$$

where r_i denotes the coordinates of electron i with mass m_e and charge e , and R_A denotes the coordinates of nucleus A with mass M_A and charge Z_A . The first two terms in the Hamiltonian represent the kinetic energy of the nuclei (T_N) and electrons (T_e), respectively. The remaining terms represent the electrostatic repulsion between the nuclei (V_{NN}), the electrostatic attraction between the nuclei and electrons (V_{Ne}), and the electrostatic repulsion between the electrons (V_{ee}), respectively.

The molecular Hamiltonian may be simplified by recognizing, via the Born-Oppenheimer approximation, that the mass of the electron is much smaller than that of the nuclei and as such they move much faster. The nuclear coordinates can be regarded as fixed ($T_N = 0$) during the motions of the electrons, thereby simplifying the Hamiltonian by removing T_N and regarding V_{NN} as a constant. The resulting electronic Hamiltonian has the form (in atomic units):

$$\hat{H} = -\frac{1}{2} \sum_{i=1}^n \nabla_i^2 - \sum_{i=1}^n \sum_{A=1}^N \frac{Z_A}{r_{iA}} + \sum_{i=1}^n \sum_{i>j}^n \frac{1}{r_{ij}} + V_{NN}, \quad (1.3)$$

and the electronic Schrödinger equation may be expressed as:

$$\left(-\frac{1}{2} \sum_{i=1}^n \nabla_i^2 - \sum_{i=1}^n \sum_{A=1}^N \frac{Z_A}{r_{iA}} + \sum_{i=1}^n \sum_{i>j}^n \frac{1}{r_{ij}} + V_{NN} \right) \Psi(r_1, r_2, \dots, r_n; R) = E \Psi(r_1, r_2, \dots, r_n; R). \quad (1.4)$$

The wavefunction has a parametric dependence on the nuclear coordinates, represented collectively as R . Through Equation (1.4), the potential energy surface of a molecule can be mapped out as a function of the nuclear coordinates.

An exact solution to the electronic Schrödinger equation is possible only for the very simplest of systems (the H atom, the H_2^+ molecule, the harmonic oscillator, the rigid rotor, and the anharmonic oscillator), for all other systems only approximate solutions can be found. The Hartree-Fock (HF) method is a very popular method employed to obtain approximate solutions to the electronic Schrödinger equation. It has proven to be a valuable theoretical approach to the study of atoms and molecules and forms the basis of a number of more elaborate methods.

In the HF method for a closed-shell system, the wavefunction takes the form of a single antisymmetrized product (a Slater determinant) of spin orbitals, $\psi_i(x_j)$:

$$\Psi_0 = \frac{1}{\sqrt{n!}} \begin{vmatrix} \psi_1(x_1) & \psi_1(x_2) & \cdots & \psi_1(x_n) \\ \psi_2(x_1) & \psi_2(x_2) & \cdots & \psi_2(x_n) \\ \psi_3(x_1) & \psi_3(x_2) & \cdots & \psi_3(x_n) \\ \vdots & \vdots & \ddots & \vdots \\ \psi_n(x_1) & \psi_n(x_2) & \cdots & \psi_n(x_n) \end{vmatrix} = \frac{1}{\sqrt{n!}} \det|\psi_1(x_1)\psi_2(x_2)\cdots\psi_n(x_n)| \quad (1.5)$$

Using the variational method, with the wavefunction of Equation (1.5) and the Hamiltonian of Equation (1.4), the problem of solving the n -electron Schrödinger equation is reduced to the problem of solving n one-electron HF integro-differential equations of the form:

$$f(x_1)\psi_i(x_1) = \varepsilon_i\psi_i(x_1) \quad , \quad (1.6)$$

where $f(x_1)$ is an effective one-electron operator known as the Fock operator, and $\psi_i(x_1)$ is a spin-orbital with orbital energy ε_i . For a closed-shell molecule with n electrons, there is a total of n filled spin-orbitals. The spin-orbitals are taken as a product of an orbital and a spin function:

$$\psi_i(x_j) = \phi_i(r_j) \times \begin{cases} \alpha(w_j) = \phi_i(r_j) \\ \beta(w_j) = \bar{\phi}_i(r_j) \end{cases} \quad (1.7)$$

which gives rise to a total of $n/2$ doubly occupied orbitals, $\phi_i(r_j)$. By integrating over the spin functions and exploiting their orthonormality properties, the Fock operator can be expressed as:

$$f(r_1) = -\frac{1}{2}\nabla_1^2 - \sum_{A=1}^N \frac{Z_A}{r_{1A}} + V^{HF}(r_1), \quad (1.8)$$

where the first two terms represent the kinetic energy and nuclear-electron attraction, and can be collectively denoted as $h(r_1)$. The last term in the Hartree-Fock potential, $V^{HF}(r_1)$, models the electron-electron repulsion interaction, and represents the average potential felt by an electron at r_1 as it moves in the field created by the other $(n-1)$ electrons. Hence, the instantaneous electron-electron interactions are modeled in an averaged way in the HF formalism. $V^{HF}(r_1)$ is defined as:

$$V^{HF}(r_1) = \sum_{j=1}^{n/2} 2J_j(r_1) - K_j(r_1), \quad (1.9)$$

where $J_j(r_1)$ and $K_j(r_1)$ are the Coulomb and exchange operators, respectively, and are defined as:

$$J_j(r_1)\phi_i(r_1) = \left[\int \phi_j^*(r_2)\phi_j(r_2) \frac{1}{r_{12}} dr_2 \right] \phi_i(r_1) \quad (1.10)$$

$$K_j(r_1)\phi_i(r_1) = \left[\int \phi_j^*(r_2)\phi_i(r_2) \frac{1}{r_{12}} dr_2 \right] \phi_j(r_1). \quad (1.11)$$

The Coulomb operator, $J_j(r_1)$, represents the interaction between electron 1 and a “smeared out” electron distribution for electron 2, $|\phi_j(r_2)|^2$. The exchange operator, $K_j(r_1)$, arises from the necessity of the wavefunction to be antisymmetric with respect to the interchange of electrons and is harder to visualize. The HF equation may be written in terms of orbitals as:

$$\left[h(r_1) + \sum_{j=1}^{N/2} (2J_j(r_1) - K_j(r_1)) \right] \phi_i(r_1) = \varepsilon_i \phi_i(r_1). \quad (1.12)$$

At first glance, the HF equation appears to be a simple one-electron eigenvalue equation, but this is misleading since the Fock operator depends on the eigenfunctions, $\phi_i(r_1)$, through the Coulomb and exchange operators. Hence, the HF equations are non-linear equations which must be solved iteratively.

Practical solution of the system of HF equations involves expanding the orbitals in terms of a set of K known basis functions $\{\chi_s(r_1)\}^{25}$:

$$\phi_i(r_1) = \sum_{s=1}^K \chi_s(r_1) c_{si}. \quad (1.13)$$

The resultant HF equations, known as the Hartree-Fock-Roothaan-Hall (HFRH) equations, have the following form:

$$f(r_1) \sum_{s=1}^K \chi_s(r_1) c_{si} = \varepsilon_i \sum_{s=1}^K \chi_s(r_1) c_{si}. \quad (1.14)$$

The system of HFRH equations may be conveniently represented in matrix form:

$$\mathbf{FC} = \mathbf{SC}\boldsymbol{\varepsilon}, \quad (1.15)$$

where \mathbf{F} is the Fock matrix, \mathbf{C} is the matrix of molecular orbital coefficients, \mathbf{S} is the overlap matrix, and $\boldsymbol{\varepsilon}$ is the matrix of orbital energies. All of the matrices are of dimension $K \times K$. The elements of the Fock matrix are defined as:

$$\begin{aligned} F_{rs} &= \langle \chi_r(r_1) | f(r_1) | \chi_s(r_1) \rangle \\ &= \int \chi_r^*(r_1) h(r_1) \chi_s(r_1) dr_1 + \sum_{j=1}^{N/2} \left[2 \int \chi_r^*(r_1) J_j(r_1) \chi_s(r_1) dr_1 - \int \chi_r^*(r_1) K_j(r_1) \chi_s(r_1) dr_1 \right] \\ &= \int \chi_r^*(r_1) h(r_1) \chi_s(r_1) dr_1 + \sum_{j=1}^{N/2} \left[2 \int \chi_r^*(r_1) J_j(r_1) \chi_s(r_1) dr_1 - \int \chi_r^*(r_1) K_j(r_1) \chi_s(r_1) dr_1 \right] \end{aligned} \quad (1.16)$$

while the elements of the overlap matrix are defined as:

$$S_{rs} = \langle \chi_r(r_1) | \chi_s(r_1) \rangle = \int \chi_r^*(r_1) \chi_s(r_1) dr_1 \quad (1.17)$$

Solving the HFRH equations reduces to a matrix algebra problem of determining the matrices $\mathbf{\epsilon}$ and \mathbf{C} . However, since the Fock matrix elements depend on the expansion coefficients (\mathbf{C}), which are the desired solutions, the HFRH matrix equation must be solved iteratively. The iterative technique, known as the self-consistent field (SCF) method, begins with an initial guess of the MO coefficients, \mathbf{C}^0 , and continues until there are no significant changes in \mathbf{C} from one iterative cycle to the next. Once converged, the total energy of the system, including nuclear-nuclear repulsion, is computed along with the expectation values of any desired molecular properties (e.g. the dipole moment).

Using spin-orbitals, the HF total energy of the system is given by:

$$E_{total} = \sum_{i=1}^n \langle \psi_i(x_1) | h(x_1) | \psi_i(x_1) \rangle + \frac{1}{2} \sum_{i=1}^n \sum_{j=1}^n [\langle ij | ij \rangle - \langle ij | ji \rangle] + \sum_{A=1}^N \sum_{B=1}^N \frac{Z_A Z_B}{R_{AB}}, \quad (1.18)$$

where the following shorthand notation has been employed for the two-electron integrals (arising from the Coulomb and exchange operators):

$$\langle ij | kl \rangle = \iint \psi_i^*(x_1) \psi_j^*(x_2) \frac{1}{r_{12}} \psi_k(x_1) \psi_l(x_2) dx_1 dx_2. \quad (1.19)$$

For a closed-shell molecule with n electrons the same set of orbitals are used for the α and β spin functions, resulting in the familiar chemical picture of a set of $n/2$ doubly occupied MOs. The HF method as applied to closed-shell systems is known as the restricted Hartree-Fock (RHF) method. For an open-shell molecule, in which the number of α and β electrons differ, there are two possible approaches within the HF scheme. The first, known as the restricted open-shell Hartree-Fock (ROHF) method, treats all paired electrons the same as in the RHF scheme, giving rise to a set of doubly occupied orbitals, while the unpaired electrons are placed into unique orbitals. In the second approach, referred to as the unrestricted Hartree-Fock (UHF) method, different orbitals are used for the α and β electrons. The UHF wavefunction has more flexibility than the ROHF wavefunction and as such will give a lower energy. However, the UHF wavefunction, unlike the ROHF (and RHF) wavefunction, is not an eigenfunction of the spin operator, S^2 , and higher spin states may contaminate the UHF wavefunction. For example, a UHF calculation of a triplet state may be contaminated by the quintet, septet, etc. states.

1.2 Post Hartree-Fock Methods (Electron Correlation Methods)

The presence of low lying electronic states in transition metal complexes makes the single-determinant HF representation of the wavefunction inadequate for these compounds, requiring a more complicated multi-determinantal wavefunction.^{9,10} Davidson²⁰ has stated that for modeling transition metal compounds the *ab initio* Hartree-Fock method “is hopelessly in error”, and these sentiments have been echoed by other researchers as well.⁶⁻⁸

One of the most popular multi-determinant wavefunction methods used in modeling transition metal compounds is configuration interaction (CI), which constructs an improved wavefunction by adding determinants for excited states to the HF determinantal wavefunction (Ψ_0).^{18,22,24} The K basis functions used in the MO expansion give rise to a total of $2K$ spin-orbitals, of which the lowest n are occupied at the HF level. The remaining $(2K-n)$ orbitals are unoccupied and form the set of virtual spin-orbitals. However, this is not the only possible configuration of the n electrons amongst the $2K$ spin-orbitals. Starting from the HF configuration (determinant), other configurations (determinants) can be generated by promoting electrons from the occupied spin-orbitals to the virtual spin-orbitals. The total wavefunction can then be expressed as a linear combination of Slater determinants for each configuration:

$$\begin{aligned} |\Psi_{total}\rangle &= \sum a_i |\Psi_i\rangle \\ &= a_0 |\Psi_0\rangle + \sum_{ur} a_a^r |\Psi_a^r\rangle + \sum_{\substack{a<b \\ r<s}} a_{ab}^{rs} |\Psi_{ab}^{rs}\rangle + \sum_{\substack{a<b<c \\ r<s<t}} a_{abc}^{rst} |\Psi_{abc}^{rst}\rangle + \sum_{\substack{a<b<c<d \\ r<s<t<u}} a_{abcd}^{rstu} |\Psi_{abcd}^{rstu}\rangle + \dots \end{aligned} \quad (1.20)$$

where electrons are excited from occupied spin-orbitals, indexed by $\{a,b,c,d\}$, into virtual spin-orbitals, indexed by $\{r,s,t,u\}$. The Slater determinants are classified in terms of the number of electrons excited. A singly-excited determinant (Ψ_a^r) is formed by exciting a single electron from an occupied spin-orbital ψ_a to a virtual spin-orbital ψ_r . A doubly-excited determinant (Ψ_{ab}^{rs}) is formed by exciting two electrons from spin-orbitals ψ_a and ψ_b into virtual spin-orbitals ψ_r and ψ_s . A schematic of how singly- and doubly-excited configurations arise is given in Figure 1.1. Triply-, quadruply-, and n -tuply-excited configurations are formed in an analogous manner by exciting three, four and n electrons from the occupied spin-orbitals into virtual spin-orbitals. As the size of the molecule increases, the number of configurations in the wavefunction expansion grows very quickly and it soon becomes necessary to limit their number. The doubly-excited configurations make the largest contribution to the total wavefunction followed by the quadruple, single

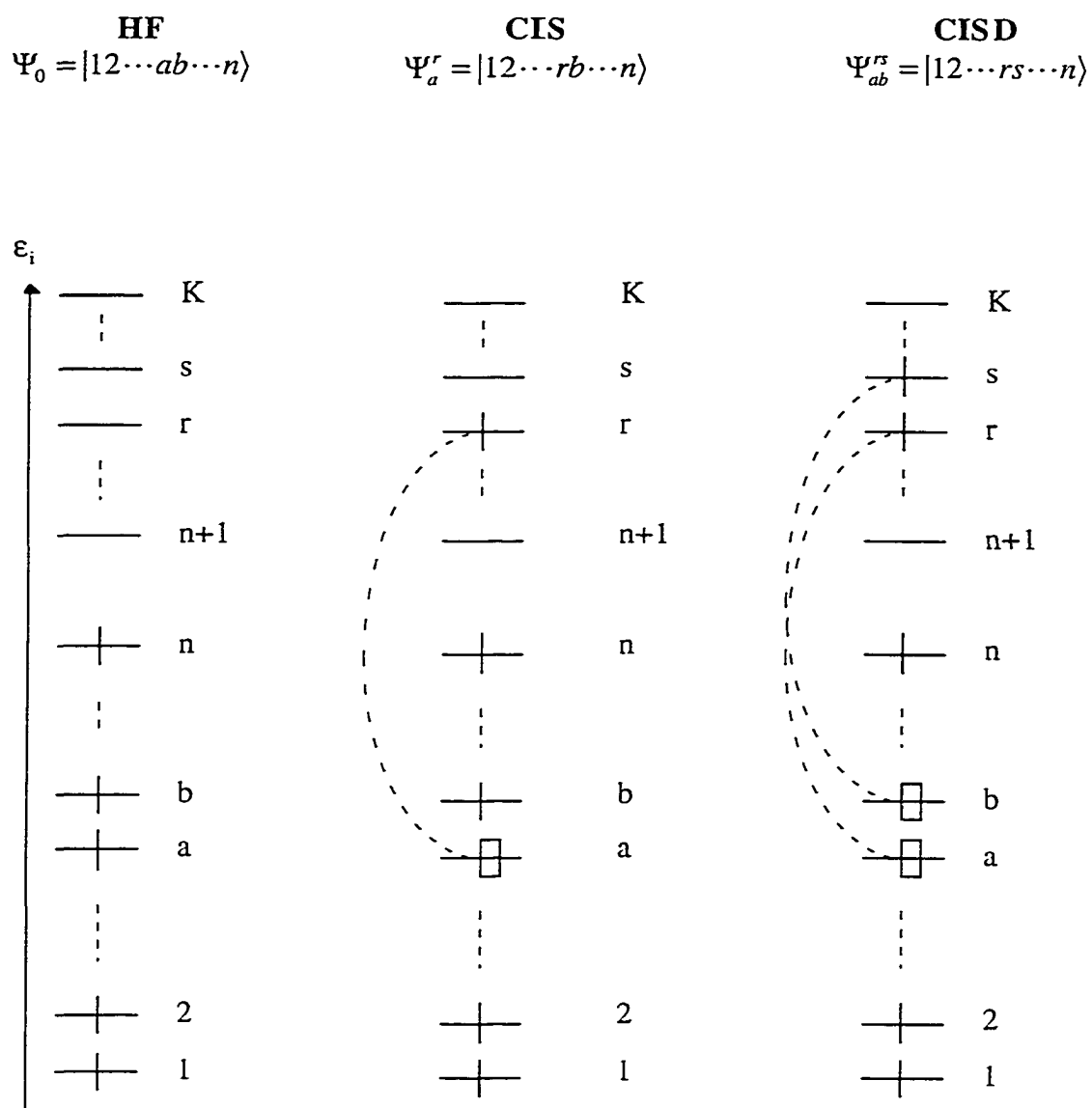


Figure 1.1: Schematic to illustrate how excited configurations are generated in a CISD calculation. (Adapted from Szabo and Ostlund²²)

and triple excitations.²² Not surprisingly, the most popular type of CI calculation includes all singly- and doubly-excited configurations and is termed CISD.

The total wavefunction is determined via a linear variational method in which the wavefunction expansion coefficients $\{a_i\}$ are varied in order to minimize the energy of the system. If a complete basis set is employed, and all possible configurations are included, a CI calculation will give the exact Born Oppenheimer non-relativistic molecular wavefunction, Ψ_{true} , and energy E_{true} . In practice, a finite basis set is employed and the number of configuration must be limited.

The difference between the HF energy (E_0) and the exact non-relativistic energy (E_{true}) of the system is referred to as the correlation energy (E_{corr}). Normally, the exact energy of the system is not known, and a related quantity, the basis set correlation energy, is defined as the difference between the HF energy (E_0) and the full-CI energy (E_{CI}), computed with the same finite basis set. Comparing the CISD correlation energy ($E_0 - E_{\text{CISD}}$) to the basis set correlation energy ($E_0 - E_{\text{CI}}$) gives an indication of how well the CISD method approximates the full CI method. Harrison and Handy²⁶ have shown that for small molecules (less than 10 electrons) CISD recovers about 94 % of the basis set correlation energy, however the results worsen as the size of the molecule increases. For example, Sasaki²⁷ has shown that CISD recovers 68-78 % of the basis set electron correlation energy in 50 electron molecules, while 55-67 % is recovered for molecules with about 100 electrons. The results are improved when triple and quadruple excitations (CISDTQ) are included in the wavefunction expansion. CISDTQ recovers 90-96 % of the basis set electron correlation energy for molecules containing 50 electrons, while 80-90 % is recovered for molecules containing 100 electrons.²⁷

Unfortunately, the CISD method is computationally demanding, formally scaling as K^5 , where K is the number of basis functions, and therefore requires powerful computing resources to treat large transition metal compounds. Møller-Plessett perturbation theory is an alternative approach to the incorporation of electron correlation effects which is much less computationally demanding.^{22,24} If the HF wavefunction is a good representation of the true wavefunction (i.e. the value of the expansion coefficient for the HF wavefunction, a_0 , is large relative to the remaining expansion coefficients) then one can consider electron correlation to be a perturbation to the HF Hamiltonian:

$$\begin{aligned} \hat{H} &= H - H^{(0)} \\ &= \sum_{i=1}^n \sum_{j>i}^n \frac{1}{r_{ij}} - \sum_{j=1}^n \sum_{k=1}^n [J_k(j) - K_k(j)] \end{aligned} \quad (1.21)$$

where H is the true non-relativistic Hamiltonian and $H^{(0)}$ is the sum of one-electron Fock operators. The perturbation H' is the difference between the true electron-electron repulsion and the HF model. In molecular calculations of transition metal compounds Møller-Plessett corrections to the second-order (MP2) are commonly included. The MP2 correction to the energy of the ground state of a molecule is given by:

$$\begin{aligned}
 E_0^{(2)} &= \sum_{s \neq 0} \frac{|\langle \psi_s^{(0)} | H' | \Psi_0^{(0)} \rangle|^2}{E_0^{(0)} - E_s^{(0)}} \\
 &= \sum_{b=1}^{n-1} \sum_{a=b+1}^n \sum_{r=n+1}^{K-1} \sum_{s=r+1}^K \frac{|\langle rs|ab \rangle - \langle rs|ba \rangle|^2}{\epsilon_a + \epsilon_b - \epsilon_r - \epsilon_s}
 \end{aligned}
 \tag{1.22}$$

where the shorthand notation of Equation (1.19) was employed for the two-electron integrals. MP2 calculations are similar in nature to CISD calculations, involving double excitations from the occupied spin-orbitals (a, b) to the virtual spin-orbitals (r, s).

The MP2 method behaves properly near the equilibrium molecular geometry, but tends to fail as the geometry is distorted far from the equilibrium.^{22,24} Bartlett has shown that the MP2 method, employing double-zeta plus polarization basis sets, recovers about 85-95 % of the basis set correlation energy for small closed-shell molecules.²⁸ The low computational cost of the MP2 approach, which scales as about K^4 , coupled with its ability to properly treat molecules at their equilibrium geometries, has led to its popularity in modeling transition metal complexes.

Other post-HF electron correlation methods exist which are extensions of the CI method (e.g. MC-SCF, CAS-SCF and MR-CI), or are based on the coupled cluster formalism (i.e. CCSD(TQ)).²² However, these methods were not used in the work described in this thesis and will not be discussed.

1.3 Density Functional Theory

Over the last decade, density functional theory (DFT) has established itself as an alternative to the HF and post-HF approaches. The n -electron wavefunction (a Slater determinant or a linear combination of a number of Slater determinants) is at the centre of the conventional HF-based methods, and since each electron is expressed in terms of three spatial coordinates (and a spin coordinate) the wavefunction depends on $3n$ coordinates. On the other hand, in the DFT formalism the ground state molecular energy, and all other molecular properties are determined by the electron density, $\rho(x,y,z)$. Hence, DFT formally simplifies the computational problem by focusing on the three-dimensional

electron density, $\rho(r)$, instead of the $3n$ -dimensional wavefunction, $\Psi(r_1, r_2, \dots, r_n)$, where r represents a point in cartesian space. Furthermore, the electron density, $\rho(r)$, is a real physical quantity with a direct meaning, while the wavefunction, $\Psi(r_1, r_2, \dots, r_n)$, is a more abstract entity which is harder to conceptualize.^{7,8,29-32}

The foundations of the DFT formalism are rooted in the seminal work of Hohenberg and Kohn³³ who, in 1964, proved that the total energy of a molecule in a non-degenerate ground electronic state can be completely and uniquely determined through its electron density $\rho(r)$. In other words, the energy of the system can be expressed as a functional of the electron density:

$$E_0 = E_0[\rho(r)] . \quad (1.23)$$

Unfortunately, the theorem did not indicate what the correct form of the energy functional is, nor did it provide the details necessary to determine it.

Kohn and Sham³⁴ extended the Hohenberg-Kohn theorem by deriving a set of one-electron eigenvalue equations similar to the HF equations:

$$F^{KS}(r_1)\psi_i^{KS}(r_1) = \epsilon_i^{KS}\psi_i^{KS}(r_1), \quad (1.24)$$

where $\psi_i^{KS}(r_1)$ is known as a Kohn-Sham (KS) orbital, with orbital energy ϵ_i^{KS} . The electron density is defined in terms of the KS orbitals:

$$\rho(r) = \sum_{i=1}^n |\psi_i^{KS}(r_i)|^2 . \quad (1.25)$$

The Kohn-Sham operator, $F^{KS}(r_1)$, is defined as:

$$F^{KS}(r_1) = -\frac{1}{2}\nabla_1^2 - \sum_{\alpha=1}^N \frac{Z_\alpha}{r_{1\alpha}} + \sum_{j=1}^n J_j(r_1) + V_{xc}(r_1). \quad (1.26)$$

The first two terms are the usual kinetic energy and nuclear-electron attraction terms, while the third term is the familiar Coulomb repulsion term defined in the DFT formalism as:

$$J_j(r_1) = \int \frac{\rho(r_2)}{r_{12}} dv_2 . \quad (1.26)$$

The last term, $V_{xc}(r_1)$, is the exchange-correlation potential term.

In the DFT ansatz the ground state energy of the system is given by:

$$E_0 = -\frac{1}{2} \sum_{i=1}^n \langle \psi_i^{KS}(r_1) | \nabla_i^2 | \psi_i^{KS}(r_1) \rangle - \sum_{\alpha=1}^N \int \frac{Z_\alpha \rho(r)}{r_{1\alpha}} dv_1 + \frac{1}{2} \iint \frac{\rho(r_1)\rho(r_2)}{r_{12}} dv_1 dv_2 + E_{xc}[\rho(r)]. \quad (1.28)$$

If the correct form of the energy functional, $E_{xc}[\rho(r)]$, is employed solutions of the Kohn-Sham equations will be the exact ground state energy and electron density. Unfortunately,

the true form of $E_{xc}[\rho(r)]$ is not known, and approximate energy functionals must be employed.

The energy functional may be separated into exchange and correlation components:

$$E_{xc}[\rho(r)] = E_x[\rho(r)] + E_c[\rho(r)]. \quad (1.29)$$

A number of approximate exchange and correlation functionals have been devised for use in molecular DFT calculations. The simplest of these approximate functionals depend solely on the electron density, and are termed local functionals. Slater's exchange functional and the correlation functional of Vosko, Wilk, and Nusair (VWN) are examples of local density functionals. Local density functionals are based on fits to the homogeneous electron gas model, which models the electron density as uniformly distributed throughout space. However, the electron density distribution in a molecule is typically far from uniform and a number of approximate density functionals have been devised which attempt to correct for this non-homogeneity through an explicit dependence on the gradient of the electron density, $\nabla\rho(r)$, in the functional. These density functionals are referred to as non-local or gradient-corrected functionals and a number of them have been derived for use in molecular DFT calculations including the exchange functional due to Becke (B), and the correlation functionals devised by Lee, Yang, and Parr (LYP), Perdew (P86), and Perdew and Wang (PW91). A number of studies have demonstrated the superiority of the gradient-corrected functionals over their local counterparts, particularly in calculating dissociation energies and reaction energies.³⁵⁻³⁸

Once an approximate exchange-correlation functional is chosen, the Kohn-Sham equations, Equation (1.25), are solved in a similar manner as that used in the HF approach. The KS orbitals, $\psi_i^{KS}(r_1)$, are expanded in terms of a known basis set, $\{\chi_\mu(r_1)\}$:

$$\psi_i^{KS}(r_1) = \sum_{\mu=1}^K \chi_\mu(r_1) c_{\mu i}. \quad (1.30)$$

The expansion coefficients $\{c_{\mu i}\}$ are solved for using the linear variational method. As in the HF method, an iterative procedure is required.

The DFT formalism has emerged as the method of choice for modeling transition metal compounds.⁸ In the density functional theory approach electron correlation effects are incorporated in a very straightforward way, by specifying the approximate correlation functional to be used. On the other hand, inclusion of electron correlation effects via the post-HF approach is not as easy, typically involving a number of difficult decisions to be made by the researcher which may have a significant impact on the results. The accuracy of the results from gradient-corrected DFT calculations has been shown to be comparable to that obtained with post-HF methods.^{7,8} However, the computational demands of the DFT

approach are only slightly higher than that for the HF method. Research is currently under way to further improve the computational scaling of the DFT calculations. Along with the ease of incorporating electron correlation effects and the decreased computational demands, it has been shown that smaller basis sets, with fewer polarization functions, are required to obtain convergence of the results in DFT calculations than in the post-HF methods.

Generally, the quality of a DFT calculation depends directly on the approximate energy functional employed. Unfortunately, the DFT approach is not variational with respect to the choice of the approximate density functional. Essentially, there is no recipe for choosing the best approximate exchange-correlation functional and furthermore, an approximate density functional which works well for one molecular system may not necessarily work for another. A number of density functionals must be thoroughly tested, by trial and error, for each molecular system of interest. This is a significant drawback of the DFT approach and, in a sense, makes it more empirical than the wavefunction approach.

Questions have been raised regarding the applicability of the DFT formalism to studies of the excited states of molecules. The Hohenberg-Kohn theorem refers specifically to the ground electronic state of a molecule and it is not clear whether it can be extended to include the excited states of molecules. This issue has been addressed recently using a time-dependent DFT approach by Casida and co-workers.³⁹⁻⁴³ The exact meaning and nature of the KS orbitals has also been addressed recently by Hoffmann *et al.*⁴⁴ The HF orbitals are routinely used to qualitatively describe changes in bonding and chemical reactivities, however, the use of the KS orbitals in this manner has not been as widely accepted. Formally the KS orbitals are constructs used to produce the total electron density, Equation (1.27), and should not be regarded in the same light as the HF orbitals. The KS orbitals have been shown to resemble the HF orbitals and one could argue that since DFT incorporates electron correlation effects, the KS orbitals are more suitable than their HF counterparts.

1.4 Semiempirical Methods

Semiempirical methods provide an economical alternative to the *ab initio* and DFT methods. In HF, post-HF, and DFT calculations, evaluation of the two-electron integrals:

$$(ij|kl) = \iint \chi_i^*(r_1) \chi_k^*(r_2) \frac{1}{r_{12}} \chi_j(r_1) \chi_l(r_2) dr_1 dr_2 \quad (1.31)$$

is a computationally demanding task. Semiempirical techniques employ a number of approximations based on the neglect of diatomic overlap (NDO) approximation to reduce the number of integrals which must be evaluated. Furthermore, the integrals retained are not evaluated, but rather are represented by parameters whose values are obtained by fitting to geometric structures, ionization potentials, electron affinities, and other molecular properties from experiment or high level *ab initio* calculations.⁴⁵

Semiempirical methods have long been used in modeling organic chemistry, from the early qualitative schemes like the simple Huckel molecular orbital method used in treating conjugated and aromatic hydrocarbons, to the more quantitative schemes such as: MNDO (modified neglect of diatomic overlap)⁴⁶⁻⁵¹, AM1 (Austin model 1)^{52,53}, and PM3 (parameterized method 3)⁵⁴. The application of semiempirical methods to molecules containing transition metal elements has not been as common and parameter sets for the transition metals are rarer than those for the lighter elements. The main problem in applying semiempirical methods to the transition elements is associated with the transferability of the atomic parameters. A single set of semiempirical parameters is defined for each atom and these parameters should be representative of the atom in a large variety of different molecules. This is challenging for the transition metal atoms, since they are found in such varied chemical environments (coordination geometries, ligand sets, spin and oxidation states). The PM3(tm) semiempirical method has been recently developed by researchers at Wavefunction Inc., and implemented into their program Spartan.⁵⁵ Parameters were derived by fitting to experimental structure and are currently available for about half of the transition elements. Unfortunately, the full details of the parameterization have not been published, and although a number of studies have appeared as of late⁵⁶⁻⁶⁰, more work is needed to fully gauge its reliability. Another set of semiempirical parameters, known as ZINDO, have been derived for the first two transition series by Zerner and co-workers.^{61,62} These parameter sets were specifically designed for the prediction of spectroscopic properties of molecules, and have been implemented into the Cerius² program package.⁶³

The main advantage of semiempirical methods is their modest computational cost compared to *ab initio* HF and DFT methods. Semiempirical methods are said to incorporate “nature’s electron correlation”, since the atomic parameters are based on fits to experimental data. However, the overall accuracy of a semiempirical calculation relies heavily on the atomic parameters, and the best results are usually obtained for molecules which closely resemble the ones used in the parameter fitting process.

1.5 Basis Sets

In both the wavefunction and DFT approaches, the molecular orbitals are expanded in terms of a known basis set. The choice of basis set plays a fundamental role in determining the accuracy of the calculations.^{18,22,64,65} Two types of basis functions are commonly employed in most HF and DFT based calculations: Slater Type Orbitals (STOs) and Gaussian Type Functions (GTFs). STOs are normally expressed in spherical coordinates as:

$$\chi_{nlm}(r, \theta, \phi) = R_{nl}(r)Y_{lm}(\theta, \phi) \quad (1.32)$$

$$R_{nl}(r) = Nr^{n-1}e^{-\zeta r} \quad (1.33)$$

$$N = (2\zeta)^{n+1/2}[(2n)!]^{-1/2} \quad (1.34)$$

where $R_{nl}(r)$ designates the radial function and $Y_{lm}(\theta, \phi)$ is a spherical harmonic function, defining the angular component of the basis function. The indices n , ℓ , m are the principal, angular momentum, and magnetic quantum numbers, respectively. The normalization constant is denoted by N , and ζ is the exponent, determining the extent of the radial function. GTFs may also be expressed in terms of spherical coordinates as:

$$\chi_{nlm}(r, \theta, \phi) = R_{nl}(r)Y_{lm}(\theta, \phi) \quad (1.35)$$

$$R_{nl}(r) = Nr^{n-1}e^{-\alpha r^2} \quad (1.36)$$

$$N = 2^{n+1}[(2n-1)!!]^{-1/2}(2\pi)^{-1/2}\alpha^{(2n+1)/2}, \quad n = \ell + 1, \ell + 3, \ell + 5, \dots \quad (1.37)$$

where the same notation has been used with the exception of the exponent, which is denoted here by α instead of ζ . In molecular calculations, GTFs are normally used in their Cartesian gaussian form:

$$\chi_{lmn}(x, y, z) = Nx^{\ell}y^mz^n e^{-\alpha r^2} \quad (1.38)$$

$$N = (2\pi)^{3/2}[(2\ell-1)!!(2m-1)!!(2n-1)!!]^{-1/2}\alpha^{(\ell+m+n+3/2)} \quad (1.39)$$

where N is the normalization constant, $x^{\ell}y^mz^n$ defines the angular portion of the gaussian function (with $\ell+m+n=0$ for an s -type gaussian function, $\ell+m+n=1$ for a p -type gaussian function, $\ell+m+n=2$ for a d -type gaussian function, etc.), and the exponent again denoted by α .

In choosing a basis set two main considerations must be weighed against one another. First, the basis functions should have correct limiting properties (as $r \rightarrow 0$ and $r \rightarrow \infty$). Secondly, it is desirable to use those basis functions which are the most computationally efficient in evaluating the time consuming two-electron integrals. The

STOs are the most suitable choice to fulfill the first criterion, since they exhibit the proper “cusp” behaviour at the point nucleus:

$$\left. \frac{d\chi_{1s}^{STO}(r)}{dr} \right|_{r=0} \neq 0, \quad (1.40)$$

while a GTF does not:

$$\left. \frac{d\chi_{1s}^{GTF}(r)}{dr} \right|_{r=0} \propto -2\alpha r e^{-\alpha r^2} \Big|_{r=0} = 0. \quad (1.41)$$

An STO also decays exponentially at large values of r , while a GTF decays too fast. On the other hand integration over GTFs is much simpler than integration over STOs, leading to large savings in the computational cost. By employing a large number of gaussian functions it is possible to correct for the poor cusp and tail behaviour of GTFs. However, this quickly increases the computing time; consequently, linear combinations of gaussian functions with fixed coefficients are used:

$$\chi_{\mu,X}^{GTF}(r) = \sum_{i=1}^K G_X(\alpha_i; r) d_{\mu i}^X. \quad (1.42)$$

The superscript X designates the type of gaussian function (s, p, d, f , etc.). The expanded basis functions, $\chi_X^{GTF}(r)$, are called contracted gaussian type functions (CGTFs) while those used in the expansion, $G_X(\alpha; r)$, are referred to as primitive gaussian type functions (PGTFs). The expansions are normally obtained by varying the exponents $\{\alpha_i\}$ and contraction coefficients $\{d_{\mu i}^X\}$ to minimize Hartree-Fock atomic energies.

The nomenclature and symbols used to represent basis sets in quantum chemistry calculations are far from systematic; however, some terms commonly used in the literature are described below. A minimal atomic basis set is one in which the number of CGTFs equals the number of occupied atomic orbitals. A number of minimal basis sets have been devised including; the STO-3G basis sets of Hehre and co-workers⁶⁶⁻⁷⁰ and the MINI-n basis sets of Huzinaga and co-workers⁶⁴. The small size of these basis sets makes them favorable for calculations involving large molecules, but they are capable of qualitative results at best. Minimal basis sets do not have the necessary flexibility to expand and contract when the atom is placed in different chemical environments in a molecule. To correct for this a double-zeta atomic basis set can be used, where the number of CGTFs equals twice the number of occupied atomic orbitals. The contribution from the two CGTFs of the same symmetry is varied to produce a function intermediate between the two, as illustrated in Figure 1.2 (a). Related to the double-zeta basis sets are the split valence basis sets. Split valence basis sets consist of a minimal representation for the core atomic orbitals and a double-zeta representation for the valence atomic orbitals. There are

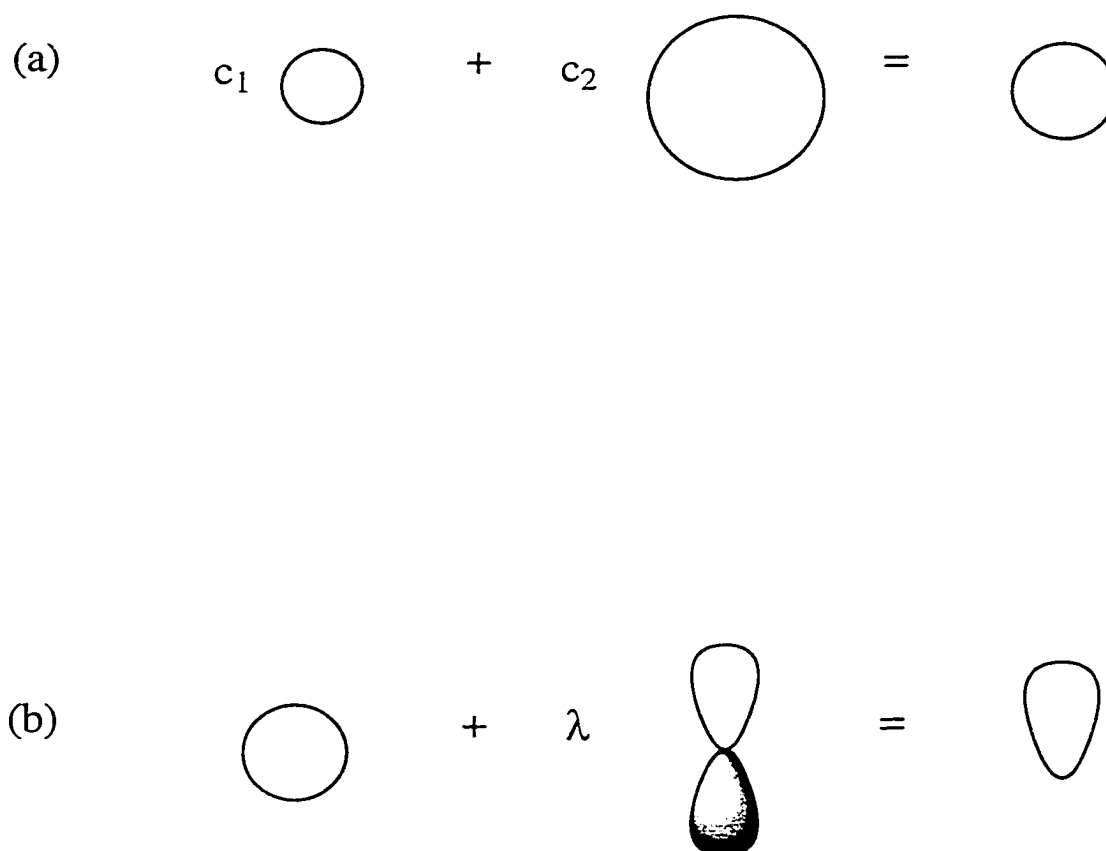


Figure 1.2: Schematic to illustrate basis set effects. (a) The effect of mixing two basis functions of varying exponents, as in a double-zeta atomic basis set, and (b) the effect of adding a polarization function to an atomic basis set. (Adapted from Hehre, Radom, Schleyer, and Pople¹⁸)

many split-valence double-zeta quality basis sets including: the 3-21G⁷¹⁻⁷⁵, 4-31G⁷⁶⁻⁷⁹, and 6-31G⁸⁰⁻⁸² of Pople *et al.*, the MIDI-n basis sets of Huzinaga and co-workers⁶⁴, the VDZ basis sets of Ahlrichs *et al.*⁸³, and the DZ basis sets of Dunning and Hay^{84,85}. Split-valence basis sets have been developed which are of triple-zeta (6-311G, VTZ⁸⁶, cc-pVTZ⁸⁷), quadruple-zeta (cc-pVQZ⁸⁷), quintuple-zeta (cc-pv5Z⁸⁷) valence quality and higher. The basis sets used to represent the occupied valence atomic orbitals may be expanded as desired, assuming the necessary computing resources are available.

The electronic charge distribution of atoms becomes highly distorted in a molecule, and atomic basis sets account for this by employing one or more polarization functions (i.e. a basis function with higher angular momentum quantum number ℓ than the highest occupied atomic shell). For example, a *d*-type polarization function is added to the basis sets of the main group elements, a *p*-type polarization function to the hydrogen basis set, and an *f*-type polarization function to transition metal atom basis sets. The polarization function mixes with the valence basis functions producing hybrid functions with an anisotropic distribution of electronic charge, as illustrated in Figure 1.2(b).

Basis sets used in molecular calculations should be well balanced, with basis sets of similar quality used for each atom in the molecule. Expansion of the basis set should be accompanied by the addition of appropriate polarization functions, to generate a high quality basis set. Typically, single polarization functions are added to valence double-zeta quality basis sets. Triple-zeta valence quality basis sets usually require the addition of two polarization functions to the heavy atom basis sets, along with a *p* polarization function to the hydrogen atom basis sets.⁶⁵

The notation employed to describe CGTF basis sets is quite varied. One of the simpler schemes, and the one used throughout this thesis, will be described here. The popular 6-31G* split valence double-zeta plus polarization basis set of Pople and co-workers, consists of a single CGTF, comprised of six PGTFs, for each of the occupied core shells and two CGTFs, of three and one PGTFs, respectively, for each of the occupied valence shells of the atom, plus a single *d* polarization function added to all of the main group atoms. Using carbon as an example, another notation for the 6-31G* basis sets is (631/31/1*). This notation describes the contraction pattern of each atomic shell starting with the *s*-shell, followed by the *p*- and *d*-shells, where slashes (/) are used to separate the shells. A general contraction pattern is expressed as $(n_{1s}n_{2s}\dots/n_{2p}n_{3p}\dots/n_{3d}n_{4d}\dots)$, where the number of PGTFs used to represent the individual occupied *s*-, *p*-, and *d*-shells is given by $\{n_{1s}, n_{2s}, \dots\}$, $\{n_{2p}, n_{3p}, \dots\}$ and $\{n_{3d}, n_{4d}, \dots\}$. This notation is advantageous in that it gives the number of PGTFs used in each CGTF. Polarization functions are represented by 1* in this notation. Hence, the (631/31/1*)

notation for the 6-31G* basis set of carbon, indicates that there is a single CGTF expanded in terms of six PGTFs for the 1s core shell, and two CGTFs, expanded in terms of three and one PGTFs, for each of the 2s and 2p valence shells. The single *d* polarization function is represented by 1* in the *d*-space.

1.6 Pseudopotential Methods

As mentioned earlier, one of the primary challenges of modeling transition metal compounds is their large size, both in terms of the number of atoms and the number of electrons. From a computational chemistry point of view, it is the large number of electrons which pose the main problem, since basis functions are employed to represent the occupied shells of each atom in the molecule. However, by realizing that the bonding between the atoms in a molecule arises primarily from the interaction of the valence atomic orbitals, with the core orbitals being inert, the computational cost can be reduced. The valence orbitals are more diffuse and able to deform as required for proper overlap with the orbitals on adjacent atoms to form a bond, while the core orbitals are contracted about the nuclei, and distort only slightly in the molecular environment. The core electrons act to effectively shield the nuclei, creating an effective nuclear charge in which the valence electrons move. This principle is convincingly demonstrated in the Periodic Table, where families of chemically related atoms (those in a single column) share identical valence electron configurations and, consequently, exhibit similar chemical properties. This principle can be exploited in computational chemistry through the use of pseudopotentials.

The idea behind the pseudopotential formalism, first introduced by Hellman^{88,89} in the 1930's, is to reduce the computational expense of the calculation. By replacing the chemically inert core electrons with a suitable potential function only the valence electrons are treated explicitly in the calculation.

The wavefunction, for the core and valence electrons may be written as:

$$\Psi_{total} = A[\Psi_{core}(1,2,\dots,n_c)\Psi_{val}(1,2,\dots,n_v)] \quad (1.43)$$

where Ψ_{core} and Ψ_{val} represent antisymmetrized wavefunctions for the n_c core and n_v valence electrons, respectively.⁹⁰⁻⁹³ The symbol *A* is an antisymmetrizer enabling permutations between core and valence electrons. The exact wavefunction cannot be factored in this fashion but approximate wavefunctions, like the HF wavefunction, can.⁹¹ The core potential acts to modify the one-electron Hamiltonian for the valence electrons as follows:

$$H^{val}(1, 2, \dots, n_v) = \sum_{i=1}^{n_v} \left(h(r_i) + \sum_{i < j}^{n_v} \frac{1}{r_{ij}} \right), \quad (1.44)$$

where the last term represents the electron-electron interaction between each pair of valence electrons and the one-electron operator, $h(r_i)$, is given by:

$$h(r_i) = -\frac{1}{2} \nabla_i^2 - \frac{(Z - n_c)}{r_i} + V_{core}. \quad (1.45)$$

The first term of $h(r_i)$ is the kinetic energy of valence electron i , while the second corresponds to the electrostatic attraction potential for a valence electron, i , interacting with an effective nuclear charge resulting from perfect screening of the nucleus by the n_c core electrons. The term V_{core} is the core potential, representing the Coulomb and exchange interactions between the core and valence electrons. This term is non-local in nature due to the exchange interaction, but is approximated in most pseudopotential methods by a simpler, local potential for computational efficiency. There are two pseudopotential techniques commonly employed: the model core potential (MCP) and the effective core potential (ECP). Typically, V_{core} is represented as a linear combination of gaussian-type functions, with adjustable parameters determined through fits to atomic Hartree-Fock calculations. The valence electrons not replaced by the core potential function are represented by basis functions as in all-electron calculations.

1.6.1 Model Core Potentials

The model core potential method was devised by Bonifacic and Huzinaga in the mid-1970s⁹⁴⁻⁹⁸ and has been reviewed recently⁹⁰⁻⁹³. The one-electron Hamiltonian, $h(r_i)$, in the model core potential formalism is given by:

$$h(r_i) = -\frac{1}{2} \nabla_i^2 - \frac{(Z - n_c)}{r} + V_{core}^{MCP} + P^{MCP} \quad (1.46)$$

where the core potential models the Coulomb and exchange interactions between the core and valence electrons, and the term P^{MCP} is a projection operator which ensures that the valence orbitals remain orthogonal to the core orbitals, preventing them from collapsing onto the core region. It has the following form:

$$P^{MCP} = \sum_{c=1}^{n_c} B_c |\phi_c\rangle \langle \phi_c|. \quad (1.47)$$

where ϕ_c are fixed core orbitals obtained from reference atomic HF calculations and B_c is a constant defined as:

$$B_c = -f_c \varepsilon_c, \quad 1 \leq f_c \leq 2. \quad (1.48)$$

The projection operator shifts the energy of any valence orbital which collapses onto a core orbital by the factor B_c , leaving the remaining valence orbital energies intact. The MCP method models the core-valence interactions with a local potential of the form:

$$V_{core}^{MCP} = \frac{1}{r} \sum_m A_m r^{\alpha_m - 1} e^{-\alpha_m r^2} \quad (1.49)$$

where $\{A_m; \alpha_m\}$ are the adjustable parameters. The parameters of the MCP core potential for each atom, $\{A_m; \alpha_m\}$, are optimized by fitting the valence orbital energies and shapes from reference atomic Hartree-Fock calculations. The following function is minimized:

$$\Delta = \sum_{v=1}^{NVS} \left(w_v |\varepsilon_v^{ref} - \varepsilon_v^{MCP}| + \sum_i W_v [r_i R_v^{ref}(r_i) - r_i R_v^{MCP}(r_i)]^2 \right), \quad (1.50)$$

where ε_v^{ref} and $R_v^{ref}(r_i)$ are the orbital energy and radial function of the v^{th} valence orbital, obtained from the reference atomic Hartree-Fock calculation, and ε_v^{MCP} and $R_v^{MCP}(r_i)$ are the corresponding values computed with the MCP. The radial functions are evaluated at discrete radial points, r_i , and the deviations between the orbital energies and radial functions are weighted using w_v and W_v , respectively. The core orbitals in the projection operator are taken directly from the reference atomic HF calculations, and the value of f_c is sometimes adjusted for molecular calculations. The valence electron shells not replaced by the core potential are represented by contracted gaussian basis functions, derived in the same manner used to derive all-electron basis sets.

The presence of the projection operator enables the valence orbitals to retain some of their nodal structure. The amount of nodal structure retained depends on the number of basis functions used for the valence shells. If the valence basis set is very flexible (i.e. contains a large number of primitive gaussian functions) the exact nodal structure of the valence orbitals may be reproduced. It is this feature of the MCP formalism which sets it apart from its ECP counterparts.

1.6.2 Effective Core Potentials

The following gives a brief overview of the ECP formalism, more detailed accounts are available from Krauss and Stevens⁹⁹, Cundari *et al.*¹⁰⁰ and Frenking *et. al.*¹⁰¹ In the ECP approach none of the nodal structure of the valence orbitals is retained. The valence atomic orbitals from reference atomic HF calculations are converted to nodeless ECP pseudo-orbitals by maximizing the fit to the radial function of the reference valence orbital at large values of r . This ensures a very good representation of the ECP pseudo-orbital in

the valence region, at the expense of the region near the nucleus. For example, the radial function for the ECP valence pseudo-orbital of the 5s shell of iodine would contain no nodes, while that for the all-electron reference orbital would contain four nodes.

The ECP pseudo-orbitals (χ_v) and corresponding energy eigenvalues are used to generate a numerical potential, via “inversion” of the Hartree-Fock equations which amounts to determining a numerical ECP which will reproduce the reference atomic HF wavefunction and energy. The numerical potential must then be transformed into an analytical form for use in computational chemistry calculations. The analytical form of the ECPs usually takes the form of a linear combination of gaussian functions:

$$r^2 V_\ell(r) = \sum_k A_{\ell,k} r^{n_{\ell,k}} e^{-B_{\ell,k} r^2} \quad (1.51)$$

where n and ℓ are the principal and angular momentum quantum number, respectively, and A_ℓ and B_ℓ are the ECP core potential parameters.

A number of different techniques have been used to optimize the ECP parameters $\{A_{\ell,k}; B_{\ell,k}\}$. The approach taken by Hay and Wadt¹⁰²⁻¹⁰⁴ and by Ermler and Christiansen¹⁰⁵⁻¹¹¹ was to fit the numerical potentials to the analytical form of the core potential, Equation (1.51), using a straightforward least squares fitting procedure. Unfortunately, this approach can lead to a large number of terms in the core potential which decreases the computational efficiency when employed in molecular calculations. Stevens *et al.*¹¹²⁻¹¹⁴ took a slightly different approach, generating their ECP core potentials by fitting to the valence orbitals and orbital energies obtained from accurate all-electron reference calculations. These ECPs, called compact effective core potentials, contain a small number of terms, typically less than six. A third approach, taken by Stoll and Preuss¹¹⁵⁻¹²¹, minimizes the differences in atomic excitation energies computed from the ECPs and all-electron reference calculations.

As in the MCP method, the final step in ECP preparation involves the optimization of the valence basis sets for those electrons not replaced by the core potential via fitting to the results of atomic calculations, as in the generation of all-electron basis sets.

1.6.3 Quasi-Relativistic Pseudopotentials

Relativistic effects are minor for compounds containing light elements, but their importance grows rapidly as one descends the rows of the periodic table. Relativistic effects are particularly important for the transition metal atoms, especially for members of the third row.^{9,10} Taking proper account of the major relativistic effects in computational studies of transition metal compounds presents another challenge to the computational

chemist. The HF formalism can be expanded to incorporate the major relativistic effects (i.e. the mass-velocity and Darwin terms) yielding the Quasi-Relativistic-Hartree-Fock (QRHF) approach.¹²² In all-electron calculations solving the QRHF equations is very time consuming and is limited to atoms and small molecules. These effects may be incorporated indirectly through the MCP and ECP core potential parameters. If the reference atomic calculations used to derive the MCP and ECP core potential parameters were carried out at the QRHF level, the resultant core potential parameters will carry the major relativistic effects for the core orbitals. In subsequent calculations employing these pseudopotentials, the valence shells remain non-relativistic, but the core shells, for which the relativistic effects are largest, indirectly incorporate the relativistic effects. Pseudopotentials which indirectly incorporate relativistic effects in this manner are referred to as quasi-relativistic pseudopotentials.^{123,124}

1.6.4 Comparison of MCPs and ECPs

The results of molecular calculations employing pseudopotentials do not differ significantly from those in which all of the electrons have been treated explicitly (see for instance the review by Cundari *et al.* and the references contained therein¹⁰⁰). Pseudopotentials afford a dramatic saving in computational cost without sacrificing accuracy, and as such have proven to be very popular in theoretical studies of transition metal compounds.

Studies performed thus far have shown that the incorporation of proper nodal structure into the MCP valence orbitals has not resulted in a significant increase in the accuracy of computed bond energies, geometries and spectroscopic parameters when compared to their ECP counterparts.^{101,125} The advantage of employing valence orbitals with nodal structure is more apparent in calculations of expectation values which exhibit a stronger dependence on the behaviour of the electrons in the region close to the nucleus, such as spin-orbit coupling constants.¹²⁶

Smaller basis set expansions are required for the valence orbitals in the ECP approach than in the MCP approach since fewer PGTFs are needed to expand a nodeless radial function than one containing multiple nodes. The smaller number of PGTFs reduces the computing time required for evaluating the two-electron integrals.

The use of pseudopotentials in modeling transition metal complexes raises the question of which electron shells should be included in the valence space. In general, there are two types of transition metal pseudopotentials: the large core and small core pseudopotential. In the large-core pseudopotential, the valence space contains only the ns

and $(n-1)d$ electron shells, with the remaining electronic shells replaced by the core potential. The small-core transition metal atom pseudopotentials also include the penultimate valence shell in the valence space. The $(n-1)p$ shell is included in the small-core transition metal atom MCPs, while both the $(n-1)s$ and $(n-1)p$ shells are included in the small-core transition metal atom ECPs. The small-core pseudopotentials, with an extended valence space, are recommended over their large-core counterparts, even though they are more computationally demanding.¹⁰¹

MCPs have been derived for nearly all of the elements of the periodic table. All of the main group elements, transition metal elements and actinides have been parameterized and work is currently underway to parameterize the lanthanides.¹²⁷⁻¹³⁰ The MCP core potential parameters and valence basis sets have been incorporated into a number of common quantum chemistry programs including: CADPAC¹³¹, and the development version of GAMESS^{132,133}. The ECPs of Hay and Wadt¹⁰²⁻¹⁰⁴ have been developed for all elements up to the lanthanides, while those of Stevens *et al.*¹¹²⁻¹¹⁴ have been developed for all of the elements, except the actinides. These two ECPs are very popular and have been directly implemented into the Gaussian¹³⁴ and GAMESS programs. The ECPs of Ermler and Christiansen¹⁰⁵⁻¹¹¹ and Stoll and Preuss¹¹⁵⁻¹²¹ have been developed for all of the elements of the periodic table, and the latter have been included directly in the Turbomole¹³⁵ and Molpro¹³⁶ programs.

1.7 Interpreting the Energy and Wavefunction

Under the Born-Oppenheimer approximation the electronic energy is computed at a fixed set of nuclear coordinates. If the energy is computed for a variety of nuclear coordinates then the potential energy hypersurface of the molecule may be mapped out. Hence, it is possible to optimize the geometry of the molecule by locating the set of coordinates which yield the minimum total energy. Although manually mapping out the computed energy at a number of geometric orientations is possible for very small molecules, a more automated procedure is required for larger systems. Geometry optimization amounts to minimization of the energy with respect to the nuclear coordinates:

$$\frac{\partial E}{\partial X_i} = 0 \quad (1.52)$$

where X_i represents a nuclear coordinate. Geometry optimizations may be carried out using numerical or analytical differentiation. Numerical differentiation approximates the required derivatives as:

$$\frac{\partial E}{\partial X_i} \approx \frac{\Delta E}{\Delta X_i} \quad (1.53)$$

where ΔE is the change in the energy as the nuclear coordinate is modified by an amount ΔX_i . For analytical differentiation the required derivatives are expressed in terms of an explicit formula. There is a dependence of the energy on the nuclear coordinates X_i in the two-electron integrals, as well as in the nuclear-electron attraction terms. Analytical gradient evaluation is more reliable than numerical differentiation and is currently available in a variety of quantum chemistry programs.^{18,22}

Chemically interesting points on the potential energy hypersurface are the local minima (corresponding to reactants, intermediates, and products as shown in Figure 1.3) and the first order saddle points (corresponding to transition states). Unfortunately, minimization of the gradient of the energy does not give any indication as to what type of chemical entity the located stationary point corresponds to. Hence, once located, stationary points should be further analyzed via the second derivatives of the energy with respect to the nuclear coordinates (hessian) in order to characterize them. The hessian is normally computed via numerical differentiation of analytical gradients:

$$\frac{\partial^2 E}{\partial X_i \partial X_j} \approx \frac{\Delta \left(\frac{\partial E}{\partial X_j} \right)}{\Delta X_i} \quad (1.54)$$

or via analytical second derivative evaluation. The vibrational frequencies are proportional to the hessian of the energy. At local minima, the second derivatives of the energy with respect to the nuclear coordinates are positive in all directions, resulting in all of the computed harmonic vibrational frequencies being real. At a transition state all of the harmonic vibrational frequencies but one are real. The single imaginary vibrational frequency corresponds to motion along the nuclear coordinate for which the transition state is a maximum.¹⁸ Higher order saddle points, with more than one imaginary frequency, may also be located during geometry optimization. Interpretation of these stationary points, in a chemical sense, is more difficult.

Prediction of molecular structures, relative energies and the nature of the species involved in chemical processes is the starting point for any theoretical investigation. However, calculations also provide important information regarding the nature of the bonding of chemical species. This is perhaps the most beneficial use of computational chemistry, although the interpretation of the numbers obtained from the calculations in terms of useful chemical concepts is not an easy task. The wavefunction or electron density (in the case of DFT) and the constituent molecular orbitals are available for

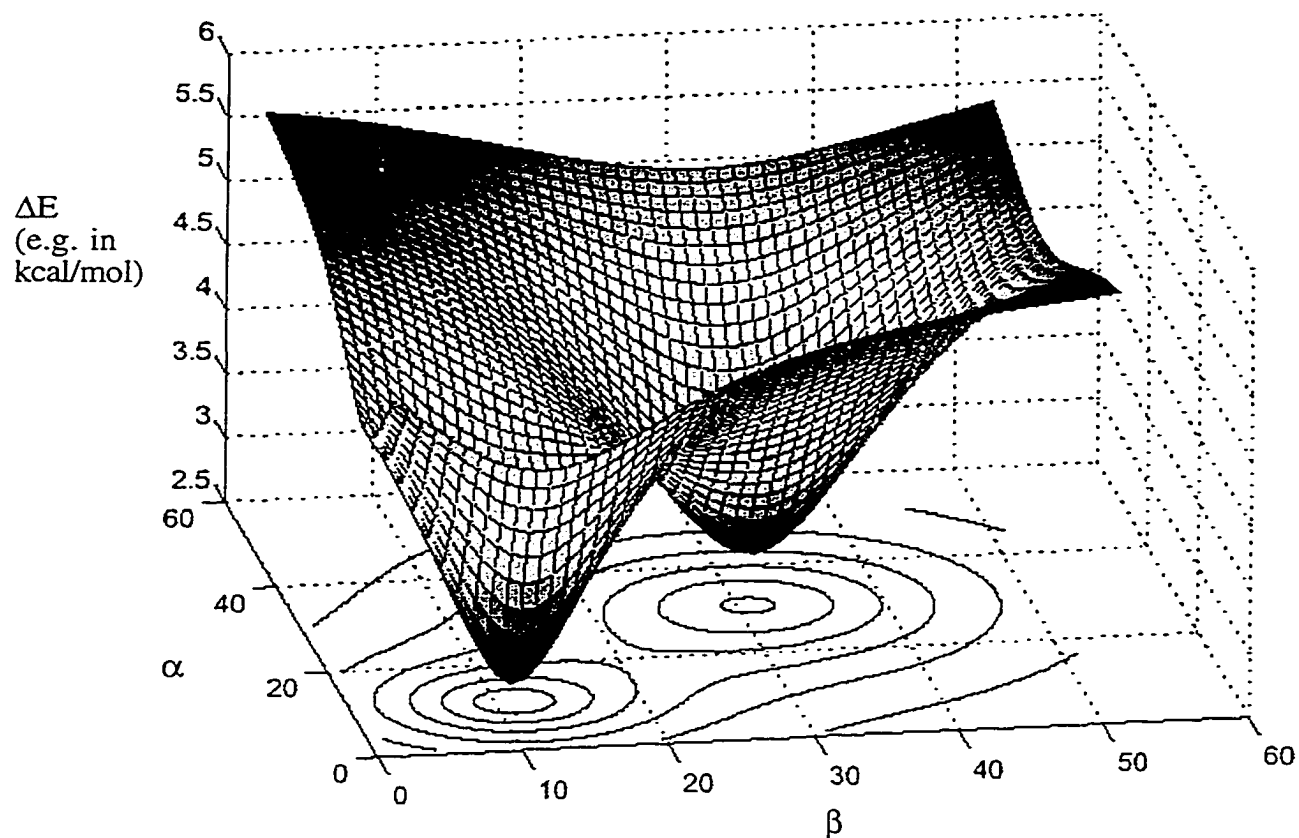


Figure 1.3: The potential energy hypersurface (in three dimensions; for example two angles α and β and the relative energy ΔE) for a hypothetical chemical reaction connecting one equilibrium (with $\alpha = 10^\circ$, $\beta = 10^\circ$) to a second equilibrium (with $\alpha = 30^\circ$, $\beta = 30^\circ$) by traversing a barrier (a transition state with $\alpha = 20^\circ$, $\beta = 20^\circ$). (Taken from the background material of the 1998 Nobel Prize in Chemistry Awards web site.⁴)

interpretation at each stationary point. A number of different schemes have been developed to analyze the wavefunction or electron density, in terms of simple chemical concepts. Population analysis, such as the natural bond orbital (NBO) analysis of Weinhold and co-workers¹³⁷, yield atomic charges, bond orders and atomic densities useful in understanding the changes which occur during a chemical process. Bader's atoms in molecules (AIM) method analyses the electron density topology of a molecule to gain information about the nature of the bonding between the atoms.¹³⁸ Morokuma^{139,140} and Ziegler¹⁴¹ have both developed schemes which decompose the coordination energy into a variety of components related to aspects of chemical bonding. A particularly useful bonding analysis scheme, known as the charge decomposition analysis (CDA) scheme was developed by Frenking and co-workers to probe the nature of metal-ligand interactions.¹⁴²

Computational chemistry allows the researcher to investigate all of the intricate details of a chemical process in a manner often not accessible to experiment. Reaction mechanisms can be mapped out, complete with changes in energy, molecular structure, and the nature of the bonding between constituent atoms as the reaction proceeds.

1.8 Scope of the Thesis

The present thesis focuses on the testing, development, and application of a variety of computational chemistry techniques for modeling transition metal compounds. One of the aims of the research was to gain an understanding of the advantages and limitations of the various theoretical methodologies commonly employed to study these compounds. The thesis is comprised of three sections: testing, development and applications. The first part involves benchmarking of the MCP technique with particular emphasis on species containing transition metals. The need for improved basis sets to regain the performance lost due to longer expansions of the MCP valence basis sets is addressed in the second part of the thesis, which reports the development of more computationally efficient MCP valence basis set for the main group elements. Finally, two particularly interesting problems in organometallic chemistry are studied in the applications section of the thesis.

A systematic study aimed at determining the reliability and predictive power of the MCP method in molecular calculations is reported in Chapter 2. The capabilities of the MCP method were initially tested on a variety of small molecules, a number of which are commonly found as ligands in transition metal complexes.¹⁴³ The second phase of the benchmarking study focused on the group four metal tetrahalogen complexes (MX_4 , where $M = Ti, Zr, Hf$ and $X = F, Cl, Br, I$) as a test of the MCP method in modeling small

transition metal complexes. Of utmost concern in the benchmarking studies was the accuracy of the molecular geometries predicted using the MCP method. Whenever possible, comparisons are made to experimental structures, as well as those optimized using various ECP methods. Calculations for the small molecules were carried out at the HF, MP2 and CISD levels of theory, while those for the MX_4 complexes were carried out at the HF and MP2 levels of theory.

Chapter 3 summarizes the development of new MCP valence basis sets for the main group elements which incorporate L-shell structure in order to improve computational efficiency. Details of the procedure used to generate the new L-shell basis sets are given, along with the results of atomic and molecular calculations.

The results of a study focusing on the carbonyl scrambling phenomenon commonly found in organometallics is described in Chapter 4. Calculations were carried out at the DFT (with all-electron and ECP basis sets) and semiempirical, PM3(tm), levels to probe the carbonyl fluxionality in $\text{Mn}_2(\text{CO})_6(\text{dppm})_2$ and its absence in the parent complex, $\text{Mn}_2(\text{CO})_{10}$. A hybrid DFT//PM3(tm) methodology, where the less expensive semiempirical method was used to optimize the geometry, and the more accurate DFT method was used to compute the energy, was found to be a very useful and efficient approach for computing internal reaction barriers.^{59,144}

In Chapter 5, the gradient-corrected DFT approach was employed, in conjunction with ECPs, to probe the increased reactivity of the alkyne complexes of the Group 8 metals, $\text{M}(\text{CO})_4(\text{C}_2\text{R}_2)$ where $\text{M} = \text{Fe}, \text{Ru}, \text{Os}$. The first bond dissociation energies of the alkyne complexes were computed and compared to those values found for the parent pentacarbonyl complexes, $\text{M}(\text{CO})_5$. The nature of the alkyne-metal bond was analyzed using the CDA scheme of Frenking and Bader's AIM scheme in an effort to rationalize the experimental and theoretical findings.¹⁴⁵

The common theme throughout the thesis is the critical evaluation of the computed results in an effort to ascertain the advantages and limitations of the various computational methods commonly employed in theoretical investigations of transition metal complexes. Theoretical results must be rigorously tested in order for the researcher to be fully confident in them and the chemical rationalizations which are made based on them. This was the driving force behind the MCP benchmarking studies. The aim of the two applied studies was to employ a number of popular computational chemistry methods to gain chemical insight from the numerical results.

1.9 References

1. Sheridan, R. P.; Venkataraghavan, R. *Acc. Chem. Res.* **1987**, *20*, 322.
2. Dean, P. M. *Molecular Foundations of Drug-receptor Interaction*; Cambridge University Press: Cambridge, 1987.
3. Wilson, E. K. *Chem. Eng. News* **1999**, *77*, 24.
4. *The Nobel Foundation: www.nobel.se/laureates/chemistry-1998.html* **1999**.
5. Salahub, D. R.; Zerner, M. C. E. *The Challenge of d and f Electrons: Theory and Computation*; American Chemical Society: Washington, D. C., 1989; Vol. 394.
6. Veillard, A. *Chem. Rev.* **1991**, *91*, 743.
7. Ziegler, T. *Chem. Rev.* **1991**, *91*, 651.
8. Ziegler, T. *Can. J. Chem.* **1995**, *73*, 743.
9. Siegbahn, P. E. M. In *Advances in Chemical Physics*; Prigogine, I. and Rice, S. A., Ed.; John Wiley and Sons: New York, 1996; Vol. 93, pp 333.
10. Gordon, M. S.; Cundari, T. R. *Coord. Chem. Rev.* **1996**, *147*, 87.
11. Cotton, F. A.; Wilkinson, G. *Advanced Inorganic Chemistry*; Fifth ed.; Wiley Interscience: New York, 1988.
12. Fischer-Hjalmars, I.; Henriksson-Enflo, A. In *Advances in Quantum Chemistry*; Academic Press: New York, 1982; Vol. 16, pp 1.
13. Rosenberg, B. *Biochimie* **1978**, *69*, 859.
14. Lippard, S. J. E. *Platinum, Gold, and other Metal Chemotherapeutic Agents*; American Chemical Society: Washington, D. C., 1983; Vol. 209.
15. Clarke, M. J.; Podbielski, L. *Coord. Chem. Rev.* **1987**, *78*, 253.
16. Collman, J. P.; Hegedus, L. S.; Norton, J. R.; Finke, R. G. *Principles and Applications of Organotransition Metal Chemistry*; University Science Books: Mill Valley, CA, 1987.
17. Crabtree, R. H. *The Organometallic Chemistry of the Transition Metals*; John Wiley and Sons: New York, 1988.
18. Hehre, W. J.; Radom, L.; von Rague Schleyer, P.; Pople, J. A. *Ab Initio Molecular Orbital Theory*; John Wiley and Sons: New York, 1986.
19. Salahub, D. R.; Zerner, M. C. In *The Challenge of d and f Electrons: Theory and Computation*, 394 ed.; Salahub, D. R. and Zerner, M. C., Ed.; American Chemical Society: Washington, D. C., 1989, pp 1.

20. Davidson, E. R. In *The Challenge of d and f Electrons: Theory and Computation*, 394 ed.; Salahub, D. R. and Zerner, M. C., Ed.; American Chemical Society: Washington, D. C., 1989, pp 153.
21. Pykko, P. *Chem. Rev.* **1988**, *88*, 563.
22. Szabo, A.; Ostlund, N. S. *Modern Quantum Chemistry. Introduction to Advanced Electronic Structure Theory*; Dover Publications, Inc.: Minneola, NY, 1989.
23. McQuarrie, D. A.; Simon, J. D. *Physical Chemistry: A Molecular Approach*; University Science Books: Sausalito, CA, 1997.
24. Levine, I. N. *Quantum Chemistry*; Fourth ed.; Prentice Hall: Engelwood Cliffs, NJ, 1991.
25. Roothaan, C. C. J. *Rev. Mod. Phys.* **1951**, *23*, 69.
26. Harrison, R. J.; Handy, N. C. *Chem. Phys. Lett.* **1983**, *95*, 386.
27. Sasaki, F. *Int. J. Quantum Chem. Symp.* **1977**, *11*, 125.
28. Bartlett, R. J. *Ann. Rev. Phys. Chem.* **1981**, *32*, 359.
29. Parr, R. G.; Yang, W. *Density-Functional Theory of Atoms and Molecules*; Oxford University Press: New York, 1989.
30. Borman, S. *Chem. Eng. News* **1990**, *68*, 22.
31. Weber, J.; Huber, H.; Weber, H. P. *Chimia* **1993**, *47*, 57.
32. St-Amant, A. In *Reviews in Computational Chemistry*; Lipkowitz, K. B. and Boyd, D. B., Ed.; VCH Publishers, Inc.: New York, 1996; Vol. 7, pp 217.
33. Hohenberg, P.; Kohn, W. *Phys. Rev.* **1964**, *136*, B864.
34. Kohn, W.; Sham, L. J. *Phys. Rev.* **1965**, *140*, A1133.
35. Andzelm, J.; Wimmer, E. *J. Chem. Phys.* **1992**, *96*, 1280.
36. Johnson, B. G.; Gill, P. M. W.; Pople, J. A. *J. Chem. Phys.* **1993**, *98*, 5612.
37. Chen, H.; Krasowski, M.; Fitzgerald, G. *J. Chem. Phys.* **1993**, *98*, 8710.
38. Hertwig, R. H.; Koch, W. *J. Comput. Chem.* **1995**, *16*, 576.
39. Casida, M. E. In *Recent Advances in Density Functional Methods, Part 1*; Chong, D. P., Ed.; World Scientific: Singapore, 1995, pp 155.
40. Casida, M. E. In *Recent Developments and Applications of Modern Density Functional Theory*; Seminario, J. M., Ed.; Elsevier: Amsterdam, 1996, pp 391.
41. Jamorski, C.; Casida, M. E.; Salahub, D. R. *J. Chem. Phys.* **1996**, *104*, 5134.
42. Casida, M. E.; Jamorski, C.; Casida, K. C.; Salahub, D. R. *J. Chem. Phys.* **1998**, *108*, 4439.

43. Casida, M. E.; Casida, K. C.; Salahub, D. R. *Int. J. Quantum Chem.* **1998**, *70*, 933.
44. Stowasser, R.; Hoffmann, R. *J. Am. Chem. Soc.* **1999**, *121*, 3414.
45. Zerner, M. C. In *Reviews in Computational Chemistry*; Lipkowitz, K. B. and Boyd, D. B., Ed.; VCH Publishers, Inc.: New York, 1991; Vol. 2, pp 313.
46. Dewar, M. J. S.; Thiel, W. *J. Am. Chem. Soc.* **1977**, *99*, 4899.
47. Dewar, M. J. S.; Thiel, W. *J. Am. Chem. Soc.* **1977**, *99*, 4907.
48. Dewar, M. J. S.; McKee, M. L. *J. Am. Chem. Soc.* **1977**, *99*, 5231.
49. Dewar, M. J. S.; Rzepa, H. S. *J. Am. Chem. Soc.* **1978**, *100*, 58.
50. Dewar, M. J. S.; Rzepa, H. S. *J. Am. Chem. Soc.* **1978**, *100*, 777.
51. Dewar, M. J. S.; Rzepa, H. S. *J. Am. Chem. Soc.* **1978**, *100*, 784.
52. Dewar, M. J. S.; Zoebisch, E. G.; Healy, E. F.; Stewart, J. J. P. *J. Am. Chem. Soc.* **1985**, *107*, 3902.
53. Dewar, M. J. S.; Zoebisch, E. G. *J. Mol. Struct. (Theochem)* **1988**, *49*, 1.
54. Stewart, J. J. P. *J. Comput. Chem.* **1989**, *10*, 209.
55. *Spartan*; 4.0.3 ed.; Wavefunction, Inc.: Irvine, CA, 1995.
56. Adam, K. R.; Atkinson, I. M.; Lindoy, L. F. *J. Mol. Struct.* **1996**, *384*, 183.
57. Borge, K. J.; Jensen, V. R.; Karlsen, T.; Stovneng, J. A.; Swang, O. *J. Mol. Model.* **1997**, *3*, 193.
58. Cundari, T. R.; Saunders, L. C.; Sisterhen, L. L. *J. Phys. Chem. A* **1998**, *102*, 997.
59. Decker, S. A.; Klobukowski, M. *Can. J. Chem.* **1999**, *77*, 65.
60. Cundari, T. R.; Deng, J. *J. Chem. Inf. Comp. Sci.* **1999**, *39*, 376.
61. Anderson, W. P.; Cundari, T.; Drago, R.; Zerner, M. C. *Inorg. Chem.* **1990**, *29*, 1.
62. Anderson, W. P.; Cundari, T.; Zerner, M. C. *Int. J. Quantum Chem.* **1990**, *39*, 31.
63. *Molecular Simulations Inc.*: www.msi.com **1999**.
64. Huzinaga, S.; Andzelm, J.; Klobukowski, M.; Radzio-Andzelm, E.; Sakai, Y.; Tatewaki, H. *Gaussian Basis Sets for Molecular Calculations*; Elsevier: Amsterdam, 1984.
65. Davidson, E. R.; Feller, D. F. *Chem. Rev.* **1986**, *86*, 681.
66. Hehre, W. J.; Stewart, R. F.; Pople, J. A. *J. Chem. Phys.* **1969**, *51*, 2657.
67. Hehre, W. J.; Ditchfield, R.; Stewart, R. F.; Pople, J. A. *J. Chem. Phys.* **1970**, *52*, 2769.
68. Pietro, W. J.; Levi, B. A.; Hehre, W. J.; Stewart, R. F. *Inorg. Chem.* **1980**, *19*, 2225.

69. Pietro, W. J.; Blurock, E. S.; Hout, R. S.; Hehre, W. J.; DeFrees, D. J.; Stewart, R. F. *Inorg. Chem.* **1981**, *20*, 3650.
70. Pietro, W. J.; Hehre, W. J. *J. Comput. Chem.* **1983**, *4*, 241.
71. Binkley, J. S.; Pople, J. A.; Hehre, W. J. *J. Am. Chem. Soc.* **1980**, *102*, 939.
72. Gordon, M. S.; Binkley, J. S.; Pople, J. A.; Pietro, W. J.; Hehre, W. J. *J. Am. Chem. Soc.* **1982**, *104*, 2797.
73. Dobbs, K. D.; Hehre, W. J. *J. Comput. Chem.* **1986**, *7*, 359.
74. Dobbs, K. D.; Hehre, W. J. *J. Comput. Chem.* **1987**, *8*, 861.
75. Dobbs, K. D.; Hehre, W. J. *J. Comput. Chem.* **1987**, *8*, 880.
76. Ditchfield, R.; Hehre, W. J.; Pople, J. A. *J. Chem. Phys.* **1971**, *54*, 724.
77. Hehre, W. J.; Pople, J. A. *J. Chem. Phys.* **1972**, *56*, 4233.
78. Dill, J. D.; Pople, J. A. *J. Chem. Phys.* **1975**, *62*, 2921.
79. Hehre, W. J.; Lathan, W. A. *J. Chem. Phys.* **1972**, *56*, 5255.
80. Hehre, W. J.; Ditchfield, R.; Pople, J. A. *J. Chem. Phys.* **1972**, *56*, 2257.
81. Binkley, J. S.; Pople, J. A. *J. Chem. Phys.* **1977**, *66*, 879.
82. Francl, M. M.; Pietro, W. J.; Hehre, W. J.; Binkley, J. S.; Gordon, M. S.; DeFrees, D. J.; Pople, J. A. *J. Chem. Phys.* **1982**, *77*, 3654.
83. Schafer, A.; Horn, H.; Ahlrichs, R. *J. Chem. Phys.* **1992**, *97*, 2571.
84. Dunning, T. H. *J. Chem. Phys.* **1970**, *53*, 2823.
85. Dunning, T. H. J.; Hay, P. J. In *Modern Theoretical Chemistry*; Schaefer, H. F., III, Ed.; Plenum Press: New York, 1977; Vol. 2, pp 1.
86. Schafer, A.; Huber, C.; Ahlrichs, R. *J. Chem. Phys.* **1994**, *100*, 5829.
87. Dunning, T. H. *J. Chem. Phys.* **1989**, *90*, 1007.
88. Hellman, H. *J. Chem. Phys.* **1935**, *3*, 61.
89. Hellman, H. *J. Chem. Phys.* **1936**, *4*, 325.
90. Huzinaga, S. *J. Mol. Struct. (Theochem)* **1991**, *234*, 51.
91. Huzinaga, S. *Can. J. Chem.* **1995**, *73*, 619.
92. Huzinaga, S. *Int. J. Quantum Chem.* **1996**, *60*, 83.
93. Klobukowski, M.; Sakai, Y.; Huzinaga, S. In *Computational Chemistry: Reviews of Current Trends*; Lesczynski, J., Ed.; World Scientific: Singapore, 1999; Vol. 3, pp 49.
94. Bonifacic, V.; Huzinaga, S. *J. Chem. Phys.* **1974**, *60*, 2779.
95. Bonifacic, V.; Huzinaga, S. *J. Chem. Phys.* **1975**, *62*, 1507.

96. Bonifacic, V.; Huzinaga, S. *J. Chem. Phys.* **1975**, *62*, 1509.
97. Bonifacic, V.; Huzinaga, S. *J. Chem. Phys.* **1976**, *64*, 956.
98. Bonifacic, V.; Huzinaga, S. *J. Chem. Phys.* **1976**, *65*, 2322.
99. Krauss, M.; Stevens, W. J. *Ann. Rev. Phys. Chem.* **1984**, *35*, 357.
100. Cundari, T. R.; Benson, M. T.; Lutz, M. L.; Sommerer, S. O. In *Reviews in Computational Chemistry*; Lipkowitz, K. B. and Boyd, D. B., Ed.; VCH Publishers: New York, 1996; Vol. 8, pp 145.
101. Frenking, G.; Antes, I.; Bohme, M.; Dapprich, S.; Ehlers, A. W.; Jonas, V.; Neuhaus, A.; Otto, M.; Stegmann, R.; Veldkamp, A.; Vyboishchikov, S. F. In *Reviews in Computational Chemistry*; Lipkowitz, K. B. and Boyd, D. B., Ed.; VCH Publishers: New York, 1996; Vol. 8, pp 63.
102. Hay, P. J.; Wadt, W. R. *J. Chem. Phys.* **1985**, *82*, 270.
103. Wadt, W. R.; Hay, P. J. *J. Chem. Phys.* **1985**, *82*, 284.
104. Hay, P. J.; Wadt, W. R. *J. Chem. Phys.* **1985**, *82*, 299.
105. Pacios, L. F.; Christiansen, P. A. *J. Chem. Phys.* **1985**, *82*, 2664.
106. Hurley, M. M.; Pacios, L. F.; Christiansen, P. A.; Ross, R. B.; Ermler, W. C. *J. Chem. Phys.* **1986**, *84*, 6840.
107. LaJohn, L. A.; Christiansen, P. A.; Ross, R. B.; Atashroo, T.; Ermler, W. C. *J. Chem. Phys.* **1987**, *87*, 2812.
108. Ross, R. B.; Powers, J. M.; Atashroo, T.; Ermler, W. C.; LaJohn, L. A.; Christiansen, P. A. *J. Chem. Phys.* **1990**, *93*, 6654.
109. Ross, R. B.; Gayen, S.; Ermler, W. C. *J. Chem. Phys.* **1994**, *100*, 8151.
110. Ermler, W. C.; Ross, R. B.; Christiansen, P. A. *Int. J. Quantum Chem.* **1991**, *40*, 829.
111. Nash, C. S.; Bursten, B. E.; Ermler, W. C. *J. Chem. Phys.* **1997**, *106*, 5133.
112. Stevens, W. J.; Basch, H.; Krauss, M. *J. Chem. Phys.* **1984**, *81*, 6026.
113. Krauss, M.; Stevens, W. J.; Basch, H.; Jasien, P. *Can. J. Chem.* **1992**, *70*, 612.
114. Cundari, T. R.; Stevens, W. J. *J. Chem. Phys.* **1993**, *98*, 5555.
115. Wedig, U.; Dolg, M.; Stoll, H.; Preuss, H. In *Quantum Chemistry: The Challenge of Transition Metals and Coordination Chemistry*; Veillard, A., Ed.; Reidel: Dordrecht, Germany, 1986, pp 79.
116. Igel-Mann, G.; Stoll, H.; Preuss, H. *Mol. Phys.* **1988**, *65*, 1321.
117. Dolg, M.; Wedig, U.; Stoll, H.; Preuss, H. *J. Chem. Phys.* **1987**, *86*, 866.

118. Dolg, M.; Stoll, H.; Savin, A.; Preuss, H. *Theor. Chim. Acta* **1989**, *75*, 173.
119. Dolg, M.; Stoll, H.; Preuss, H. *J. Chem. Phys.* **1989**, *90*, 1730.
120. Andrae, D.; Haussermann, U.; Dolg, M.; Stoll, H.; Preuss, H. *Theor. Chim. Acta* **1990**, *77*, 123.
121. Bergner, A.; Dolg, M.; Kuchle, W.; Stoll, H.; Preuss, H. *Mol. Phys.* **1993**, *80*, 1431.
122. Cowan, R. D.; Griffin, D. C. *J. Opt. Soc. Am.* **1976**, *66*, 1010.
123. Christiansen, P. A.; Ermler, W. C.; Pitzer, K. S. *Ann. Rev. Phys. Chem.* **1985**, *36*, 407.
124. Gropen, O. In *Methods in Computational Chemistry*; Wilson, S., Ed.; Plenum Press: New York, 1988; Vol. 2, pp 109.
125. Klobukowski, M. *Theor. Chim. Acta* **1992**, *83*, 239.
126. Klobukowski, M. *Chem. Phys. Lett.* **1990**, *172*, 361.
127. Sakai, Y.; Miyoshi, E.; Klobukowski, M.; Huzinaga, S. *J. Comput. Chem.* **1987**, *8*, 226.
128. Sakai, Y.; Miyoshi, E.; Klobukowski, M.; Huzinaga, S. *J. Comput. Chem.* **1987**, *8*, 264.
129. Sakai, Y.; Miyoshi, E.; Klobukowski, M.; Huzinaga, S. *J. Chem. Phys.* **1997**, *106*, 8084.
130. Sakai, Y.; Miyoshi, E.; Tatewaki, H. *J. Mol. Struct. (Theochem)* **1998**, *451*, 143.
131. Amos, R. D.; Alberts, I. L.; Andrews, J. S.; Colwell, S. M.; Handy, N. C.; Jayatilaka, D.; Knowles, P. J.; Kobayashi, R.; Laidig, K. E.; Laming, G.; Lee, A. M.; Maslen, P. E.; Murray, C. W.; Rice, J. E.; Simandiras, E. D.; Stone, A. J.; Su, M.-D.; Tozer, D. J. *CADPAC: The Cambridge Analytical Derivatives Package*; Sixth ed.; Cambridge, U. K., 1995.
132. Schmidt, M. W.; Baldrige, K. K.; Boaltz, J. A.; Jensen, J. H.; Koseki, S.; Gordon, M. S.; Nguyen, K. A.; Windus, T. L.; Elbert, S. T. *QCPE Bull.* **1990**, *10*, 52.
133. Schmidt, M. W.; Baldrige, K. K.; Boaltz, J. A.; Elbert, S. T.; Gordon, M. S.; Jensen, J. H.; Koseki, S.; Matsunaga, N.; Nguyen, K. A.; Su, S.; Windus, T. L.; Dupuis, M. *J. Comput. Chem.* **1993**, *14*, 1347.
134. Frisch, M. J.; Trucks, G. W.; Schlegel, H. B.; Gill, P. M. W.; Johnson, B. G.; Robb, M. A.; Cheeseman, J. R.; Keith, T.; Petersson, G. A.; Montgomery, J. A.; Raghavachari, K.; Al-Laham, M. A.; Zakrzewski, V. G.; Ortiz, J. V.; Foresman, J. B.; Cioslowski, J.; Stefanov, B. B.; Nanayakkara, A.; Challacombe, M.; Peng, C. Y.; Ayala,

- P. Y.; Chen, W.; Wong, M. W.; Andres, J. L.; Replogle, E. S.; Gomperts, R.; Martin, R. L.; Fox, D. J.; Binkley, J. S.; DeFrees, D. J.; Baker, J.; Stewart, J. J. P.; Head-Gordon, M.; Gonzalez, C.; Pople, J. A. *Gaussian 94*; D3 ed.; Gaussian, Inc.: Pittsburgh, PA, 1995.
135. Ahlrichs, R.; Bar, M.; Haser, M.; Horn, H.; Kolmel, C. *Chem. Phys. Lett.* **1989**, *162*, 165.
136. Werner, H.-J.; Knowles, P. J. *Molpro*; 98.1 ed.; University of Birmingham: Birmingham, U. K., 1998.
137. Reed, A. E.; Curtiss, L. A.; Weinhold, F. *Chem. Rev.* **1988**, *88*, 899.
138. Bader, R. F. W. *Atoms in Molecules: A Quantum Theory*; Clarendon Press: Oxford, 1990.
139. Kitaura, K.; Morokuma, K. *Int. J. Quantum Chem.* **1976**, *10*, 325.
140. Morokuma, K. *Acc. Chem. Res.* **1977**, *10*, 294.
141. Ziegler, T.; Rauk, A. *Theor. Chim. Acta* **1977**, *46*, 1.
142. Dapprich, S.; Frenking, G. *J. Phys. Chem.* **1995**, *99*, 9352.
143. Decker, S. A.; Klobukowski, M.; Sakai, Y.; Miyoshi, E. *J. Mol. Struct. (Theochem)* **1998**, *451*, 215.
144. Decker, S. A.; Donini, O.; Klobukowski, M. *J. Phys. Chem. A* **1997**, *101*, 8734.
145. Decker, S. A.; Klobukowski, M. *J. Am. Chem. Soc.* **1998**, *120*, 9342.

Chapter 2

**Benchmarking of Model Core Potentials:
Application to Small Molecules
and the Group 4 Metal Halogen Complexes
(MX₄: M = Ti, Zr, Hf and X = F, Cl, Br, I)[‡]**

[‡] Reproduced in part with permission from Decker, S. A.; Klobukowski, M.; Sakai, Y.; Miyoshi, E. *Journal of Molecular Structure (Theochem)* **1998**, *451*, 215. Copyright 1998 Elsevier.

2.1 Introduction

As discussed in Chapter 1, the pseudopotential formalism has been very successful in extending computational chemistry to the study of the structures, energetics, properties, and reactions of molecules containing transition metals.¹⁻⁶ Pseudopotentials, such as the MCPs, are a necessity in studying such systems, where the molecules are typically large and contain a number of heavy atoms, both amongst the metal atoms themselves and in the main group elements present in the ligands. These methods are beneficial in that they reduce the number of basis functions required for modeling transition metal complexes and they provide a simple mechanism to incorporate relativistic effects, which are important for the heavy elements, into the calculations. Pseudopotentials enable one to probe the metal-dependent trends observed experimentally as one descends a column of the Periodic Table, with no increase in computational cost since all of the metal atoms contain the same number of valence electrons. Consider three identical complexes differing only in the metal atom (for example Ti, Zr, and Hf), the number of electrons, and more importantly the number of orbitals (and thus basis functions) nearly doubles as one goes from Ti to Zr and Zr to Hf. An all-electron HF calculation, which scales roughly as K^4 (where K is the number of basis functions, and is related to the number of atomic orbitals), for the Hf complex will be 256 times more computationally demanding than that for the Ti analogue, whereas the computational costs will be approximately the same for all three metal analogues if pseudopotentials are employed in the HF calculation.⁵

The present Chapter focuses on one of the two pseudopotential methods commonly employed in modern quantum chemistry calculations, the model core potential (MCP) approach, developed by Huzinaga and co-workers.⁷ A complete description of the MCP formalism was given in Chapter 1 (section 1.6), and will not be discussed in detail here. There are currently three versions of the model potential in use: version 1^{8,9}, which was used in all of the calculations in this thesis, and is denoted simply as the model core potential (MCP) method, version 2, known as the *ab initio* model potential (AIMP) method¹⁰, and version 3¹¹. The three differ in the way the core-valence Coulomb and exchange interactions are accounted for. Version 1 represents the core-valence exchange interactions using a local potential (refer to chapter 1, section 1.6), while versions 2 and 3 use a non-local representation of the potential function.¹

Given the nature of approximations in the MCP method, both the parameters and valence basis sets should be benchmarked and, if necessary, calibrated before commencing actual studies of the organometallics. MCPs have been used in several benchmarking studies as well as in applications focusing on transition metal chemistry. The review article

of Klobukowski *et al.*¹ gives a very good overview of the studies which have employed MCPs in studies of transition metal compounds. Miyoshi and Sakai carried out a detailed benchmarking of the MCP potentials and valence basis sets for a number of small transition metal complexes at the restricted Hartree-Fock (RHF) level using both large-core (denoted MCP-SD) and small-core (denoted MCP-SPD) metal atom MCPs.¹² They found very good overall agreement between MCP-SPD geometries and harmonic vibrational frequencies and those computed using all-electron basis sets of similar quality. Frenking *et al.*¹³ compared the performance of the SD- and SPD-type MCPs to the corresponding ECPs of Hay and Wadt¹⁴⁻¹⁶ at the Hartree-Fock (HF) level, in a study involving complexes of the type $\text{Ti}(\text{CH}_3)_n(\text{Cl})_{4-n}$. They found the SD-type MCPs and ECPs to be inferior to their respective SPD counterparts, and they found a slight preference for the ECPs over the MCPs in predicting geometries, harmonic vibrational frequencies, bond energies, and reaction energies. MCPs were also employed by Sakai and co-workers in a number of studies focusing on the electron affinities of a number of transition metal complexes of the type MF_6 , MF_6^- , and MF_6^{2-} (where $\text{M}=\text{Cr}$, Mo , and W)^{17,18}, as well as complexes of the type AuF_6^q (where $q = 0, -1, -2$, and -3)¹⁹. MCP calculations were carried out at the HF and configuration interaction (CI) levels, and the results agreed well with experiment. The use of MCPs has not been restricted to HF and post-HF calculations, as several reports have appeared in the literature whereby the MCP formalism has been merged with density functional theory (DFT). Salahub *et al.*²⁰, in a study of complexes of the type MCO , MCO^+ , $\text{M}(\text{CO})_2$, and $\text{M}(\text{CO})_2^{2+}$, showed that the DFT/MCP approach works quite well. Furthermore, Yang *et al.*²¹⁻²³, used MCPs in DFT studies of a number of triniobium clusters (Nb_3O , Nb_3O^+ , Nb_3C_2 , Nb_3C_2^+ , and Nb_3N_2). MCPs have been employed in a number of studies, both HF (and post-HF) based and DFT based, focusing on the chemisorption of atoms and small molecules on a variety of metal surfaces, including: Pt, Pd, Rh, Ni, Sc, Fe and Cu.²⁴⁻³⁴

In the first part of this Chapter, results are reported for calculations on a number of ligands commonly encountered in organometallic chemistry, as well as their heavier homologues. The molecules studied include: homonuclear diatomics (Group 15: N_2 , P_2 , As_2 , Sb_2 and the halogens: F_2 , Cl_2 , Br_2 , I_2); heteronuclear diatomics (CO analogues XY , where $\text{X}=\text{C}$, Si , Ge , Sn , and $\text{Y}=\text{O}$, S , Se , Te ; and the mixed halogens); triatomic hydrides AH_2 (OH_2 , SH_2 , SeH_2 , TeH_2), triatomic oxides (CO_2 and SO_2), tetraatomic hydrides AH_3 (NH_3 , PH_3 , AsH_3 , SbH_3), tetraatomic analogues of NF_3 , and small hydrocarbons (C_2H_2 , C_2H_4 , CH_2). With the exception of CH_2 , only ground electronic states were considered in this work. The reliability and accuracy of the MCPs in treating these small systems is gauged through predictions of geometric structures, as well as harmonic vibrational

frequencies (for diatomic molecules). Discussion also focuses on the correlation energies computed using the MCP and ECP approaches, computed at the MP2 and CISD levels of theory.

The second part of the Chapter focuses on the reliability of the MCP method as applied to a set of small transition metal complexes, the Group 4 metal tetrahalogen complexes (MX_4 ; $\text{M} = \text{Ti, Zr, Hf}$ and $\text{X} = \text{F, Cl, Br, I}$). The geometries of these tetrahedral complexes were computed using small-core MCP and ECP approaches and compared, wherever possible, to experiment. Reaction energies for a simple set of halogen diatomic substitution reactions of the MX_4 complexes, leading to the mixed halogen complex, MX_2Y_2 , were also computed. These MX_4 metal halogen complexes are commonly encountered as starting compounds in organometallic syntheses³⁵, and experimental M-X distances are available for comparison.

2.2 Computational Methods

2.2.1 Small Molecules

A progression of methodologies was utilized to study the effectiveness of the model core potentials for the small main group molecules: Hartree-Fock (HF), Møller-Plesset (MP2), and configuration interaction (CISD). MCPs were employed in all of the calculations, along with the effective core potentials of Stevens *et al.*³⁶⁻³⁸, which were used in several reference calculations. In the calculations, MCP valence basis sets of double-zeta valence (DZ) and triple-zeta valence (TZ) quality were used. The DZ basis sets were supplemented with a single d polarization function (denoted as DZ1d), while two d polarization functions were added to the TZ basis sets (denoted as TZ2d). All of the polarization functions were taken from the compilation of Huzinaga *et al.*³⁹ For hydrogen atoms, standard DZV and TZV library basis sets were used.

Equilibrium geometries were optimized using a modified Powell method of searches along conjugate directions.⁴⁰ For diatomics the total energy curve was fit at several points bracketing the equilibrium to a simple polynomial in r , and the harmonic vibrational frequency, ω_e , was determined from:

$$\omega_e = \frac{1}{2\pi} \left(\frac{E''(r_e)}{\mu} \right)^{\frac{1}{2}} \quad (2.1)$$

where $E''(r_e)$ is the second derivative of the energy with respect to r , evaluated at r_e and μ is the reduced mass.⁴¹ Electron correlation energies were calculated using MCPs and compared to the values obtained using ECPs, at the MP2 and CISD levels.

All calculations were carried out using the development version of the GAMESS package.^{42,43}

2.2.2 MX_4 Molecules

As discussed in Chapter 1, the valence space for a transition metal atom pseudopotential may be defined as either the outermost ns and $(n-1)d$ shells, termed an SD or large-core pseudopotential, or the $(n-1)p$ shell and/or the $(n-1)s$ shell may be included in the valence space and treated explicitly as well, yielding an SPD or small-core pseudopotential.^{5,6} Although, the SD-type pseudopotentials offer greater computational savings than their SPD counterparts, Sakai and Miyoshi¹⁷, as well as Frenking and co-workers¹³ have shown them to be inferior in predicting molecular properties of transition metal complexes, particularly for those in which the metal atom is in a high oxidation state. Our preliminary calculations on the MX_4 complexes using the MCP-SD and ECP-SD pseudopotentials are in line with these previous findings, with computed M-X distances typically deviating from experiment by 0.1 Å or more. Hence, the SD pseudopotentials were not used further in the benchmarking study, and the results presented here employed only the SPD-type pseudopotentials. The small-core MCPs for Ti, Zr, and Hf, denoted MCP-SPD, treat ten valence electrons explicitly in the calculation (the $(n-1)p^6 ns^2 (n-1)d^2$ electrons). In the ECP of Stevens and co-workers³⁶⁻³⁸, denoted ECP1-SPD, the metal atom valence configuration is defined as: $(n-1)s^2 (n-1)p^6 ns^2 (n-1)d^2$, thereby treating a total of twelve electrons explicitly in the calculation. The SPD-type ECPs of Hay and Wadt¹⁶, termed ECP2-SPD, define the metal atom valence configuration in a manner analogous to that used by Stevens, treating a total of twelve electrons explicitly. The valence space for the halogen atoms was identical for all of the pseudopotential methods employed, and consisted of the outermost seven electrons in the ns and np atomic orbitals. Quasi-relativistic pseudopotentials were used for the second and third row metal atoms, as well as for iodine.

The valence basis set contractions employed for the metal atom are displayed in Table 2.1. The naming convention adopted to describe the valence basis sets is similar to that used in describing the valence basis sets employed in calculations of the main group molecules. The terms DZ and TZ denote basis sets of double-zeta and triple-zeta quality, while 1f and 1p designate the addition of f and p type polarization functions, respectively,

Table 2.1: Summary of the Metal Atom Pseudopotential Valence Basis Sets Employed in Calculations of the MX_4 Complexes.

Basis	Contraction Scheme		
	Ti	Zr	Hf
		MCP-SPD	
DZ	(51/31/41)	(71/41/41)	(71/51/51)
DZ1f	(51/31/41/1*)	(71/41/41/1*)	(71/51/51/1*)
DZ1p	(51/311*/41)	(71/411*/41)	(71/511*/51)
DZ1p1f	(51/311*/41/1*)	(71/411*/41/1*)	(71/511*/51/1*)
TZ	(411/211/311)	(611/311/311)	(611/411/411)
TZ1f	(411/211/311/1*)	(611/311/311/1*)	(611/411/411/1*)
TZ1p	(411/2111*/311)	(611/3111*/311)	(611/4111*/411)
TZ1p1f	(411/2111*/311/1*)	(611/3111*/311/1*)	(611/4111*/411/1*)
		ECP1-SPD	
TZ	(4211/4211/411)	(4211/4211/311)	(4111/4111/311)
TZ1f	(4211/4211/411/1*)	(4211/4211/311/1*)	(4111/4111/311/1*)
		ECP2-SPD	
DZ	(441/311/41)	(441/321/31)	(441/321/21)
DZ1f	(441/311/41/1*)	(441/321/31/1*)	(441/321/21/1*)
DZ'		(441/3111/31)	(441/3111/21)
DZ'1f		(441/3111/31/1*)	(441/3111/21)
TZ	(4311/311/311)	(4311/321/211)	(4311/321/111)
TZ1f	(4311/311/311/1*)	(4311/321/211/1*)	(4311/321/111/1*)
TZ'		(4311/3111/211)	(4311/3111/111)
TZ'1f		(4311/3111/211/1*)	(4311/3111/111/1*)

to the basis set. The f polarization functions were taken from the compilation of Frenking and co-workers⁴⁴, while the p polarization functions were taken from the compilation of Huzinaga and co-workers³⁹. As seen from Table 2.1, DZ and TZ basis sets were used in calculations involving the MCP-SPD pseudopotentials. The MCP-SPD valence basis sets were also augmented by the addition of an f, a p, and both an f and a p polarization function. Metal atom valence basis sets of TZ and TZ1f quality were employed in conjunction with the ECP1-SPD pseudopotentials. The exponents of the of the outermost p basis functions (Ti 0.030, Zr 0.028, Hf 0.035) resembled the exponents of the p polarization functions employed (Ti 0.065, Zr 0.059, Hf 0.059), hence, a p polarization function was not added to the ECP1-SPD basis sets. Both DZ and TZ basis sets were employed in conjunction with the ECP2-SPD pseudopotentials. An f polarization function was added to the DZ and TZ basis sets, yielding DZ1f and TZ1f basis sets, however, no p polarization functions were added since the exponents of the outermost p functions were again found to be close to those of the p polarization functions. In addition, basis set contractions denoted as DZ' and TZ' (as well as DZ' 1f and TZ' 1f) were employed in calculations involving the ECP2-SPD pseudopotentials in which the second-outermost p contracted function for Zr and Hf was further expanded. In all of the calculations, the valence basis sets for the halogen atoms were of double-zeta plus polarization quality, with a single d polarization function taken from the compilation of Huzinaga *et al.*³⁹

Molecular geometries were optimized using a modified Powell method⁴⁰ at the RHF and MP2 levels of theory, using the development version of the GAMESS package.^{42,43} The MX_4 geometries were optimized under T_d symmetry constraints while C_{2v} symmetry was imposed on the MX_2Y_2 systems.

2.3 Results and Discussion

In order to assess the reliability of the MCP method, the average absolute errors of each molecular property (geometric parameter or harmonic vibrational frequency) was calculated for each family of compounds studied. For the main group molecules, the families of compounds used in averaging were: the homonuclear diatomics, the heteronuclear chalcogenide diatomics of Group 14, the mixed halogen diatomics, the diatomic ions, the triatomics, the tetra-atomics, and the hydrocarbons. Three families of compounds were defined for the MX_4 molecules: the TiX_4 , ZrX_4 , and HfX_4 complexes. The average errors $\sigma_{\text{av}}(\text{X})$ are defined as:

$$\sigma_{av}(P:M|B) = \sum_{i=1}^N \frac{|P_i^{calc} - P_i^{exp}|}{N}, \quad (2.2)$$

where N is the number of molecules in the sample, and P is the property of interest ($P = r_e$, ω_e , or bond angle θ_e) evaluated using method M ($M = \text{RHF}$, MP2 , or CISD) with associated basis set B .

2.3.1 Main Group Molecules

The structural results calculated with the MCP method are collected in Figures 2.1-2.6 and Tables 2.3 and 2.4, along with their respective experimental values. The harmonic vibrational frequencies for selected diatomic molecules computed using the MCP pseudopotential at the RHF, MP2, and CISD levels of theory, are given in Table 2.2. All of the experimental data was taken either from Huber and Herzberg⁴⁵ or from the Landolt-Börnstein compilations.⁴⁶⁻⁴⁸

The equilibrium bond distances for the homonuclear diatomics computed using the MCP-DZ1d, MCP-TZ2d and ECP-DZ1d methods are plotted as a function of the respective experimental distances in Figure 2.1. The average error in the MCP computed bond length, σ_{av} , is 0.06 Å at the CISD/DZ1d level, and decreases to 0.04 Å when the larger TZ2d basis set is used. At the CISD level the MCP harmonic vibrational frequencies remain too large by about 40 - 50 cm^{-1} , as illustrated in Table 2.2. At all levels of theory employed, the distances predicted for the lighter systems (N_2 , P_2 , and F_2) using the ECPs of Stevens are larger than those predicted using the MCPs, while the reverse relationship holds for the heavier diatomics (As_2 , Sb_2 , Cl_2 , Br_2 , and I_2). Inclusion of electron correlation effects via the MP2 method results in computed distances which overshoot experiment. CISD performs much better in this respect, particularly with the larger, TZ2d basis set. The large error found for Sb_2 reflects the fact that the experimental distance does not correspond to r_e , but rather to r_2 .⁴⁵

The computed equilibrium bond distances for the chalcogenides of carbon, silicon, germanium, and selenium are plotted in Figure 2.2 as a function of the experimental distance. The average errors in the MCP bond length, $\sigma_{av}(r_e)$, are on the order of 0.02 Å at both the CISD/DZ1d and CISD/TZ2d levels, while the deviations for the MCP computed vibrational frequencies differ by 35 - 45 cm^{-1} . In general, the distances predicted by the ECPs of Stevens are larger than those predicted using the MCP method (with SnO being a notable exception). As with the homonuclear diatomics, the trend in MCP computed equilibrium distances amongst the different methods is: $r_e(\text{MP2}) > r_e(\text{CISD}) > r_e(\text{RHF})$.

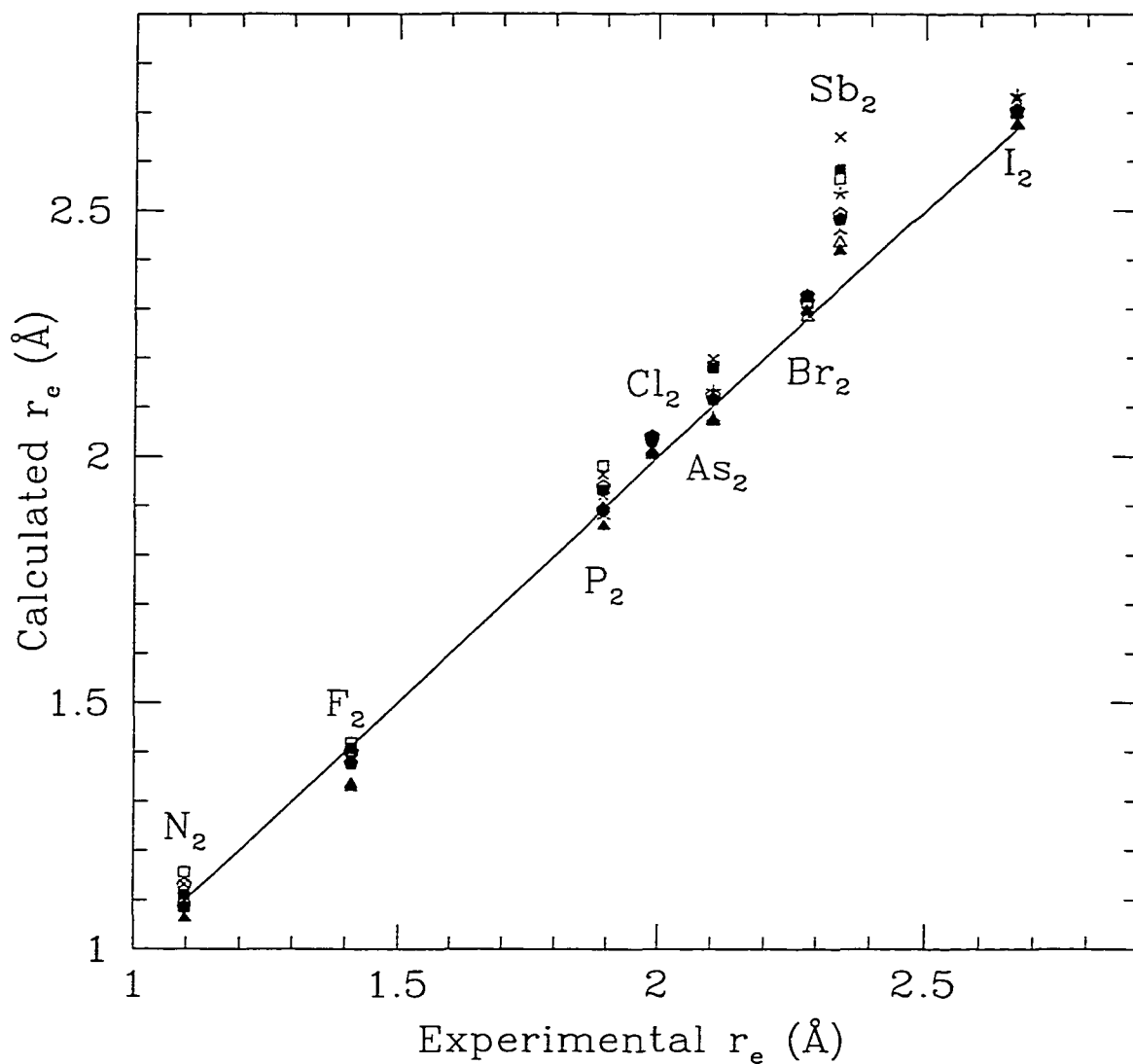


Figure 2.1: Comparison of calculated and experimental bond lengths for the homonuclear diatomic molecules. Triangles, squares, and pentagons refer to HF, MP2, and CISD results, respectively; open, skeletal (centre connected to vertices), and solid refer to ECP-DZ1d, MCP-DZ1d, and MCP-TZ2d, respectively.

Table 2.2: Summary of the Harmonic Vibrational Frequencies of Selected Diatomic Molecules.^a

System	RHF		MP2		CISD		Expt. ^b
	DZ1d	TZ2d	DZ1d	TZ2d	DZ1d	TZ2d	
N ₂	2926	2742	2209	2148	2523	2471	2359
As ₂	498	497	356	368	445	452	430
Cl ₂	601	585	560	527	560	538	560
I ₂	236	231	221	214	218	214	215
CO	2470	2424	2131	2165	2271	2337	2170
SiS	814	826	739	754	770	787	750
GeO	1166	1171	972	978	1062	1109	986
SnS	502	508	451	455	473	478	487
ClF	887	904	782	779	797	832	786
IF	642	668	586	600	593	723	610
ICl	401	403	376	375	374	375	384
OH ⁻	3900	3924	3753	3721	3705	3730	3700
NO ⁺	2950	2805	2169	2067	2588	2476	2376
CN ⁻	2342	2335	1981	1975	2152	2075	2069 ^c
CN ⁺	2279	2151	2265	2296	2128	2073	2033

^a Harmonic vibrational frequencies are given in units of cm⁻¹. ^b Experimental values taken from the compilation of Huber and Herzberg.⁴⁵ ^c The experimental values given correspond to the X²Σ⁺ state of neutral CN.⁴⁵

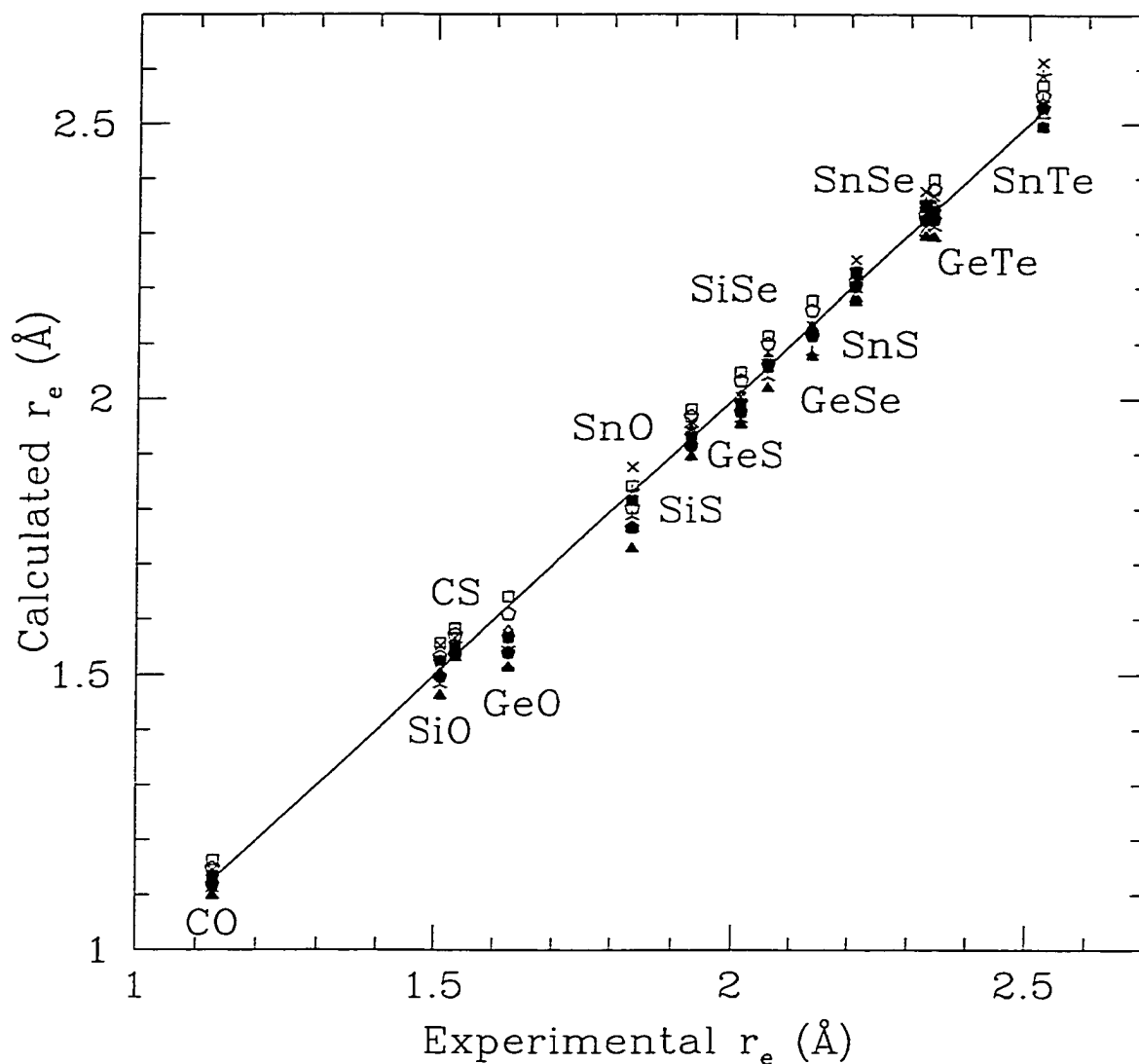


Figure 2.2: Comparison of calculated and experimental bond lengths for the heteronuclear diatomic chalcogenides of the Group 14 elements. Triangles, squares, and pentagons refer to HF, MP2, and CISD results, respectively; open, skeletal (centre connected to vertices), and solid refer to ECP-DZ1d, MCP-DZ1d, and MCP-TZ2d, respectively.

The MCP $\sigma_{av}(r_e)$ and $\sigma_{av}(\omega_e)$ values for the mixed halogen diatomics (Figure 2.3 and Table 2.2) were found to be in the range 0.04 to 0.06 Å and 8 - 36 cm^{-1} , respectively. Comparison of the distances predicted using MCPs and ECPs indicates that as above, $r_e(\text{ECP}) > r_e(\text{MCP})$ (with the exception of ClF).

The interatomic distances predicted using the MCP pseudopotentials agree very well with experiment for the diatomic ions (Figure 2.4) with $\sigma_{av}(r_e)$ values less than 0.01 Å, despite the fact that no diffuse functions were added to the basis sets for the negative ions. On the other hand, the MCP vibrational frequencies deviated from experiment by 60 - 90 cm^{-1} . For all of the diatomic ions studied, including the two anions for which no experimental data was available, SH^- and CN^- , $r_e(\text{ECP}) > r_e(\text{MCP})$.

For the polyatomic molecules only structural data were reported, with the harmonic vibrational frequencies awaiting the implementation of MCP gradients into the GAMESS^{42,43} program. Computed structural parameters for the triatomic molecules, r_e and θ_e , are plotted as functions of their experimental values in Figures 2.5 and 2.6, respectively. The MCP structures agree very well with experiment, exhibiting $\sigma_{av}(r_e:\text{CISD})$ values of 0.005 to 0.01 Å, and $\sigma_{av}(\theta_e:\text{CISD})$ values smaller than 1°. As in the diatomics, the distances predicted using the ECP formalism of Stevens were larger than those predicted using the MCP formalism (with the exception of TeH_2).

Values for the bond lengths and bond angles of the tetratomic molecules studied are collected in Table 2.3. For molecules with ligands heavier than hydrogen only MP2 calculations were performed due to computer limitations. For the tetratomic systems studied, the errors $\sigma_{av}(r_e)$ and $\sigma_{av}(\theta_e)$ were found to be very small, 0.004 Å and 0.2°, respectively, indicating very good agreement between the MCP calculations and experiment.

The results for the small sample of hydrocarbons studied are collected in Table 2.4. At the CISD level, values of $\sigma_{av}(r_e)$ were between 0.005 and 0.01 Å, while the computed bond angle for C_2H_4 agreed with experiment to within 1°. It is interesting to note that for the methylene radical CH_2 , electron correlation is critical for a correct value of the bond angle. It is also worth mentioning that the calculated singlet-triplet splitting was 11 kcal/mol, in good agreement with the experimental value of 9 kcal/mol.⁴⁷

The basis set correlation energies calculated using the MCP-DZ1d and ECP-DZ1d pseudopotential methods are collected in Table 2.5 for a selected set of diatomic molecules (a more complete compilation is available in Appendix A), and Table 2.6 for the heavy-atom polyatomic hydrides studied. The results in Tables 2.5 and 2.6 show that, as expected from previous studies, $E_{\text{corr}}(M:\text{ECP}) > E_{\text{corr}}(M:\text{MCP})$, where $M = \text{MP2}, \text{CISD}$. The only exceptions found were Cl_2 , SH_2 , Sb_2 , and BrCl (MP2). It has been shown

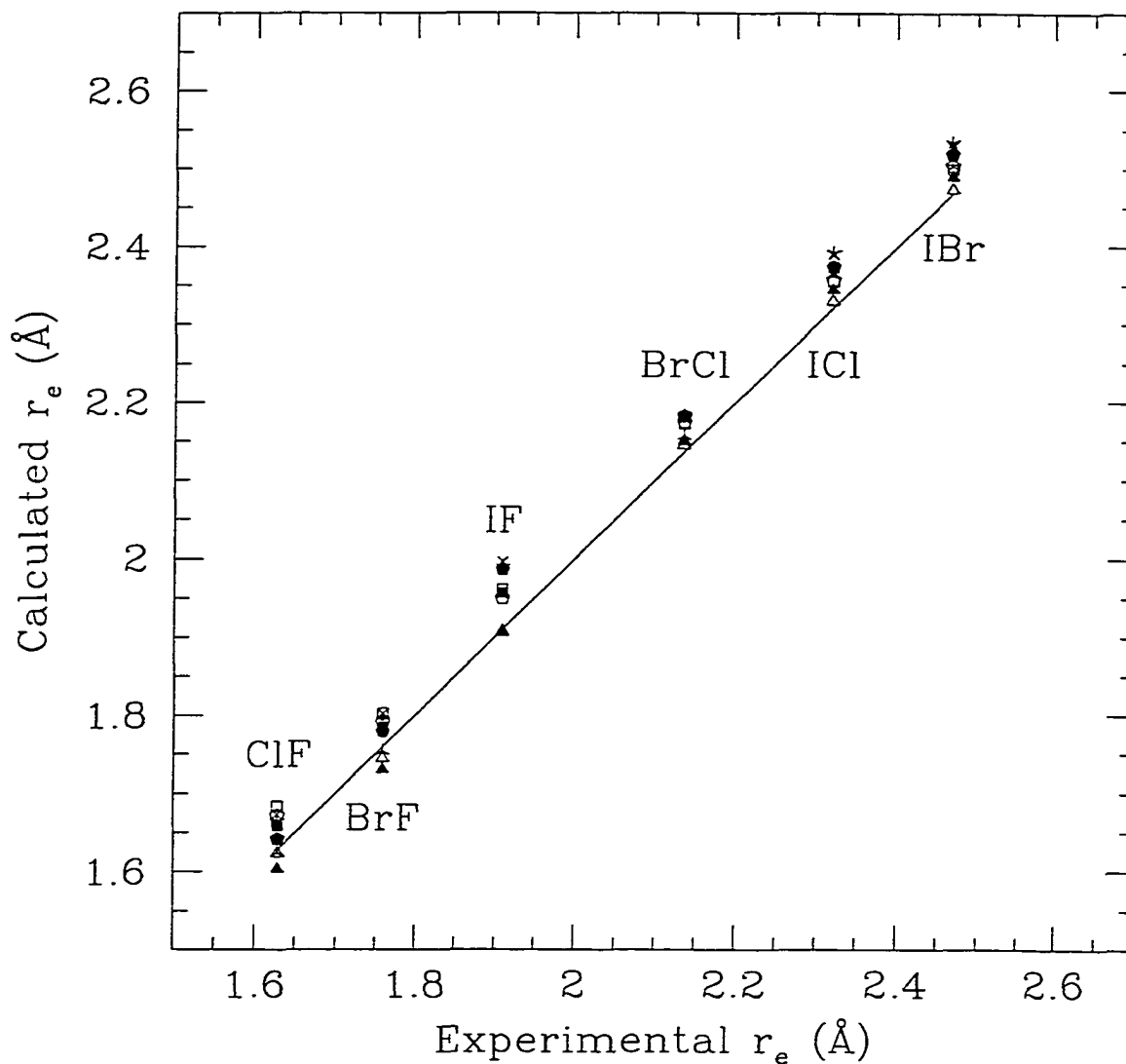


Figure 2.3: Comparison of calculated and experimental bond lengths for the mixed halogen diatomic molecules. Triangles, squares, and pentagons refer to HF, MP2, and CISD results, respectively; open, skeletal (centre connected to vertices), and solid refer to ECP-DZ1d, MCP-DZ1d, and MCP-TZ2d, respectively.

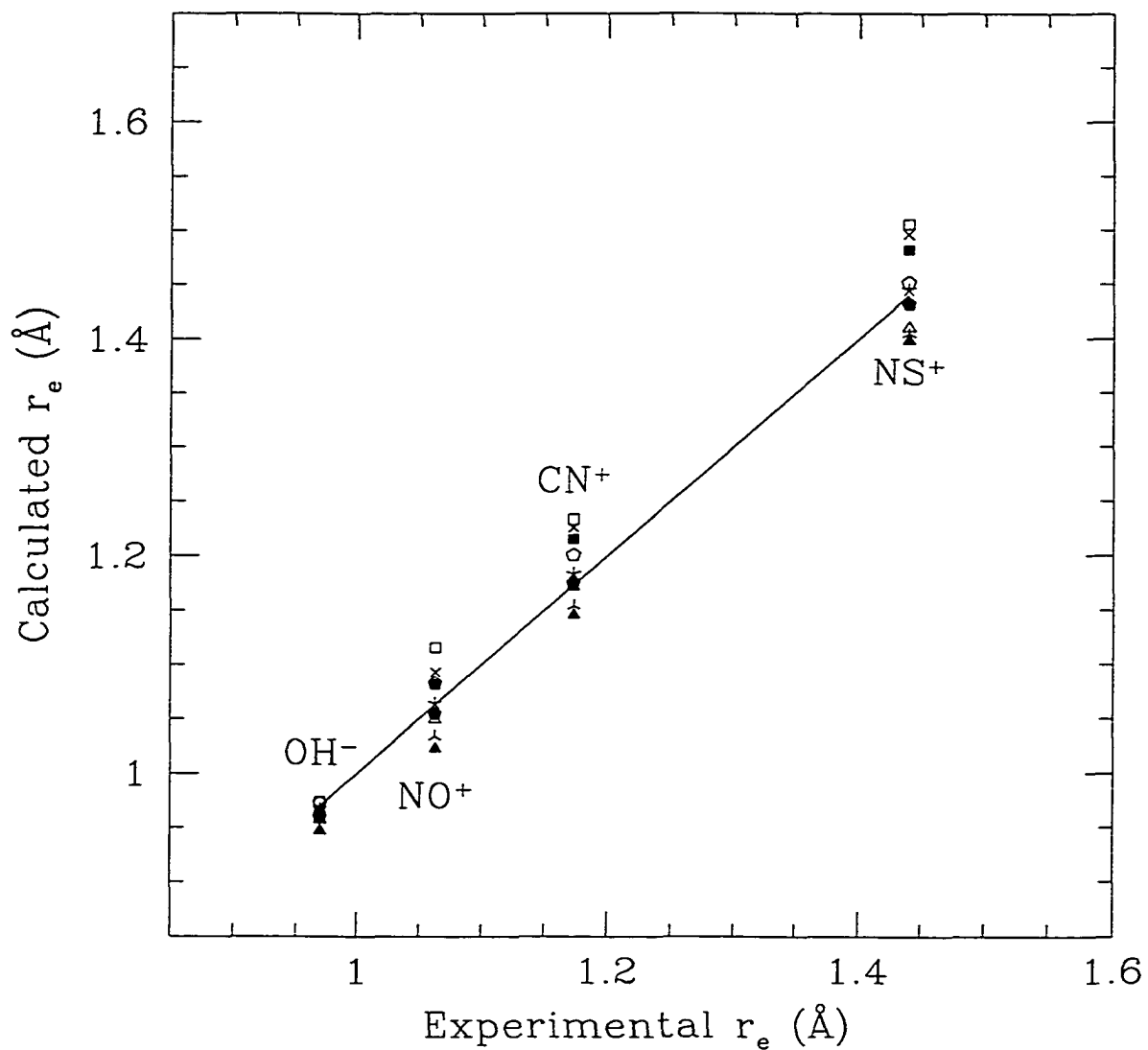


Figure 2.4: Comparison of calculated and experimental bond lengths for the heteronuclear diatomic ions. Triangles, squares, and pentagons refer to HF, MP2, and CISD results, respectively; open, skeletal (centre connected to vertices), and solid refer to ECP-DZ1d, MCP-DZ1d, and MCP-TZ2d, respectively.

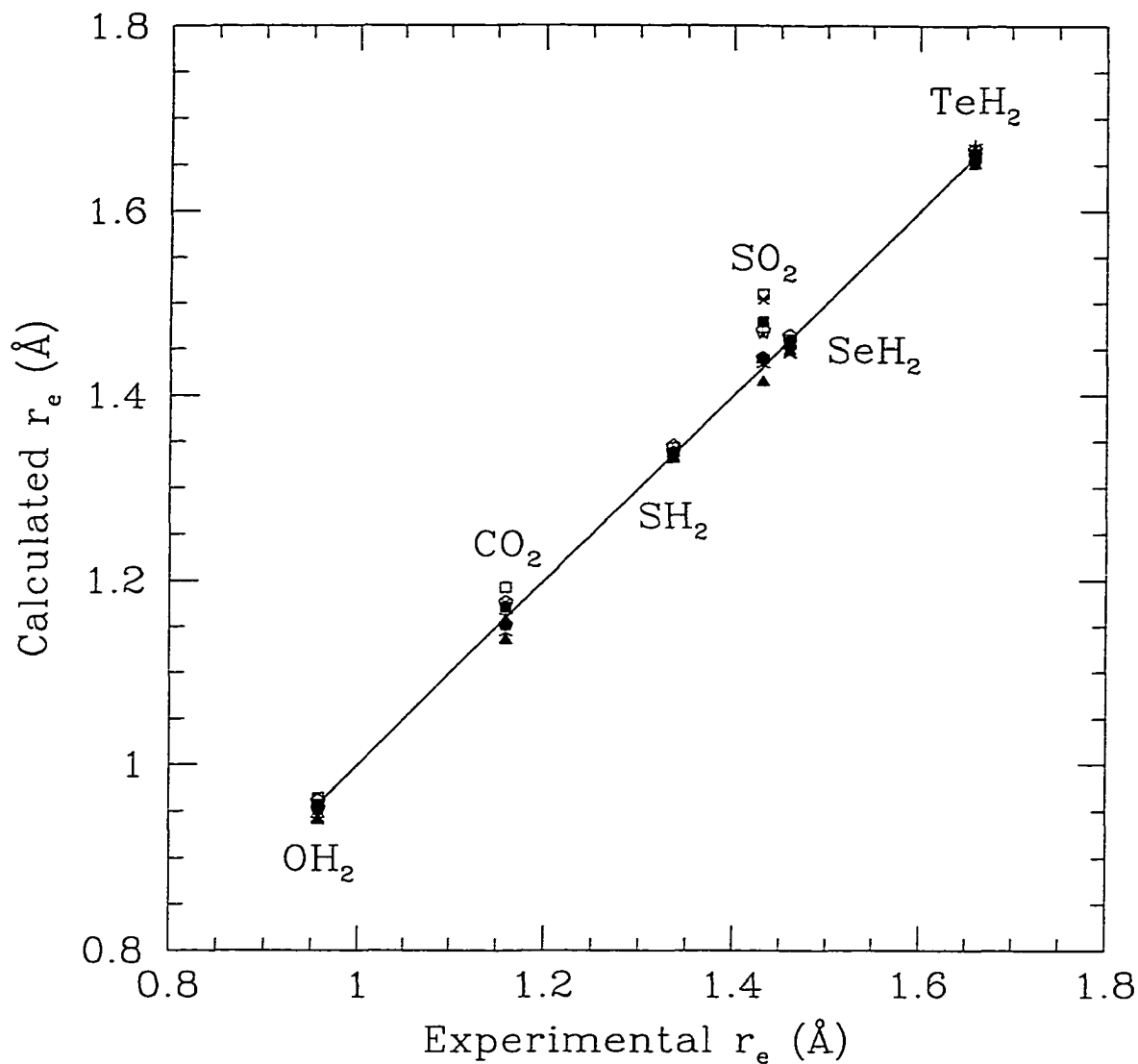


Figure 2.5: Comparison of calculated and experimental bond lengths for the triatomic molecules. Triangles, squares, and pentagons refer to HF, MP2, and CISD results, respectively; open, skeletal (centre connected to vertices), and solid refer to ECP-DZ1d, MCP-DZ1d, and MCP-TZ2d, respectively.

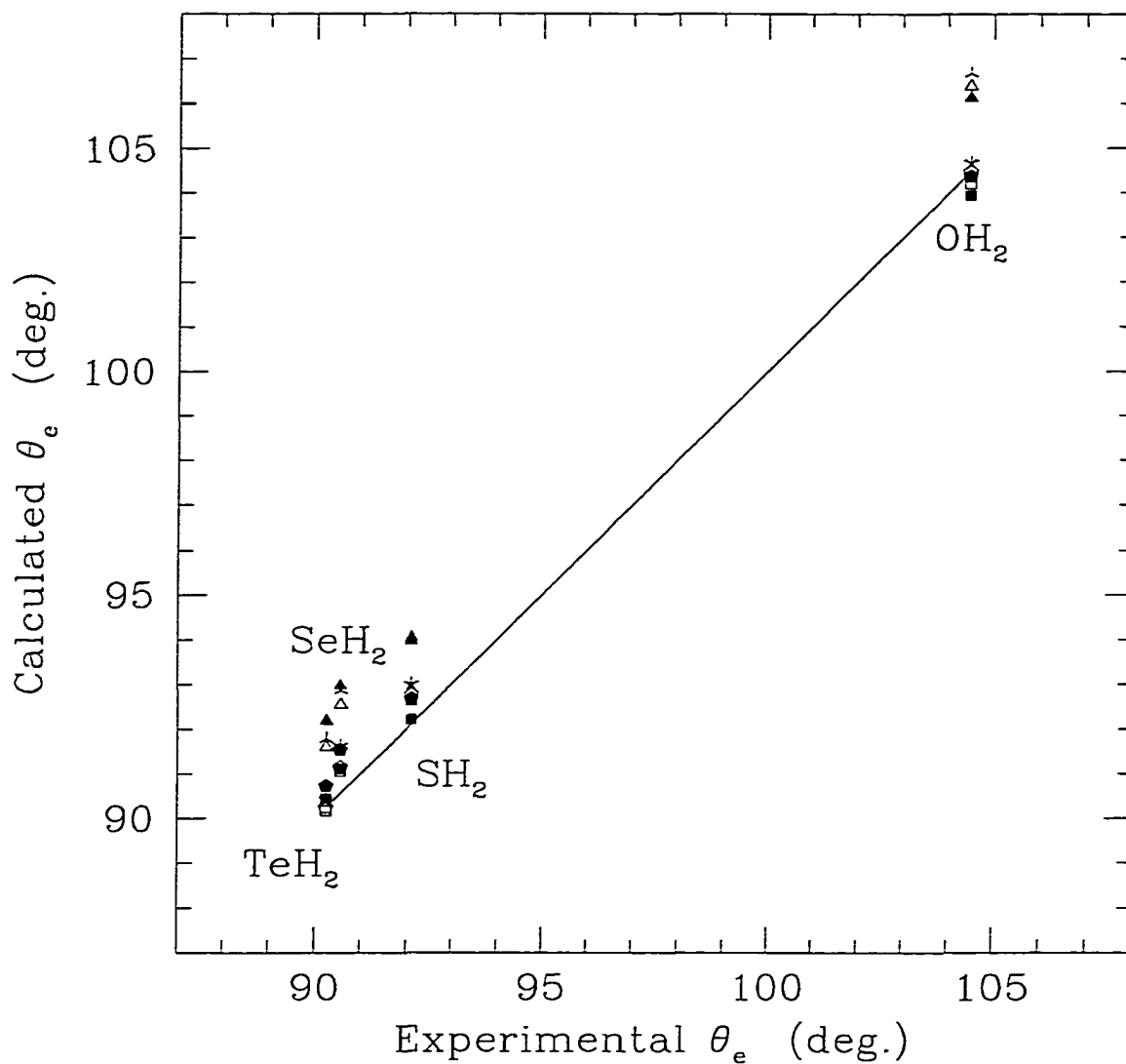


Figure 2.6: Comparison of calculated and experimental bond angles for the triatomic molecules. Triangles, squares, and pentagons refer to HF, MP2, and CISD results, respectively; open, skeletal (centre connected to vertices), and solid refer to ECP-DZ1d, MCP-DZ1d, and MCP-TZ2d, respectively.

Table 2.3: Calculated (MCP) and Experimental Structural Parameters for the tetratomic molecules studied.^{a,b}

System	Method	$r_e(\text{A-B})$		$\theta_e(\text{B-A-B})$	
		DZ1d	TZ2d	DZ1d	TZ2d
NF ₃	RHF	1.3193	1.3200	102.8	102.7
	MP2	1.3684	1.3831	102.1	100.7
	Expt.	1.3648		102.4	
PCl ₃	RHF	2.0778	2.0591	99.9	100.4
	MP2	2.0962	2.0807	99.6	99.4
	Expt.	2.0430		100.1	
AsBr ₃	RHF	2.3596	2.3522	99.9	100.2
	MP2	2.3789	2.3744	99.9	99.4
	Expt.	2.3290		99.7	
SbI ₃	RHF	2.7651	2.7304	99.2	99.8
	MP2	2.7808	2.7478	99.3	99.6
	Expt.	2.7190		99.7	
NH ₃	RHF	1.0005	0.9980	108.1	107.2
	MP2	1.0107	1.0087	106.6	105.9
	CISD	1.0101	1.0062	106.5	106.2
	Expt.	1.0016		106.7	
PH ₃	RHF	1.4151	1.4112	95.1	95.3
	MP2	1.4180	1.4159	93.5	93.5
	CISD	1.4209	1.4180	93.5	93.8
	Expt.	1.4130		93.5	
AsH ₃	RHF	1.5162	1.5204	94.2	94.3
	MP2	1.5185	1.5263	92.6	92.5
	CISD	1.5229	1.5299	92.5	92.7
	Expt.	1.5130		92.1	
SbH ₃	RHF	1.7097	1.6970	93.1	93.7
	MP2	1.7125	1.7027	91.5	92.1
	CISD	1.7210	1.7085	91.5	92.2
	Expt.	1.7039		91.6	

^a Values of r_e and θ_e are given in units of Å and degrees, respectively. ^b Experimental values taken from the Landolt-Börnstein compilation of structural data.⁴⁶⁻⁴⁸

Table 2.4: Calculated (MCP) and Experimental Structural Parameters for the hydrocarbons studied.^{a,b}

System	Method	$r_e(\text{C-C})$		$r_e(\text{C-H})$		$\theta_e(\text{H-C-H})$	
		DZ1d	TZ2d	DZ1d	TZ2d	DZ1d	TZ2d
C ₂ H ₂	RHF	1.2044	1.1744	1.0591	1.0513		
	MP2	1.2362	1.2054	1.0659	1.0575		
	CISD	1.2231	1.1910	1.0643	1.0551		
	Expt.	1.2031		1.0608			
C ₂ H ₄	RHF	1.3318	1.3102	1.0769	1.0712	117.1	116.8
	MP2	1.3520	1.3292	1.0839	1.0770	117.5	117.3
	CISD	1.3465	1.3217	1.0819	1.0743	117.2	117.0
	Expt. ^c	1.3390		1.0850		117.8	
CH ₂ (³ B ₁)	RHF			1.0725	1.0680	129.4	129.4
	MP2			1.0776	1.0704	131.3	132.3
	CISD			1.0809	1.0736	131.7	132.6
	Expt.			1.0748		133.8	
CH ₂ (¹ A ₁)	GVB ^d			1.1002	1.0958	102.2	102.3
	CISD			1.1110	1.1034	101.8	102.0
	Expt.			1.1075		102.5	

^a Values of r_e and θ_e are given in units of Å and degrees, respectively. ^b Experimental values taken from the Landolt-Börnstein compilation of structural data.⁴⁶⁻⁴⁸ ^c The experimental values correspond to r_0 and θ_0 values. ^d Two-configurational GVP-PP wavefunction was used as the reference:

$$\Psi = c_1\psi_1[1a_1^2 1b_2^2 2a_1^2] + c_2\psi_2[1a_1^2 1b_2^2 1b_1^2].$$

There is no MP2 implementation for a GVB reference function in GAMESS.^{42,43}

Table 2.5: Valence Electron Correlation Energies (E_{corr} , in E_h) of Selected Diatomic Molecules.

System	Method	$E_{\text{corr}}(\text{ECP})$	$E_{\text{corr}}(\text{MCP})$	ΔE_{corr}^a
N ₂	MP2	0.3114	0.2960	0.0154
	CISD	0.2857	0.2744	0.0112
As ₂	MP2	0.2209	0.2109	0.0100
	CISD	0.2046	0.1952	0.0093
Cl ₂	MP2	0.2627	0.2735	-0.0107
	CISD	0.2632	0.2706	-0.0073
I ₂	MP2	0.2027	0.1865	0.0161
	CISD	0.2014	0.1883	0.0131
CO	MP2	0.2791	0.2683	0.0108
	CISD	0.2681	0.2579	0.0101
SiS	MP2	0.2003	0.1981	0.0022
	CISD	0.2027	0.2011	0.0015
GeSe	MP2	0.1877	0.1803	0.0074
	CISD	0.1871	0.1820	0.0051
SnTe	MP2	0.1694	0.1603	0.0091
	CISD	0.1679	0.1597	0.0082
ClF	MP2	0.3095	0.3082	0.0012
	CISD	0.3018	0.2993	0.0025
BrCl	MP2	0.2478	0.2481	-0.0003
	CISD	0.2478	0.2474	0.0005
IBr	MP2	0.2175	0.2042	0.0134
	CISD	0.2167	0.2059	0.0108

^a Value corresponds to the difference in correlation energies computed from:

$$\Delta E_{\text{corr}} = E_{\text{corr}}(\text{ECP}) - E_{\text{corr}}(\text{MCP}).$$

Table 2.6: Valence Electron Correlation Energies (E_{corr} , in E_h) of the Heavy Atom Hydride Polyatomic Molecules.

System	Method	$E_{\text{corr}}(\text{ECP})$	$E_{\text{corr}}(\text{MCP})$	$\Delta E_{\text{corr}}^{\text{a}}$
C_2H_2	MP2	0.2571	0.2551	0.0019
	CISD	0.2517	0.2497	0.0021
C_2H_4	MP2	0.2689	0.2670	0.0019
	CISD	0.2748	0.2721	0.0027
CH_2 ($^3\text{B}_1$)	MP2	0.0950	0.0930	0.0020
	CISD	0.1125	0.1093	0.0032
CH_2 ($^1\text{A}_1$) ^b	CISD	0.1125	0.1092	0.0033
OH_2	MP2	0.1930	0.1880	0.0050
	CISD	0.1948	0.1892	0.0056
SH_2	MP2	0.1383	0.1389	-0.0007
	CISD	0.1521	0.1525	-0.0003
SeH_2	MP2	0.1255	0.1231	0.0024
	CISD	0.1389	0.1365	0.0024
TeH_2	MP2	0.1124	0.1068	0.0056
	CISD	0.1266	0.1209	0.0057
NH_3	MP2	0.1818	0.1796	0.0023
	CISD	0.1895	0.1862	0.0032
PH_3	MP2	0.1277	0.1278	-0.0001
	CISD	0.1467	0.1467	-0.0001
AsH_3	MP2	0.1205	0.1171	0.0034
	CISD	0.1387	0.1349	0.0038
SbH_3	MP2	0.1080	0.1058	0.0021
	CISD	0.1268	0.1248	0.0019

^a Value corresponds to the difference in correlation energies computed from:

$\Delta E_{\text{corr}} = E_{\text{corr}}(\text{ECP}) - E_{\text{corr}}(\text{MCP})$. ^b There is no MP2 implementation for GVB reference functions in GAMESS.^{42,43}

previously that calculations employing pseudopotentials tend to overestimate electron correlation energies when compared to accurate all-electron calculations. This overestimation has been attributed to the reduced nodal structure of the pseudopotential valence orbitals involved in the calculation.⁴⁹⁻⁵¹ As discussed in Chapter 1, since some of the valence orbital nodal structure is retained in the MCP formalism while all of it is lost in the ECP formalism, this overestimation should be more dramatic for the ECP pseudopotential methods than for the MCP pseudopotential method, and our calculations corroborate this.

2.3.2 MX_4 Molecules

A. Geometries

To reduce the vast amount of results to a more palatable amount, $\sigma_{\text{av}}(r_e:MB)$ values (where r_e refers to the M-X distance, M = RHF, MP2, and B is one of the pseudopotentials and corresponding basis sets in Table 2.1) were computed for the three families of compounds: TiX_4 , ZrX_4 , and HfX_4 and are displayed graphically in Figures 2.7 - 2.9. In addition, $\sigma_{\text{av}}(r_e:MB)$ values, computed by averaging over all twelve MX_4 complexes for each pseudopotential/valence basis set combination are compiled in Table 2.7. It should be mentioned that all of the experimental M-X distances were taken from the Landolt-Börnstein compilations.⁴⁶⁻⁴⁸ A complete listing of the M-X distances computed with the different pseudopotentials, at both the RHF and MP2 levels, is tabulated in Appendix A, along with their respective experimental values.

From Figures 2.7 - 2.9 the MCP-SPD predicted M-X distances agree very well with the experimental values, with $\sigma_{\text{av}}(r_e:M:\text{MCP-SPD})$ values below 0.05 Å. Furthermore, the errors averaged over all twelve MX_4 species (Table 2.7) are between 0.02 to 0.03 Å, depending on the basis set contraction. Comparison of the $\sigma_{\text{av}}(r_e:M:\text{MCP-SPD})$ values to those obtained using the two ECP approaches employed here, $\sigma_{\text{av}}(r_e:M:\text{ECP1-SPD})$ and $\sigma_{\text{av}}(r_e:M:\text{ECP2-SPD})$, reveals that there is little difference between them, indicating equivalent accuracies of the M-X distances predicted using the MCP and ECP pseudopotentials.

The addition of an f polarization function to the MCP-SPD metal atom basis sets reduces the M-X bond length by 0.005 to 0.03 Å indicating d orbital participation in the bonding between the metal and the halogen. The addition of a p polarization function to the MCP-SPD Ti basis sets resulted in a slight reduction in $\sigma_{\text{av}}(r_e:\text{MCP-SPD})$, while no significant effect was observed upon addition to the Zr and Hf basis sets. For ZrX_4 and

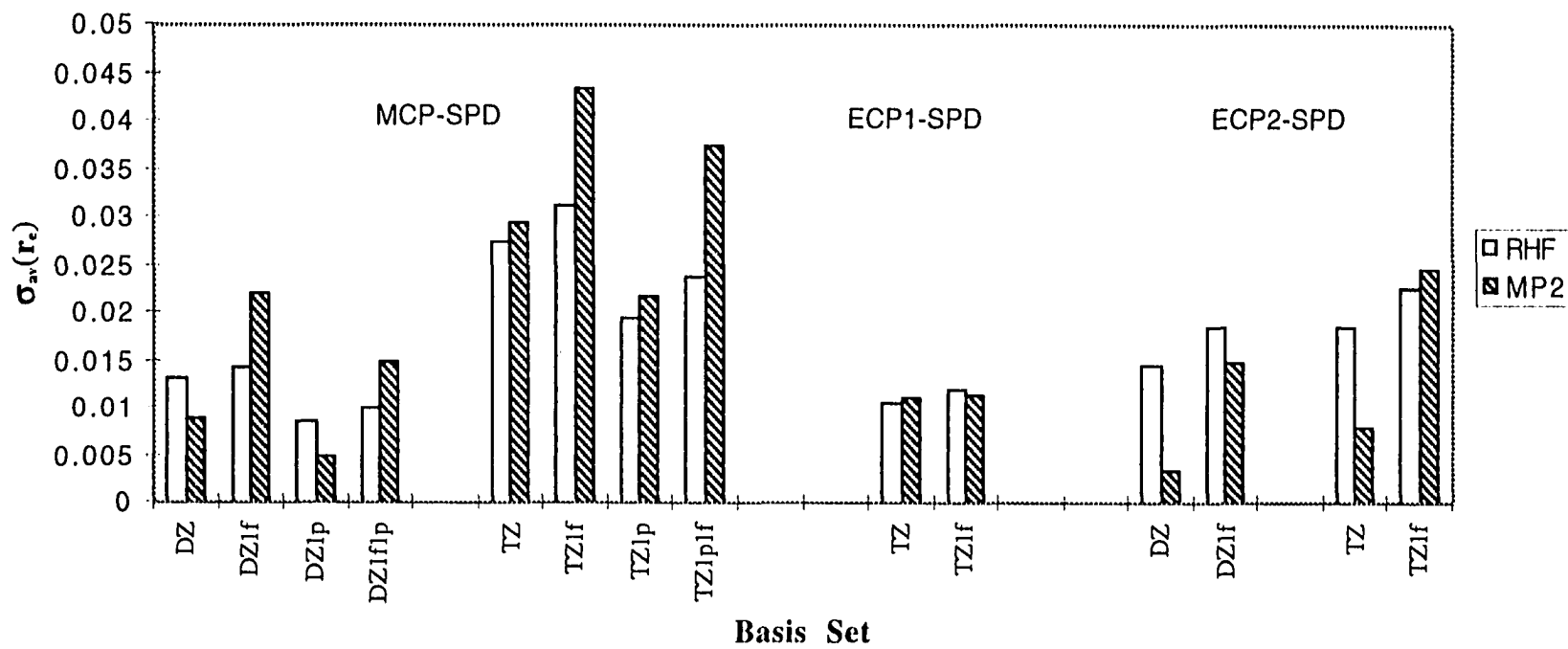


Figure 2.7: Magnitudes of the experimental M-X deviations (in Å), averaged over the four halogen complexes of TiX_4 , plotted as a function of the metal atom valence basis set.

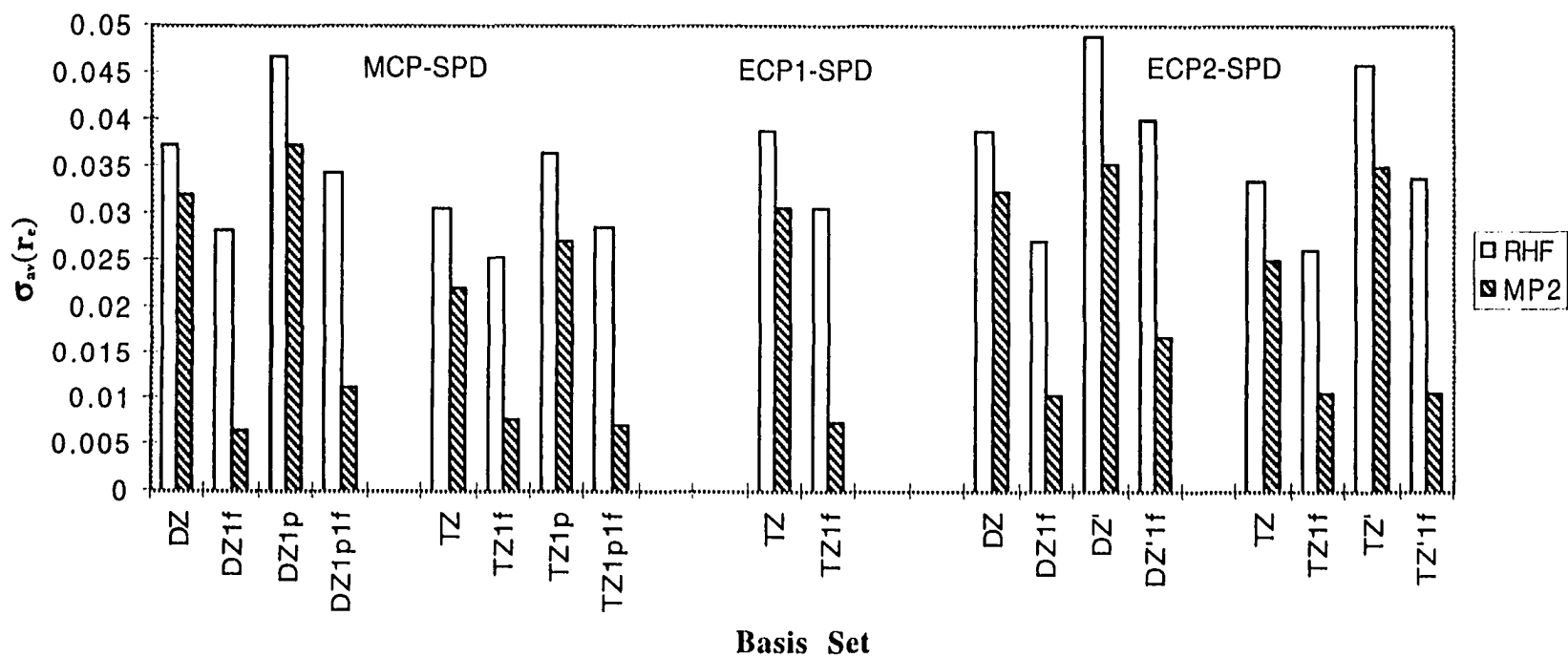


Figure 2.8: Magnitudes of the experimental M-X deviations (in Å), averaged over the four halogen complexes of ZrX_4 , plotted as a function of the metal atom valence basis set.

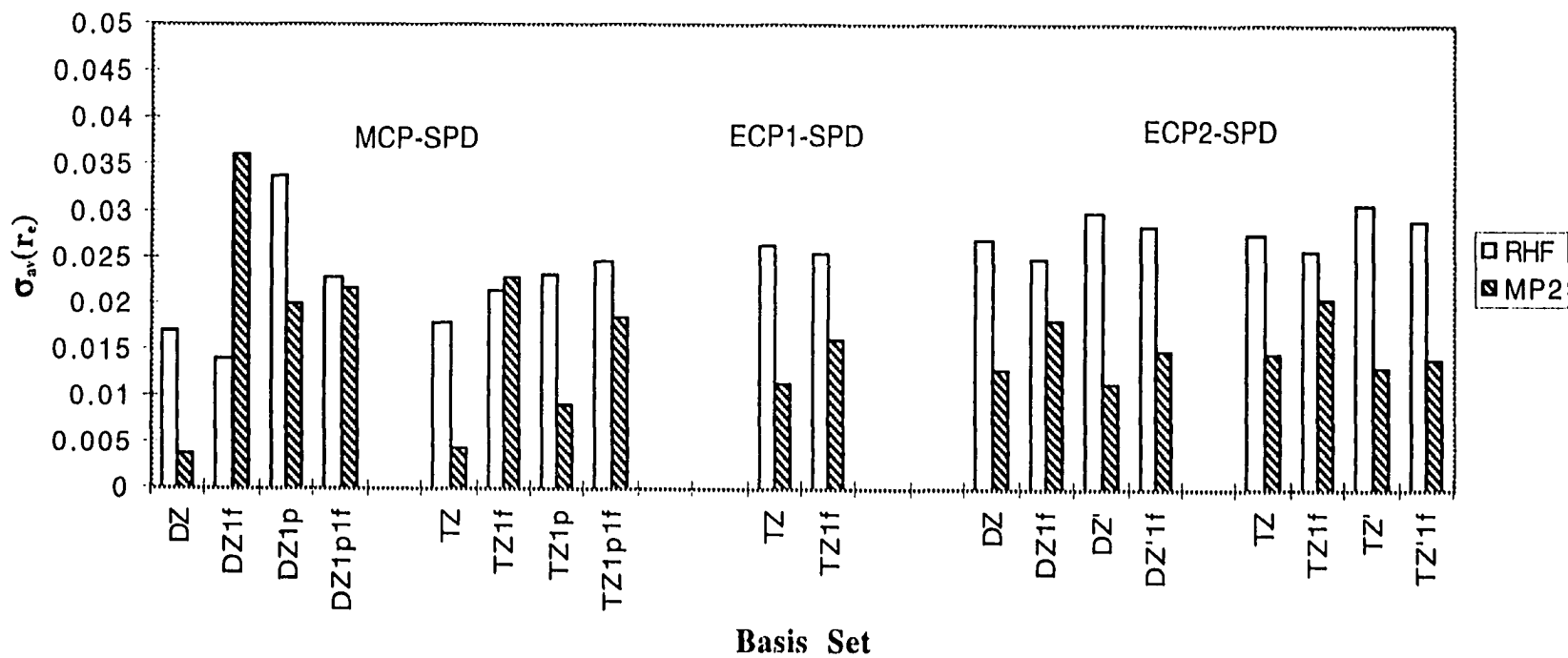


Figure 2.9: Magnitudes of the experimental M-X deviations (in Å), averaged over the four halogen complexes of HfX_4 , plotted as a function of the metal atom valence basis set.

Table 2.7: Summary of the Deviations (in Å) Between the Calculated and Experimental M-X Distances Averaged over all Twelve MX_4 Complexes.^a

Metal Atom Basis Set	$\sigma_{\text{av/all}}(r_e:\text{RHF})$	$\sigma_{\text{av/all}}(r_e:\text{MP2})$
MCP-SPD		
DZ	0.023	0.016
DZ1f	0.020	0.015
DZ1p	0.030	0.021
DZ1p1f	0.023	0.016
TZ	0.025	0.019
TZ1f	0.026	0.025
TZ1p	0.026	0.019
TZ1p1f	0.026	0.022
ECP1-SPD		
TZ	0.025	0.018
TZ1f	0.023	0.012
ECP2-SPD		
DZ	0.027	0.016
DZ1f	0.024	0.014
DZ'	0.040	0.023
DZ'1f	0.034	0.016
TZ	0.027	0.012
TZ1f	0.025	0.019
TZ'	0.038	0.024
TZ'1f	0.031	0.012

^a Experimental values taken from the Landolt-Börnstein compilation of structural data.⁴⁶⁻⁴⁸

HfX₄ (Figures 2.8 and 2.9) values of $\sigma_{av}(r_c:MCP-SPD)$ are decreased slightly, if at all, upon expanding the metal atom basis set from double-zeta to triple-zeta quality for calculations carried out at the RHF and MP2 levels. For the TiX₄ systems, changing to the larger triple-zeta valence basis sets actually increases the deviation between the computed and experimental Ti-X bond length values.

As mentioned previously, the partially filled d electrons of the transition metal atom usually lead to several low lying unoccupied molecular orbitals when ligands coordinate to the metal. These low-lying virtual orbitals are involved in low lying electronic excited states, making single-determinant RHF calculations unreliable for modeling transition metal complexes. The presence of these low lying excited states requires that electron correlation effects be incorporated into the calculation, either via the wavefunction approach or via density functional theory.⁵²⁻⁵⁵ In general, better agreement was found between the computed and experimental M-X distances when the correlated MP2 method was utilized, than when the RHF method was employed.

B. Dihalogen Substitution Reaction Energies

To gauge the ability of the MCPs to model reactions of transition metal complexes, reaction energies, ΔE_{rxn} , were computed for a very simple set of dihalogen substitution reactions of the type shown below



where M is Ti, Zr or Hf and X, and Y are Cl, Br or I.

A summary of the computed geometric parameters of the MX₂Y₂ complexes, as well as the dihalides, may be found in Appendix A. No experimental geometries could be found for these mixed halogen systems for comparison.

The reaction energy, ΔE_{rxn} , was computed as the difference between the total energies of the products (MX₂Y₂ and X₂) and the reactants (MX₄ and Y₂), at their respective optimized geometries. Values of ΔE_{rxn} for all possible reactions involving TiX₄, ZrX₄, and HfX₄, computed using the MCP-SPD, ECP1-SPD and ECP2-SPD pseudopotentials employing the TZ metal basis sets, are collected in Table 2.8. It should be added that ΔE_{rxn} values computed using DZ metal basis sets induced only minor changes.

At both the RHF and MP2 levels of theory, all of the pseudopotentials predict a negative ΔE_{rxn} value, hence the products are more stable than the reactants, for reactions in which the dihalide added, Y₂, is lighter than the one departing, X₂ (for example

Table 2.8: Summary of the Computed ΔE_{rxn} Values (in kcal/mol) for the Dihalogen Substitution Reactions of MX_4 .^a

Method	Ti		Zr		Hf	
	RHF	MP2	RHF	MP2	RHF	MP2
			$\text{MCl}_4 + \text{Br}_2$			
MCP-SPD	22	17	18	16	19	18
ECP1-SPD	24	19	22	20	22	21
ECP2-SPD	30	23	27	24	29	26
			$\text{MCl}_4 + \text{I}_2$			
MCP-SPD	52	41	45	39	48	43
ECP1-SPD	52	40	49	43	50	45
ECP2-SPD	59	46	54	49	57	53
			$\text{MBr}_4 + \text{Cl}_2$			
MCP-SPD	-22	-17	-18	-16	-19	-18
ECP1-SPD	-24	-18	-22	-20	-23	-21
ECP2-SPD	-29	-22	-27	-24	-28	-26
			$\text{MBr}_4 + \text{I}_2$			
MCP-SPD	31	23	27	23	29	25
ECP1-SPD	29	21	27	22	28	24
ECP2-SPD	29	22	27	24	28	26
			$\text{MI}_4 + \text{Cl}_2$			
MCP-SPD	-53	-38	-45	-38	-49	-42
ECP1-SPD	-53	-37	-49	-41	-50	-44
ECP2-SPD	-59	-41	-54	-46	-57	-51
			$\text{MI}_4 + \text{Br}_2$			
MCP-SPD	-31	-22	-27	-22	-29	-25
ECP1-SPD	-29	-20	-27	-22	-28	-24
ECP2-SPD	-30	-21	-27	-23	-28	-25

^a All ΔE_{rxn} values were computed using the TZ metal valence basis set.

TiBr₄ + Cl₂). This is in agreement with what one would expect based on the experimental values of the average M-X bond enthalpies for the gas-phase MX₄ complexes. The general trend amongst the experimental average M-X bond enthalpies is: M-Cl (Ti: 103, Zr: 117, Hf: 118 kcal/mol) > M-Br (Ti: 88, Zr: 101, Hf: 103 kcal/mol) > M-I (Ti: 71, Zr: 83, Hf: 86 kcal/mol).⁵⁶ The experimental dihalide bond dissociation energies vary as follows: Cl-Cl (58 kcal/mol) > Br-Br (46 kcal/mol) > I-I (36 kcal/mol).⁵⁷ The substitution reaction may be summarized as the breaking of two M-X bonds and a Y-Y bond coupled with the formation of two M-Y bonds and an X-X bond. Since two M-X bonds are broken and two M-Y bonds are formed, while only a single X-X is broken and a single Y-Y bond is formed during the reaction, the metal-halogen bond strength will determine whether the product is favored or not with respect to the reactants. Thus, from the experimental bond enthalpies, the products will be favored when the halogen being added to the complex, Y, is lighter than the departing halogen, X, which our MCP and ECP calculations predict.

The ΔE_{rxn} values computed with the MCP-SPD potential tend to be smaller than those computed using the ECP-SPD potentials. Although a number of exceptions exist, the following trend for the magnitudes of the ΔE_{rxn} values was found: MCP-SPD < ECP1-SPD < ECP2-SPD. Unfortunately, the lack of experimental thermodynamic data for these reactions precludes an assessment of the accuracy of the computed ΔE_{rxn} values. The variation amongst the ΔE_{rxn} values computed using the different pseudopotentials are usually small, on the order of 2-3 kcal/mol, but can be as large as 10 kcal/mol. The inclusion of correlation effects, at the MP2 level, results in a decrease in the magnitudes of the computed ΔE_{rxn} values, of about 5 to 10 kcal/mol, but may be as little as 1 kcal/mol or as large as 20 kcal/mol in some cases.

2.4 Conclusions

The MCP formalism (Version 1) performs very well in modeling the small molecules studied here. The results presented indicate that the model core potentials, employing double-zeta plus polarization and triple-zeta plus double polarization quality valence basis sets, predict geometric structures which agree very well with experimental data, typically within 0.02 Å, although slightly worse agreement was obtained for the homonuclear diatomics. The agreement could be improved further, if larger polarization sets were used (in particular if f polarization functions are added to the valence basis sets), however, such extensively polarized basis sets for ligands would lead to prohibitively large basis sets for post-HF calculations of organometallic compounds. For the molecules

studied here inclusion of electron correlation effects at the CISD level is preferred to the MP2 level. The intruder core orbitals that could be present in the virtual space⁴⁹ do not seem to cause any problems in the present calculations because of ineffective overlap between the valence and intruder core orbitals. For the set of small molecules studied here, the equilibrium bond distances predicted using the MCP formalism are generally smaller than those predicted using the ECP formalism of Stevens.

Values of the harmonic vibrational frequencies for the neutral diatomic molecules studied, obtained by differentiating the fitted polynomial representation of the potential energy surface near the equilibrium. In general, the MCP frequencies agreed with the experimental frequency values to within 50 cm⁻¹. The agreement was poorer for the diatomic ions, with deviations from the experimental vibrational frequencies as large as 90 cm⁻¹ in some cases.

The electron correlation energies of the small main group molecules computed using the MCP formalism are typically smaller than those computed using the ECP formalism of Stevens, at both the MP2 and CISD levels. This follows the trend found in previous studies by Klobukowski⁴⁹, Teichteil⁵⁰ and Pittel⁵¹.

Confident in the performance of the MCP method in dealing with small molecules, the benchmarking study was extended to a systematic study of the Group 4 metal halogen complexes of the type MX₄, where M = Ti, Zr, Hf and X = F, Cl, Br, I. The results obtained clearly indicate that the MCP formalism (Version 1) works well in modeling these small metal complexes, provided the outermost (n-1) p electrons are included in the valence space and treated explicitly. The MCP-SPD methodology predicts M-X bond distances to within 0.02 to 0.03 Å of their experimental values, for all of the MX₄ complexes. Preliminary calculations showed that the large-core, MCP-SD, metal atom potentials are inferior to their small-core counterparts and should be avoided in accord with the previous findings of Sakai and co-workers¹⁷ and Frenking *et al.*¹³ There appears to be little difference between the accuracies of the M-X distances predicted by the MCP-SPD and the two ECP-SPD pseudopotentials of Hay and Wadt and Stevens *et al.*

The results for the MX₄ systems indicate that the agreement between the MCP-SPD computed M-X distances and experiment does not improve significantly when the metal atom valence basis set is expanded from double-zeta to triple-zeta quality. The addition of an f polarization function to the MCP-SPD metal atom valence basis set resulted in a significant decrease in the M-X distance, while the addition of a p polarization function produced only minor changes.

The SPD pseudopotentials predict the direction of the set of dihalide substitution reactions in accord with that expected on the basis of experimental measurements of the

M-X and X-X bond strengths. In general, the ΔE_{rxn} values computed using the MCP-SPD potentials were smaller in magnitude than those computed using the ECP1-SPD and ECP2-SPD potentials. The inclusion of correlation effects, at the MP2 level, resulted in a substantial decrease in the magnitude of the reaction energy, by about 5 to 10 kcal/mol, regardless of the pseudopotential employed.

2.5 References

1. Klobukowski, M.; Sakai, Y.; Huzinaga, S. In *Computational Chemistry: Reviews of Current Trends*; Leszczynski, J., Ed.; World Scientific: Singapore, 1999; Vol. 3, pp 49.
2. Huzinaga, S. *J. Mol. Struct. (Theochem)* **1991**, *234*, 51.
3. Huzinaga, S. *Can. J. Chem.* **1995**, *73*, 619.
4. Huzinaga, S. *Int. J. Quantum Chem.* **1996**, *60*, 83.
5. Cundari, T. R.; Benson, M. T.; Lutz, M. L.; Sommerer, S. O. In *Reviews in Computational Chemistry*; Lipkowitz, K. B. and Boyd, D. B., Ed.; VCH Publishers: New York, 1996; Vol. 8, pp 145.
6. Frenking, G.; Antes, I.; Bohme, M.; Dapprich, S.; Ehlers, A. W.; Jonas, V.; Neuhaus, A.; Otto, M.; Stegmann, R.; Veldkamp, A.; Vyboishchikov, S. F. In *Reviews in Computational Chemistry*; Lipkowitz, K. B. and Boyd, D. B., Ed.; VCH Publishers: New York, 1996; Vol. 8, pp 63.
7. Bonifacic, V.; Huzinaga, S. *J. Chem. Phys.* **1974**, *60*, 2779.
8. Sakai, S. *J. Chem. Phys.* **1981**, *75*, 1303.
9. Sakai, S.; Huzinaga, S. *J. Chem. Phys.* **1982**, *76*, 2537.
10. Huzinaga, S.; Seijo, L.; Barandiaran, Z.; Klobukowski, M. *J. Chem. Phys.* **1987**, *86*, 2132.
11. Katsuki, S.; Huzinaga, S. *Chem. Phys. Lett.* **1988**, *152*, 203.
12. Miyoshi, E.; Sakai, Y. *J. Comput. Chem.* **1988**, *9*, 719.
13. Jonas, V.; Frenking, G.; Reetz, M. *J. Comput. Chem.* **1992**, *13*, 919.
14. Hay, P. J.; Wadt, W. R. *J. Chem. Phys.* **1985**, *82*, 270.
15. Wadt, W. R.; Hay, P. J. *J. Chem. Phys.* **1985**, *82*, 284.
16. Hay, P. J.; Wadt, W. R. *J. Chem. Phys.* **1985**, *82*, 299.
17. Sakai, Y.; Miyoshi, E. *J. Chem. Phys.* **1987**, *87*, 2885.
18. Miyoshi, E.; Sakai, Y.; Murakami, A.; Iwaki, H.; Terashima, H.; Shoda, T.; Kawaguchi, T. *J. Chem. Phys.* **1988**, *89*, 4193.
19. Miyoshi, E.; Sakai, Y. *J. Chem. Phys.* **1988**, *89*, 7363.

20. Papai, I.; Goursot, A.; St-Amant, A.; Salahub, D. R. *Theoret. Chim. Acta* **1992**, *84*, 217.
21. Yang, D.-S.; Zgierski, M. K.; Rayner, D. M.; Hackett, P. A.; Martinez, A.; Salahub, D. R.; Roy, P.-N.; Carrington, T. J. *J. Chem. Phys.* **1995**, *103*, 5335.
22. Yang, D.-S.; Zgierski, M. K.; Berces, A.; Hackett, P. A.; Roy, P.-N.; Martinez, A.; Carrington, T. J.; Salahub, D. R.; Fournier, R.; Pang, T.; Chen, C. *J. Chem. Phys.* **1996**, *105*, 10663.
23. Yang, D.-S.; Zgierski, M. K.; Berces, A.; Hackett, P. A.; Martinez, A.; Salahub, D. R. *Chem. Phys. Lett.* **1997**, *277*, 71.
24. Miyoshi, E.; Sakai, Y.; Mori, S. *Chem. Phys. Lett.* **1985**, *113*, 457.
25. Miyoshi, E.; Sakai, Y.; Mori, S. *Surface Sci.* **1985**, *158*, 667.
26. Miyoshi, E.; Sakai, Y.; Mori, S. *Mem. Fac. Sci. Kyushu Univ. Ser. C* **1985**, *15*, 37.
27. Sakai, Y.; Miyoshi, E. *Phys. Rev. B* **1995**, *52*, 14150.
28. Sumi, T.; Sakai, Y.; Miyoshi, E. *Phys., Rev. B* **1997**, *55*, 4755.
29. Rochefort, A.; Andzelm, J.; Russo, N.; Salahub, D. R. *J. Am. Chem. Soc.* **1990**, *112*, 8239.
30. Fournier, R.; Andzelm, J.; Goursot, A.; Russo, N.; Salahub, D. R. *J. Chem. Phys.* **1990**, *93*, 2919.
31. Andzelm, J.; Rochefort, A.; Russo, N.; Salahub, D. R. *Surface Sci.* **1990**, *235*, L319.
32. Papai, I.; St-Amant, A.; Ushio, J.; Salahub, D. R. *Surface Sci.* **1990**, *236*, 241.
33. Goursot, A.; Papai, I.; Salahub, D. R. *J. Am. Chem. Soc.* **1992**, *114*, 7452.
34. Sirois, S.; Castro, M.; Salahub, D. R. *Int. J. Quantum Chem. Symp.* **1994**, *28*, 645.
35. Cotton, F. A.; Wilkinson, G. *Advanced Inorganic Chemistry*; Fifth ed.; Wiley Interscience: New York, 1988.
36. Stevens, W. J.; Basch, H.; Krauss, M. *J. Chem. Phys.* **1984**, *81*, 6026.
37. Krauss, M.; Stevens, W. J.; Basch, H.; Jasien, P. G. *Can. J. Chem.* **1992**, *70*, 612.
38. Cundari, T. R.; Stevens, W. J. *J. Chem. Phys.* **1993**, *98*, 5555.
39. Huzinaga, S.; Andzelm, J.; Klobukowski, M.; Radzio-Andzelm, E.; Sakai, Y.; Tatewaki, H. *Gaussian Basis Sets for Molecular Calculations*; Elsevier: Amsterdam, 1984.
40. Powell, M. J. D. *Comput. J.* **1964**, *7*, 155.
41. Levine, I. N. *Quantum Chemistry*; Allyn and Bacon: Boston, 1970; Vol. 2: Molecular Spectroscopy.
42. Schmidt, M. W.; Baldridge, K. K.; Boaltz, J. A.; Jensen, J. H.; Koseki, S.; Gordon, M. S.; Nguyen, K. A.; Windus, T. L.; Elbert, S. T. *QCPE Bull.* **1990**, *10*, 52.

43. Schmidt, M. W.; Baldrige, K. K.; Boaltz, J. A.; Elbert, S. T.; Gordon, M. S.; Jensen, J. H.; Koseki, S.; Matsunaga, N.; Nguyen, K. A.; Su, S.; Windus, T. L.; Dupuis, M. *J. Comput. Chem.* **1993**, *14*, 1347.
44. Ehlers, A. W.; Bohme, M.; Dapprich, S.; Gabbi, A.; Hollwarth, A.; Jonas, V.; Kohler, K. F.; Stegmann, R.; Veldkamp, A.; Frenking, G. *Chem. Phys. Lett.* **1993**, *208*, 111.
45. Huber, K. P.; Herzberg, G. *Molecular Spectra and Molecular Structure*; Van Nostrand Reinhold: New York, 1979; Vol. 4. Constants of Diatomic Molecules.
46. Hellwege, K.-H.; Hellwege, A. M. E. *Landolt-Bornstein Numerical Data and Functional Relationships in Science and Technology*; Springer: Berlin, 1976; Vol. 7. Structure Data of Free Polyatomic Molecules.
47. Hellwege, K.-H.; Hellwege, A. M. E. *Landolt-Bornstein Numerical Data and Functional Relationships in Science and Technology*; Springer: Berlin, 1987; Vol. 15. Structure Data of Free Polyatomic Molecules.
48. Kuchitsu, K. E. *Landolt-Bornstein Numerical Data and Functional Relationships in Science and Technology*; Springer: Berlin, 1992; Vol. 22. Structure Data of Free Polyatomic Molecules.
49. Klobukowski, M. *Chem. Phys. Lett.* **1990**, *172*, 361.
50. Teichteil, C.; Malrieu, J. P.; Barthelat, J. C. *Mol. Phys.* **1977**, *33*, 181.
51. Pittel, B.; Schwarz, W. H. E. *Chem. Phys. Lett.* **1977**, *46*, 121.
52. Siegbahn, P. E. M. In *Advances in Chemical Physics*; Prigogine, I. and Rice, S. A., Ed.; John Wiley and Sons, Inc.: New York, 1996; Vol. 93, pp 333.
53. Salahub, D. R.; Zerner, M. C. In *The Challenge of d and f Electrons*, 394 ed.; Salahub, D. R. and Zerner, M. C., Ed.; American Chemical Society: Washington, D. C., 1989, pp 1.
54. Veillard, A. *Chem. Rev.* **1991**, *91*, 743.
55. Gordon, M. S.; Cundari, T. R. *Coord. Chem. Rev.* **1996**, *147*, 87.
56. Huheey, J. E. *Inorganic Chemistry. Principles of Structure and Reactivity*; Harper and Row: New York, 1978, Appendix F.
57. Lide, D. R. E. *CRC Handbook of Chemistry and Physics*; 76th ed.; CRC Press: Boca Raton, 1995.

Chapter 3

Incorporation of L-Shell Structure into the Model Core Potential Valence Basis Sets for the Main Group Elements

3.1 Introduction

As discussed previously, the model core potentials reduce times of calculations by decreasing the number of electrons treated explicitly. It is possible to reduce the computational expense further by modifying the MCP valence basis sets to incorporate L-shell structure, whereby the s and p exponents of the primitive gaussian functions are constrained to be the same.¹

Recall that the atomic (or molecular) orbitals, ϕ_i , are formed as a linear combination of atom-centred basis functions χ_μ :

$$\phi_i(1) = \sum_{\mu=1}^N \chi_\mu(1) c_{\mu i} . \quad (3.1)$$

In atoms, the basis functions (χ_μ) usually take the form of gaussian functions defined as:

$$X_\mu(r, \theta, \phi) = G_{n\ell m}(r, \theta, \phi) = R_{n\ell}(r) Y_{\ell m}(\theta, \phi) \quad (3.2)$$

$$R_{n\ell}(r) = N(n, \alpha) r^{n-1} e^{-\alpha r^2} \quad (3.3)$$

where n , ℓ , and m are the principal, angular momentum, and magnetic quantum numbers, and α is the gaussian exponent. $Y_{\ell m}(\theta, \phi)$ is a spherical harmonic function, representing the angular portion of the gaussian function. $N(n, \alpha)$ is the normalization constant:

$$N(n, \alpha) = 2^{n+1} [(2n-1)!!]^{-\frac{1}{2}} (2\pi)^{-\frac{1}{2}} \alpha^{\frac{(2n+1)}{2}}, \quad n = \ell + 1, \ell + 3, \ell + 5, \dots \quad (3.4)$$

For practical reasons², all of the radial functions for the ns atomic orbitals are expanded in terms of 1s-type gaussian functions (i.e. $R_{1,0}$). Similarly, the radial component of the gaussian functions for the np atomic orbitals are expanded solely in terms of 2p-type gaussian functions (i.e. $R_{2,1}$), those of the nd orbitals are expanded in terms of the 3d-type gaussians (i.e. $R_{3,2}$), and so on. For example the radial component of the gaussians for the 3s and 3p atomic orbitals of an atom are represented as:

$$R_{3s}^{atom}(r) = R_{1,0}(r) = N(1, \alpha) e^{-\alpha r^2} \quad (3.5)$$

$$R_{3p}^{atom}(r) = R_{2,1}(r) = N(2, \alpha) r e^{-\alpha r^2} \quad (3.6)$$

with the normalization constants given by:

$$N(1, \alpha) = 2^2 [(1)!!]^{-\frac{1}{2}} (2\pi)^{-\frac{1}{2}} \alpha^{\frac{(1)}{2}} \quad (3.7)$$

$$N(2, \alpha) = 2^3 [(3)!!]^{-\frac{1}{2}} (2\pi)^{-\frac{1}{2}} \alpha^{\frac{(3)}{2}} . \quad (3.8)$$

The atom-centred gaussian basis functions, $\chi_\mu(r)$, may be either individual gaussian functions (uncontracted) or a fixed linear combination of gaussian functions:

$$\chi_\mu^X(r) = \sum_{k=1}^K G_X(\alpha_k; r) d_{\mu k}^X . \quad (3.9)$$

Omitting the explicit dependence on r for simplicity:

$$\chi_{\mu}^X = \sum_{k=1}^K G_X(\alpha_k) d_{\mu k}^X . \quad (3.10)$$

$\chi_{\mu}^X(r)$ are called contracted gaussian type functions (CGTF), while the individual gaussian functions in the expansion, $G_X(\alpha_k; r)$, are known as primitive gaussian type functions (PGTFs). The index X is used to denote the type of gaussian function, Equation (3.2). For CGTFs, the expansion coefficients, $d_{\mu k}^X$, are known and fixed at the values determined when the basis set was initially developed.^{3,4}

For the first and second row elements of groups 13-18, the MCP valence space consists of the ns and np subshells (MCP-SP); for elements in rows three through five, the MCP valence space may comprise either the ns and np subshells, or the $(n-1)d$ subshell may also be included along with the ns and np subshells (MCP-DSP). In both types of MCPs, the valence basis sets were originally designed with a different set of exponents for the PGTFs of the s and p subshells.⁵⁻⁷ This can be seen in the MCP-SP valence basis set of carbon, given in Table 3.1, in its simplest minimal form. The CGTFs representing the $2s$ and $2p$ atomic orbitals of carbon are given by the following expansions:

$$\chi_{2s} = -0.08G_{s,1}(36.199) - 0.26G_{s,2}(5.179) + 0.65G_{s,3}(0.436) + 0.45G_{s,4}(0.138) \quad (3.11)$$

$$\chi_{2p} = 0.05G_{p,1}(8.428) + 0.26G_{p,2}(1.654) + 0.54G_{p,3}(0.443) + 0.38G_{p,4}(0.126) \quad (3.12)$$

where the exponents of the primitive gaussians are enclosed in parentheses, and the explicit dependence on r is removed for simplicity. The subscript s, l defines the first s -type PGTF, etc. The $2s$ and $2p$ CGTFs are represented by an expansion in terms of four PGTFs, each with its own unique exponent. An L-shell MCP valence basis set for carbon is given at the bottom of Table 3.1: the exponents of the ns and np primitive functions are the same, but the contraction coefficients are different. The MCP L-shell minimal CGTFs for the $2s$ and $2p$ orbitals of carbon are expanded as:

$$\chi_{2s} = -0.11G_{s,1}(29.320) - 0.31G_{s,2}(3.691) + 0.46G_{s,3}(0.730) + 0.72G_{s,4}(0.178) \quad (3.13)$$

$$\chi_{2p} = 0.01G_{p,1}(29.320) + 0.14G_{p,2}(3.691) + 0.51G_{p,3}(0.730) + 0.56G_{p,4}(0.178) \quad (3.14)$$

using the same notation as above.

Two-electron integral evaluation is a necessary step in the SCF procedure as well as in calculating the first and second derivatives of the energy with respect to the nuclear coordinates (for optimizing structures and computing vibrational frequencies).^{3,4} Hehre and Pople¹ showed that it is possible to improve the computational efficiency of two-electron integral evaluation if the basis set incorporates L-shell structure. The two-electron repulsion integrals take the form:

Table 3.1: Sample MCP Valence Basis Sets for C.

α_k	c_s	c_p
Conventional MCP-SP Basis Set		
36.199	-0.082	
5.179	-0.258	
0.436	0.647	
0.138	0.455	
8.428		0.050
1.654		0.264
0.443		0.542
0.126		0.380
L-shell MCP-SP Basis Set		
29.320	-0.106	0.008
3.691	-0.309	0.141
0.730	0.457	0.510
0.178	0.718	0.556

$$(pr|st) = \iint \chi_p^*(1)\chi_s^*(2)\left(\frac{1}{r_{12}}\right)\chi_r(1)\chi_t(2)d\tau \quad (3.15)$$

where $\chi_p(i)$ is a CGTF on atom p for electron i . If each of the CGTFs is expanded in terms of K PGTFs, then the two-electron integrals formally scale as K^4 , and their evaluation becomes quite laborious. Under the L-shell constraint, it is possible to use the information from the integrals involving the exponential over the s-type primitive functions in computing the integrals over the p-type primitive functions. Since the exponents for the s and p functions are identical, they will have the same radial behavior and may be treated as one function during evaluation of the exponential portion of the integral, thereby reducing the computational expense.

L-shell structure has been incorporated into a number of commonly used all-electron basis sets (STO-3G⁸⁻¹², 3-21G¹³⁻¹⁷, 6-311G¹⁸⁻²² etc.) and in the basis sets for the effective core potentials of Stevens and co-workers²³⁻²⁵. Tests performed in the original papers have shown that the decreased flexibility associated with the L-shell basis sets (due to the common set of s and p exponents) does not result in any significant loss in accuracy when employed in molecular calculations. Many popular quantum chemistry programs make use of L-shell structure (GAMESS^{26,27}, HONDO²⁸, CADPAC²⁹, Gaussian94³⁰).

This chapter describes the results of re-parameterizing the MCP valence ns and np basis functions to incorporate L-shell structure for the elements of Groups 13-18, in order to take advantage of the efficient computer codes for two-electron integral evaluation. Even though the primary focus of the work in this thesis is transition metal complexes, atoms from the main group elements are normally present in the ligands in large numbers. As a result, much of the computational cost of calculations on transition metal complexes is associated with the presence of the main group elements. By incorporating L-shell structure into the MCP valence basis sets for the main group elements, the computational time of studies on transition metal complexes may be reduced.

The L-shell exponents were derived by simultaneously fitting, in a least-squares sense, the ns and np radial functions expanded in terms of the original MCP s and p PGTFs, under the constraint of a common set of exponents. The MCP core parameters were kept at their original values. Details of the fitting process are described in section 3.2.1.

The newly developed L-shell MCP valence basis sets were tested in atomic calculations (section 3.2.2) for all of the main group elements, with the results compared to those obtained using the original MCP basis sets. In addition, the new L-shell MCP

valence basis sets were evaluated in molecular calculations of the octahedral SF₆, SeF₆ and TeF₆ systems (section 3.2.3).

3.2 Computational Methodologies

3.2.1 Fitting Procedures

The MCP L-shell valence basis sets were derived by simultaneously fitting the original MCP valence ns and np radial functions, under the constraint of a common set of exponent values. This procedure was analogous to that used by Dobbs and Hehre¹⁵⁻¹⁷ to generate the all electron 3-21G basis sets from Huzinaga's MINI basis sets.³¹

The original MCP valence basis sets of carbon, discussed above and given in Table 3.1, will be used to illustrate the fitting procedure. The original MCP 2s and 2p basis functions for C were used in their completely contracted, minimal form (i.e. a single contracted basis function for the 2s and 2p subshells) comprised of four PGTFs, each with its own unique exponent, giving the reference radial functions:

$$R_{2s}^{ref}(r) = \sum_{k=1}^{K_s} G_s(\alpha_{k,s}; r) d_k^s \quad (3.16)$$

$$R_{2p}^{ref}(r) = \sum_{k=1}^{K_p} G_p(\alpha_{k,p}; r) d_k^p \quad (3.17)$$

where $G_\ell(\alpha_{k,\ell}; r)$ denotes a PGTF with exponent $\alpha_{k,\ell}$ and expansion coefficients d_k^ℓ , $\ell=s, p$. There are a total of K_s and K_p primitive gaussian functions in the expansions of the 2s and 2p radial functions. For the MCP basis set of carbon, K_s and K_p are both equal to four.

The 2s and 2p radial functions can be expanded in terms of the L-shell primitive gaussian functions in an analogous manner:

$$R_{2s}^{fit}(r) = \sum_{j=1}^J G_s(\alpha_j; r) d_j^s \quad (3.18)$$

$$R_{2p}^{fit}(r) = \sum_{j=1}^J G_p(\alpha_j; r) d_j^p. \quad (3.19)$$

The L-shell PGTFs are denoted $G_\ell(\alpha_j; r)$, with expansion coefficients d_j^ℓ , $\ell=s, p$. Notice that in this case the exponents (α_j) are the same for the s and p primitive functions, independent of the quantum number ℓ . There are a total of J primitive gaussians used in each expansion.

The function to be minimized during the fitting process is the sum of the squares of the deviation between the fitted and reference radial functions:

$$\begin{aligned} \Delta &= w_s \cdot \Delta_s + w_p \cdot \Delta_p \\ &= w_s \sum_{i=1}^N [R_s^{ref}(r_i) - R_s^{fit}(r_i)]^2 + w_p \sum_{i=1}^N [R_p^{ref}(r_i) - R_p^{fit}(r_i)]^2 \end{aligned} \quad (3.20)$$

where w_s and w_p are weighting factors for the s and p contributions to Δ ; they are defined as:

$$w_s = \frac{N_s}{N_s + N_p} \quad (3.21)$$

$$w_p = \frac{N_p}{N_s + N_p} \quad (3.22)$$

N_s and N_p are the number of s and p electrons for the atom, respectively, and should not be confused with the symbol N in the equation for Δ , Equation (3.20). The reference and fitted radial functions are evaluated at a total of N radial points, r_i .

Substituting the general form of the fitted radial function into Δ gives:

$$\Delta = w_s \sum_{i=1}^N \left[R_s^{ref}(r_i) - \sum_{j=1}^J G_s(\alpha_j; r_i) d_j^s \right]^2 + w_p \sum_{i=1}^N \left[R_p^{ref}(r_i) - \sum_{j=1}^J G_p(\alpha_j; r_i) d_j^p \right]^2. \quad (3.23)$$

The weighting factors, as well as the reference radial functions, are known. For a known set of exponents $\{\alpha_j\}$ the value of Δ is minimized with respect to the linear coefficients

$\{d_j^s; d_j^p\}$,

$$\frac{\partial \Delta}{\partial d_k^s} = 2w_s \sum_{i=1}^N \left[R_s^{ref}(r_i) - \sum_{j=1}^J G_s(\alpha_j; r_i) d_j^s \right] \times [-G_s(\alpha_k; r_i)] = 0; \quad k = 1, 2, \dots, J; \quad (3.24)$$

$$\frac{\partial \Delta}{\partial d_k^p} = 2w_p \sum_{i=1}^N \left[R_p^{ref}(r_i) - \sum_{j=1}^J G_p(\alpha_j; r_i) d_j^p \right] \times [-G_p(\alpha_k; r_i)] = 0; \quad k = 1, 2, \dots, J. \quad (3.25)$$

Re-arranging these equations gives the following sets of equations:

$$\begin{aligned} \sum_{i=1}^N R_s^{ref}(r_i) G_s(\alpha_k; r_i) &= \sum_{i=1}^N \sum_{j=1}^J G_s(\alpha_j; r_i) G_s(\alpha_k; r_i) d_j^s \\ &= \sum_{j=1}^J \sum_{i=1}^N G_s(\alpha_k; r_i) G_s(\alpha_j; r_i) d_j^s; \quad k = 1, 2, \dots, J \end{aligned} \quad (3.26)$$

$$\begin{aligned} \sum_{i=1}^N R_p^{ref}(r_i) G_p(\alpha_k; r_i) &= \sum_{i=1}^N \sum_{j=1}^J G_p(\alpha_j; r_i) G_p(\alpha_k; r_i) d_j^p \\ &= \sum_{j=1}^J \sum_{i=1}^N G_p(\alpha_k; r_i) G_p(\alpha_j; r_i) d_j^p; \quad k = 1, 2, \dots, J \end{aligned} \quad (3.27)$$

With the definition of the following matrix elements:

$$B_{\ell}(k) = \sum_{i=1}^N R_{\ell}^{ref}(r_i) G_{\ell}(\alpha_k; r_i); \ell = s, p \quad (3.28)$$

$$A_{\ell}(j, k) = \sum_{i=1}^N G_{\ell}(\alpha_j; r_i) G_{\ell}(\alpha_k; r_i); \ell = s, p, \quad (3.29)$$

the Equations (3.26) and (3.27) take a compact form in matrix notation:

$$\underline{A}_{\ell} \underline{d}_{\ell} = \underline{B}_{\ell}; \ell = s, p, \quad (3.30)$$

and the desired solutions for the expansion coefficients $\{d_j^{\ell}\}$ are:

$$\underline{d}_{\ell} = \underline{A}_{\ell}^{-1} \underline{B}_{\ell}; \ell = s, p. \quad (3.31)$$

The search for optimized exponents $\{\alpha_j\}$ is performed using Brent's method³². For each trial set of exponents, Δ is repeatedly minimized with respect to the expansion coefficients $\{d_j^{\ell}\}$, Equations (3.20) to (3.31), until the exponents and expansion coefficients converge within assumed criteria.

The results of the L-shell fitting for the elements of Groups 13-18 are described in detail in section 3.3.1.

3.2.2 Atomic Calculations

As a first step in validating the new L-shell MCP valence basis sets, atomic calculations were performed for atoms from Groups 13 to 18. For each atom, a number of different contraction schemes were employed for the L-shell basis sets. The smallest MCP L-shell basis set employed was of minimal quality, denoted as n , whereby the single contracted L-shell basis function, as determined in the least-squares procedure was used. If the L-shell contracted gaussian functions were expanded in terms of J primitive gaussian functions, the minimal (n) basis sets have a (n_s/n_p) contraction pattern, where $n_s=n_p=J$. In this notation, a basis set is defined with one s and one p contracted basis function, expanded in terms of n_s and n_p primitive functions. A contraction scheme defined as $(n_s 1/n_p 1)$ would define a basis set with two s and two p contracted basis functions, in which the first CGTF is expanded in terms of n_s or n_p primitive functions and the second CGTF is a single primitive function. If a d polarization function is added to the above basis set the contraction scheme would be written as $(n_s 1/n_p 1/1^*)$, whereby the second slash defines the d-space and the asterisk signifies a polarization function. A double-zeta, $n1$ type contraction, was used for the atomic calculations in which the outermost (smallest exponent) primitive function was uncontracted, giving a $(n_s 1/n_p 1)$ contraction, where $n_s=n_p=J-1$. Uncontracting the two outermost primitive functions gives the $n11$ L-shell basis

sets with a $(n_s 11/n_p 11)$ contraction pattern, where $n_s=n_p=J-2$. The L-shell basis sets denoted as $n2I$ are similar to the $n1I$ basis sets and have a $(n_s 21/n_p 21)$ contraction, with $n_s=n_p=J-3$. The $n11I$ L-shell basis sets were formed by uncontracting the three outermost primitives in a $(n_s 111/n_p 111)$ contraction pattern, where $n_s=n_p=J-3$.

The atomic calculations were performed for atoms in their ground electronic states, at the ROHF level of theory, with a version of the general atomic program of Huzinaga, Klobukowski and Sakai³³ modified to enable the use of model core potentials. The results are discussed in section 3.3.2.

3.2.3 Molecular Calculations

The MCP L-shell basis sets for the main group elements were tested further in molecular calculations of the neutral octahedral SF_6 , SeF_6 and TeF_6 molecules. The aim of these calculations was to determine if the imposition of shared s and p exponents in the L-shell basis sets results in any substantial loss in accuracy of computed molecular structures and vibrational frequencies. In addition, these calculations were used to gauge the improvements in computational efficiency gained by using the MCP L-shell basis sets in molecular calculations.

The AF_6 molecular calculations were performed using the MCP-SP and MCP-DSP core potentials with the corresponding L-shell and conventional valence basis sets. The basis set contractions used for the central atom in the AF_6 molecular calculations, along with the naming convention adopted for them, are given in Table 3.2. The conventional MCP-SP and MCP-DSP basis sets are labeled as SP- $n1$, SP- $n11$, and SP- $n21$, and DSP- $n1$, DSP- $n11$ and DSP- $n21$, respectively. For fluorine the conventional MCP basis set was contracted as (31/31) and used in combination with the central atom SP and DSP conventional MCP basis sets. The notation: $(n_s 1/n_p 1/1^*; 31/31)$, $(n_s 11/n_p 11/1^*; 31/31)$, $(n_s 11/n_p 11/1^*; 31/31)$ can be used to represent the conventional MCP-SP basis sets employed in the AF_6 molecular calculations. The conventional MCP-DSP basis sets used in the AF_6 calculations may be represented as: $(n_s 1/n_p 1/n_d 11^*; 31/31)$, $(n_s 11/n_p 11/n_d 11^*; 31/31)$, $(n_s 11/n_p 11/n_d 11^*; 31/31)$. This notation describes the basis set contractions used for the entire AF_6 molecule. The central atom basis set contraction is defined first, followed by the fluorine atom basis set contraction, separated by a semi-colon. The newly derived MCP-SP and MCP-DSP L-shell basis sets employed were labeled as SP_L- $n1$, SP_L- $n11$, and SP_L- $n21$ and DSP_L- $n1$, DSP_L- $n11$, and DSP_L- $n21$, respectively. The MCP L-shell valence basis set for fluorine, used in combination with the SP_L and DSP_L central atom basis sets, contained five primitive gaussian functions, expanded as (41/41).

Table 3.2: MCP Valence Basis Set Contractions Employed for the Central Atoms of SF₆, SeF₆ and TeF₆.

Label	S	Se	Te
SP-n1	(31/31/1*)	(41/41/1*)	(51/41/1*)
SP-n11	(211/211/1*)	(311/311/1*)	(411/311/1*)
SP-n21	(121/121/1*)	(221/221/1*)	(321/221/1*)
DSP-n1		(61/51/411*)	(71/61/511*)
DSP-n11		(511/411/411*)	(611/511/511*)
DSP-n21		(421/321/411*)	(521/421/511*)
SP_L-n1	(41/41/1*)	(41/41/1*)	(51/51/1*)
SP_L-n11	(311/311/1*)	(311/311/1*)	(411/411/1*)
SP_L-n21	(221/221/1*)	(221/221/1*)	(321/321/1*)
DSP_L-n1		(61/61/411*)	(71/71/511*)
DSP_L-n11		(511/511/411*)	(611/611/511*)
DSP_L-n21		(421/421/411*)	(521/521/511*)

The MCP-SP and MCP-DSP L-shell basis sets for AF_6 may be denoted as: (L-n1/1*; L41), (L-n11/1*; L41), (L-n21/1*; L41) and (L-n1/n_d11*; L41), (L-n11/n_d11*; L41), (L-n21/n_d11*; L41). The d polarization function on the central atom was taken from the compilation of Huzinaga and co-workers.³¹

The geometries of the octahedral AF_6 molecules were optimized using analytical gradients as implemented in the CADPAC program.²⁹ Harmonic vibrational frequencies were computed at the optimized geometries using analytical second derivatives.²⁹ The calculations were carried out at the RHF and density functional theory (DFT) levels. For the DFT calculations, Becke's three parameter gradient-corrected, hybrid exchange functional³⁴ was utilized in conjunction with the non-local correlation functional of Lee, Yang and Parr³⁵, commonly referred to as the B3LYP functional.

Timing runs were performed on a SUN Ultrasparc 10 with 128 MB of RAM to compare the performance of the conventional and L-shell MCP basis sets. During the course of these runs no other processes were run allowing nearly 100 % usage of the CPU.

The results of the geometry optimizations and harmonic frequency calculations are discussed in section 3.3.3, while those for the timings are discussed in section 3.3.4.

3.3 Results and Discussion

3.3.1 L Shell Fitting

The MCP-SP L-shell valence basis sets (SP_L) for the elements of Group 14 of the periodic table (C, Si, Ge, Sn, Pb) are displayed in Table 3.3. A complete listing of all of the MCP-SP L-shell basis sets are available in Appendix B. Also given in the tables are the values of Δ . Only the best L-shell basis sets, in terms of accuracy of the least-squares fit and computational cost, are shown.

For the first row elements, the optimum MCP-SP L-shell valence basis sets were obtained by fitting the reference radial function (expanded in terms of four s and four p primitives) with five primitive functions. An average Δ value of 2.44×10^{-3} was found for these fits, with values for the different atoms in the range 4.21×10^{-4} to 4.26×10^{-4} . Fits using four L-shell primitive functions were acceptable for some of the first row elements (B, C, N), but questionable for others (O, F, Ne).

For the second row elements, the MCP-SP reference radial functions (expanded in terms of four s and four p primitive gaussian functions) were fit well using five L-shell primitive gaussian functions. The L-shell basis sets containing four primitive functions

Table 3.3: A Representative Sample of the Optimum MCP-SP L-Shell Valence Basis Sets.

N	α	C_s	C_p	Δ^a
C				
1	37.28756443	-0.07863158	0.00447533	0.19828017E-02
2	5.48854614	-0.25023051	0.07271160	
3	1.40333400	-0.01999411	0.26824079	
4	0.42680786	0.69269460	0.50971349	
5	0.12849330	0.41980104	0.37896052	
Si				
1	59.95976956	0.06381545	-0.01786194	0.44608725E-01
2	6.28524227	-0.04375645	-0.15721876	
3	1.66596897	-0.46216760	-0.04912570	
4	0.25539492	0.73406876	0.59435329	
5	0.08544019	0.44779459	0.49533583	
Ge				
1	50.08457824	0.00703801	0.05262546	0.15274757E-01
2	8.04542517	0.22135588	-0.05363663	
3	2.42445596	-0.58518014	-0.18558600	
4	0.24009925	0.67260466	0.62626846	
5	0.07700996	0.47366802	0.47764790	
Sn				
1	24.95176834	-0.15043389	0.01462768	0.28062097E-02
2	10.49131963	0.33146528	0.07259711	
3	1.80898242	0.00722958	-0.25936823	
4	1.32519990	-0.63653685	0.03091421	
5	0.17105903	0.92133432	0.69502277	
6	0.05322037	0.27295467	0.41187489	

Pb				
1	167.14380202	0.03374899	-0.00300042	0.25183754E-02
2	34.43843758	-0.14813796	-0.02972776	
3	8.67167765	0.26230812	0.13989692	
4	3.61507485	0.19370804	-0.06569906	
5	1.34132932	-0.86311655	-0.27211317	
6	0.17518741	1.01849589	0.64041541	
7	0.05689278	0.19584036	0.48047142	

^a Values correspond to the sum of the squares of the deviations between the L-shell and reference radial functions evaluated at each radial point in the grid, Equation (3.20).

were not flexible enough to fit the original s and p primitives, resulting in a large average Δ value of 1.23×10^{-1} , and individual values in the range 9.80×10^{-2} - 1.76×10^{-1} . The increased flexibility of the L-shell basis sets containing five primitive functions, improved the accuracy of the fits to the reference radial functions by about an order of magnitude (average Δ value of 1.77×10^{-2} and individual values of 4.33×10^{-3} - 4.46×10^{-2}). The increased flexibility outweighs the additional computational cost associated with an additional primitive function.

Satisfactory fits were obtained for the third row elements, when the reference radial functions, expanded using five s and five p primitive gaussians, were fit with five L-shell primitive functions. The average Δ value was 1.15×10^{-2} , with individual values between 6.42×10^{-4} and 1.55×10^{-2} . Better fits to the reference radial functions were obtained if a sixth L-shell primitive was employed (an average Δ value of 1.41×10^{-3} , and individual values in the range 1.04×10^{-3} to 2.25×10^{-3}) but the added computational cost was deemed not necessary in this case.

For the fourth row elements, the reference radial functions, expanded in terms of six s and five p primitive gaussians, were fit well using six L-shell primitive functions, with the exception of I and Xe. The average Δ value for these fits was 3.73×10^{-3} , with individual Δ values of 2.81×10^{-3} - 4.91×10^{-3} . For I and Xe unconstrained optimization converged to four terms. This problem was rectified by using a seventh primitive function in the least squares fits (Δ values of 8.60×10^{-4} and 8.31×10^{-4} for I and Xe).

The reference radial functions for the fifth row elements were expanded in terms of seven s and five p primitive functions. These were successfully fit using seven L-shell primitive gaussians, with an average Δ value of 2.42×10^{-3} , and individual values of 2.04×10^{-3} to 2.98×10^{-3} .

A representative sample (Ge, Sn and Pb) of the MCP-DSP L-shell valence basis sets (DSP_L) are given in Table 3.4. A complete listing of all of the DSP_L basis sets is available in Appendix B. For these basis sets, L-shell structure was imposed on the ns and np subshells of the original MCP-DSP basis sets, keeping the (n-1)d primitive gaussian functions intact. As above, values of Δ are also included in the table. Only the optimum L-shell basis sets, in terms of accuracy and computational cost, are displayed.

For the third row elements, satisfactory fits to the reference radial functions (comprised of seven s and six p primitive functions) were obtained using seven L-shell primitive functions. An average Δ value of 3.09×10^{-3} was obtained with individual values between 2.66×10^{-3} and 3.33×10^{-3} .

In the case of the fourth row elements, satisfactory fits to the DSP reference radial functions (expanded in terms of eight s and seven p primitive gaussians) were obtained

Table 3.4: A Representative Sample of the Optimum MCP-DSP L-Shell Valence Basis Sets.

N	α	C_s	C_p	C_d	Δ^a
Ge					
L 7					
1	433.95753699	-0.03064237	0.00012487		0.33351300E-02
2	57.90269674	-0.00448577	0.06766028		
3	16.79986773	0.18437122	-0.00543316		
4	2.93909717	-0.26115159	-0.21538174		
5	1.35072018	-0.31338912	0.02205936		
6	0.23516329	0.81418056	0.59534843		
7	0.07215178	0.37701010	0.50464304		
D 5					
1	64.68981000			0.04148314	
2	17.23871600			0.20000632	
3	5.74528800			0.42195557	
4	1.95628290			0.46240145	
5	0.62347294			0.20170133	
Sn					
L 8					
1	1167.3462694	0.02208456	-0.00017264		0.31197295E-02
2	163.62294314	-0.00476628	-0.03502374		
3	40.62021102	-0.13892294	0.00742133		
4	10.08103646	0.31944181	0.13574029		
5	2.92536012	0.05074317	-0.15342790		
6	1.36050241	-0.71716513	-0.17314076		
7	0.17891996	0.84811504	0.63833475		
8	0.05803607	0.34734083	0.47128929		

D 6				
1	184.5279100			-0.01939517
2	50.37842000			-0.10614361
3	17.36772800			-0.20023220
4	2.68458570			0.44852175
5	1.03915190			0.52427474
6	0.36984112			0.18036569
Pb				
L 9				
1	5189.0091253	-0.01933773	0.00006906	0.20206700E-02
2	541.84252411	0.00179099	0.01478791	
3	146.53024167	0.09484682	-0.00463845	
4	38.54342693	-0.22729470	-0.05770203	
5	7.64348648	-7.06638108	7.02169796	
6	7.58994103	7.53136651	-6.89139258	
7	1.42691801	-0.82254451	-0.30508114	
8	0.17591141	0.94327938	0.61100348	
9	0.05671249	0.24926751	0.50774940	
D 7				
1	323.9735300			0.02747020
2	86.87383800			0.11884049
3	14.67477400			-0.12188661
4	9.20980570			-0.22690564
5	1.78420470			0.50246896
6	0.72224252			0.49116934
7	0.26678258			0.16060479

^a Values correspond to the sum of the squares of the deviations between the L-shell and reference radial functions evaluated at each radial point in the grid, Equation (3.20).

using eight L-shell primitive functions. An average Δ value of 3.39×10^{-3} was obtained, with all of the individual values in the range 3.05×10^{-3} to 3.76×10^{-3} .

The reference radial functions for the fifth row elements, expanded in terms of nine s and eight p primitive functions were fit very well with nine L-shell primitive functions. The least-squares fits exhibited an average Δ value of 2.30×10^{-3} , with all of the individual values between 1.88×10^{-3} and 2.69×10^{-3} .

3.3.2 Atomic Calculations

The ns and np valence atomic orbital energies computed using the MCP L-shell basis sets, in a variety of contraction schemes likely to be used in molecular calculations, were compared to those orbital energies computed using the uncontracted conventional MCP basis sets. The deviations between the ns and np orbital energies ($\Delta\epsilon_s$ and $\Delta\epsilon_p$) computed using the two families of basis sets are plotted against atomic number in Figures 3.1 and 3.2 for the SP potential and Figures 3.3 and 3.4 for the DSP potential. The plots show a very good agreement between the L-shell and conventional orbital energy values with differences typically smaller than 25 mE_h ; the majority of which agree within 10 mE_h . The ϵ_s values predicted by the totally contracted SP_L-n basis sets for the late members of the third and fourth row, as well as those computed using the DSP_L basis sets for the late members of the fourth and fifth row elements are exceptions and have deviations as large as $30\text{-}40 \text{ mE}_h$.

Not surprisingly, the $\Delta\epsilon_s$ and $\Delta\epsilon_p$ values are largest for the minimal, SP_L-n and DSP_L-n basis sets. A minimal basis set has the least flexibility, with only one contracted basis function to represent each of the ns and np subshells. The agreement is better for the extended SP_L and DSP_L basis sets (*nI*, *nII*, *n2I*, and *nIII*).

From the plots for the SP basis sets (Figures 3.1 and 3.2), the $\Delta\epsilon_s$ and $\Delta\epsilon_p$ are largest for the third row elements. Averaging the magnitudes of the $\Delta\epsilon_s$ and $\Delta\epsilon_p$ values over the elements of each row, for each basis set contraction employed, reveals the same finding. The average $\Delta\epsilon_s$ and $\Delta\epsilon_p$ values of $10\text{-}25 \text{ mE}_h$ and $2\text{-}10 \text{ mE}_h$, respectively, are largest for the third row elements. The first and fifth rows exhibit the best agreement with the reference orbital energy values, with average $\Delta\epsilon_s$ and $\Delta\epsilon_p$ values smaller than 3 mE_h . The agreement for the second and fourth row elements is intermediate, with average $\Delta\epsilon_s$ and $\Delta\epsilon_p$ values of $3\text{-}10 \text{ mE}_h$ and $1\text{-}3 \text{ mE}_h$, respectively. The variation amongst the different rows reflects the number of L-shell primitive functions used to fit the reference radial functions. The agreement is best for those L-shell basis sets which contain more L-shell primitive functions than in the conventional basis set, due to the increased flexibility. The

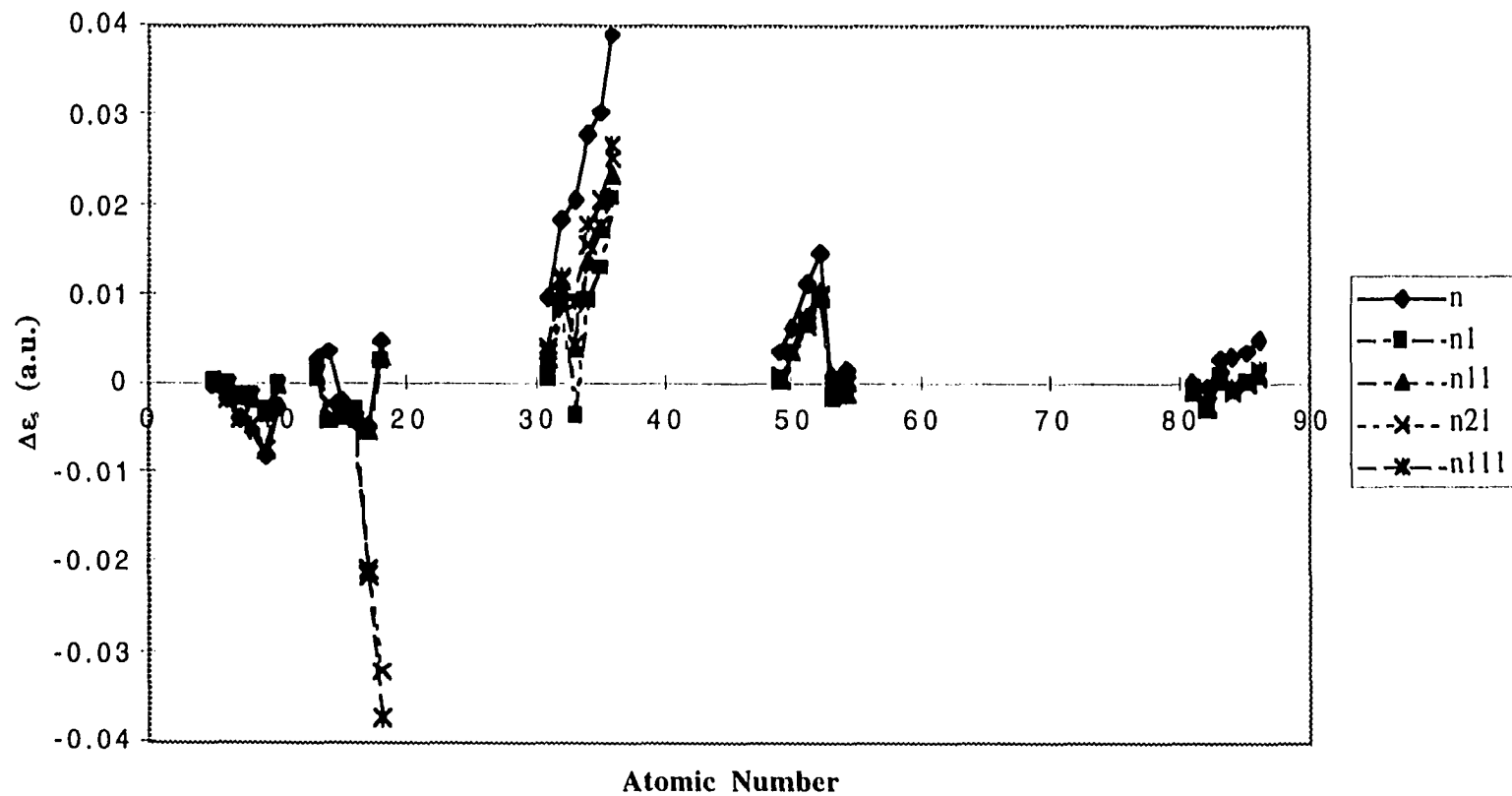


Figure 3.1: Plots of the deviations (in a.u.) between the ns atomic orbital energies computed using the MCP-SP L-shell and conventional basis sets at the ROHF level.

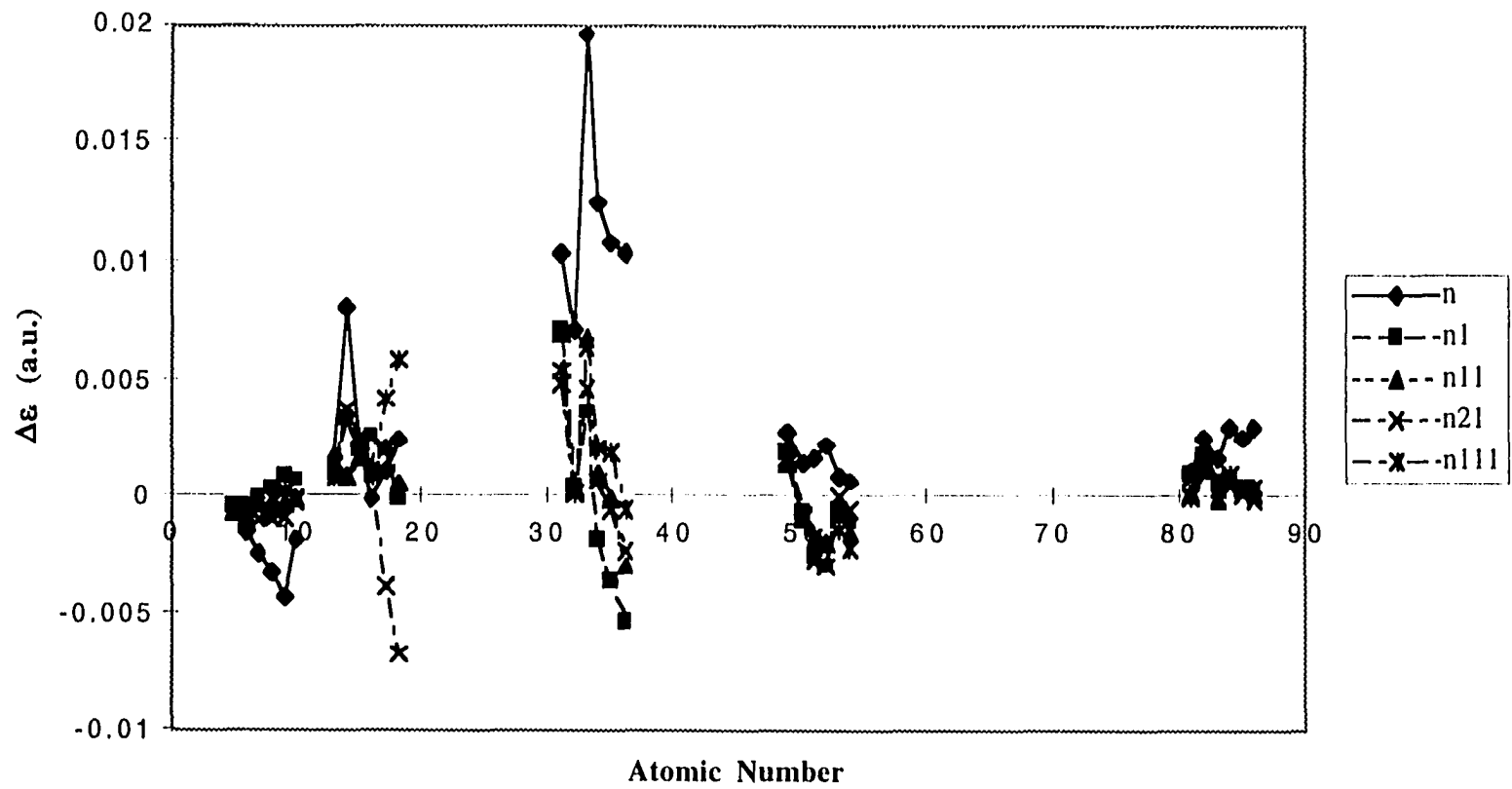


Figure 3.2: Plots of the deviations (in a.u.) between the np atomic orbital energies computed using the MCP-SP L-shell and conventional basis sets at the ROHF level.

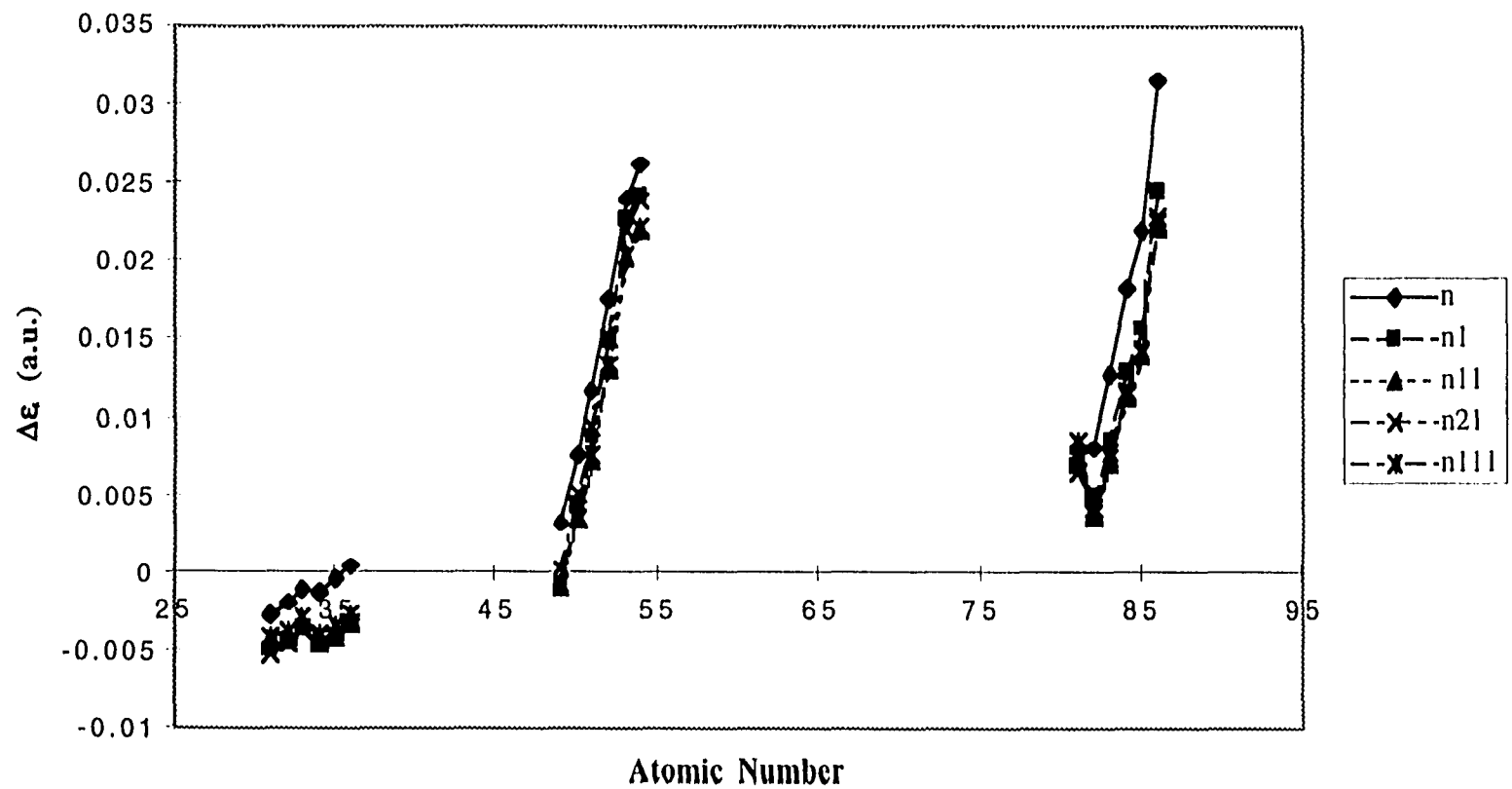


Figure 3.3: Plots of the deviations (in a.u.) between the ns atomic orbital energies computed using the MCP-DSP L-shell and conventional basis sets at the ROHF level.

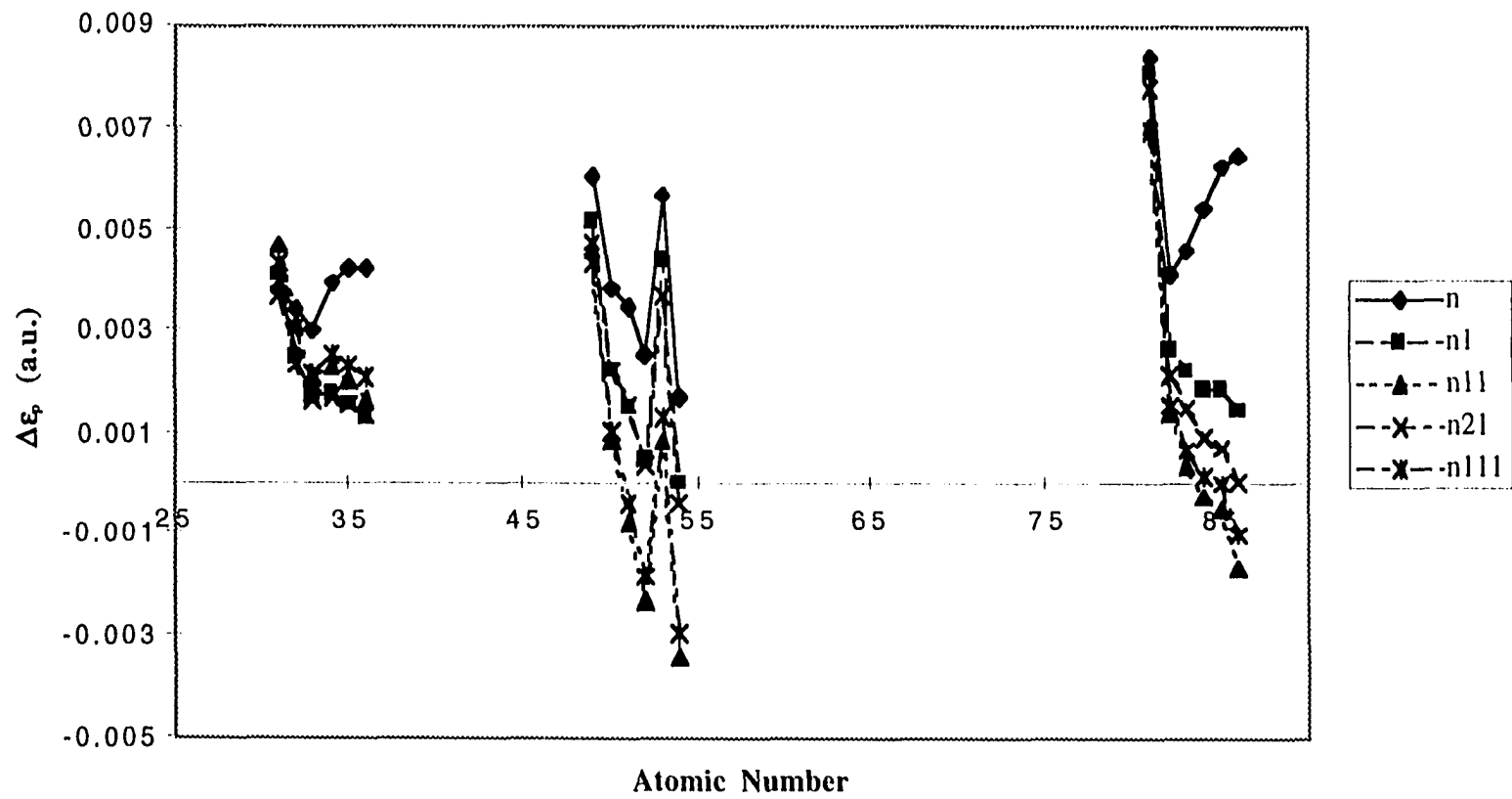


Figure 3.4: Plots of the deviations (in a.u.) between the np atomic orbital energies computed using the MCP-DSP L-shell and conventional basis sets at the ROHF level.

SP_L basis sets for the elements of the third row contain the same number of primitive gaussian functions as the conventional SP basis sets, while the SP_L basis sets for the elements of the other rows contain additional primitive gaussian functions than found in the conventional basis sets.

The orbital energies predicted by the DSP_L basis sets (Figures 3.3 and 3.4) show the best agreement to the reference orbital energies for the third row elements (average $\Delta\epsilon_s$ values of 1-4 mE_h). The agreement for the fourth and fifth row is not as good, with average $\Delta\epsilon_s$ values of 10-15 mE_h , while the agreement for the np reference orbital energies does not vary amongst the rows, with average $\Delta\epsilon_p$ values of 2-5 mE_h . The DSP_L basis sets all contain more primitive gaussian functions than found in the conventional basis sets.

The results for the DSP_L basis sets reveal a characteristic trend in the $\Delta\epsilon_s$ and $\Delta\epsilon_p$ values across a row of the periodic table. The $\Delta\epsilon_s$ values increase as one goes from left to right in the periodic table, while the $\Delta\epsilon_p$ values decrease. These trends reflect the weights given to the s and p components of the L-shell radial function (w_s and w_p , Equations (3.21) and (3.22)) during the least-squares fitting procedure, which is based on the number of valence ns and np electrons. As one goes across the row, the number of p electrons increases, and consequently more weight is given to the p component in the least-square fit. The exponents of the L-shell primitive functions for the elements to the right of the row will more closely resemble those of the conventional p primitive functions. Hence, the elements to the right of the row should be more capable of reproducing the reference ϵ_p values, at the expense of the ϵ_s values. The trend is much less apparent for the SP_L basis set results, but is visible for the third row elements, for which the deviations are largest.

In summary, the newly developed MCP-SP and MCP-DSP L-shell valence basis sets performed very well in atomic calculations for the main group elements, reproducing the ns and np atomic orbital energies to within 25 mE_h of the values predicted by the conventional MCP valence basis sets. The agreement is improved when the L-shell basis sets are expanded beyond single-zeta quality, predicting orbital energies within 10 mE_h of the values computed using the conventional basis sets.

3.3.3 Molecular Calculations

The primary focus of the molecular calculations was to gauge the accuracy and effectiveness of the new L-shell basis sets. The results of the AF_6 (A=S, Se, Te) geometry optimizations are summarized in Table 3.5 for the SP_L and DSP_L basis sets, along with those distances computed using the conventional MCP basis sets, for calculations carried out at the RHF and B3LYP levels of theory. Also given are the experimental S-F, Se-F and

Table 3.5: Summary of the Optimized A-F Distances (in Å) in AF_6 (A=S, Se, Te).

Basis	S-F		Se-F		Te-F	
	RHF	B3LYP	RHF	B3LYP	RHF	B3LYP
SP-L-n1	1.561	1.612	1.688	1.740	1.873	1.929
SP_L-n11	1.560	1.610	1.681	1.735	1.869	1.924
SP_L-n21	1.561	1.612	1.685	1.735	1.872	1.929
SP-n1	1.564	1.616	1.691	1.745	1.891	1.950
SP-n11	1.563	1.613	1.684	1.741	1.870	1.928
SP-n21	1.564	1.616	1.685	1.740	1.882	1.944
DSP_L-n1			1.696		1.859	
DSP_L-n11			1.694		1.855	
DSP_L-n21			1.694		1.858	
DSP-n1			1.703		1.871	
DSP-n11			1.694		1.852	
DSP-n21			1.700		1.862	
Expt.	1.561 ^a		1.685 ^a		1.824 ^b	

^a Experimental values taken from the Landolt-Bornstein collection.³⁶ ^b Experimental value taken from the work of Gimarc and co-workers.³⁷

Te-F bond lengths, even though good agreement cannot be expected if no polarization functions are added to the fluorine atom basis sets.

The A-F distances predicted by the SP_L and DSP_L basis sets agree very well with those predicted by the conventional SP and DSP basis sets. The distances predicted by the SP_L basis sets differ by less than 0.005 Å for SF₆ and SeF₆, for all of the basis set contractions employed and at all levels of theory (RHF, B3LYP). The maximum deviation between the SP_L and SP predicted Te-F distances is larger (about 0.02 Å). The agreement between the A-F distances computed using the DSP_L and DSP basis sets is also quite good, with deviations smaller than 0.007 Å and 0.012 Å for the Se-F and Te-F bonds, respectively. In all cases the A-F bond lengths predicted by the L-shell basis sets are slightly shorter than those predicted by the conventional basis sets.

The agreement between the calculated and experimental distances is poor, especially at the correlated level, with computed bond lengths longer than the experimental ones. The good agreement at the RHF level is fortuitous. Improved results require polarization functions on all atoms. In order to observe the effect of a single d-type polarization function on the fluorine atom, the structure of SeF₆ was optimized using the following expanded SP_L and SP basis set contractions: (L41/1*; L311/1*), (L311/1*; L311/1*), (L221/1*; L311/1*) and (41/41/1*; 211/211/1*), (311/311/1*; 211/211/1*), (221/221/1*; 211/211/1*), respectively. The d polarization function added to the fluorine atom basis set was taken from the compilation of Huzinaga.³¹ These expanded basis sets resulted in a reduction of the Se-F bond by 0.02 Å, for both the L-shell and conventional basis sets, at the RHF level. At the B3LYP level the Se-F distance was reduced by about 0.015 Å. It is worth noting that the MCP L-shell and conventional basis sets behaved in the same manner when changes were made to the basis set contraction scheme and polarization space.

The harmonic vibrational frequencies for the AF₆ systems were computed with the L-shell and conventional MCP-SP valence basis sets and are compiled in Table 3.6. The harmonic vibrational frequencies for SeF₆ and TeF₆, computed at the RHF level using the L-shell and conventional MCP-DSP basis sets are given in Table 3.7. Again, the focus is on comparison of the frequencies computed using the L-shell and conventional basis sets.

As seen in Table 3.6 and 3.7, the SP_L and DSP_L basis sets successfully reproduce the conventional SP and DSP frequencies to within 25 cm⁻¹ (with a few exceptions), depending on the molecule and the basis set expansion employed. In general, the frequencies computed with the L-shell basis sets are larger than those computed with the conventional basis sets.

Table 3.6: Summary of the AF_6 Harmonic Vibrational Frequencies (in cm^{-1}) Computed with the MCP-SP Basis Sets.^a

Basis	T_{2u} (v₆)	T_{2g} (v₅)	T_{1u} (v₄)	E_g (v₂)	A_{1g} (v₁)	T_{1u} (v₃)
SF6						
RHF						
SP_L-n1	370	548	643	732	839	1078
SP_L-n11	370	549	644	730	840	1075
SP_L-n21	370	548	644	732	840	1078
SP-n1	366	542	637	728	832	1077
SP-n11	367	544	639	727	833	1074
SP-n21	366	542	637	728	832	1077
B3LYP						
SP_L-n1	316	472	554	623	703	922
SP_L-n11	319	473	555	623	706	924
SP_L-n21	317	472	555	622	704	922
SP-n1	312	465	547	617	697	919
SP-n11	314	468	550	619	700	922
SP-n21	312	465	548	617	697	919
SeF6						
RHF						
SP_L-n1	292	413	459	713	756	867
SP_L-n11	292	420	468	712	759	857
SP_L-n21	294	415	462	718	762	871
SP-n1	284	406	452	704	743	849
SP-n11	287	414	459	707	752	849
SP-n21	286	413	458	711	753	854

B3LYP						
SP_L-n1	246	355	396	614	640	737
SP_L-n11	246	359	402	616	642	733
SP_L-n21	248	358	400	621	648	744
SP-n1	237	345	387	601	625	716
SP-n11	238	350	391	605	629	718
SP-n21	239	350	392	607	631	721
TeF6						
RHF						
SP_L-n1	181	284	306	653	659	730
SP_L-n11	184	287	311	658	659	733
SP_L-n21	182	284	308	653	659	732
SP-n1	163	268	285	631	657	722
SP-n11	191	290	316	660	665	735
SP-n21	173	276	295	643	657	726
B3LYP						
SP_L-n1	150	242	262	558	574	621
SP_L-n11	154	246	266	564	575	626
SP_L-n21	152	243	264	558	573	622
SP-n1	132	225	240	540	573	619
SP-n11	156	245	266	561	569	616
SP-n21	138	229	246	551	570	619

^a The numbering scheme of Nakamoto³⁸ is given in brackets.

Table 3.7: Summary of the SeF₆ and TeF₆ Harmonic Vibrational Frequencies (in cm⁻¹) Computed Using the MCP-DSP Basis Sets at the RHF Level of Theory.^a

System	MCP Basis Set	T _{2u} (ν ₆)	T _{2g} (ν ₅)	T _{1u} (ν ₄)	E _g (ν ₂)	A _{1g} (ν ₁)	T _{1u} (ν ₃)
SeF ₆	DSP_L-n1	275	405	446	705	745	836
	DSP_L-n11	276	406	447	705	746	834
	DSP_L-n21	276	406	447	706	748	835
	DSP-n1	257	394	423	694	720	824
	DSP-n11	272	403	441	694	732	825
	DSP-n21	262	397	429	700	727	823
TeF ₆	DSP_L-n1	177	294	307	673	688	752
	DSP_L-n11	183	296	311	678	692	750
	DSP_L-n21	180	294	309	677	691	753
	DSP-n1	157	281	289	659	663	748
	DSP-n11	189	298	315	669	683	740
	DSP-n21	175	289	302	674	677	741

^a The numbering scheme of Nakamoto³⁸ is given in brackets.

The inclusion of electron correlation via the density functional theory formalism causes a consistent reduction in the RHF values of the MCP-SP harmonic frequencies by as little as 30 cm^{-1} and as much as 150 cm^{-1} , depending on the vibrational mode.

These results show that the shape of the conventional MCP potential energy hypersurfaces are well reproduced using the new L-shell basis sets.

3.3.4 Timings

Despite the constraint of shared s and p exponents in the primitive gaussian functions, the newly developed MCP L-shell valence basis sets experience no significant loss in accuracy in computing atomic orbital energies, as well as molecular geometries and harmonic vibrational frequencies, when compared to the conventional MCP basis sets. The impetus behind the incorporation of L-shell structure into the MCP basis sets was to take advantage of the existing algorithms which improve the computational efficiency of two-electron integral evaluation. In this section we compare the timings of the conventional and L-shell MCP-SP basis sets in some routine molecular calculations on the SeF_6 molecule. The following MCP-SP L-shell and conventional basis sets were employed: (L41/1*; L211/1*), (L311/1*; L211/1*), (L221/1*; L211/1*) and (41/41/1*; 211/211/1*), (311/311/1*; 211/211/1*), (221/221/1*; 211/211/1*) in computing single point energies, optimizing structures (gradient calculations), and computing harmonic vibrational frequencies (hessian calculations). The fluorine atom SP_L basis set used contained only four primitive functions, in order to constrain it to the same number of primitives found in the conventional basis set.

The timing results for SeF_6 are displayed in Table 3.8 for calculations carried out at both the RHF and B3LYP levels of theory. At both levels of theory, the L-shell MCP basis sets show a substantial reduction in the time to perform gradient and hessian calculations compared to the time required by the conventional MCP basis sets. The gradient calculations for the SP_L basis sets are about 25 % faster than those employing the conventional SP basis sets, at the RHF level and about 20 % faster at the B3LYP level. The speed of hessian calculations performed with the L-shell basis sets is increased by about of 40 % at the RHF level, and about 10% at the B3LYP level. The results also indicate a speed-up of about 15 % for the SCF procedure at the RHF level, when the L-shell basis sets are used. At the B3LYP level there is no apparent speed-up observed for the SCF procedure. The smaller times required for SCF make these times more prone to errors and therefore not as reliable as the gradient and hessian timings. In computational studies

Table 3.8: Summary of MCP-SP SCF, Geometry Optimization and Hessian Timings for SeF₆.^a

Basis	Property	RHF		Δ (%) ^b	B3LYP		Δ (%) ^b
		SP_L	SP		SP_L	SP	
n1	SCF	5	6	+17	61	56	-9
	Gradient	207	276	+25	337	410	+18
	Hessian	162	280	+42	1203	1351	+11
n11	SCF	6	7	+14	61	59	-3
	Gradient	229	290	+21	357	443	+20
	Hessian	171	291	+41	1248	1423	+12
n21	SCF	6	7	+14	58	58	0
	Gradient	222	303	+27	350	460	+24
	Hessian	166	304	+45	1257	1362	+8
Avg ^c	SCF			+15			-4
	Gradient			+24			+21
	Hessian			+43			+10

^a In units of seconds. ^b Δ (%) = $\frac{Time(SP) - Time(SP_L)}{Time(SP)} \times 100\%$. ^c Avg denotes the average values.

probing chemical reactions and processes, much of the computational cost is associated with locating the local stationary points on the potential energy hypersurface, much more demanding than computing the total energy of a molecule at a fixed geometry. Hence, the increased computational efficiency of gradient and hessian evaluation is important.

3.4 Conclusions

The results presented in this chapter have shown that the L-shell MCP valence basis sets were successfully derived via simultaneously fitting the s and p exponents of the original MCP valence basis sets with a common set of exponents. L-shell valence basis sets were generated for both the MCP-SP and MCP-DSP potentials of the main group elements. Generally, it was necessary to use extra primitive functions in the L-shell basis sets to satisfactorily mimic the reference s and p radial functions.

Atomic ROHF calculations for the main group elements in their ground electronic states show that the MCP L-shell basis sets were able to successfully reproduce the ns and np atomic orbital energies computed using the conventional MCP basis sets to within $25 mE_h$. Not surprisingly, the agreement improves as the MCP L-shell basis sets are expanded from a minimal contraction to double and triple-zeta contractions.

Geometry optimizations of the octahedral AF_6 systems ($A = S, Se$ or Te) revealed that the L-shell MCP basis sets predict A-F bond lengths very close to the values obtained using the conventional MCP basis sets. The A-F distances computed, at the RHF and B3LYP levels, using the L-shell and conventional MCP-SP basis sets deviate from one another by less than 0.005 \AA for the S-F and Se-F bonds, and by less than 0.02 \AA for the Te-F bond. The agreement between the A-F distances predicted by the conventional and L-shell MCP-DSP basis sets is also quite good, with Se-F and Te-F bond length deviations smaller than 0.007 \AA and 0.012 \AA , respectively.

The MCP-SP and MCP-DSP L-shell basis sets predicted very similar potential energy hypersurfaces near the minima as that found using the conventional basis sets: the harmonic vibrational frequencies agree to within 25 cm^{-1} . In general, the frequencies computed with the L-shell basis sets are larger than those computed using the conventional MCP basis sets, indicating stiffer potential energy hypersurfaces.

Finally, the MCP L-shell basis sets were shown to be computationally more efficient than the conventional MCP valence basis sets, especially in the calculation of gradients and Hessians. The L-shell basis sets displayed speed-ups of about 20 % in computing the gradient of the energy at both the RHF and B3LYP levels of theory, and

10-40 % in computing the second derivatives of the energy, depending on the level of theory employed. The improvements in computing gradients and Hessians with the newly derived L-shell MCP basis sets are very important since these calculations are more difficult, usually demanding about an order of magnitude more CPU time than the SCF process. Much of the computational cost in routine studies of chemical reactions and processes is associated with optimizing chemical structures and then characterizing the various local minima and maxima located on the potential energy hypersurface.

3.5 References

1. Pople, J. A.; Hehre, W. J. *J. Comput. Chem.* **1978**, *27*, 161.
2. Huzinaga, S. *J. Chem. Phys.* **1965**, *42*, 1293.
3. Hehre, W. J.; Radom, L.; von Rague Schleyer, P.; Pople, J. A. *Ab Initio Molecular Orbital Theory*; John Wiley & Sons: New York, 1986.
4. Szabo, A.; Ostlund, N. S. *Modern Quantum Chemistry. Introduction to Advanced Electronic Structure Theory*; Dover Publications, Inc.: Mineola, New York, 1989.
5. Sakai, Y. *J. Chem. Phys.* **1981**, *75*, 1303.
6. Sakai, Y.; Huzinaga, S. *J. Chem. Phys.* **1982**, *76*, 2537.
7. Sakai, Y.; Miyoshi, E.; Klobukowski, M.; Huzinaga, S. *J. Chem. Phys.* **1997**, *106*, 8084.
8. Hehre, W. J.; Stewart, R. F.; Pople, J. A. *J. Chem. Phys.* **1969**, *51*, 2657.
9. Hehre, W. J.; Ditchfield, R.; Stewart, R. F.; Pople, J. A. *J. Chem. Phys.* **1970**, *52*, 2769.
10. Pietro, W. J.; Levi, B. A.; Hehre, W. J.; Stewart, R. F. *Inorg. Chem.* **1980**, *19*, 2225.
11. Pietro, W. J.; Hout, R. F. J.; Blurock, E. S.; Hehre, W. J.; DeFrees, D. J.; Stewart, R. F. *Inorg. Chem.* **1981**, *20*, 3650.
12. Pietro, W. J.; Hehre, W. J. *J. Comput. Chem.* **1983**, *4*, 241.
13. Binkley, J. S.; Pople, J. A.; Hehre, W. J. *J. Am. Chem. Soc.* **1980**, *102*, 939.
14. Gordon, M. S.; Binkley, J. S.; Pople, J. A.; Pietro, W. J.; Hehre, W. J. *J. Am. Chem. Soc.* **1982**, *104*, 2797.
15. Dobbs, K. D.; Hehre, W. J. *J. Comput. Chem.* **1986**, *7*, 359.
16. Dobbs, K. D.; Hehre, W. J. *J. Comput. Chem.* **1987**, *8*, 861.
17. Dobbs, K. D.; Hehre, W. J. *J. Comput. Chem.* **1987**, *8*, 880.
18. MacLean, A. D.; Chandler, G. S. *J. Chem. Phys.* **1980**, *72*, 5639.

19. Krishnan, R.; Binkley, J. S.; Seeger, R.; Pople, J. A. *J. Chem. Phys.* **1980**, *72*, 650.
20. Wachters, A. J. H. *J. Chem. Phys.* **1970**, *52*, 1033.
21. Hay, P. J. *J. Chem. Phys.* **1977**, *66*, 4377.
22. Raghavachari, K.; Trucks, G. W. *J. Chem. Phys.* **1989**, *91*, 1062.
23. Stevens, W. J.; Basch, H.; Krauss, M. *J. Chem. Phys.* **1984**, *81*, 6026.
24. Stevens, W. J.; Basch, H.; Krauss, M.; Jasien, P. *Can. J. Chem.* **1992**, *70*, 612.
25. Cundari, T. R.; Stevens, W. J. *J. Chem. Phys.* **1993**, *98*, 5555.
26. Schmidt, M. W.; Baldridge, K. K.; Boaltz, J. A.; Jensen, J. H.; Koseki, S.; Gordon, M. S.; Nguyen, K. A.; Windus, T. L.; Elbert, S. T. *QCPE Bull.* **1990**, *10*, 52.
27. Schmidt, M. W.; Baldridge, K. K.; Boaltz, J. A.; Elbert, S. T.; Gordon, M. S.; Jensen, J. H.; Koseki, S.; Matsunaga, N.; Nguyen, K. A.; Su, S.; Windus, T. L.; Dupuis, M. *J. Comput. Chem.* **1993**, *14*, 1347.
28. Dupuis, M.; Marquez, A.; Davidson, E. R. *HONDO*; 95.6 ed.; IBM Corporation: Kingston, NY, 1996.
29. Amos, R. D.; Alberts, I. L.; Andrews, J. S.; Colwell, S. M.; Handy, N. C.; Jayatilaka, D.; Knowles, P. J.; Kobayashi, R.; Laidig, K. E.; Laming, G.; Lee, A. M.; Maslen, P. E.; Murray, C. W.; Rice, J. E.; Simandiras, E. D.; Stone, A. J.; Su, M.-D.; Tozer, D. J. *CADPAC: The Cambridge Analytical Derivatives Package*; Sixth ed.; Cambridge, U. K., 1995.
30. Frisch, M. J.; Trucks, G. W.; Schlegel, H. B.; Gill, P. M. W.; Johnson, B. G.; Robb, M. A.; Cheeseman, J. R.; Keith, T.; Petersson, G. A.; Montgomery, J. A.; Raghavachari, K.; Al-Laham, M. A.; Zakrzewski, V. G.; Ortiz, J. V.; Foresman, J. B.; Cioslowski, J.; Stefanov, B. B.; Nanayakkara, A.; Challacombe, M.; Peng, C. Y.; Ayala, P. Y.; Chen, W.; Wong, M. W.; Andres, J. L.; Replogle, E. S.; Gomperts, R.; Martin, R. L.; Fox, D. J.; Binkley, J. S.; DeFrees, D. J.; Baker, J.; Stewart, J. P.; Head-Gordon, M.; Gonzalez, C.; Pople, J. A. *GAUSSIAN 94*; Gaussian Inc.: Pittsburgh, PA, 1995.
31. Huzinaga, S.; Andzelm, J.; Klobukowski, M.; Radzio-Andzelm, E.; Sakai, Y.; Tatewaki, H. *Gaussian Basis Sets for Molecular Calculations*; Elsevier: Amsterdam, 1984.
32. Press, W. H.; Teukolsky, S. A.; Vetterling, W. T.; Flannery, B. P. *Numerical Recipes in Fortran: The Art of Scientific Computing*; Second ed.; Cambridge University Press.: Cambridge, 1992.
33. Huzinaga, S.; Klobukowski, M.; Sakai, Y. *An Atomic Gaussian-Type Orbital Roothaan-Hartree-Fock Program*; Computer Phys. Commun., 1983.
34. Becke, A. D. *J. Chem. Phys.* **1993**, *98*, 5648.
35. Lee, C.; Yang, W.; Parr, R. G. *Phys. Rev. B* **1988**, *37*, 785.

36. Kuchitsu, K. E. *Landolt-Bornstein Numerical Data and Functional Relationships in Science and Technology*; Springer: Berlin, 1992; Vol. 22. Structure Data of Free Polyatomic Molecules.
37. Gimarc, B. M.; Liebman, J. F.; Kohn, M. *J. Am. Chem. Soc.* **1978**, *100*, 2334.
38. Nakamoto, K. *Infrared and Raman Spectra of Inorganic and Coordination Compounds*; Third ed.; Wiley Interscience: New York, 1978.

Chapter 4

An Investigation into the Carbonyl Fluxionality of $\text{Mn}_2(\text{CO})_{10}$ and $\text{Mn}_2(\text{CO})_6(\text{H}_2\text{PCH}_2\text{PH}_2)_2$.[‡]

[‡] Reproduced in part with permission from Decker, S. A.; Donini, O.; Klobukowski, M. *Journal of Physical Chemistry A* **1997**, *101*, 8734, Copyright 1997 American Chemical Society and Decker, S. A.; Klobukowski, M. *Canadian Journal of Chemistry* **1999**, *77*, 65, Copyright 1999 National Research Council of Canada.

4.1 Introduction

Ever since its discovery in the mid 1950's by Wilkinson and Piper¹, ligand fluxionality in transition metal complexes has been a source of interest for the inorganic chemist. Ligand migration is quite universal and has been observed in a variety of transition metal compounds of varying nuclearity from mononuclear complexes to multicentre metal clusters.^{2,3}

The conventional experimental means of studying the dynamic fluxionality of ligands is NMR spectroscopy. This detection scheme does however place some limitations on the process to be studied. If the exchange process is to be detected by NMR, its rate must fall within the range 10^{-1} to 10^6 s⁻¹. Furthermore, the solvents employed restrict the range of temperatures at which the process can be followed, thereby imposing limitations on the activation energy. Generally, these dynamic processes must have an activation energy which falls within 3-25 kcal/mol in order for the process to be studied by NMR.²

Migration of the carbonyl group is the most common ligand exchange process studied and it has been observed in a large number of transition metal compounds. Dimer complexes are perhaps the best model systems to study, both experimentally and theoretically, in order to elucidate the mechanistic details of the ligand exchange process. Two mechanistic schemes are widely employed to describe carbonyl scrambling in binuclear complexes: pairwise exchange and one-for-one exchange. In the pairwise exchange mechanism, proposed by Adams and Cotton⁴ in the early 1970's, two migrating carbonyl ligands are mutually exchanged between the two metal atoms. Symmetrical ligand bridges are opened and closed pairwise in a trans, co-planar, concerted fashion. This is the most common mechanism proposed for carbonyl migration, and may proceed from an initial all-terminal or symmetrically-bridging ground state. In the one-for-one mechanism, proposed by Evans *et al.*^{5,6} for carbonyl exchange in trans-(η^5 -C₅H₅)₂Rh₂(CO)₃ and (η^5 -C₅H₅)₂Rh₂(CO)₂P(OC₆H₅)₃, the migrating ligands are not co-planar and are exchanged unsymmetrically in a step-wise fashion.

The fluxional behaviour of the carbonyl ligands in the two Mn dimers, Mn₂(CO)₁₀ and Mn₂(CO)₆(dppm)₂, where dppm denotes bis-(diphenylphosphino)-methane is particularly interesting. ¹³C and ¹⁷O NMR studies have shown^{7,8} that the carbonyl ligands in Mn₂(CO)₁₀ remain fixed up to the temperature of 130°C. Replacing four of the carbonyls with two bidentate dppm ligands induces fluxionality of the carbonyl ligands, as observed by ¹³C and ³¹P NMR at temperatures as low as -75°C.⁹ Marsella and Caulton⁹ have proposed that carbonyl scrambling in Mn₂(CO)₆(dppm)₂ proceeds via the pairwise exchange (merry-go-round) mechanism from the most stable all-terminal conformer

through a symmetrically di-bridged transition state or intermediate with an energy barrier of 10.2 kcal/mol. They attributed the observed differences in fluxional behaviour between $\text{Mn}_2(\text{CO})_6(\text{dppm})_2$ and $\text{Mn}_2(\text{CO})_{10}$ to conformational differences. In the lowest-energy conformer of $\text{Mn}_2(\text{CO})_{10}$ the equatorial carbonyls are staggered and must undergo an initial rotation about the Mn-Mn bond to give the eclipsed conformation required for the merry-go-round scrambling of the carbonyls; this rotation then contributes to the overall activation energy for the exchange process. On the other hand, the six carbonyls in $\text{Mn}_2(\text{CO})_6(\text{dppm})_2$ are believed to be already co-planar in the most stable conformation, and may proceed directly to scrambling without any prerequisite rotation about the Mn-Mn bond. Although there is no experimental structure for $\text{Mn}_2(\text{CO})_6(\text{dppm})_2$, the crystal structure of $\text{Mn}_2(\text{CO})_5(\text{dppm})_2$ shows the carbonyls to be co-planar with one of them bound to the metal in a semi-bridging mode.

The $\text{Mn}_2(\text{CO})_{10}$ dimer has been the subject of several theoretical studies, however, none of them have focused on the dynamic fluxionality of the carbonyl ligands. Electron diffraction studies, both in the gas phase¹⁰ and in the crystal^{11,12} show that it has one of the longest metal-metal bonds known, about 2.9 Å, and the structure exhibits a characteristic bending of the four equatorial carbonyls towards the Mn atom to which they are not directly bound. A number of theoretical studies have focused on these unique structural features of $\text{Mn}_2(\text{CO})_{10}$.¹³⁻¹⁶ A number of theoretical papers have also appeared which probe the photochemistry of $\text{Mn}_2(\text{CO})_{10}$.¹⁷⁻²⁰ Folga and Ziegler²¹, employing non-local density functional theory (DFT), computed the energy barrier for rotation about the Mn-Mn bond, going from the staggered (D_{4d}) ground state conformation to the eclipsed (D_{4h}) conformation.

Density functional theory employing non-local, gradient-corrected functionals has become the method of choice for calculations involving small to medium-sized transition metal complexes.²² However, using the workstation hardware typically available in research groups, the computational cost of DFT ($\sim K^3$, where K is the number of basis functions) often makes it prohibitively expensive for modeling large transition metal systems. Semiempirical methods address the need for more cost-efficient computational techniques. The PM3(tm) method has recently been developed by Wavefunction Inc. and made available within the Spartan program.²³ A survey of the literature shows only a few papers which have tested the reliability of this new semiempirical method for calculations involving transition metal elements. Adam and co-workers²⁴ employed the PM3(tm) method to predict the molecular structures of some high- and low-spin nickel (II) teraza-macrocyclic complexes. Looking solely at geometric structures, they found PM3(tm) to be inferior to an MM2 force field derived specifically for macrocycles of low-spin nickel(II).

Cundari and Deng²⁵ found the PM3(tm) method to successfully reproduce the experimental geometries of nearly 100 different metal complexes, with accuracies similar to that found at the MP2 level employing ECP basis sets. Børve *et al.*²⁶ performed a comparative study of PM3(tm) vs. DFT in calculations of Ti, Cr, and Zr complexes. They found the PM3(tm) method to be quite successful in predicting geometries of stable, closed-shell complexes, in close agreement with both experiment and the DFT calculations. However, the PM3(tm) method gave poor relative energies and activation barriers for the ethylene insertion reactions studied. Single-point energy calculations, using non-local density functional theory at the PM3(tm) optimized geometries, yielded more reliable and accurate activation barriers, reasonably close to those obtained if the DFT method was used throughout.

In the present chapter, the DFT, PM3(tm), and the hybrid DFT//PM3(tm) approaches were used to study the carbonyl scrambling behaviour in $\text{Mn}_2(\text{CO})_{10}$ and $\text{Mn}_2(\text{CO})_6(\text{dhpm})_2$, as a model of the experimental $\text{Mn}_2(\text{CO})_6(\text{dppm})_2$ complex. Assuming that carbonyl scrambling proceeds via the planar, pairwise exchange (merry-go-round) mechanism, the process was simulated by obtaining optimized geometries, frequencies and energies of the conformers which play an integral role in the scheme. Calculations were also performed at the Hartree-Fock (HF) level to illustrate the importance of electron correlation in modeling transition metal containing systems.

4.2 Computational Methods

4.2.1 $\text{Mn}_2(\text{CO})_{10}$

Assuming that carbonyl migration follows the pairwise exchange mechanism calculations were carried out at the DFT, HF, and PM3(tm) levels of theory for the various conformers of $\text{Mn}_2(\text{CO})_{10}$ involved in the migration process. For the DFT calculations, the gradient-corrected exchange functional of Becke²⁷ was used in conjunction with the non-local correlation functional of Lee, Yang, and Parr²⁸. (This combination is commonly referred to as the BLYP functional.) This functional has proven to yield reliable geometries and frequencies in a number of studies of transition metal carbonyls.²⁹ Additional calculations were performed using the B3LYP functional, comprised of Becke's three-parameter hybrid exchange functional³⁰ in combination with the correlation function of Lee, Yang, and Parr²⁸. For these calculations, an all-electron basis set of triple-zeta-valence quality, with two polarization functions (both p type) was used for the Mn atom, with a (533111/531*1*/311) contraction pattern. All-electron basis sets of double-zeta plus

polarization (a single d polarization function) quality were employed for the C and O atoms, with the following contraction pattern (421/31/1*). This basis set was also used for the HF calculations. All atomic basis sets and polarization functions were taken from the compilation of Huzinaga and co-workers.³¹ Baerends *et al.*¹⁶ in a previous study of $\text{Mn}_2(\text{CO})_{10}$ found that the addition of an f polarization function to the Mn basis set had no significant effect on the results, hence f polarization functions were not used in the present work. The final molecular basis set for $\text{Mn}_2(\text{CO})_{10}$ contained a total of 346 contracted Gaussian functions. All of the DFT calculations were carried out using the Gaussian 92/DFT³² and Gaussian 94³³ programs, while HONDO³⁴ was employed for the HF calculations.

The unpublished PM3(tm) set of parameters, as contained within the Spartan program²³ were employed. The choice of the semiempirical method was governed by the availability of parameters for the Mn atom.

All geometries were fully optimized using analytical gradient techniques, and the nature of the resulting stationary point was characterized by harmonic vibrational analysis, either using analytical second derivatives or via numerical evaluation of analytical first derivatives. In order to gain insight into the carbonyl scrambling mechanism, one must know not only the structures and relative energies of the species involved but also what, in chemical terms, the species correspond to.

4.2.2 $\text{Mn}_2(\text{CO})_6(\text{dhpm})_2$

To reduce computational costs, the phenyl rings of the bidentate dppm ligand were replaced with hydrogen atoms, resulting in the bis-(dihydrophosphino)-methane ligand, denoted as dhpm. Assuming that carbonyl scrambling in both the experimental $\text{Mn}_2(\text{CO})_6(\text{dppm})_2$ and model $\text{Mn}_2(\text{CO})_6(\text{dhpm})_2$ systems proceeds via the pairwise exchange mechanism, the geometries of the conformers which play an integral role in the scheme were optimized using the PM(tm) semiempirical method. In addition, since experimental structure data is available for $\text{Mn}_2(\text{CO})_5(\text{dppm})_2$, structural parameters for $\text{Mn}_2(\text{CO})_5(\text{dhpm})_2$ were obtained at the PM3(tm) level. All of the geometries, with the exception of one of the $\text{Mn}_2(\text{CO})_6(\text{dhpm})_2$ conformers with constrained angles (see below), were fully optimized using analytical gradient techniques, and the nature of the resulting stationary point was characterized by harmonic vibrational analysis. The choice of semiempirical method was based solely on the availability of PM3(tm) parameters for Mn, and the Spartan program was used²³.

The total energies of the $\text{Mn}_2(\text{CO})_6(\text{dhpm})_2$ conformers involved in the carbonyl migration process were computed via single-point energy DFT calculations at their respective PM3-optimized geometries. A variety of density functionals were employed in this hybrid DFT//PM3(tm) method including: BLYP (Becke's non-local exchange functional²⁷ in conjunction with the non-local correlation functional of Lee, Yang and Parr²⁸), BP86 (Becke's non-local exchange functional²⁷ coupled with Perdew's non-local correlation functional³⁵), B3LYP (comprised of Becke's three-parameter hybrid gradient-corrected exchange functional³⁰ coupled with the gradient-corrected correlation functional of Lee, Yang, and Parr²⁸), and B3PW91 (Becke's three-parameter hybrid gradient-corrected exchange functional³⁰ in conjunction with the gradient-corrected correlation functional of Perdew and Wang³⁶). In the DFT calculations the ECPs of Stevens *et al.*³⁷⁻³⁹ were used for all heavy atoms, with the following contraction schemes for the valence space of the constituent atoms: (31/31/1*) for P, C and O and (4211/4211/3111) for Mn. The d polarization functions for the main group elements were taken from the compilation of Huzinaga and co-workers.³¹ The 3-21G basis set was used for the H atoms.⁴⁰ All of the DFT calculations were carried out using the Gaussian94 program.³³

4.3 Results and Discussion

4.3.1 $\text{Mn}_2(\text{CO})_{10}$

The structures of the three $\text{Mn}_2(\text{CO})_{10}$ conformers involved in the carbonyl migration process; staggered (D_{4d}), eclipsed (D_{4h}), and bridged (D_{2h}) are displayed in Figure 4.1. Values of the optimized geometrical parameters are presented in Table 4.1, along with the corresponding experimental values for the staggered conformer along with values from a number of previous theoretical studies. The following naming convention has been adopted to distinguish between the different carbonyl ligands in the three $\text{Mn}_2(\text{CO})_{10}$ conformers. In the staggered and eclipsed conformers the *axial* carbonyls are defined to be co-linear to the Mn-Mn bond, while the remaining eight carbonyls are labelled as *equatorial*. In the bridged conformer *bridged* labels the two μ_2 -CO ligands, *terminal* is used to label the four carbonyls co-planar to the two bridging carbonyls, and *perpendicular* labels the remaining four carbonyls.

The geometrical parameters of the staggered conformer predicted using the non-local DFT (BLYP) approach agree very well with those from experiment. The BLYP method predicts the Mn-Mn bond to be nearly identical to its gas-phase diffraction value,

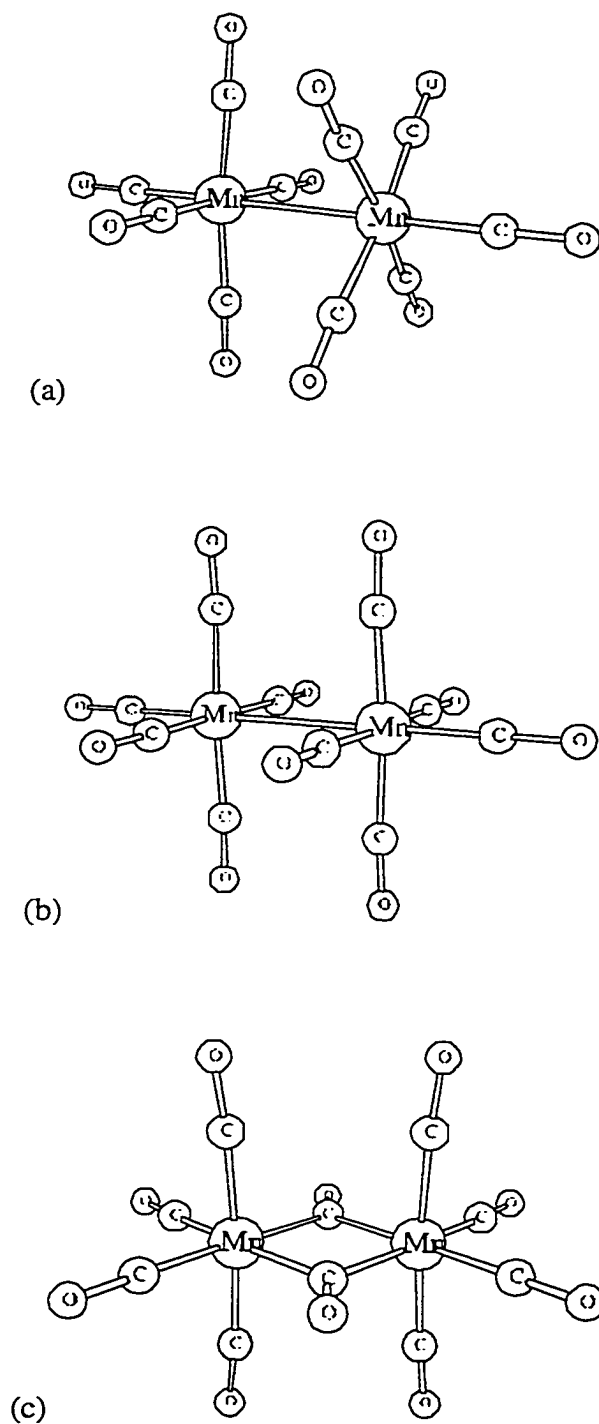


Figure 4.1: The three conformers of $\text{Mn}_2(\text{CO})_{10}$ studied: (a) staggered (D_{4d}); (b) eclipsed (D_{4h}); (c) bridged (D_{2h}).

Table 4.1: Predicted Geometrical Parameters for the Three Conformers of $\text{Mn}_2(\text{CO})_{10}$ ^a

Parameter	This Work					Expt. ^e
	BLYP	PM3(tm) ^b	HF	Ziegler ^c	Rosa ^d	
Staggered (D_{4d}) Conformer						
Mn-Mn	2.979	2.919	3.298	2.902	2.876	2.977
Mn-C _{ax}	1.827	1.788	2.006	1.813	1.747	1.803
Mn-C _{eq}	1.874	1.852	2.028	1.859	1.799	1.873
C _{ax} -O _{ax}	1.165	1.168	1.111	1.158	1.172	1.147 ^f
C _{eq} -O _{eq}	1.162	1.161	1.116	1.153	1.169	1.147 ^f
C _{eq} -Mn-Mn	86.6	86.8	84.2	85.0		86.1
O _{eq} -C _{eq} -Mn	177.2	179.8	176.1	175.9		
C _{eq} -Mn-C _{ax}	93.4	93.1	95.8	93.0		93.4
Eclipsed (D_{4h}) Conformer						
Mn-Mn	3.116	2.966	3.518	2.965		
Mn-C _{ax}	1.823	1.789	2.014	1.812		
Mn-C _{eq}	1.874	1.851	2.031	1.850		
C _{ax} -O _{ax}	1.165	1.169	1.111	1.157		
C _{eq} -O _{eq}	1.162	1.161	1.116	1.156		
C _{eq} -Mn-Mn	87.5	88.7	85.5	89.1		
O _{eq} -C _{eq} -Mn	175.3	176.2	178.5	174.4		
C _{eq} -Mn-C _{ax}	92.5	91.3	94.5	90.9		
Bridged (D_{2h}) Conformer						
Mn-Mn	2.846		3.062			
Mn-C _{perp}	1.871		2.042			
Mn-C _{term}	1.853		1.994			
Mn-C _{br}	2.109		2.214			
C _{perp} -O _{perp}	1.160		1.112			
C _{term} -O _{term}	1.160		1.112			
C _{br} -O _{br}	1.183		1.153			
C _{term} -Mn-Mn	130.3		131.3			
O _{term} -C _{term} -Mn	176.6		175.9			
C _{term} -Mn-C _{perp}	88.3		89.9			

^a Bond lengths in Å, angles in deg. ^b A limitation of the Spartan program package and unavailability of the source code prevented selection of the correct electronic configuration in the D_{2h} conformer and made the study of the bridged structure impossible. ^c DFT study²¹ using nonlocal exchange and correlation functionals (the BP86 functional). ^d DFT study^{19,20} using a local spin density functional (the SVWN functional). ^e Gas phase electron diffraction study at room temperature.¹⁰ ^f Averaged distances.

while the Mn-C and C-O distances appear to be slightly overestimated. At this level the computed bond distances deviate from experiment by an average of 0.01 Å, while the bond angles agree to within 1°. Not surprisingly, our BLYP results are superior to the local DFT results of Rosa *et al.*^{16,19} while there is little difference between the BLYP predicted values and those obtained by Folga and Ziegler²¹ using the BP86 functional. Direct comparisons of this sort are of limited value since the basis set was not kept constant in the different calculations.

The semiempirical PM3(tm) method also predicts the geometry of the staggered conformer in good agreement with experiment. The PM3(tm) parameterization leads to Mn-Mn and Mn-C distances which are too short, and overestimates the C-O distances. However, the PM3(tm) computed bond distances and bond angles deviate from their experimental values by an average of 0.03 Å and 1°, respectively.

On the other hand, comparison of the calculated and experimental geometries of the staggered conformer convincingly shows the shortcomings of the HF method. The HF method predicts Mn-Mn and Mn-C bond distances which are too long by as much as 0.3 Å. The calculated C-O distances are also slightly underestimated, although it is hard to make any strict comparison here as the gas phase diffraction data represent averaged values. The bond distances predicted by the HF method deviate from their experimental values by 0.15 Å on average, with individual deviations as large as 0.32 Å. The bond angles predicted by the HF method are more in accord with experiment, with errors of about 2° on average. Clearly, the *ab initio* HF method is unable to correctly describe the single metal-metal bond in Mn₂(CO)₁₀.

Conversion from a staggered arrangement of the carbonyls to a planar eclipsed conformation via rotation about the Mn-Mn bond, a necessary step if carbonyl scrambling in Mn₂(CO)₁₀ proceeds via the pairwise exchange mechanism, induces large changes in the bond distances and angles, as illustrated in Table 4.1. The present calculations, as well as those of Folga and Ziegler²¹, show that rotation about the Mn-Mn bond results in a large increase in the Mn-Mn distance, as expected based on simple steric or electrostatic arguments. At the BLYP level, the Mn-Mn bond is lengthened by 0.04 Å, while the PM3(tm) method predicts increase of 0.05 Å from its value in the staggered conformation. The HF method predicts an increase of 0.22 Å, leading to an incredibly long Mn-Mn bond of over 3.5 Å for the eclipsed conformer. Interestingly, regardless of the computational method used, rotation about the Mn-Mn bond has only a slight effect on the Mn-C and C-O distances, as well as the bond angles.

The next step in the merry-go-round scrambling process involves the formation of the di-bridged conformer. Conversion of the eclipsed conformer to the bridged conformer

results in a reduction of the Mn-Mn distance by 0.27 Å and 0.46 Å at the BLYP and HF levels, respectively. This decrease is not unexpected, since the presence of two μ_2 -CO ligands will bring the Mn atoms closer together. Unfortunately, optimization of the geometry of the bridged conformer at the PM3(tm) level was unsuccessful due to convergence problems. At the BLYP level, the Mn-C distance of the equatorial carbonyls in the bridged dimer were predicted to be shorter than those of the staggered and eclipsed conformers. On the other hand, the Mn-C distance of the axial carbonyls were predicted to be longer than those of the staggered and eclipsed conformers. At the BLYP level of theory, the following trend was observed amongst the various Mn-C distances for the bridged conformer: $\text{Mn-C}_{\text{br}} > \text{Mn-C}_{\text{eq}} > \text{Mn-C}_{\text{ax}}$.

The relative energies of the three $\text{Mn}_2(\text{CO})_{10}$ conformers involved in the carbonyl scrambling process are given in Table 4.2. All of the methods employed predict the staggered conformation to be the ground state for $\text{Mn}_2(\text{CO})_{10}$. Subsequent characterization of the stationary points via harmonic vibrational analysis revealed it to be a local minimum on the potential energy hypersurface, at all levels of theory. The eclipsed conformer was predicted to lie about 5 kcal/mol above the staggered conformer using the BLYP and HF methods, while the PM3(tm) method predicts the energy gap to be twice as large. Folga and Ziegler²¹, using the BP86 functional, predict a surprisingly large energy difference of 34 kcal/mol between the staggered and eclipsed conformers. The eclipsed conformer was found to be a genuine transition state at the BLYP and HF levels of theory, with imaginary harmonic frequencies of $28i \text{ cm}^{-1}$ and $33i \text{ cm}^{-1}$, respectively, while it was found to be a third-order saddle point, with imaginary frequencies of $47i \text{ cm}^{-1}$ and $30i \text{ cm}^{-1}$ (twice), at the PM3(tm) level. Examination of the normal mode associated with the single negative eigenvalue of the hessian matrix in the DFT and HF calculations, as well as the largest, most negative hessian eigenvalue in the PM3(tm) calculations, reveals that the eclipsed conformer is a transition state connecting two ground state staggered conformers. The motions of the nuclei in this vibrational mode are displayed in Figure 4.2. The bridged conformer is predicted to lie a further 14 kcal/mol above the eclipsed conformer at the BLYP level, while the HF method predicts it to lie 47 kcal/mol above the eclipsed conformation. As stated earlier, optimization of the bridged species using the PM3 method was unsuccessful. Due to the prohibitively long computational time of evaluating the hessian with the DFT method, the hessian of the bridged conformer was evaluated using only the HF method, at the respective HF geometry. At this level, the bridged species corresponds to a second-order saddle point with associated imaginary frequencies of $370i$ and $49i \text{ cm}^{-1}$. The normal mode at $370i \text{ cm}^{-1}$ corresponds to the desired carbonyl scrambling motion between two eclipsed conformers, as shown in Figure 4.3. It should be

Table 4.2: Relative Energies of the $\text{Mn}_2(\text{CO})_{10}$ Conformers.

Conformer	Method	Relative Energy ^a
Eclipsed (D_{4h})	DFT-BLYP	4.8
	HF-SCF	5.3
	PM3	10.8
Bridged (D_{2h})	DFT-BLYP	18.6
	HF-SCF	52.2

^a In kcal/mol, with respect to the staggered (D_{4d}) conformer. The reference total energies are: $E(\text{BLYP}) = -3433.75626 E_h$, $E(\text{HF}) = -3424.87128 E_h$, $\Delta H_f^\circ(\text{PM3}(\text{tm})) = -698.7$ kcal/mol.

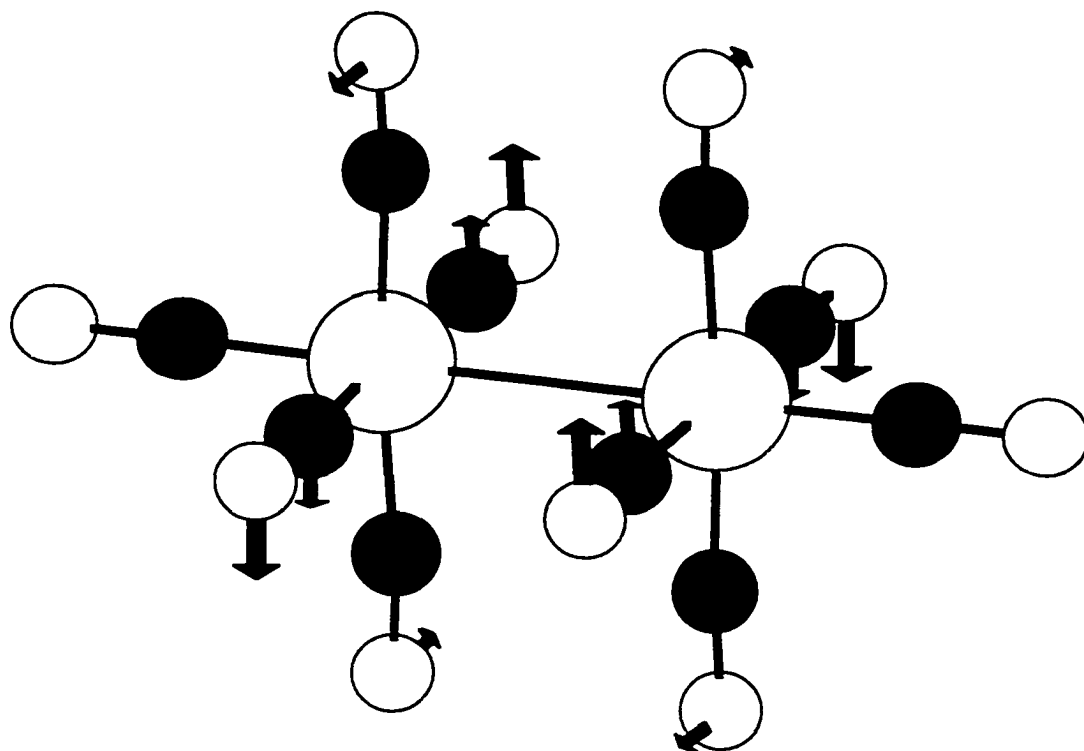


Figure 4.2: Motions of the nuclei in the harmonic mode corresponding to the single negative curvature of the HF and DFT potential energy surfaces in the eclipsed (D_{4h}) transition state.

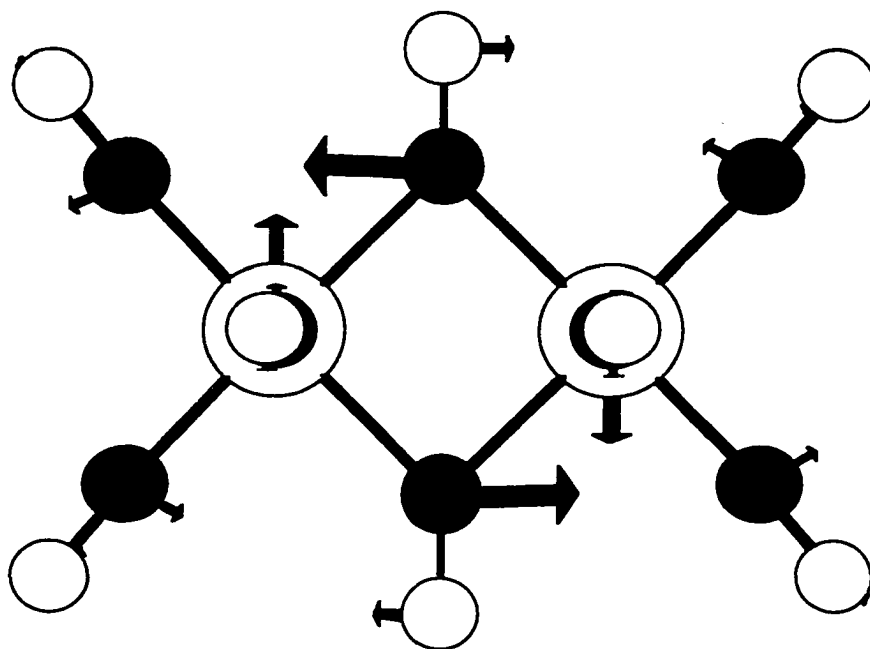


Figure 4.3: Motions of the nuclei in the harmonic vibrational mode connecting the bridged (D_{2h}) and eclipsed (D_{4h}) $Mn_2(CO)_{10}$ conformers.

added that vibrational analysis of all three conformers indicates that the potential energy hypersurfaces near the stationary points are quite flat, with a large number of modes with small frequencies. For example, in the staggered conformer, there were 38, 34, and 44 vibrational modes (over half of all modes) with frequencies smaller than 500 cm^{-1} , as predicted by our DFT, PM3(tm), and HF calculations.

In summary, DFT calculations performed using the BLYP functional predict an energy barrier of 19 kcal/mol for carbonyl migration in $\text{Mn}_2(\text{CO})_{10}$. This energy barrier is increased to 21 kcal/mol if the B3LYP functional is employed. Recall that the maximum value of ΔG_{rxn} for a process, in solution, to be detected by NMR has been estimated to be 25 kcal/mol. Our energy barrier estimates are close to this upper limit, but still lie below it. However, we have calculated only ΔE , and have not taken into account zero point energies or entropy changes, which may increase the barrier for carbonyl migration. Recall that Marsella and Caulton⁹ believed that it was the barrier to rotation about the Mn-Mn bond which prevented carbonyl migration in $\text{Mn}_2(\text{CO})_{10}$, however our DFT calculations predict this activation barrier to be quite small, at only 5 to 6 kcal/mol, indicating that this rotation should be rapid.

4.3.2 $\text{Mn}_2(\text{CO})_6(\text{dhpm})_2$

The geometrical parameters of five different conformers of $\text{Mn}_2(\text{CO})_6(\text{dhpm})_2$, as well as the lowest energy conformer of $\text{Mn}_2(\text{CO})_5(\text{dhpm})_2$, calculated at the PM3(tm) level, are listed in Table 4.3. Also given in the Table are values from the experimental crystal structure of the related $\text{Mn}_2(\text{CO})_5(\text{dppm})_2$ complex.⁴¹ Conformers A and B, Figure 4.4 (a) and (b), differing only in the orientation of the two methylene units, have a planar arrangement of the six CO ligands with two of them symmetrically bridging the Mn atoms. In conformers C and D, Figure 4.4 (c) and (d), all of the CO ligands are in the terminal position but they adopt a pseudo-staggered arrangement, similar to the staggered (D_{4d}) conformer of $\text{Mn}_2(\text{CO})_{10}$. In conformer E, Figure 4.4 (e), all of the CO ligands adopt a planar arrangement and occupy terminal positions, as in the eclipsed (D_{4h}) conformer of $\text{Mn}_2(\text{CO})_{10}$. The following naming convention for the carbonyl ligands is used: in the all-terminal conformers (C, D, and E) the *axial* carbonyls are co-linear to the Mn-Mn bond, while the remaining carbonyls are labelled *equatorial*, in the planar, di-bridged conformers (A and B) *bridged* is used to label the two μ_2 -CO ligands while *terminal* labels the remaining four carbonyls. For the $\text{Mn}_2(\text{CO})_5(\text{dhpm})_2$ complex (conformer F, Figure 4.4 (f)) *bridged* labels the lone μ_2 -CO, *axial* labels the two CO ligands co-linear to the

Table 4.3 Structural Parameters of the $\text{Mn}_2(\text{CO})_n(\text{dhpm})_2$ Conformers ($n = 6, 5$).^a

Parameter	n=6 ^b					n=5 ^c		Expt ^d	
	A		B	C	D	E	F		
	PM3 ^e	DFT ^f	PM3	PM3	PM3	PM3	DFT	PM3	
Mn-Mn	2.988	2.878	2.986	3.101	3.101	3.077	3.288	3.328	2.934
Mn-C _{ax}				1.722	1.722	1.731	1.802	1.729	1.73
Mn-C _{eq}	1.743	1.825	1.742	1.818	1.817	1.821	1.852	1.728	1.67
Mn-C _{br}	2.112	2.096	2.112					2.042	1.93
Mn-P	2.245	2.322	2.245	2.221	2.221	2.219	2.298	2.212	2.272
C _{ax} -O _{ax}				1.194	1.193	1.192	1.191	1.194	1.20
C _{eq} -O _{eq}	1.189	1.188	1.187	1.179	1.802	1.178	1.189	1.192	1.18
C _{br} -O _{br}	1.198	1.211	1.195					1.232	1.10
P-CH ₂	1.860	1.898	1.859	1.866	1.866	1.855	1.899	1.867	1.83
Mn-Mn-C _{eq}	133.5	132.4	133.4	86.4	86.4	90.0 ^g	85.8	96.4	94
O _{eq} -C _{eq} -Mn	178.1	179.3	178.1	175.8	175.8	174.8	174.4	170.9	176
O _{ax} -C _{ax} -Mn				180.0	180.0	179.7	179.9	168.9	173
O _{br} -C _{br} -Mn	135.0	136.6	135.0					125.5	173
P-CH ₂ -P	113.4	106.3	113.5	115.5	115.5	112.4	108.1	117.9	113.2
Mn-P-P-Mn	0.1	0.1	0.0	18.9	18.4	0.0 ^g	0.1	0.1	
C _{eq} -Mn-Mn-C _{eq}	0.1	0.1	0.0	19.6	19.2	0.0 ^g	0.2	0.1	

^a Bond lengths in Å, bond angles in degrees. ^b The $\text{Mn}_2(\text{CO})_6(\text{dhpm})_2$ conformers are: A. cis- $\text{Mn}_2(\text{CO})_4(\mu_2\text{-CO})_2(\text{dhpm})_2$ (see Figure 4.4 (a)), B. trans- $\text{Mn}_2(\text{CO})_4(\mu_2\text{-CO})_2(\text{dhpm})_2$, (see Figure 4.4 (b)), C. cis- $\text{Mn}_2(\text{CO})_6(\text{dhpm})_2$ (see Figure 4.4 (c)), D. trans- $\text{Mn}_2(\text{CO})_6(\text{dhpm})_2$ (see Figure 4.4 (d)), E. cis- $\text{Mn}_2(\text{CO})_6(\text{dhpm})_2$ (planar, all-terminal, see Figure 4.4 (e)). ^c The lowest energy conformer of $\text{Mn}_2(\text{CO})_5(\text{dhpm})_2$ (conformer F), Figure 4.5. ^d Values taken from the experimental crystal structure of the related complex $\text{Mn}_2(\text{CO})_5(\text{dppm})_2$.⁴¹ ^e Values correspond to those obtained from optimization using the PM3(tm) semiempirical method. ^f Values correspond to those obtained from optimization at the DFT level of theory using the BLYP density functional. ^g Parameter fixed during optimization.

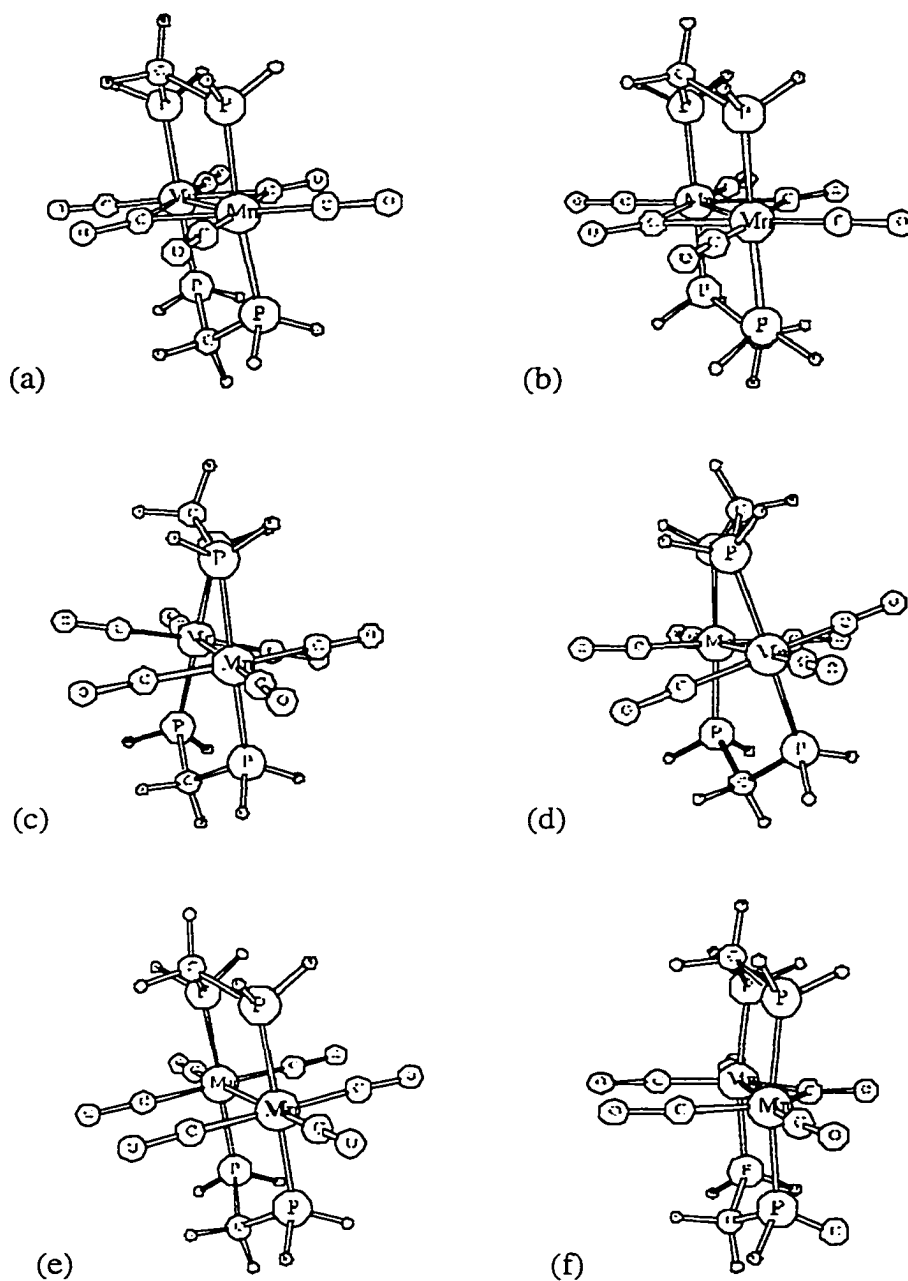


Figure 4.4: The conformers of $\text{Mn}_2(\text{CO})_6(\text{dhpm})_2$ and $\text{Mn}_2(\text{CO})_5(\text{dhpm})_2$ studied: (a) $\text{cis-Mn}_2(\text{CO})_4(\mu_2\text{-CO})_2(\text{dhpm})_2$ (Conformer A), (b) $\text{trans-Mn}_2(\text{CO})_4(\mu_2\text{-CO})_2(\text{dhpm})_2$ (Conformer B), (c) $\text{cis-Mn}_2(\text{CO})_6(\text{dhpm})_2$ (Conformer C), (d) $\text{trans-Mn}_2(\text{CO})_6(\text{dhpm})_2$ (Conformer D), (e) planar, all-terminal $\text{Mn}_2(\text{CO})_6(\text{dhpm})_2$ (Conformer E), (f) $\text{cis-Mn}_2(\text{CO})_4(\mu_2\text{-CO})(\text{dhpm})_2$ (Conformer F).

Mn-Mn bond, and *equatorial* is used to represent the two remaining carbonyls.

Interestingly, whenever a geometry optimization was commenced from a structure in which the six carbonyls were co-planar, the carbonyls in the final optimized structure remain planar with two of them becoming symmetrically bridging (conformers A and B). This planarity was maintained even though no symmetry constraints were placed on the system (i.e. the C_1 point group was used). When an optimization was initiated from a structure in which the six carbonyls were pseudo-staggered, the final optimized structure was also pseudo-staggered with all of the carbonyls in the terminal positions (conformers C and D). The co-planar, all-terminal species (conformer E) could only be optimized by constraining certain angles. This behaviour is indicative of a very complicated potential energy hypersurface with a large number of local minima.

As illustrated in Table 4.3, the PM3(tm) method predicts structural parameters which agree reasonably well with the corresponding parameters of $Mn_2(CO)_5(dppm)_2$ given the steric differences between the model and experimental bidentate phosphine ligands. The PM3(tm) predicted Mn-Mn distance for the planar, all-terminal conformer (E) is 0.14 Å longer than that found in the experimental structure, reflecting the presence of the semi-bridging CO ligand which will bring the Mn atoms closer together. As expected, the Mn-Mn distance predicted by the PM3(tm) method for the symmetrically bridging conformers is much closer to the experimental value, overestimating it by 0.05 Å. The difference could be ascribed to either the shortcomings of PM3(tm), or to crystal packing effects, or both. There also appears to be a significant difference between the computed and experimental Mn-C distance for the equatorial or terminal CO ligands in both the bridged and all-terminal conformers. The experimental Mn-C_{eq} distances are shorter, by about 0.07 to 0.15 Å, than the PM3(tm) computed values, and may be due to the different coordination at the Mn atoms in the model and experimental structures. One less equatorial CO ligand in the experimental species should make the Mn atoms more electron rich and thus more capable of back-donation to the remaining equatorial carbonyls, resulting in a shorter Mn-C_{eq} distance. Overall, the agreement between the PM3(tm) computed values and experimental values for those geometric parameters least sensitive to the semi-bridging CO ligand and the differing steric demands of the phosphines (e.g. the Mn-C_{ax}, Mn-P, P-CH₂, and C-O distances) is very good.

As a further test of the ability of the PM3(tm) method to predict geometric structures of transition metal complexes, one of the bridging CO ligands was removed from conformer A, and the resultant $Mn_2(CO)_5(dhpm)_2$ complex optimized. This complex was labeled as conformer F, and is displayed in Figure 4.4 (f), as well as Table 4.3. As shown in Figure 4.4 (f), the lone bridging CO ligand is oriented symmetrically between the two

Mn atoms, normal to the Mn-Mn bond. The experimental structure on the other hand, shows the semi-bridging nature of the μ_2 -CO ligand (being bound to one of the Mn atoms through the C atom and to the other through the C-O triple bond). Generally, there is good agreement between the PM3(tm) computed and experimental bond lengths, with deviations smaller than 0.06 Å, with the exception of the Mn-Mn and Mn-C_{br} distances, predicted to be too long by 0.39 Å and 0.11 Å, respectively. Of course, the deviation between the computed and experimental Mn-C_{br}-O_{br} bond angle is largest, 125° vs. 173°, reflecting the different bonding nature of the bridging carbonyl ligands. There is reasonable agreement between computation and experiment for the remaining bond angles, with deviations typically less than 5°. It should be added that conformer F was found to be a minimum on the potential energy hypersurface, reached from several different initial geometries with no symmetry constraints imposed on the system (C₁ symmetry). One of the lowest frequency modes at 42 cm⁻¹ corresponds to the Mn-Mn stretch, indicating that the potential energy hypersurface is very flat and that the molecule may be easily compressed in the crystalline environment, perhaps explaining why our gas phase PM3(tm) calculations exaggerated the Mn-Mn distance. As shown in Table 4.3, this compression may be simulated in the gas phase by the addition of a second bridging carbonyl, as in conformers A and B.

A comparison of the Mn-Mn distance in the bridged (A and B) and non-bridged, all-terminal (C, D, and E) conformers shows that the formation of the μ_2 -CO ligands results in a shortening of the Mn-Mn distance by over 0.1 Å. In accord with the available experimental data for symmetrically bridged species⁴² our PM3(tm) calculations predict the bridging carbonyls to have the longest Mn-C and C-O distances. Interestingly, the arrangement of the phosphine moiety remains nearly constant in all five of the Mn₂(CO)₆(dhpm)₂ conformers studied. The Mn-P distance is shorter, by about 0.02 Å, in the pseudo-staggered conformers (C and D) than in the planar, dibridged conformers (A and B). Furthermore, the P-CH₂-P angle appears to be more affected by the planarity of the six carbonyls (conformers A, B, and E vs. conformers C and D), than the cis or trans arrangement of the methylene unit in the bidentate phosphine ligand (conformers A, C, and E vs. conformers B and D).

At the PM3(tm) level, the stationary points corresponding to the optimized geometries of conformers A, B, C, and D were found to be local minima by harmonic vibrational analysis. The stationary point for the planar, all-terminal conformer (E) was found to be a second-order saddle point, with imaginary frequencies of 25*i* and 13*i* cm⁻¹. The normal mode for the frequency at 25*i* cm⁻¹ corresponds to scrambling of the CO ligands towards the planar, di-bridged conformer A, while the mode at 13*i* cm⁻¹ corresponds to rotation about the Mn-Mn bond to form the pseudo-staggered conformer C.

It should be added that, as found in the $\text{Mn}_2(\text{CO})_{10}$ conformers a large number of the computed vibrational modes, about one third, for each conformer of $\text{Mn}_2(\text{CO})_6(\text{dhpm})_2$ are smaller than 500 cm^{-1} , indicating very flat potential energy hypersurfaces near the minima.

The relative energies of the conformers of $\text{Mn}_2(\text{CO})_6(\text{dhpm})_2$ are displayed in Table 4.4. Based on the PM3(tm) energies of the species at their respective PM3(tm)-optimized geometries (the PM3(tm)//PM3(tm) method) a planar arrangement of the CO ligands with two of them symmetrically bridging the two Mn atoms was found to be the most stable conformation (conformers A and B). At this level, the energy of the planar, all-terminal conformer (E) is predicted to be 32 kcal/mol higher in energy than conformer A. The PM3(tm)//PM3(tm) energies of the pseudo-staggered conformers (C and D) are predicted to be 29 kcal/mol higher than the energy conformer A. It should be added that the PM3(tm)//PM3(tm) method finds a slight preference for a cis arrangement of the methylene units in the two bidentate dhpm ligands, in agreement with the arrangement observed in the crystal structure of $\text{Mn}_2(\text{CO})_5(\text{dppm})_2$.

The PM3(tm)//PM3(tm) results imply that carbonyl scrambling in the model $\text{Mn}_2(\text{CO})_6(\text{dhpm})_2$ system proceeds from the co-planar, symmetrically bridged conformation (A) to the co-planar, all-terminal conformer (E) and back to conformer A, with an activation barrier of 32 kcal/mol. This energy barrier is higher than the upper limit for an NMR-detectable process² (25 kcal/mol) and much higher than the barrier of 10 kcal/mol for carbonyl scrambling in $\text{Mn}_2(\text{CO})_6(\text{dppm})_2$ reported by Marsella and Caulton⁹. This overestimation of the energy barrier based on the PM3(tm) energies is consistent with the previous findings of Børve *et al.*²⁶ in modeling ethylene insertion reactions of some Ti, Zr, and Cr complexes. Following the recommendations of Børve *et al.*²⁶ the reaction barrier was computed using the hybrid DFT//PM3 scheme in which more accurate DFT energies are calculated for the conformers at their respective PM3(tm)-optimized geometries. The results of the hybrid DFT//PM3(tm) calculations are collected in Table 4.4. For all of the functionals employed, the DFT//PM3(tm) scheme predicts the planar, all-terminal conformer (E) to be the lowest in energy, lying 15 - 19 kcal/mol lower in energy than the planar, symmetrically bridged conformer (A). Furthermore, at this level, the pseudo-staggered conformer (C) was found to be slightly higher in energy (less than 1 kcal/mol) than the lowest-energy conformer (E). Based on the computed energy differences, the DFT//PM3(tm) approach models the carbonyl scrambling in $\text{Mn}_2(\text{CO})_6(\text{dhpm})_2$ as proceeding from the planar, all-terminal conformer E to the planar, di-bridged conformer A, and back to conformer E. This mechanism is similar to that predicted for carbonyl scrambling in $\text{Mn}_2(\text{CO})_{10}$.⁴³ Depending on the functional used, the DFT//PM3(tm) approach yields an energy barrier of 15 to 19 kcal/mol for carbonyl

Table 4.4: Relative Energies of the $\text{Mn}_2(\text{CO})_6(\text{dhpm})_2$ Conformers.

	PM3 ^b	BLYP ^c	BP86 ^c	B3LYP ^c	B3PW91 ^c
B	0.1				
C	29.3	-16.9	-14.2	-18.3	-16.2
D	29.3				
E	32.2	-17.4 (-13.1) ^d	-14.9	-18.6	-16.8

^a In kcal/mol, calculated with respect to conformer A, Figure 4.4 (a). ^b Values computed from the PM3(tm) energies at the respective PM3(tm)-optimized geometries. (The PM3(tm) reference energy is $\Delta H_f^\circ = -555.3$ kcal/mol.) ^c Values computed from the DFT total energies, using the density functionals specified, at their respective PM3(tm)-optimized geometries. (The reference energies are: $E(\text{BLYP}) = -381.53866 E_h$; $E(\text{BP86}) = -382.69665 E_h$; $E(\text{B3LYP}) = -382.03884 E_h$; $E(\text{B3PW91}) = -382.39817 E_h$.) ^d Value computed from the BLYP energies at their respective BLYP-optimized geometries. (The BLYP//BLYP reference energy is $E(\text{BLYP}) = -381.69354 E_h$.)

migration in the $\text{Mn}_2(\text{CO})_6(\text{dhpm})_2$ system, nearly halved with respect to the PM3(tm)//PM3(tm) barrier, and more in accord with Marsella and Caulton's estimated barrier of 10 kcal/mol.

The energy barrier for scrambling is reduced to only 13 kcal/mol when the total energies of conformers A and E are evaluated at their respective DFT-optimized geometries (the DFT//DFT method). This further lowering of the DFT//PM3(tm) energy barrier upon re-optimization of the geometries using the DFT approach was not unexpected, since the PM3(tm) parameters were not trained on any bridging systems similar to the one studied here.⁴⁴ From Table 4.3, the BLYP optimized Mn-Mn bond length in conformer A was predicted to be shorter than the corresponding PM3(tm) value, while in conformer E the BLYP method predicts a longer Mn-Mn bond than the PM3(tm) method. Furthermore, optimization of the geometries at the BLYP level also predicts longer Mn-C distances for the axial and equatorial/terminal carbonyls in conformers A and E, and a shorter Mn-C_{br} distance in conformer A than those values obtained using the PM3(tm) method. There are also some differences between the geometry of the dhpm ligand as optimized at the DFT and PM3(tm) levels, as indicated by the significant changes in the Mn-P and P-CH₂ distances and the P-CH₂-P angle.

4.4 Conclusions

The current gradient-corrected density functional theory calculations predict carbonyl migration in $\text{Mn}_2(\text{CO})_{10}$ to proceed from the most stable staggered (D_{4d}) conformation to the eclipsed (D_{4h}) conformation, with a barrier of 5 kcal/mol, and then on to the bridged (D_{2h}) conformation, with an additional barrier of 14 - 15 kcal/mol. The staggered conformer was found to be a local minimum on the potential energy hypersurface. The eclipsed conformer corresponded to a transition state for the simple rearrangement from one staggered conformer to another. The bridged conformer was found to be a second-order saddle point, at the HF level, with the largest negative curvature of the potential energy surface corresponding to the transition state for the carbonyl migration process connecting two eclipsed conformers. The fluxional process induces substantial changes in the Mn-Mn and Mn-C distances, and proceeds with an activation energy of 19 to 21 kcal/mol. This barrier for carbonyl fluxionality, calculated for the interconversion in the gas phase, is fairly close to the upper limit of 25 kcal/mol for processes in solution that may be followed by NMR spectroscopy².

Carbonyl migration in the $\text{Mn}_2(\text{CO})_6(\text{dhpm})_2$ model system is predicted to proceed from the planar, di-bridged conformer (A) to the planar, all-terminal conformer (E) and back to conformer A at the PM3(tm)//PM3(tm) level. At this level the energy barrier for migration is predicted to be 32 kcal/mol, much larger than the experimental estimate of 10 kcal/mol for the experimental $\text{Mn}_2(\text{CO})_6(\text{dppm})_2$ system⁹. However, the energy barrier was halved, to 14 - 19 kcal/mol, when the energies of the conformers were evaluated using the DFT method at their respective PM3(tm)-optimized geometries. In addition, the relative energy ordering of conformers was altered, and carbonyl scrambling was predicted to proceed in a manner similar to that for $\text{Mn}_2(\text{CO})_{10}$, from the planar, all-terminal conformation (E) to the planar, di-bridged conformation (A) and then back to the original conformation. Although, the DFT//PM3(tm) hybrid approach significantly improves the PM3(tm)//PM3(tm) energy barrier it still overestimates experiment by 5-10 kcal/mol. The energy barrier was further reduced to 13 kcal/mol, now overestimating experiment by only 3 kcal/mol, when the energies of the conformers were evaluated at their respective DFT-optimized geometries. This improvement was not unexpected, since the training set used to develop the PM3(tm) parameters contained more complexes with terminal carbonyls than bridging carbonyls, and as a result the lowest energy all-terminal conformer (E) should be better represented at the PM3(tm) level than the symmetrically bridged conformer (A). The remaining error may reflect differences in the potential energy hypersurfaces of the experimental $\text{Mn}_2(\text{CO})_6(\text{dppm})_2$ and the model system, $\text{Mn}_2(\text{CO})_6(\text{dhpm})_2$.

The results presented indicate that the DFT approach is indeed the method of choice, if the necessary computer resources are available, yielding accurate geometries and energy barriers. The less computationally demanding PM3(tm) semiempirical method worked remarkably well in predicting molecular structures, but was less successful in predicting energy barriers. The PM3(tm) energy barriers may be corrected by employing the hybrid DFT//PM3(tm) method, in which the energies of the species are computed using the more accurate DFT approach at their respective PM3(tm) geometries. This hybrid DFT//PM3(tm) scheme should be a very useful one in studies of large transition metal complexes, taking advantage of the smaller computational demands of the PM3(tm) semiempirical method for the more involved geometry optimization task, as well as the ability of the PM3(tm) method to accurately predict molecular structures, while utilizing the energies from the more rigorous DFT approach. As expected, the single-determinant Hartree-Fock method was unsuccessful in modeling $\text{Mn}_2(\text{CO})_{10}$ yielding poor geometries and a very large activation barrier for carbonyl migration.

4.5 References

1. Wilkinson, G.; Piper, T. S. *J. Inorg. Nucl. Chem.* **1956**, *2*, 23.
2. Band, E.; Muetterties, E. L. *Chem. Rev.* **1978**, *78*, 639.
3. de Mayo, P. *Rearrangements in Ground and Excited States*; Academic Press: New York, 1980.
4. Adams, R. D.; Cotton, F. A. *J. Am. Chem. Soc.* **1973**, *95*, 6589.
5. Evans, J.; Johnson, B. F. G.; Lewis, J.; Norton, J. R. *Chem. Commun.* **1973**, *73*, 79.
6. Evans, J.; Johnson, B. F. G.; Lewis, J.; Matheson, T. W. *Chem. Commun.* **1975**, *75*, 576.
7. Todd, L. J.; Wilkinson, J. R. *J. Organomet. Chem.* **1974**, *77*, 1.
8. Aime, S.; Milone, L.; Osella, D.; Hawkes, G. E.; Randall, E. W. *J. Organomet. Chem.* **1979**, *178*, 171.
9. Marsella, J. A.; Caulton, K. G. *Organometallics* **1982**, *1*, 274.
10. Almenningen, A.; Jacobsen, G. G.; Seip, H. M. *Acta Chem. Scand.* **1969**, *23*, 685.
11. Dahl, L. F.; Rundle, R. E. *Acta Cryst.* **1963**, *16*, 419.
12. Martin, M.; Rees, B.; Mitschler, A. *Acta Cryst.* **1982**, *B38*, 6.
13. Veillard, A.; Rohmer, M.-M. *Int. J. Quantum Chem.* **1992**, *42*, 965.
14. Bo, C.; Sarasa, J.-P.; Poblet, J.-M. *J. Phys. Chem.* **1993**, *97*, 6362.
15. Nakatsuji, H.; Hada, M.; Kawashima, A. *Inorg. Chem.* **1992**, *31*, 1740.
16. Rosa, A.; Ehlers, A. W.; Baerends, E. J.; Snijders, J. G.; te Velde, G. *J. Phys. Chem.* **1996**, *100*, 5690.
17. Levenson, R. A.; Gray, H. B. *J. Am. Chem. Soc.* **1975**, *97*, 6042.
18. Marquez, A.; Fernandez Sanz, J.; Gelize, M.; Dargelos, A. *J. Organomet. Chem.* **1992**, *434*, 235.
19. Rosa, A.; Ricciardi, G.; Baerends, E. J.; Stufkens, D. J. *Inorg. Chem.* **1995**, *34*, 3425.
20. Rosa, A.; Ricciardi, G.; Baerends, E. J.; Stufkens, D. J. *Inorg. Chem.* **1996**, *35*, 2886.
21. Folga, E.; Ziegler, T. *J. Am. Chem. Soc.* **1993**, *115*, 5169.
22. Ziegler, T. *Chem. Rev.* **1991**, *91*, 651.
23. *Spartan*; 4.0.3 ed.; Wavefunction, Inc.: Irvine, CA, 1995.
24. Adam, K. R.; Atkinson, I. M.; Lindoy, L. F. *J. Mol. Struct.* **1996**, *384*, 183.
25. Cundari, T. R.; Deng, J. *J. Chem. Inf. Comp. Sci.* **1999**, *39*, 376.
26. Borve, K. J.; Jensen, V. R.; Karlsen, T.; Stovneng, J. A.; Swang, O. *J. Mol. Mod.* **1997**, *3*, 193.

27. Becke, A. *Phys. Rev. A* **1988**, *38*, 3098.
28. Lee, C.; Yang, W.; Parr, R. G. *Phys. Rev. B* **1988**, *37*, 785.
29. Delley, B.; Wrinn, M.; Luthi, H. P. *J. Chem. Phys.* **1994**, *100*, 5785.
30. Becke, A. *J. Chem. Phys.* **1993**, *98*, 5648.
31. Huzinaga, S.; Andzelm, J.; Klobukowski, M.; Radzio-Andzelm, E.; Sakai, Y.; Tatewaki, H. *Gaussian Basis Sets for Molecular Calculations*; Elsevier: Amsterdam, 1984.
32. Frisch, M. J.; Trucks, G. W.; Schlegel, H. B.; Gill, P. M. W.; Johnson, B. G.; Wong, M. W.; Foresman, J. B.; Robb, M. A.; Head-Gordon, M.; Replogle, E. S.; Gomperts, R.; Andres, J. L.; Raghavachari, K.; Binkley, J. S.; Gonzalez, C.; Martin, R. L.; Fox, D. J.; DeFrees, D. J.; Baker, J.; Stewart, J. J. P.; Pople, J. A. *Gaussian 92/DFT*; F2 ed.; Gaussian, Inc.: Pittsburgh, PA, 1993.
33. Frisch, M. J.; Trucks, G. W.; Schlegel, H. B.; Gill, P. M. W.; Johnson, B. G.; Robb, M. A.; Cheeseman, J. R.; Keith, T.; Petersson, G. A.; Montgomery, J. A.; Raghavachari, K.; Al-Laham, M. A.; Zakrzewski, V. G.; Ortiz, J. V.; Foresman, J. B.; Cioslowski, J.; Stefanov, B. B.; Nanayakkara, A.; Challacombe, M.; Peng, C. Y.; Ayala, P. Y.; Chen, W.; Wong, M. W.; Andres, J. L.; Replogle, E. S.; Gomperts, R.; Martin, R. L.; Fox, D. J.; Binkley, J. S.; DeFrees, D. J.; Baker, J.; Stewart, J. J. P.; Head-Gordon, M.; Gonzalez, C.; Pople, J. A. *Gaussian 94*; D3 ed.; Gaussian, Inc.: Pittsburgh, PA, 1995.
34. Dupuis, M.; Marquez, A.; Davidson, E. R. *HONDO*; 95.6 ed.; IBM Corporation: Kingston, N. Y., 1995.
35. Perdew, J. P. *Phys. Rev. B* **1986**, *33*, 8822.
36. Perdew, J. P.; Wang, Y. *Phys. Rev. B* **1992**, *45*, 13244.
37. Stevens, W. J.; Basch, H.; Krauss, M. *J. Chem. Phys.* **1984**, *81*, 6026.
38. Krauss, M.; Stevens, W. J.; Basch, H.; Jasien, P. *Can. J. Chem.* **1992**, *70*, 612.
39. Cundari, T. R.; Stevens, W. J. *J. Chem. Phys.* **1993**, *98*, 5555.
40. Binkley, J. S.; Pople, J. A.; Hehre, W. J. *J. Am. Chem. Soc.* **1980**, *102*, 939.
41. Commons, C. J.; Hoskins, C. F. *Aust. J. Chem.* **1975**, *28*, 1663.
42. Collman, J. P.; Hegedus, L. S.; Norton, J. R.; Finke, R. G. *Principles and Applications of Organotransition Metal Chemistry*; University Science Books: Mill Valley, CA, 1987.
43. Decker, S. A.; Donini, O.; Klobukowski, M. *J. Phys. Chem. A* **1997**, *101*, 8734.
44. Yu, J. *personal communication* **1998**.

Chapter 5

**The First Carbonyl Bond Dissociation Energies of
M(CO)₅ and M(CO)₄(C₂H₂) (M = Fe, Ru, Os):
The Role of the Acetylene Ligand from a
Density Functional Perspective.[‡]**

[‡] Reproduced in part with permission from Decker, S. A.; Klobukowski, M. *Journal of the American Chemical Society* **1998**, *120*, 9342. Copyright 1998 American Chemical Society.

5.1 Introduction

Transition metal carbonyls are among the best known and most widely studied organometallic complexes.¹⁻⁵ They are commonly used as starting materials in organometallic syntheses, and as catalytic precursors. However, they are typically saturated 18-electron species, and thus relatively inert.⁶ It has been known for some time that certain spectator ligands in a metal complex can facilitate, either sterically or electronically, dissociation of CO. Numerous papers have demonstrated that when the ancillary ligand is a π -donor ligand, such as a halide, acetate, or chelating amido group, then the carbonyl ligand in the cis position tends to be labilized. This effect known as cis-labilization, has been observed and studied extensively via solution kinetics in d^6 (Cr, W) and d^7 (Mn, Re) complexes of the type $M(CO)_3L^{-2}$ and $M(CO)_5L$.⁷⁻¹² The proposed rationalization of this effect involves a stabilization of the dissociative unsaturated 16-electron transition state via π -donation from the ancillary ligand. This hypothesis has been supported in theoretical studies by Lichtenberger and Brown¹³ (with the Fenske-Hall method) and Davy and Hall¹⁴ (at the RHF level of theory), and the importance of π stabilization has recently been reviewed by Caulton.¹⁵

Recently Takats and Jordan^{16,17} demonstrated that the presence of an η^2 -alkyne ligand accelerates simple CO substitution reactions in complexes of the type $M(CO)_4(\eta^2\text{-alkyne})$, where the metal is a member of the iron triad and the alkyne is hexafluorobut-2-yne or acetylene. X-ray crystal structures of $Ru(CO)_4[C_2(CF_3)_2]$ and $Os(CO)_4[C_2(CF_3)_2]$ revealed trigonal bipyramidal structures for the complexes, with the alkyne ligand occupying an in-plane equatorial site.¹⁸ The kinetics of the carbonyl substitution process, with phosphines or phosphites, was monitored using IR spectroscopy. It was determined that when the alkyne was hexafluorobut-2-yne (HFB), the phosphine/phosphite occupies an axial position (cis to the alkyne) in the monosubstituted product while both the axial positions are occupied by phosphine/phosphite groups in the di-substituted product. No further carbonyl substitution was observed beyond the disubstituted species in the HFB complexes.¹⁶ Synthetic studies of the acetylene complex of Os have indicated that the substitution of a second phosphine leads to both the expected di-substituted product along with a number of acyl complexes, in which a CO ligand has inserted into the metal-acetylene bond.¹⁷

All of the carbonyl substitution reaction rates were found to be independent of the nature and concentration of the incoming phosphine/phosphite group. This result, coupled with the positive value of ΔS^\ddagger , led to the conclusion that the carbonyl substitution proceeds via a dissociative mechanism, in which the rate-determining step corresponds to loss of CO

from $M(\text{CO})_4(\eta^2\text{-alkyne})$ leading to the monosubstituted product. Comparison of the dissociation rate constants for these alkyne-substituted species with that of their respective parent carbonyls, $M(\text{CO})_5$, indicated that the presence of the alkyne ligand has a profound influence. The rate constants for CO dissociation from the HFB complexes were found to be 3×10^{13} (Fe), 2×10^2 (Ru), and 1×10^7 (Os) faster than those of the corresponding pentacarbonyl complexes. The kinetics data also showed that it is the lowering of ΔH^\ddagger by 3 - 19 kcal/mol in the alkyne complexes relative to the pentacarbonyls that is responsible for the observed increased reactivity.¹⁶

In order to account for the increased reactivity of the alkyne complexes either: (1) a ground state destabilization effect or (2) a transition state stabilization effect may be invoked. According to Takats and Jordan¹⁶, there appear to be no significant geometric or spectroscopic differences between the $M(\text{CO})_4[\text{C}_2(\text{CF}_3)_2]$ and $M(\text{CO})_5$ reactant complexes to account for the increased CO lability. Hence, it was postulated that the increased CO lability must be due to stabilization of the dissociative 16-electron transition state, via increased π -donation from the alkyne ligand through participation of its π orbital perpendicular to the equatorial plane, in the direction of the vacated site. The variable electron donor ability of alkyne ligands in transition metal complexes, from two to four electrons, has been well documented.¹⁹ For example, Templeton and Ward²⁰ have shown that ^{13}C NMR can be used to gauge the number of electrons formally donated by the alkyne to the metal.

The present computational study was undertaken to provide computational support for the role of the alkyne in enhancing CO substitution rates in $M(\text{CO})_4(\eta^2\text{-alkyne})$ complexes. Although numerous theoretical papers have focused on the transition metal carbonyls, as illustrated in the review article of Veillard²¹, far fewer have centered on alkyne complexes. The bonding between acetylene and a naked metal atom (or cation) has been analyzed in several studies. For example, Mitchell *et al.*²² probed the bonding between Ni and acetylene, using non-local density functional theory (DFT). Bauschlicher *et al.*²³ examined the bonding between acetylene and the cations of the first- and second-row transition series, using modified coupled-pair functional (MCPF) theory. Siegbahn²⁴ studied the C-H activation of acetylene by bare second-row transition metal atoms, at the CISD level of theory. Sellers²⁵ modelled the binding of acetylene to the Pd(111) surface at the MP2 level. Perhaps most relevant to the present study are the reports from the groups of Geurts, Frenking, and Morokuma which have examined aspects of the metal-acetylene bond in various transition metal complexes. Geurts *et al.*²⁶ examined the bonding between acetylene and Ni, in $\text{Ni}(\text{CO})_2(\text{C}_2\text{H}_2)$, $\text{Ni}(\text{CNH})_2(\text{C}_2\text{H}_2)$, and $\text{Ni}_2(\text{CNH})_4(\mu_2\text{-C}_2\text{H}_2)$, at the local spin density level of theory. The transformation of coordinated η^2 -acetylene to its

vinylidene isomer in the Ru(II) complex, $\text{Ru}(\text{PH}_3)_2\text{Cl}_2(\text{C}_2\text{H}_2)$, and the Rh(I) complexes, $\text{Rh}(\text{PH}_3)_2\text{Cl}(\text{C}_2\text{H}_2)$ and $\text{Rh}(\text{P}(\text{iPr})_3)_2(\text{Cl})(\text{C}_2\text{H}_2)$, was studied by Morokuma and co-workers^{27,28} using the MP2 and IMOMM (MP2+MM3) methods. Frenking *et al.*²⁹⁻³² using their recently developed charge decomposition analysis (CDA) scheme, probed the nature of the metal-acetylene bond in complexes of the type $\text{MX}_4(\text{C}_2\text{H}_2)$, $\text{MX}_5(\text{C}_2\text{H}_2)^-$, and $\text{M}(\text{CO})_5(\text{C}_2\text{H}_2)$, where $\text{M} = \text{Cr}, \text{Mo}, \text{W}$, and $\text{X} = \text{F}, \text{Cl}$. There are no theoretical papers which focus specifically on the $d^8 \text{M}(\text{CO})_4(\text{C}_2\text{R}_2)$ complexes of the iron triad studied experimentally by Takats and Jordan.¹⁶

5.2 Computational Methods

The present study focuses on the rate determining dissociative loss of CO from the alkyne complexes and the parent pentacarbonyls. Non-local, gradient corrected density functional theory was employed in conjunction with Frenking's charge decomposition analysis scheme,³³ and Bader's atoms in molecules (AIM)³⁴⁻³⁷ topological analysis of the electron density to probe the origins of the increased reactivity of the alkyne-substituted complexes. In order to reduce the computational complexity of the present DFT calculations, acetylene was chosen as a model of the hexafluorobut-2-yne alkyne ligand used in the kinetics study. A recent kinetics study involving the Os alkyne complexes¹⁷ showed that changing the alkyne ligand from hexafluorobut-2-yne to acetylene resulted in only a minor reduction in the value of ΔH^\ddagger for the CO dissociation from 23.8 kcal/mol to 21.8 kcal/mol. Hopefully, the simplified acetylene model complex used in the calculations will not hinder comparison to the experimental hexafluorobut-2-yne complexes.

The primary basis set employed in the present study, denoted BS1, consists of the effective core potential (ECP) basis set of Stevens *et al.*³⁸⁻⁴⁰ with a slight modification of the valence space to triple zeta quality for the main group elements and quadruple zeta quality for the metals. The basis was augmented with a single d polarization function on C and O, and a single p polarization function on H, all of which were taken from Huzinaga *et al.*⁴¹. For the metal atoms a total of 16 electrons were included in the valence space, with a contracted Gaussian basis set of triple-zeta valence quality for the s and p space, and of quadruple-zeta valence quality for the d space. The overall contraction for Fe is (4211/4211/3111), while for Ru and Os it is (4111/4111/2111). The valence electrons of C and O were described using a triple-zeta valence basis set with a (211/211/1*) contraction. The 4-31G basis set⁴² augmented with a p polarization function was used for the H atoms. To probe the metal-acetylene bonding with the CDA and AIM schemes the

all-electron double-zeta plus polarization basis sets of Salahub *et al.*⁴³ were used and denoted BS2. In the BS2 basis set Fe and Ru have contraction schemes of (63321/531/41) and (633321/53211/531) respectively (there was no basis set available for Os), while C and O have a (621/41/1*) contraction and H has a (41) contraction. It was necessary to replace the ECP basis set (BS1) with the all-electron basis set (BS2) because the AIM module as contained within the Gaussian94 package⁴⁴ is limited to all electron basis sets.

A variety of different functionals were employed in the DFT calculations. The primary functional used in the calculations was the BLYP functional, comprised of Becke's gradient-corrected exchange functional⁴⁵ in conjunction with the gradient-corrected correlation functional of Lee, Yang and Parr⁴⁶. This functional was used in all geometry optimizations and subsequent hessian calculations, as well as for determination of the CO bond dissociation energies (BDEs), the CO dissociation trajectories, and the CDA and AIM analyses. The BP86 (Becke's non-local exchange functional⁴⁵ coupled with Perdew's non-local correlation functional⁴⁷), B3LYP (Becke's three-parameter hybrid gradient-corrected exchange functional,⁴⁸ Becke3, coupled with the gradient-corrected correlation functional of Lee, Yang and Parr⁴⁶), and B3PW91 (Becke3 functional,⁴⁸ coupled with Perdew and Wang's non-local correlation functional⁴⁹) functionals were employed to calculate the CO BDEs of the alkyne and parent carbonyl complexes from total energy differences at the respective BLYP optimized geometries. To test the validity of the assumption that the BLYP potential energy surface minima closely resemble those which would be obtained using other functionals, the geometries of several reactant and CO dissociation product complexes were optimized with the B3LYP functional and the resulting CO BDE determined. In all cases optimization of the geometries with the B3LYP functional resulted in no significant differences in the values of the CO BDEs when compared to those values obtained using the BLYP optimized geometries.

All geometries were optimized using analytical gradient techniques and the stationary points characterized by harmonic vibrational analysis, accomplished via numerical differentiation of the analytical first derivatives. The zero point energy corrections from the harmonic vibrational frequencies were included in the CO BDE determinations, for the BLYP functional only.

The Gaussian94 program⁴⁴ was used throughout the study for all single point energy calculations, geometry optimizations, and hessian calculations, as well as for Bader's AIM analysis. The CDA2.1 program⁵⁰, was used in conjunction with the standard output of the Gaussian92 package⁵¹ to analyze the metal-acetylene bonding within the CDA scheme.

5.3 Results and Discussion

5.3.1 Structures of the Carbonyl Complexes

In order to calculate the first carbonyl BDE one must determine the total energies of the reactant complex, $M(\text{CO})_5$, and the CO dissociated products, $M(\text{CO})_4$ and CO. Hence, the first step involved optimization of their respective geometries in order to obtain the lowest-energy conformation in the ground electronic state.

A. $M(\text{CO})_5$

In the gas phase the saturated metal pentacarbonyls exhibit a D_{3h} trigonal bipyramidal structure⁵²⁻⁵⁶, and as such they were optimized under D_{3h} symmetry at the BLYP/BS1 level of theory. The corresponding optimized geometric parameters are given in Table 5.1, and compared with experiment and the results of previous theoretical studies. To allow for a comparison of the effects of different functionals, the Ru and Os analogues were optimized with the B3LYP/BS1 method, and the results are also presented in Table 5.1.

Comparison of the calculated BLYP/BS1 structural parameters and the experimental gas-phase diffraction values shows that the level of theory used here yields quite accurate geometries, with average deviations of the M-C and C-O bond lengths of 0.014, 0.042, and 0.030 Å for the Fe, Ru, and Os analogues, respectively. The BLYP/BS1 method consistently overestimates both the M-C and C-O bonds in all of the complexes. While the B3LYP/BS1 method still overestimates the M-C and C-O distances, the overall agreement with experiment is slightly improved, with average deviations of 0.031 and 0.026 Å for the bond lengths of the Ru and Os analogues, respectively.

Both DFT methods correctly predict the experimentally observed trend of the M-C distances (axial vs. equatorial) for $\text{Ru}(\text{CO})_5$, $\text{Ru-C}_{\text{ax}} < \text{Ru-C}_{\text{eq}}$, and $\text{Os}(\text{CO})_5$, $\text{Os-C}_{\text{ax}} > \text{Os-C}_{\text{eq}}$, although the magnitude of the differences is smaller than that observed experimentally. In the case of $\text{Fe}(\text{CO})_5$, the BLYP/BS1 calculations predict the Fe-C_{ax} bond to be slightly longer than the Fe-C_{eq} bond, by only 0.003 Å, in agreement with the trend from the experimental crystal structure⁵³, but in disagreement with the trend found from the experimental gas-phase diffraction data⁵⁴. In all of the $M(\text{CO})_5$ complexes, the C-O distances of the axial and equatorial ligands are nearly equal, both in the calculations and

Table 5.1: Geometric Parameters^a of M(CO)₅ (D_{3h}).

Method	M-C _{ax}	M-C _{eq}	(C-O) _{ax}	(C-O) _{eq}
Fe(CO)₅				
BLYP ^b	1.837	1.834	1.159	1.162
BP86/Ziegler ^c	1.817	1.813	1.153	1.156
SVWN/Delley ^d	1.776	1.774	1.145	1.147
BVWN/Delley ^d	1.846	1.851	1.154	1.159
BLYP/Delley ^d	1.837	1.834	1.156	1.158
BP86/Delley ^d	1.817	1.814	1.150	1.155
MP2/Frenking ^e	1.688	1.766	1.176	1.166
MCPF/Barnes ^f	1.878	1.847	1.168	1.177
Expt.(Gas ^g)	1.807	1.827	1.152	1.152
Expt.(Crystal ^h)	1.811	1.803	1.117	1.133
Ru(CO)₅				
BLYP ^b	1.994	2.010	1.157	1.162
B3LYP ^b	1.986	2.001	1.144	1.149
BP86/Ziegler ^c	1.968	1.960	1.150	1.157
SVWN/Delley ^d	1.945	1.946		
BVWN/Delley ^d	2.013	2.025		
BLYP/Delley ^d	2.001	2.010		
MP2/Frenking ^e	1.943	1.952	1.162	1.165
Expt. (Gas ⁱ)	1.941	1.961	1.126	1.127
Os(CO)₅				
BLYP ^b	1.992	1.983	1.159	1.165
B3LYP ^b	2.010	1.989	1.115	1.122
BP86/Ziegler ^c	2.000	1.975	1.147	1.156
MP2/Frenking ^e	1.963	1.945	1.163	1.168
Expt. (Gas ^j)	1.982	1.937	1.130	1.131

^a All distances in Å. ^b Results from the present study. ^c Values taken from the non-local DFT study of Ziegler *et al.*⁵⁷ ^d Values taken from the DFT study of Delley *et al.*⁵⁸ ^e Values taken from the MP2 study of Ehlers and Frenking.⁵⁹ ^f Values taken from the correlated *ab initio* study of Bauschlicher and co-workers.⁶³ ^g Experimental gas phase diffraction values.⁵³ ^h Experimental crystal structure values.⁵⁴ ⁱ Experimental gas phase diffraction values.⁵⁵ ^j Experimental gas phase diffraction values.⁵⁶

experiment.

Availability of several previous computational studies of the metal pentacarbonyls of the Fe triad allows for a comparison of the accuracy of the geometries predicted by the DFT methods with a variety of correlated wavefunction methods. It should be noted that a direct comparison of the different methods is not entirely valid, since different basis sets were used in the various calculations. The previous non-local DFT calculations, in particular the BP86 calculations of Ziegler and co-workers⁵⁷ and the BLYP and BP86 calculations of Delley *et al.*⁵⁸, predicted geometries which are quite close to those from the present work. In the case of Fe(CO)₅, the SVWN local DFT results show very poor agreement with the experiment; surprisingly, the agreement is remarkably good for Ru(CO)₅. The geometries obtained by Frenking *et al.*⁵⁹ with the MP2 method show very poor agreement for the first-row complex, but the agreement improves and matches the accuracy of the DFT calculations for the heavier congeners. Overall, the present BLYP/BS1 and B3LYP/BS1 geometries show better agreement with experiment than the MP2 calculations of Frenking, perhaps reflecting basis set effects.

B. M(CO)₄

The unsaturated M(CO)₄ product complexes may be formed via loss of a CO ligand from either the axial or equatorial position in the parent pentacarbonyl. Poliakoff *et al.*^{60,61}, in low-temperature matrix-isolation IR studies, have shown that in the case of Fe, the dissociation of CO proceeds via loss of an equatorial CO, leading to a distorted T_d-like structure of C_{2v} symmetry. Although there has been some controversy surrounding the ground electronic state of Fe(CO)₄, the temperature-dependent magnetic circular dichroism experiments of Poliakoff and co-workers⁶² have conclusively shown it to be paramagnetic. These findings have been supported by a number of theoretical studies^{57,58,63,64} all of which predict Fe(CO)₄ to have a ³B₂ ground electronic state, and a distorted C_{2v} structure. Bogdan and Weitz^{65,66}, in transient infrared spectroscopy kinetics studies, have concluded that the unsaturated CO dissociation products of the Ru and Os analogues have singlet ground states. These findings are fully supported by the theoretical study of Ziegler and co-workers.⁵⁷

The present BLYP/BS1 calculations of the unsaturated M(CO)₄ carbonyl dissociation products are in full agreement with the previous findings of a preference for the dissociation of a CO ligand from the equatorial position. The calculations predict Fe(CO)₄ to have a ³B₂ ground electronic state, while Ru(CO)₄ and Os(CO)₄ are predicted to have ¹A₁ ground states. The lowest energy geometric conformer of each M(CO)₄ complex

is predicted to have a distorted T_d -like, C_{2v} structure, corresponding to the product formed by the removal of an equatorial CO from the parent pentacarbonyl. As expected, in forming the $M(CO)_4$ complex the $C_{ax}-M-C_{ax}$ angle, denoted hereafter as α , compresses while the $C_{eq}-M-C_{eq}$ angle, denoted β , expands towards the vacant site. This characteristic structure is illustrated in Figure 5.1 for the Ru analogue, while the values of the geometric parameters for all three $M(CO)_4$ complexes are collected in Table 5.2, along with the results of previous theoretical studies. It should be noted that all three of the lowest-energy $M(CO)_4$ conformers in their respective lowest-energy electronic states correspond to minima on their respective potential energy surfaces, as confirmed by harmonic vibrational analysis. This supports the dissociative rate determining step proposed in the kinetics study.^{67,68} The corresponding 1A_1 $Fe(CO)_4$, and 3B_2 $Ru(CO)_4$ and 3B_2 $Os(CO)_4$ excited states (of C_{2v} symmetry) are predicted to lie 4-18 kcal/mol above their respective ground states. The $M(CO)_4$ geometric conformers of C_3 symmetry, in which an axial CO has been removed, were found to lie even higher in energy than the C_{2v} excited states. For example, in $Fe(CO)_4$ the singlet and triplet states of the C_3 conformers were 10 kcal/mol and 25 kcal/mol higher in energy than the 1A_1 excited state of the C_{2v} conformer.

In general, the BLYP/BS1 geometries of the $M(CO)_4$ complexes are very similar to those found in previous theoretical studies, as illustrated in Table 5.2. Perhaps the largest exception to this generalization are Frenking's⁵⁹ MP2-optimized parameters for the 1A_1 excited state of $Fe(CO)_4$, and the $C_{ax}-M-C_{ax}$ (α) and $C_{eq}-M-C_{eq}$ (β) angles in the 1A_1 ground state of $Ru(CO)_4$. The BLYP/BS1 $M(CO)_4$ geometries appear to be slightly more distorted from their respective parent pentacarbonyls than found in the previous *ab initio* or DFT calculations.

The present BLYP/BS1 calculations, as well as the previous theoretical calculations predict significant differences in the geometries of the triplet and singlet electronic states of $Fe(CO)_4$. The C-O distances and α angles ($C_{ax}-M-C_{ax}$) are equivalent in the two states. However, the M-C distances are slightly shorter in the 1A_1 excited state than in the 3B_2 ground state and there is a significant difference between the values of the β angle ($C_{eq}-M-C_{eq}$) in the two states. It should be noted that Poliakoff *et al.*⁶⁰ have estimated values of 145° and 120° for the α and β angles, based on their matrix isolation IR spectroscopy measurements. All of the computational results shown in Table 5.2 underestimate Poliakoff's value of the β angle.

Comparison of the BLYP/BS1 optimized geometries of the three 1A_1 $M(CO)_4$ complexes reveals that the spin-allowed dissociation of an equatorial CO ligand results in a larger compression of the axial ligands towards the vacant site in the Fe and Os complexes

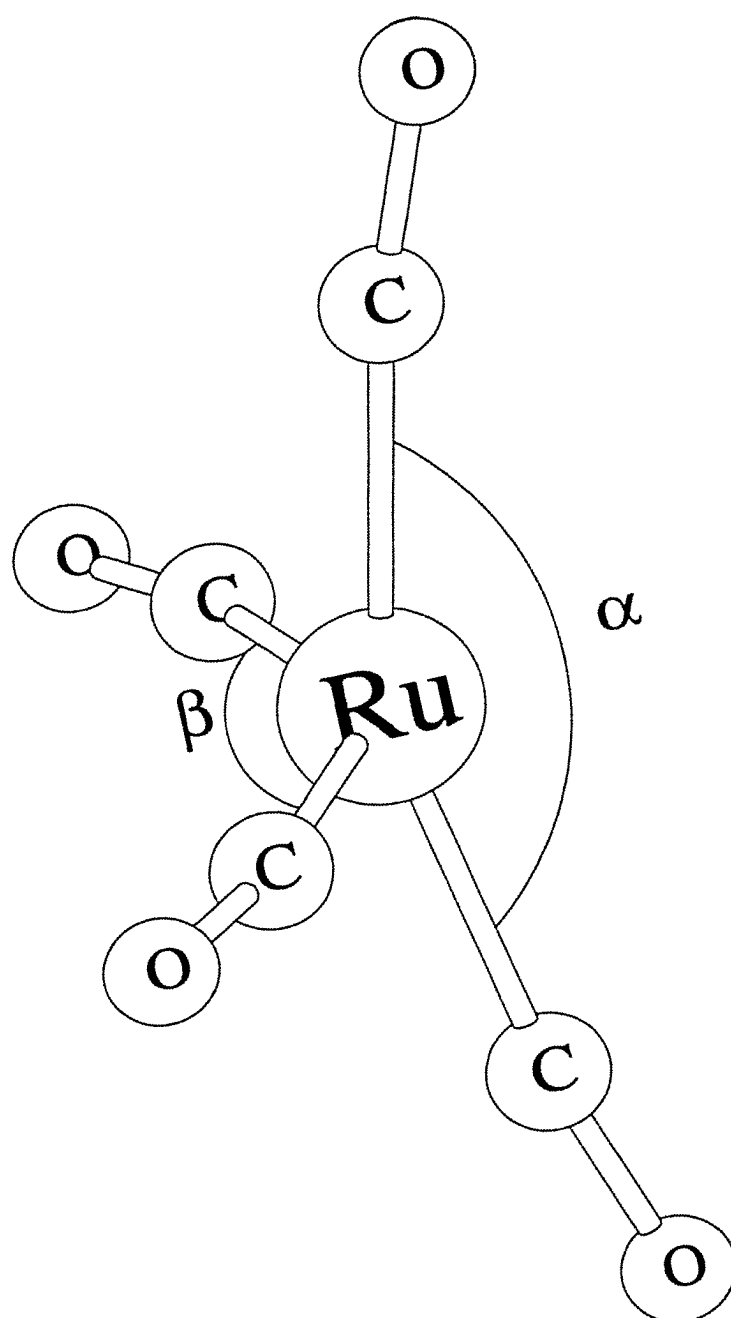


Figure 5.1: Structure of $\text{Ru}(\text{CO})_4$.

Table 5.2: Geometric Parameters^a of $M(\text{CO})_4$ (C_{2v})^b.

Method	M-C _{ax}	M-C _{eq}	(C-O) _{ax}	(C-O) _{eq}	α^c	β^d
Fe(CO) ₄ (³ B ₂)						
BLYP ^e	1.881	1.852	1.161	1.163	146	98
BP86/Ziegler ^f	1.859	1.820	1.156	1.160	147	99
MCPF/Barnes ^g	1.879	1.885	1.169	1.175	150	104
Fe(CO) ₄ (¹ A ₁)						
BLYP ^e	1.824	1.814	1.164	1.166	145	137
BP86/Ziegler ^f	1.834	1.793	1.153	1.160	167	129
MCPF/Barnes ^g	1.910	1.875	1.181	1.178	151	125
MP2/Frenking ^h	1.726	1.713	1.170	1.178	170	135
Ru(CO) ₄ (¹ A ₁)						
BLYP ^e	1.987	1.971	1.160	1.164	158	143
B3LYP ^e	1.986	1.965	1.145	1.150	169	144
BP86/Ziegler ^f	1.991	1.991	1.149	1.153	167	144
MP2/Frenking ^h	1.951	1.904	1.161	1.171	179	137
Os(CO) ₄ (¹ A ₁)						
BLYP ^e	1.958	1.959	1.166	1.165	146	146
BP86/Ziegler ^f	2.059	2.040	1.149	1.151	161	152
MP2/Frenking ^h	1.942	1.909	1.165	1.172	157	138

^a Bond lengths in Å and angles in degrees. ^b Structures correspond to that formed by loss of an equatorial CO from $M(\text{CO})_5$. ^c The C_{ax}-M-C_{ax} angle. ^d The C_{eq}-M-C_{eq} angle. ^e Results from the present study. ^f Values taken from the non-local DFT study of Ziegler *et al.*⁵⁷ ^g Values taken from the correlated *ab initio* study of Bauschlicher *et al.*⁶³ ^h Values taken from the MP2 study of Ehlers and Frenking.⁵⁹

than in the Ru complex. Interestingly, the same trend is not observed for the expansion of the $C_{eq}-M-C_{eq}$ (β) angle towards the vacant site, for which $Os > Ru > Fe$. For each of the metals of the triad, the spin-allowed dissociation process leads to a shortening of both of the M-C distances. However, the spin-forbidden CO dissociation leading to $Fe(CO)_4$ in the 3B_2 state results in a lengthening of both of the M-C distances. Based on the predicted geometric changes of the triplet and singlet states of $Fe(CO)_4$ it would appear that the spin-allowed and spin-forbidden CO dissociations proceed along quite different reaction pathways. As seen previously in the $M(CO)_5$ complexes, the 1A_1 $Ru(CO)_4$ geometry optimized with the B3LYP functional yielded shorter C-O distances, with very little change in the M-C distances relative to the BLYP optimized geometries. At the B3LYP/BS1 level the $C_{ax}-M-C_{ax}$ (α) angle is predicted to be less compressed than in the BLYP/BS1 structure.

5.3.2 Structures of the Alkyne Complexes

A. $M(CO)_4(C_2H_2)$

The geometries of the saturated alkyne substituted complexes, $M(CO)_4(C_2H_2)$, were optimized under C_{2v} symmetry, using the BLYP/BS1 approach. The results are summarized in Table 5.3, and the structure of the Ru compound is shown in Figure 5.2. Geometric parameters optimized with the B3LYP method are also presented in Table 5.3, together with experimental parameters from the crystal structures of the related alkyne complexes $Ru(CO)_4[C_2(CF_3)_2]$ and $Os(CO)_4[C_2(CF_3)_2]$.¹⁸

The BLYP/BS1 method predicts the following trend for the M-C distances: $Fe-C < Os-C < Ru-C$. Iron, with the smallest covalent radius, would be expected to have the smallest M-C bond lengths. However, as the covalent radii of Ru and Os are approximately equal, the shorter Os-C bond may be an indication of stronger bonding between the metal and the CO and C_2H_2 ligands for Os than for Ru. The C-C distances of the bound acetylene ligand increase down the triad, and are substantially longer than in free acetylene, 1.202 Å.⁶⁹ As expected, co-ordination of acetylene to the metal has decreased the C-C bond order, and rehybridized the acetylenic carbons towards ethylenic sp^2 carbons, as illustrated in Figure 5.2. There are no significant differences amongst the C-O bond lengths or the bond angles for the metals of the triad.

The agreement between the BLYP/BS1 geometries and the experimental crystal structures of the Ru and Os hexafluorobut-2-yne complexes is good considering the significant differences between the model alkyne and the experimental one. In both the Ru and Os analogues, the BLYP/BS1 calculations predict longer M-C and C-O distances than

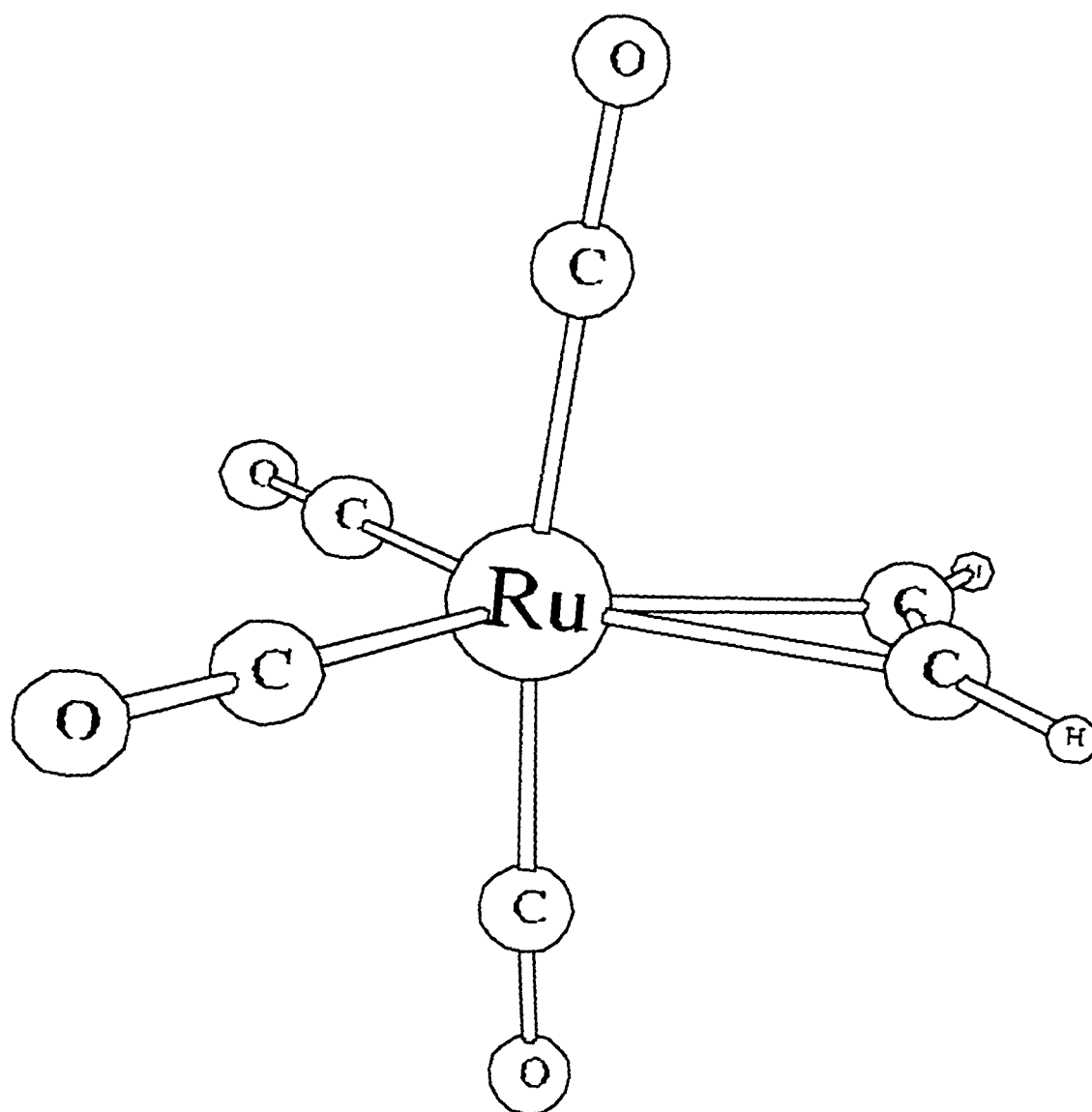


Figure 5.2: Structure of $\text{Ru}(\text{CO})_4(\text{C}_2\text{H}_2)$.

Table 5.3: Selected Geometric Parameters^a of $M(\text{CO})_4(\text{C}_2\text{H}_2)$ (C_{2v}).

Parameter	Fe		Ru		Os	
	BLYP	BLYP	Expt. ^b	BLYP	B3LYP	Expt. ^b
M-C _{ax}	1.843	1.993	1.967	1.989	1.981	1.972
M-C _{eq}	1.823	2.001	1.966	1.972	1.963	1.969
M-C _{ac}	2.140	2.264	2.125	2.247	2.220	2.142
(C-C) _{ac}	1.265	1.271	1.276	1.283	1.276	1.276
(C-O) _{ax}	1.159	1.158	1.130	1.159	1.145	1.128
(C-O) _{eq}	1.164	1.162	1.129	1.165	1.152	1.115
C _{ax} -M-C _{ax}	174	173	173	172	171	173
C _{eq} -M-C _{eq}	110	107	99	105	104	95
C _{ac} -M-C _{ac}	34	33	35	33	33	35
C _{ax} -M-C _{eq}	92	92	94	93	93	93
C _{ax} -M-C _{ac}	87	87	87	86	86	87
C _{eq} -M-C _{ac}	108	110	113	111	111	115

^a Bond lengths in Å and angles in degrees. ^b Values correspond to the crystal structures of the related $\text{Ru}(\text{CO})_4[\text{C}_2(\text{CF}_3)_2]$ and $\text{Os}(\text{CO})_4[\text{C}_2(\text{CF}_3)_2]$ species.¹⁸

observed experimentally. The only bond angle which is markedly different from its experimental value is the $C_{\text{eq}}\text{-M-C}_{\text{eq}}$ angle, perhaps due to the different steric and electronic demands of the model alkyne ligand and those of the actual complex. Again the overall agreement with experiment appears to be slightly better with the B3LYP functional than with the BLYP functional.

B. $\text{M}(\text{CO})_3(\text{C}_2\text{H}_2)$

As in the metal pentacarbonyls, CO dissociation may occur from either an axial or equatorial position in the parent $\text{M}(\text{CO})_4(\text{C}_2\text{H}_2)$ complex. The axial CO dissociation products, optimized under C_s symmetry constraints, were found to be more stable by 10-20 kcal/mol than the equatorial CO dissociation products. Harmonic vibrational analysis characterized all of the $\text{M}(\text{CO})_3(\text{C}_2\text{H}_2)$ axial CO dissociation products as stable intermediates. This agrees with the experimental kinetics study of Takats and Jordan¹⁶, which showed that the rate determining step for the CO substitution reactions in the $\text{M}(\text{CO})_4[\text{C}_2(\text{CF}_3)_2]$ complexes was the dissociative loss of CO.

Loss of an axial carbonyl ligand results in the equatorial CO and acetylene ligands bending downwards out of plane towards the vacant axial site resulting in a distorted square-pyramidal type structure, as illustrated in Figure 5.3 for the Ru congener. The BLYP/BS1 structural parameters are summarized in Table 5.4, along with the B3LYP/BS1 values. Although there are no experimental structural data for these particular unsaturated alkyne tricarbonyl complexes, the crystal structures of the related $\text{Fe}(\text{CO})_2(\text{P}(\text{C}_6\text{H}_{11})_3)[\text{C}_2(\text{CF}_3)_2]$ and $\text{Os}(\text{CO})(\text{P}(\text{iPr})_3)_2[\text{C}_2\text{Ph}_2]$ complexes exhibit a similar distorted square-pyramidal geometry and their relevant structural parameters are given in Table 5.4.^{70,71} The deviation between the experimental and calculated M-C distances is less than 0.05 Å, while that for the C-C distance of the alkyne ligand is less than 0.02 Å. The differences between the model complex and the experimental ones are too large to warrant any direct comparison of most of the angles. However, the computed $C_{\text{ac}}\text{-M-C}_{\text{ac}}$ angle is within 1° of that found experimentally for both complexes. Not surprisingly, the largest differences are for the bend-back angle of the alkyne ligand, computed to be much smaller for acetylene than found experimentally, reflecting the varying steric, electronic, and environmental effects of the different alkynes.

A comparison of the optimized geometries of the unsaturated $\text{M}(\text{CO})_3(\text{C}_2\text{H}_2)$ complexes with those of their parent molecules reveals the structural changes that occur upon dissociation of the axial carbonyl: contraction of the remaining M-C_{ax} bond and of the M-C_{ac} bonds, coupled with an elongation of the C-C bond of the acetylene ligand. There is

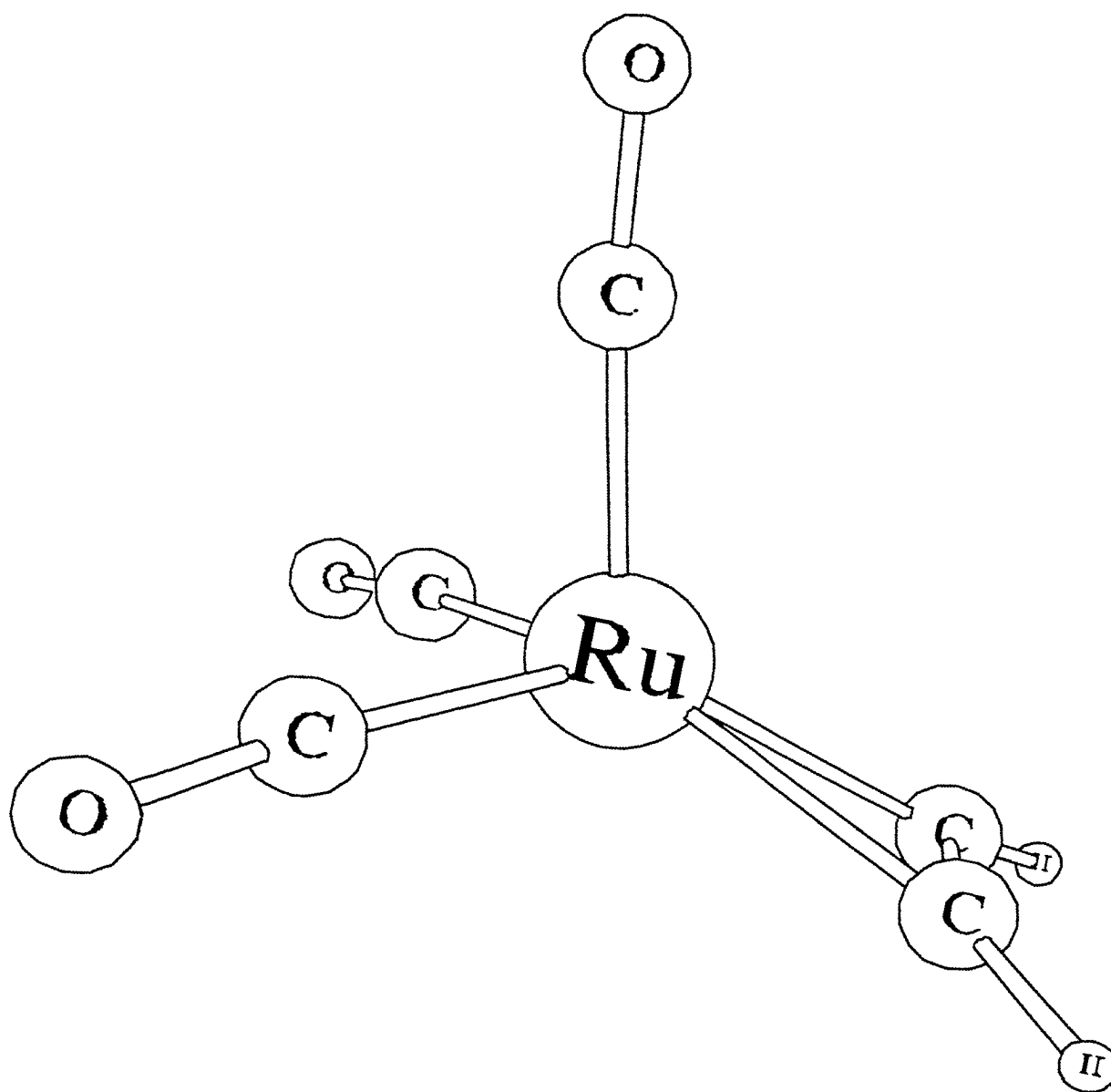


Figure 5.3: Structure of $\text{Ru}(\text{CO})_3(\text{C}_2\text{H}_2)$.

Table 5.4: Selected Geometric Parameters^a of $M(\text{CO})_3(\text{C}_2\text{H}_2)$ (C_2).

Parameter	Fe		Ru	Os		
	BLYP	Expt. ^b	BLYP	BLYP	B3LYP	Expt. ^c
M-C _{ax}	1.778		1.900	1.905	1.896	
M-C _{eq}	1.824	1.769	1.989	1.965	1.957	1.817
M-C _{ac}	1.904	1.868	2.072	2.050	2.031	2.035
(C-C) _{ac}	1.316	1.294	1.317	1.335	1.329	1.318
(C-O) _{ax}	1.166		1.168	1.170	1.156	
(C-O) _{eq}	1.164	1.149	1.163	1.166	1.152	1.181
C _{eq} -M-C _{eq}	107	103	106	103	103	
C _{ac} -M-C _{ac}	40	41	37	38	38	38
C _{ax} -M-C _{eq}	93	91	91	91	91	
C _{ax} -M-C _{ac}	118		121	123	122	
C _{eq} -M-C _{ac}	100	103	103	103	103	

^a Bond lengths in Å and angles in degrees. ^b Values taken from the crystal structure of $\text{Fe}(\text{CO})_2(\text{P}(\text{C}_6\text{H}_{11})_3)[\eta^2\text{-C}_2(\text{CF}_3)_2]$.⁷⁰ The phosphine occupies the axial position. The value for the C_{ax}-M-C_{eq} angle actually corresponds to the P-M-C_{eq} angle. ^c Values taken from the crystal structure of $\text{Os}(\text{CO})(\text{P}(\text{iPr})_3)_2[\eta^2\text{-C}_2\text{Ph}_2]$.⁷¹ The lone CO ligand occupies an equatorial position.

little change in the M-C_{eq} and C-O bond lengths upon CO loss. Hence, based on these structural changes it would appear that dissociation of the axial CO from the alkyne complexes increases the amount of bonding between the acetylene ligand and the metal, coupled with a decrease in the C-C bond order of the acetylene ligand. The structural data support the rationalization, proposed by Takats and Jordan¹⁶, for the increased CO lability of the alkyne complexes due to stabilization of the unsaturated transition state via an increased donation from the alkyne to the metal. Furthermore, the structural changes are consistent with an increased bonding character between the metal and the remaining axial CO. When compared to the BLYP optimized structures, the B3LYP functional predicts changes in the geometry of the unsaturated M(CO)₃(C₂H₂) compound similar to those discussed above for the saturated alkyne complexes.

5.3.3 Carbonyl Bond Dissociation Energies

The first carbonyl bond dissociation energies (CO BDE) of the d⁸ M(CO)₅ and M(CO)₄(C₂H₂) species (where M = Fe, Ru, Os) are summarized in Table 5.5, along with the results of previous theoretical and experimental studies. The CO BDEs were calculated from the difference in total energies of the parent complex and the dissociation products at their respective optimized geometries. The BLYP/BS1 geometries were used throughout. The validity of using the BLYP/BS1 geometries as representative geometries for the other functionals was tested by optimizing the reactant and CO dissociation product of Ru(CO)₅ and Os(CO)₄(C₂H₂) with the B3LYP functional. As shown in Table 5.5, the B3LYP/BS1//B3LYP/BS1 CO BDE values for Ru(CO)₅ and Os(CO)₄(C₂H₂) are 25.0 and 15.2 kcal/mol respectively, and they are essentially identical to the values obtained using the BLYP/BS1 geometries (B3LYP/BS1//BLYP/BS1), 25.2 and 15.0 kcal/mol. Hence, the errors introduced by not re-optimizing the geometries with each functional tend to cancel out when the CO BDE is computed.

All of the DFT calculations correctly predict a reduction in the first CO BDE values of the alkyne-substituted species relative to their respective parent carbonyl complex, by about 6-20 kcal/mol depending on the method and the metal. All of the DFT methods also predict the reduction in the CO BDE of the Ru alkynes to be the smallest among the metals of the triad (about 6-9 kcal/mol) while that for the Fe and Os alkynes is significantly larger (about 15-20 kcal/mol). These results are in accord with the kinetics studies which showed that the alkyne complexes had smaller ΔH^\ddagger values than the corresponding pentacarbonyls and that the increase in reactivity of the alkynes was spectacular for Fe, good for Os, and modest for Ru.¹⁶

Table 5.5: First Carbonyl Bond Dissociation Energies (in kcal/mol) of $M(\text{CO})_5$ and $M(\text{CO})_4(\text{C}_2\text{H}_2)$.

Method	$M(\text{CO})_5$			$M(\text{CO})_4(\text{C}_2\text{H}_2)$				
	Fe		Ru	Os	Fe		Ru	Os
	S ^a	T ^b			S ^c	T ^d		
Present Work								
BLYP ^e	37.3 (34.5)	33.6 (30.3)	24.2 (22.4)	28.7 (26.9)	12.1 (10.5)	30.7	18.0 (16.5)	14.5 (13.1)
BP86 ^f	46.1	42.6	31.6	37.0	17.8		22.6	19.7
B3LYP ^f	38.2	26.6	25.2 (25.0)	32.3	11.3		19.1	15.0 (15.2)
B3PW91 ^f	44.2	31.7	30.0	38.0	14.8		21.7	18.4
RHF				27.9			10.2	6.0
Previous Work								
BP86 ^g	45.7	43.9	33.0	34.7				
SVWN ^h	64	71						
BVWN ^h	30	32						
BLYP ^h	38	41						
CISD ⁱ		35.7 (42.8)						
CCSD(T) ^j	46.5		30.9	42.4				
MCPF ^k	39	23.9						
Expt.	41.5 $\pm 3.0^l$	55 $\pm 11^m$	27.6 $\pm 0.4^n$	31.9 $\pm 0.6^o$	21.0 $\pm 0.5^q$		25.0 $\pm 0.6^q$	23.8 $\pm 0.2^q$
				30.6 ^p (± 0.3)				

^a Value corresponds to the dissociation pathway leading to $^1A_1 \text{Fe}(\text{CO})_4$ (loss of an equatorial CO). ^b Value corresponds to the dissociation pathway leading to $^3B_2 \text{Fe}(\text{CO})_4$ (loss of an equatorial CO). ^c Value corresponds to the dissociation pathway leading to $^1A_1 \text{Fe}(\text{CO})_3(\text{C}_2\text{H}_2)$ (loss of an axial CO). ^d Value corresponds to the dissociation pathway leading to $^3A \text{FeCO}_3(\text{C}_2\text{H}_2)$ (loss of an equatorial CO). ^e The values in brackets include

zero-point energy corrections. ^f Values computed from single point energy calculations using the specified functional at the respective BLYP optimized geometries. (i.e. BP86 denotes results from BP86/BS1//BLYP/BS1) ^g Values taken from the non-local DFT calculations of Ziegler *et al.*⁵⁷ ^h Values taken from the DFT study of Delley *et al.*⁵⁸ ⁱ Values taken from the CISD study of Veillard and co-workers.⁶⁴ The value enclosed in brackets includes the Davidson correction. ^j Values taken from the CCSD(T) calculations of Ehlers and Frenking.⁵⁹ ^k Values taken from the Modified Coupled Pair Functional (MCPF) calculations of Bauschlicher and co-workers.⁶³ ^l Value determined from a pulsed laser pyrolysis study in the gas-phase by Lewis *et al.*⁷² ^m Value determined from a laser photoelectron spectroscopy study in the gas-phase by Engelking and Lineberger.⁷³ ⁿ Value corresponds to ΔH^\ddagger from the solution kinetics study of Huq *et al.*⁶⁷ ^o Value corresponds to ΔH^\ddagger from the solution kinetics study of Pearson *et al.*¹⁶ ^p Value corresponds to ΔH^\ddagger from the solution kinetics study of Basolo and co-workers.⁶⁸ ^q Value corresponds to ΔH^\ddagger from the kinetics study of the related species $M(\text{CO})_4[\text{C}_2(\text{CF}_3)_2]$.¹⁶ Recent solution kinetics experiments have found a ΔH^\ddagger value of 21.8 ± 0.2 kcal/mol for $\text{Os}(\text{CO})_4(\text{C}_2\text{H}_2)$.¹⁷

As illustrated in Table 5.5, the different DFT functionals predict a wide range of CO BDE values, especially for the pentacarbonyls. It should be noted that a direct comparison of the calculated values to the experimental ones is not entirely valid for all the systems studied. For instance, the experimental values listed in Table 5.5 for the Ru and Os analogues of both the alkyne and carbonyl complexes were taken from solution kinetics study, and they correspond to ΔH^\ddagger values and not to CO BDEs. Although the experimental CO BDE value for the dissociation to singlet $\text{Fe}(\text{CO})_4$ from the gas-phase laser pyrolysis study of Lewis *et al.*⁷² appears to be quite reasonable, the corresponding value for dissociation to the triplet state, as measured by gas-phase laser photoelectron spectroscopy by Engelking and Lineberger⁷³, is certainly questionable. Not only is there a huge error associated with it, 11 kcal/mol (20% of the value), but this value implies that the triplet state is less stable than the singlet state, in contrast to the earlier findings of a triplet ground state of Poliakoff and co-workers⁶². It is likely that these experiments were probing an excited triplet state, rather than the ground electronic state.

The dependence of the calculated CO BDE values on the metal atom is shown in Figure 5.4 for both the pentacarbonyls and the alkyne complexes, along with the respective experimental trends. From Figure 5.4, one can see that the experimental CO BDE/ ΔH^\ddagger trends amongst the $\text{M}(\text{CO})_5$ species; $\text{Fe} > \text{Os} > \text{Ru}$, and the $\text{M}(\text{CO})_4(\text{C}_2\text{R}_2)$ species; $\text{Ru} > \text{Os} > \text{Fe}$ are faithfully reproduced by all of the non-local DFT calculations. A comparison of the CO BDEs computed from the different functionals shows several interesting features. It would appear that based on the metal dependence of the CO BDE values of the $\text{M}(\text{CO})_5$ compounds, it is possible to group the four different functionals into two sets. The metal dependence predicted by the BLYP and BP86 functionals mirror one another, and therefore form one set, while the B3LYP and B3PW91 form the other. On the other hand, the CO BDEs predicted by the BLYP/BS1//BLYP/BS1 and B3LYP/BS1//BLYP/BS1 calculations, for both the pentacarbonyls and alkyne complexes, are always smaller in magnitude than those predicted by the BP86/BS1//BLYP/BS1 and B3PW91/BS1//BLYP/BS1 methods. Hence, it would appear that the exchange functional, Becke *vs.* Becke3, is crucial in determining the magnitude of the differences between the CO BDEs of the different metals, while the correlation functional affects the magnitudes of each individual CO BDE.

The compilation of CO BDE values in Table 5.5 allows for a comparison of a variety of different DFT and correlated wavefunction theory methods. However, since different basis sets were used in these studies, the differing values reflect more than mere differences in the methods themselves. Ziegler's BP86 results⁵⁷ show, not surprisingly, good agreement with the BP86 values. The CCSD(T)//MP2 computed values of Frenking

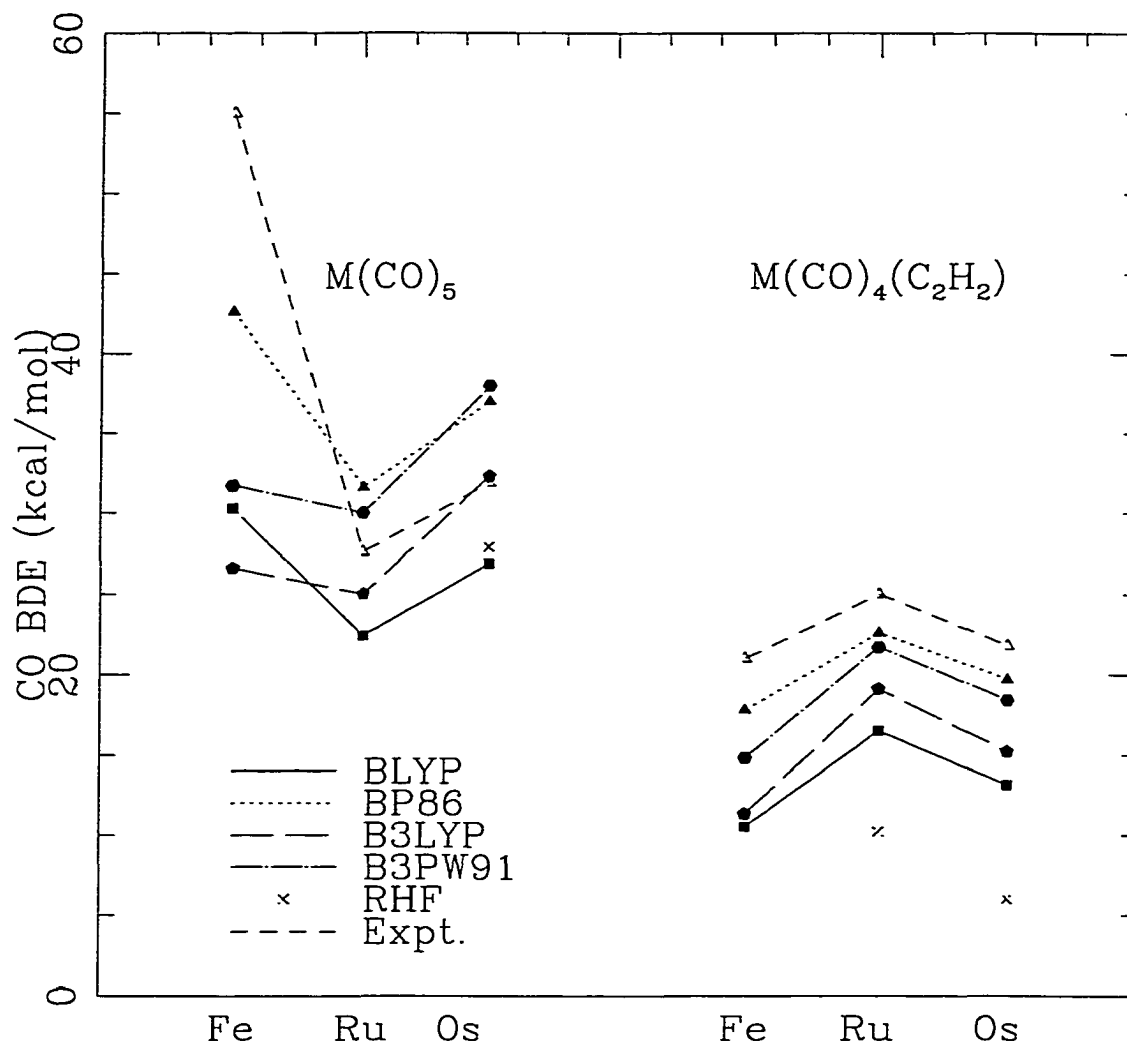


Figure 5.4: First CO bond dissociation energies of $M(\text{CO})_5$ and $M(\text{CO})_4(\text{C}_2\text{H}_2)$. The values correspond to dissociation leading to the most stable products. The filled squares correspond to the BLYP/BS1//BLYP/BS1 values, the filled triangles correspond to the BP86/BS1//BLYP/BS1 values, the filled pentagons correspond to the B3LYP/BS1//BLYP/BS1 values, the filled hexagons correspond to the B3PW91/BS1//BLYP/BS1 values, and the crosses correspond to the RHF/BS1//RHF/BS1 values. The experimental values are represented by the open triangle symbols.

*et al.*⁵⁹, are larger than the BLYP and B3LYP values, but are in accord with the BP86 and B3PW91 values. Veillard *et al.*⁶⁴ predict a value of 35.7 kcal/mol for the CO BDE of Fe(CO)₅ to the triplet state at the CISD level of theory, while Bauschlicher and co-workers⁶³ estimate it to be 23.9 kcal/mol, the lowest estimate. As discussed previously, Fe(CO)₄ is known to possess a triplet electronic ground state with a fairly low-lying excited singlet state; the singlet-triplet energy gaps for Fe(CO)₄ are summarized in Table 5.6. The BLYP and BP86 functionals predict a singlet-triplet splitting of the same magnitude but smaller than that predicted by the B3LYP and B3PW91 functionals. This suggests that the Becke3 functional has a tendency to destabilize the excited singlet state more than Becke's original gradient-corrected functional. Interestingly, Delley *et al.*⁵⁸, using a variety of local and non-local density functionals, incorrectly predict the singlet state to be lower in energy than the triplet state, by 2-7 kcal/mol. Bauschlicher *et al.*⁶³ predict a fairly large Fe(CO)₄ singlet-triplet splitting of 15.1 kcal/mol, slightly larger but of the same order of magnitude as that from the present B3LYP and B3PW91 calculations. In the case of Ru(CO)₄ and Os(CO)₄, the current BLYP calculations predict the singlet state to be lower than the triplet state by 16 and 18 kcal/mol respectively. This is in agreement with the conclusions drawn by Bogdan and Weitz based on their transient IR spectroscopy studies.^{65,66}

5.3.4 Reaction Profiles for CO Dissociation from M(CO)₅ and M(CO)₄(C₂H₂)

The differences between the present CO BDE values and the experimental ΔH^\ddagger values are much smaller for the metal pentacarbonyls than for the alkyne-substituted complexes. The energy profile along the reaction coordinate for carbonyl dissociation from the pentacarbonyls must therefore be quite flat with the top of the barrier being nearly equivalent to the energy of the dissociation products, while that of the alkyne complexes must possess a barrier which relaxes down to the products. In order to test this, the CO dissociation reaction trajectories were simulated for each of the M(CO)₅ complexes and the Ru analogue of the alkyne-substituted complex via constrained geometry optimizations of the complexes at fixed distances between the departing CO ligand and the metal. The departing CO ligand was forced to dissociate along the M-C bond, thereby constraining the optimizations to C_{2v} and C_s symmetry for the M(CO)₅ and Ru(CO)₄(C₂H₂) species, respectively. In addition, all of the CO distances were fixed.

Figure 5.5 displays the simulated CO dissociation trajectories along the spin-allowed singlet pathway for Ru(CO)₅ and Os(CO)₅. As expected, they are both flat,

Table 5.6: Singlet-Triplet Spacings^a (in kcal/mol) of Fe(CO)₄.

	This Work ^b				Previous Work				
	BLYP	BP86	B3LYP	B3PW91	BP86 ^c	SVWN ^d	BVWN ^d	BLYP ^d	MCPF ^e
$\Delta E(T-S)$	-3.8	-3.4	-11.6	-12.5	-1.7	7	2	3	-15.1

^a Computed as $\Delta E(T-S) = E(T) - E(S)$. If $\Delta E(T-S) < 0$, the triplet state is more stable, if $\Delta E(T-S) > 0$, the singlet state is more stable. ^b Values taken from the present study. The values of $\langle S^2 \rangle$ were in the range 2.02 - 2.05. ^c Value taken from the non-local DFT study of Ziegler *et al.*⁵⁷ ^d Value taken from the DFT study of Delley and co-workers.⁵⁸ ^e Value taken from the Modified Coupled Pair Functional (MCPF) calculations of Bauschlicher and co-workers.⁶³

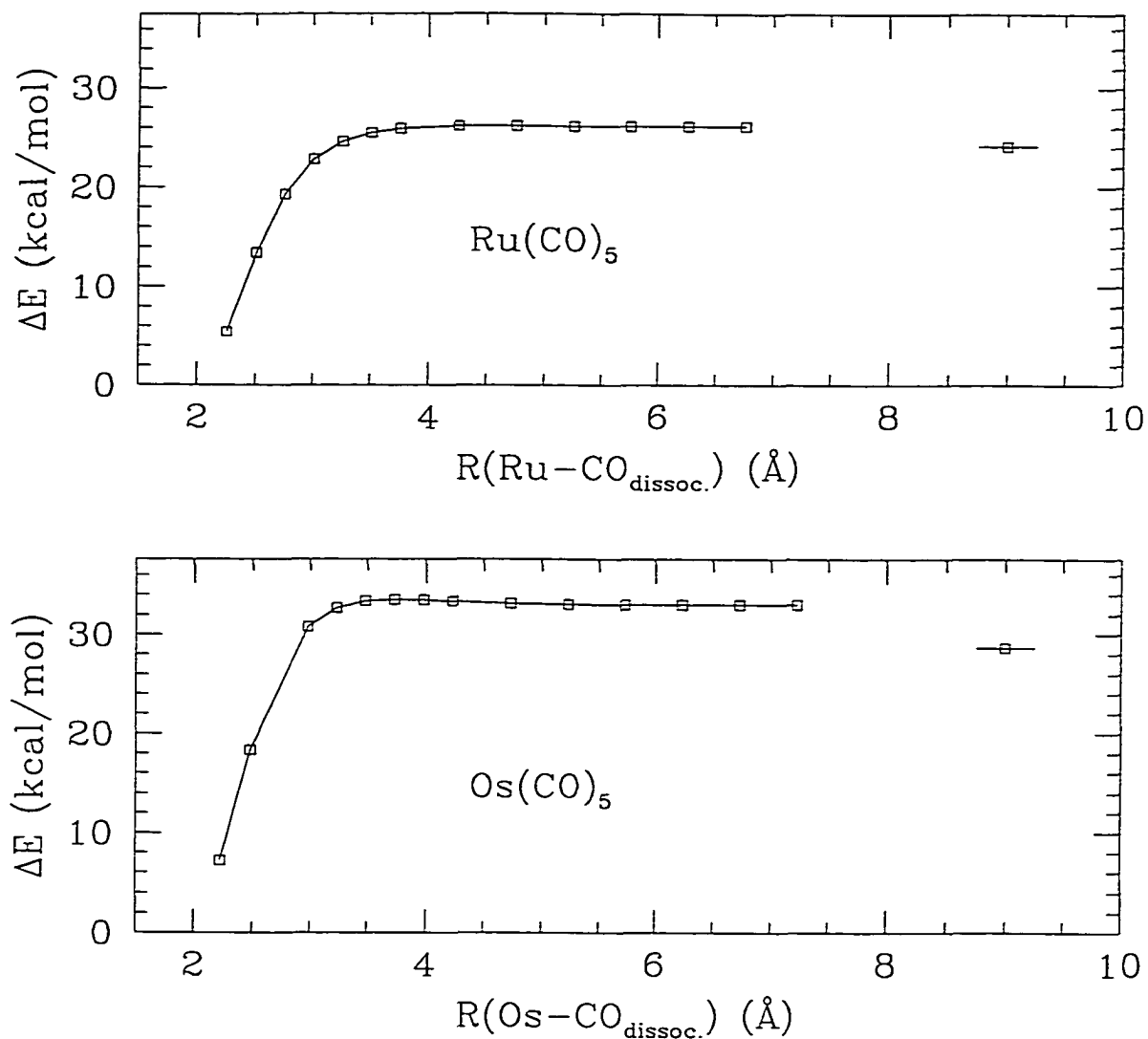


Figure 5.5: CO dissociation trajectories for Ru(CO)₅ and Os(CO)₅. The spin-allowed singlet pathways are shown. The energy is relative to that of the M(CO)₅ reactant complex. The reaction coordinate corresponds to the distance between the metal and the exiting CO ligand. The isolated point around 9 Å corresponds to the energy of the isolated dissociation products: 1A_1 M(CO)₄ + ${}^1\Sigma^+$ CO.

featureless trajectories with no apparent energy difference between the barrier maximum and the dissociation products. The difference in the total energies of the isolated products and the reaction trajectories for large values of the reaction coordinate may be attributed to the optimization (fixed C-O distances) and symmetry (C_{2v}) restrictions imposed. The maximum energy of the $\text{Ru}(\text{CO})_5$ trajectory occurs when the departing CO is roughly 4.8 Å from the metal, while in $\text{Os}(\text{CO})_5$ it occurs around 3.7 Å. Although this is a very rough estimate of the position of the transition state, the earlier transition state for $\text{Os}(\text{CO})_5$ is in agreement with the conclusions drawn by Basolo and co-workers⁶⁸, based on solution kinetics measurements. Initial characterization of these maximum energy points, via the energy hessian, revealed four imaginary frequencies for the dissociating $\text{Ru}(\text{CO})_5$ system, and three imaginary frequencies for the $\text{Os}(\text{CO})_5$ system. In both cases, all the imaginary frequencies were smaller than 50 cm^{-1} . Due to the flat nature of the potential energy surfaces near the barrier maximum, no further attempt was made to locate the true transition state. However, it is this flatness of the reaction trajectories which validates a comparison of the computed CO BDEs to experimental ΔH^\ddagger values. The reaction trajectory for CO dissociation from $\text{Fe}(\text{CO})_5$, shown in Figure 5.6, is more complicated due to the triplet ground electronic state of the unsaturated $\text{Fe}(\text{CO})_4$ product complex. Hence, it was necessary to simulate not only the dissociation of CO from $\text{Fe}(\text{CO})_5$ to singlet $\text{Fe}(\text{CO})_4$, as done in the Ru and Os trajectories, but also the trajectory leading to $^3\text{B}_2 \text{Fe}(\text{CO})_4$. This was accomplished by optimizing the geometry of the $^3\text{B}_2 \text{Fe}(\text{CO})_4 + ^1\Sigma^+ \text{CO}$ system as the CO ligand was gradually brought closer and closer to the $^3\text{B}_2 \text{Fe}(\text{CO})_4$ fragment. The reaction trajectory along the $^1\text{A}_1$ dissociation pathway is flat and featureless with no relaxation from the barrier to the products, as seen in the Ru and Os trajectories. The $^1\text{A}_1$ pathway is predicted to be the lowest-energy reaction trajectory until the dissociating CO ligand becomes separated from the metal by about 3.5-4.0 Å at which point the system would undergo a crossing to the $^3\text{B}_2$ state, and continue to the lowest energy dissociation products, $^3\text{B}_2 \text{Fe}(\text{CO})_4$ and $^1\Sigma^+ \text{CO}$. The reaction trajectory for a high lying $^3\text{A}_1$ excited state is also shown in Figure 5.6, however, it is most likely thermally inaccessible.

The simulated reaction trajectory for the dissociation of an axial carbonyl ligand from $\text{Ru}(\text{CO}_4(\text{C}_2\text{H}_2))$ is displayed in Figure 5.7. Unlike the $\text{M}(\text{CO})_5$ carbonyl dissociation trajectories, the energy profile for this trajectory increases to a maximum and then relaxes down to the products. The extent of this relaxation is quite modest, about 2-4 kcal/mol. The maximum occurs when the departing CO ligand is about 3.0-3.5 Å from the metal. An estimated 21 kcal/mol barrier may be obtained from the plot, quite close to the value of 25.0 kcal/mol obtained from kinetics measurements on the related Ru hexafluorobut-2-yne

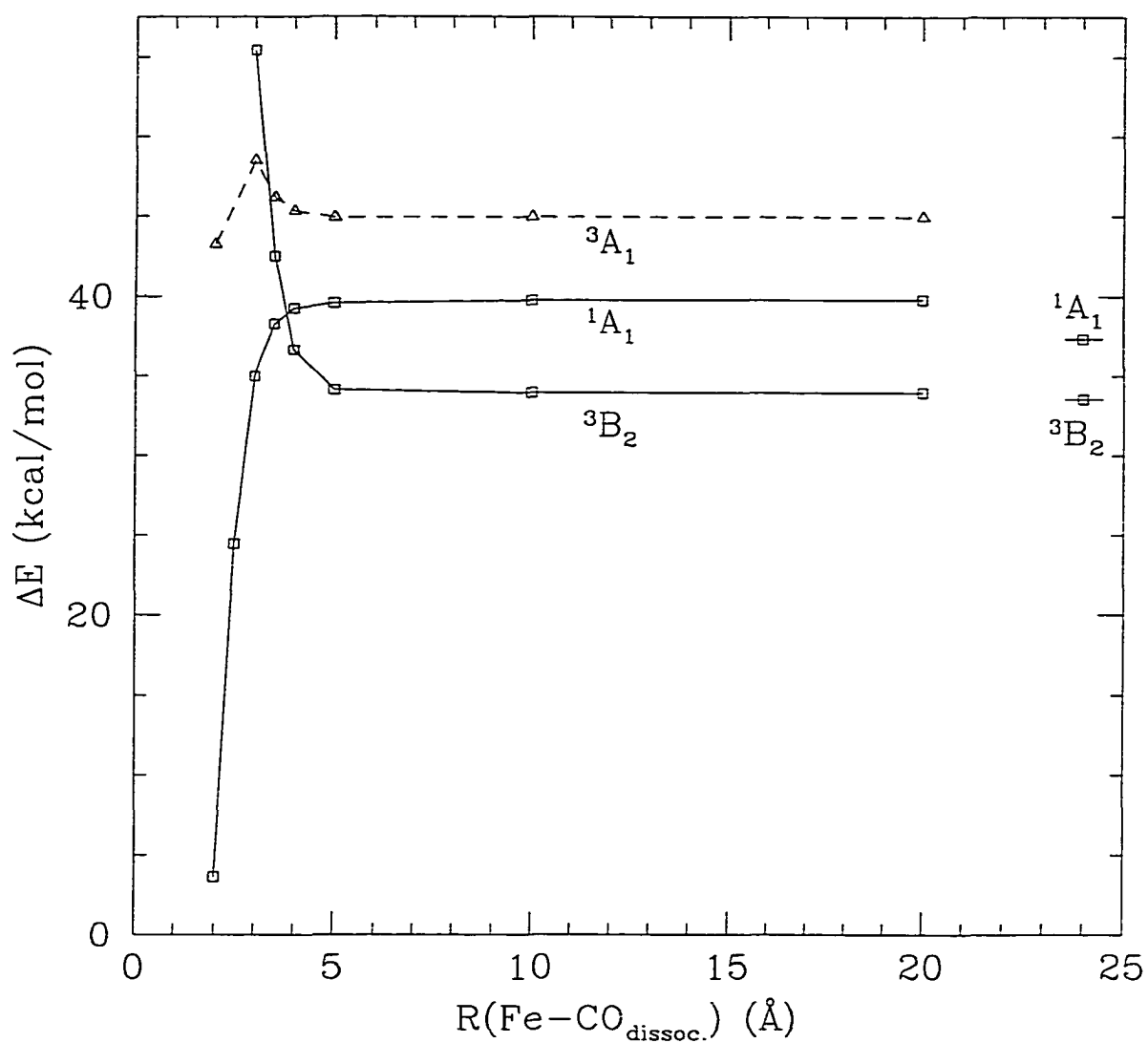


Figure 5.6: CO dissociation trajectories for $\text{Fe}(\text{CO})_5$. The energy is relative to that of the $\text{M}(\text{CO})_5$ reactant complex. The reaction coordinate corresponds to the distance between the metal and the exiting CO ligand. The isolated points around 9 Å correspond to the energy of the isolated dissociation products: ${}^1\text{A}_1 \text{Fe}(\text{CO})_4 + {}^1\Sigma^+ \text{CO}$ and ${}^3\text{B}_2 \text{Fe}(\text{CO})_4 + {}^1\Sigma^+ \text{CO}$.

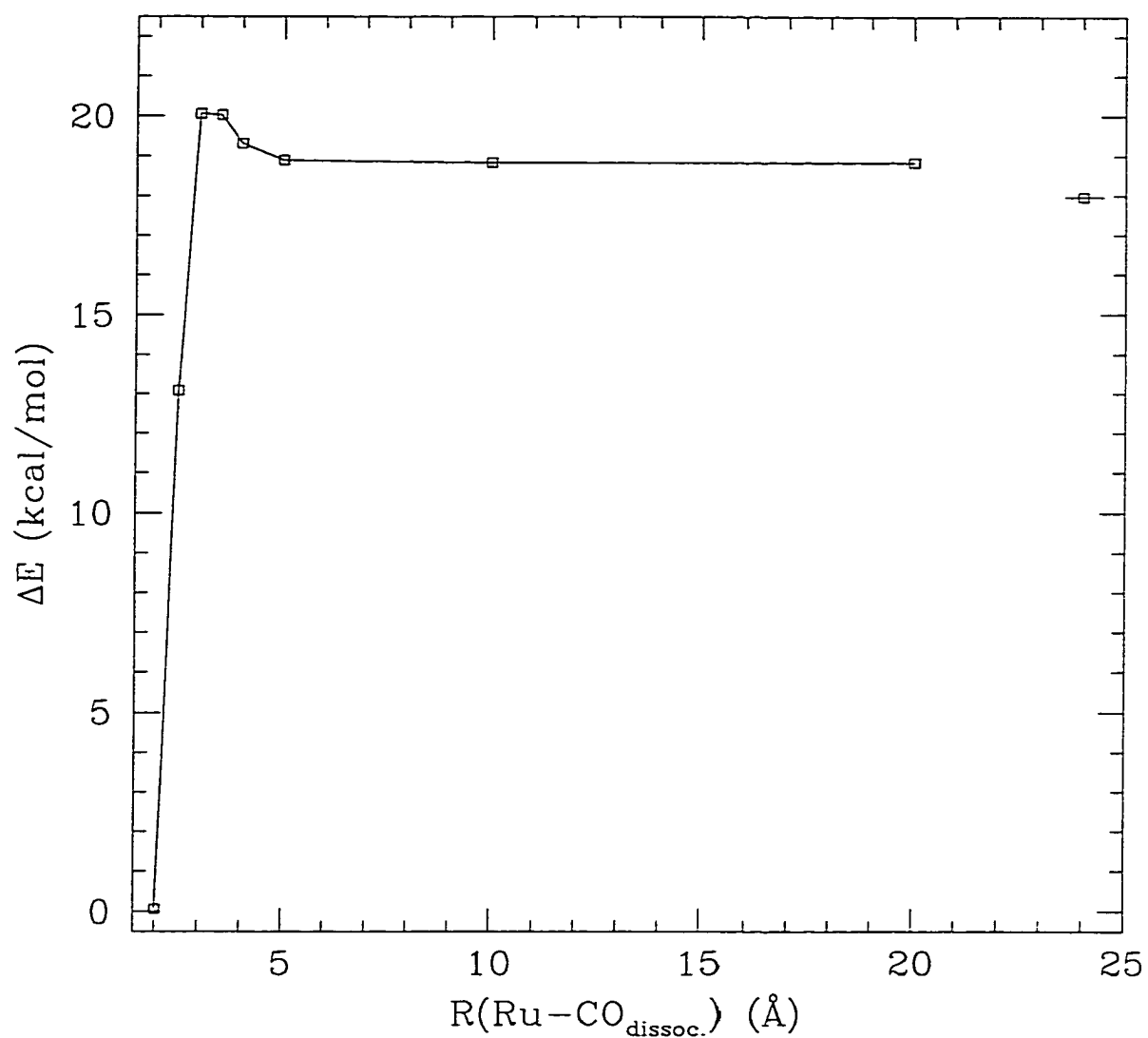


Figure 5.7: CO dissociation trajectory for $\text{Ru}(\text{CO})_4(\text{C}_2\text{H}_2)$. The energy is relative to that of the $\text{M}(\text{CO})_4(\text{C}_2\text{H}_2)$ reactant complex. The reaction coordinate corresponds to the distance between the metal and the exiting CO ligand. The isolated point around 24 Å corresponds to the energy of the isolated dissociation products: ${}^1\text{A}' \text{Ru}(\text{CO})_3(\text{C}_2\text{H}_2) + {}^1\Sigma^+ \text{CO}$.

complex. The difference between the limiting value of the reaction trajectory and the energy of the isolated products can again be attributed to the symmetry (C_s) and structural constraints (fixed C-O distances) imposed during optimization. The calculations predict an earlier transition state and thus one of less bond-breaking character for the alkyne-substituted complex than for the pentacarbonyl, at least for the Ru species.

In summary, the computed CO dissociation reaction trajectories along the spin-allowed singlet pathways for all three of the $M(CO)_5$ complexes are predicted to be flat, with no apparent stabilization of the unsaturated $M(CO)_4$ dissociation product with respect to the transition state, while in $Ru(CO)_4(C_2H_2)$ the unsaturated dissociation product is predicted to be stabilized by a few kcal/mol with respect to the transition state. As suggested by Takats and Jordan¹⁶, the alkyne ligand must be playing an active role in the stabilization of the unsaturated $M(CO)_3(\eta^2\text{-alkyne})$ intermediate. The origin of this stabilization is addressed in the following section.

5.3.5 The Role of the Acetylene Ligand

In order to probe the origin of the reduced CO BDE values of the alkyne complexes with respect to the parent pentacarbonyls, it was necessary to assess the role of the acetylene ligand in both the reactant complex, $M(CO)_4(C_2H_2)$, and the CO dissociated $M(CO)_3(C_2H_2)$ compound. Metal-olefin bonding is commonly described in terms of the well-known Dewar-Chatt-Duncanson model⁷⁴ of synergistic alkene $\rightarrow M$ σ -bonding (i.e. donation from the occupied π orbital of the alkene to an empty metal orbital of proper symmetry), and $M \rightarrow$ alkene π -backdonation (i.e. donation from an occupied metal orbital of π symmetry into the empty π^* alkene orbital). It is easy to extrapolate this model to the bonding between an alkyne and a metal, since the only difference is due to the presence of a second occupied π orbital which may donate to the metal, and a second π^* orbital available to accept electron density from the metal. In the formal electron-counting scheme alkynes may be treated as a two-electron donor when only one of the π orbitals is involved in bonding to the metal and as a four-electron donor when both of its π orbitals actively donate to the metal atom. The reactant complex, $M(CO)_4(C_2H_2)$, is a saturated 18-electron species, with the acetylene ligand contributing two electrons. Removal of a carbonyl leads to $M(CO)_3(C_2H_2)$, which is formally an unsaturated 16-electron complex, if acetylene remains a two-electron donor. On the other hand, counting acetylene as a four-electron donor gives the complex a saturated 18-electron count. It is this variable electron-donor ability of the acetylene which has been proposed by Takats and Jordan to account for the observed increased reactivity of the alkyne substituted species with respect to the parent

pentacarbonyl.¹⁶ The alkyne may act as a four-electron donor in order to stabilize the otherwise unsaturated CO dissociation transition state/product, thereby leading to an increased reactivity, and a decreased CO BDE. This stabilization is not available in the pentacarbonyl, since the CO ligand does not have a second low-lying orbital to participate in donation to the metal. In the present work, the charge decomposition analysis (CDA) scheme of Frenking *et al.*, along with Bader's atoms-in-molecules (AIM) analysis of the electron density topology were used in order to probe the stabilization of $M(\text{CO})_3(\text{C}_2\text{H}_2)$.

5.3.5.1 CDA Results

A. Background

Frenking's CDA scheme attempts to quantify donor-acceptor molecular interactions in terms of common Dewar-Chatt-Duncanson model concepts (i.e. donation, backdonation, and repulsion). CDA gives quantitative information regarding the change in the electronic structure of a complex, AB, due to the interactions between the two fragments A and B, based solely on orbital interactions. It is a linear combination of fragment orbitals-molecular orbital method. The molecular orbitals of the complex AB in the original atomic orbital basis (atom-centred basis functions) are transformed to the fragment orbital basis set. The transformation matrix contains all of the information which connects the electronic structures of the two fragments, A and B, with that of the complex AB. The interpretation of this transformation matrix is simplified in the CDA scheme by partitioning it into terms common to the Dewar-Chatt-Duncanson model: donation (q_d), backdonation (q_b), and repulsive polarization (q_r) between the two fragments. One fragment is defined to be the electron donor fragment, A, (for example a ligand) while the other fragment is the electron acceptor fragment, B, (for example the remaining fragment of the transition-metal complex). The donation term (q_d) is then defined as corresponding to the interaction between the occupied orbitals of the donor fragment A and the unoccupied orbitals of the acceptor fragment B. Backdonation (q_b) arises from the interaction between the occupied orbitals of the electron acceptor fragment B with the unoccupied orbitals of the electron donor fragment A. The repulsive polarization term accounts for the interaction between the occupied orbitals on both fragments. This partitioning is carried out for each MO of the complex, and summing the contributions from all of the MOs yields total amounts of donation, backdonation, and repulsion between the two fragments; e.g., for donation

$$q_d = \sum_i q_{d_i}.$$

B. Qualitative Aspects of Bonding

In the present study, the CDA scheme was used as a tool to characterize the nature of the acetylene ligand in both the reactant $M(\text{CO})_4(\text{C}_2\text{H}_2)$ and CO dissociation product $M(\text{CO})_3(\text{C}_2\text{H}_2)$. In each complex the acetylene ligand was defined as the electron donor fragment A, and the remaining metal-carbonyl fragment defined as the electron acceptor B. Table 5.7 summarizes the total amounts of donation, q_d ($\text{C}_2\text{H}_2 \rightarrow \text{M}$), backdonation, q_b ($\text{C}_2\text{H}_2 \leftarrow \text{M}$) and repulsion, q_r ($\text{C}_2\text{H}_2 \leftrightarrow \text{M}$) for the Fe and Ru analogues of the reactant and CO dissociation product complexes, at the BLYP/BS2//BLYP/BS1 level of theory. Also given in Table 5.7 are the CDA results for $\text{Ru}(\text{CO})_5$ and its corresponding CO dissociation product, $^1\text{A}_1 \text{Ru}(\text{CO})_4$, in which an equatorial carbonyl ligand was defined as the electron donor fragment A and the remaining $\text{Ru}(\text{CO})_n$ fragment the electron acceptor fragment B. As shown in Table 5.7, the loss of an equatorial CO from $\text{Ru}(\text{CO})_5$ results in no significant change in the amount of $\text{CO} \rightarrow \text{M}$ donation. There is, however, a decrease in the amount of $\text{CO} \leftarrow \text{M}$ backdonation, perhaps not surprising since the electron density of the metal in the unsaturated CO dissociation product is expected to decrease upon CO dissociation. In addition there is a substantial increase in the $\text{CO} \leftrightarrow \text{M}$ repulsion upon CO dissociation, which may reflect the geometrical changes associated with the dissociation.

The loss of a carbonyl from $\text{Fe}(\text{CO})_4(\text{C}_2\text{H}_2)$ and $\text{Ru}(\text{CO})_4(\text{C}_2\text{H}_2)$ leads to an increase in the total amount of donation from the acetylene to the metal fragment by 0.16 and 0.20 electrons, respectively, as seen in Table 5.7. With this increase in donation there is also an increase in the total amount of backdonation from the metal to the acetylene ligand of roughly the same magnitude, perhaps due to the presence of fewer π -acid CO ligands. As intuitively expected, removal of a CO ligand results in a decrease in the repulsion between the acetylene ligand and the metal carbonyl fragment. These results appear to be consistent with the proposed hypothesis of a stabilization of the unsaturated CO dissociation product through an increased donation from the acetylene ligand to the metal. However, there is still no direct evidence for the participation of both π orbitals of the acetylene ligand. To gain a deeper understanding of the role of the acetylene ligand, especially in the unsaturated $M(\text{CO})_3(\text{C}_2\text{H}_2)$ intermediate, each of the individual M-C₂H₂ MO interactions was analyzed with the CDA scheme. As stated previously, $\text{C}_2\text{H}_2 \rightarrow \text{M}$ bonding can take place through both π orbitals of the acetylene ligand: the π_{\parallel} orbital which lies in the equatorial plane and the π_{\perp} orbital which is perpendicular to the equatorial plane. The corresponding antibonding orbitals, π^*_{\parallel} and π^*_{\perp} , may accept electron density from the

Table 5.7: Summary of Charge Decomposition Analysis.^{a, b, c}

	Fe(CO)₄(C₂H₂)		Fe(CO)₃(C₂H₂)	
q _d		0.56		0.72
q _b		0.35		0.51
q _r		-0.37		-0.25
	Ru(CO)₅	Ru(CO)₄	Ru(CO)₄(C₂H₂)	Ru(CO)₃(C₂H₂)
q _d	0.30	0.30	0.42	0.62
q _b	0.33	0.29	0.37	0.55
q _r	-0.10	-0.18	-0.32	-0.29

^a Charge Decomposition Analysis scheme of Frenking and co-workers.³³ ^b Results shown are for the charge decomposition analysis of the BLYP/BS2 density. ^c In units of electrons.

metal through backdonation. These four Dewar-Chatt-Duncanson M-C₂H₂ interactions, referred to as: π - σ_d (C₂H₂ → M, $\pi_{||}$), π - π_d (C₂H₂ → M, π_{\perp}), π^* - π_b (M → C₂H₂, $\pi^*_{||}$), and π^* - δ_b (M → C₂H₂, π^*_{\perp}) in the following discussion, are shown in Figures 5.8 and 5.9 for the M(CO)₄(C₂H₂) and M(CO)₃(C₂H₂) complexes. As shown in Figure 5.9 (a)-(d) it would appear that the two donor and two back-donor MO interactions in M(CO)₃(C₂H₂) are hybrids of the original MO interactions in the saturated species, Figure 5.8 (a)-(d). The contributions q_{di} from the two C₂H₂ → M interactions to the CDA donation term, q_d , and the contributions q_{bi} from the two corresponding M → C₂H₂ interactions to the backdonation term, q_b , are given in Table 5.8 for both the Fe and Ru analogues of the saturated and unsaturated alkyne complexes. Since the same bonding picture between the alkyne and the metal emerges for both the Fe and Ru analogues, only the results for the Fe complexes will be discussed in detail. In the saturated Fe(CO)₄(C₂H₂) complex only one of the π orbitals, $\pi_{||}$ (i.e. π - σ_d interaction), is actively involved in donation of electron density to the metal, with a q_{di} value of 0.25 electrons. Upon removal of an axial CO, the second acetylene π orbital, π_{\perp} , becomes an active donor, and donates an equivalent amount of electron density to the metal as the $\pi_{||}$ orbital, with q_{di} values of 0.20 and 0.19 electrons, respectively. Hence, the role of the acetylene ligand changes along the CO dissociation pathway, going from a two-electron donor in the Fe(CO)₄(C₂H₂) reactant complex to a four-electron donor and thereby stabilizing the CO dissociation product Fe(CO)₃(C₂H₂). Interestingly, a similar picture of backbonding emerges from the CDA results, with only the $\pi^*_{||}$ orbital accepting electron density from the metal in the reactant complex, while both π^* orbitals actively accept electron density in the CO dissociated M(CO)₃(C₂H₂) complex. In summary, the CDA analysis of the individual Dewar-Chatt-Duncanson M-C₂H₂ interactions provides semi-quantitative evidence for the hypothesis that it is the participation of both π orbitals of the alkyne which stabilizes the CO dissociated intermediate, thereby leading to reduced CO BDE values with respect to the parent pentacarbonyls. The CDA findings are in full agreement with the structural changes which occur upon CO dissociation.

5.3.5.2 AIM Results

A. Background

Bader's atoms-in-molecules (AIM) analysis of the electron density topology was used as a further test of this transition state/product stabilization hypothesis. Using AIM theory the values of the electron density, $\rho(r)$, and the Laplacian of the electron density,

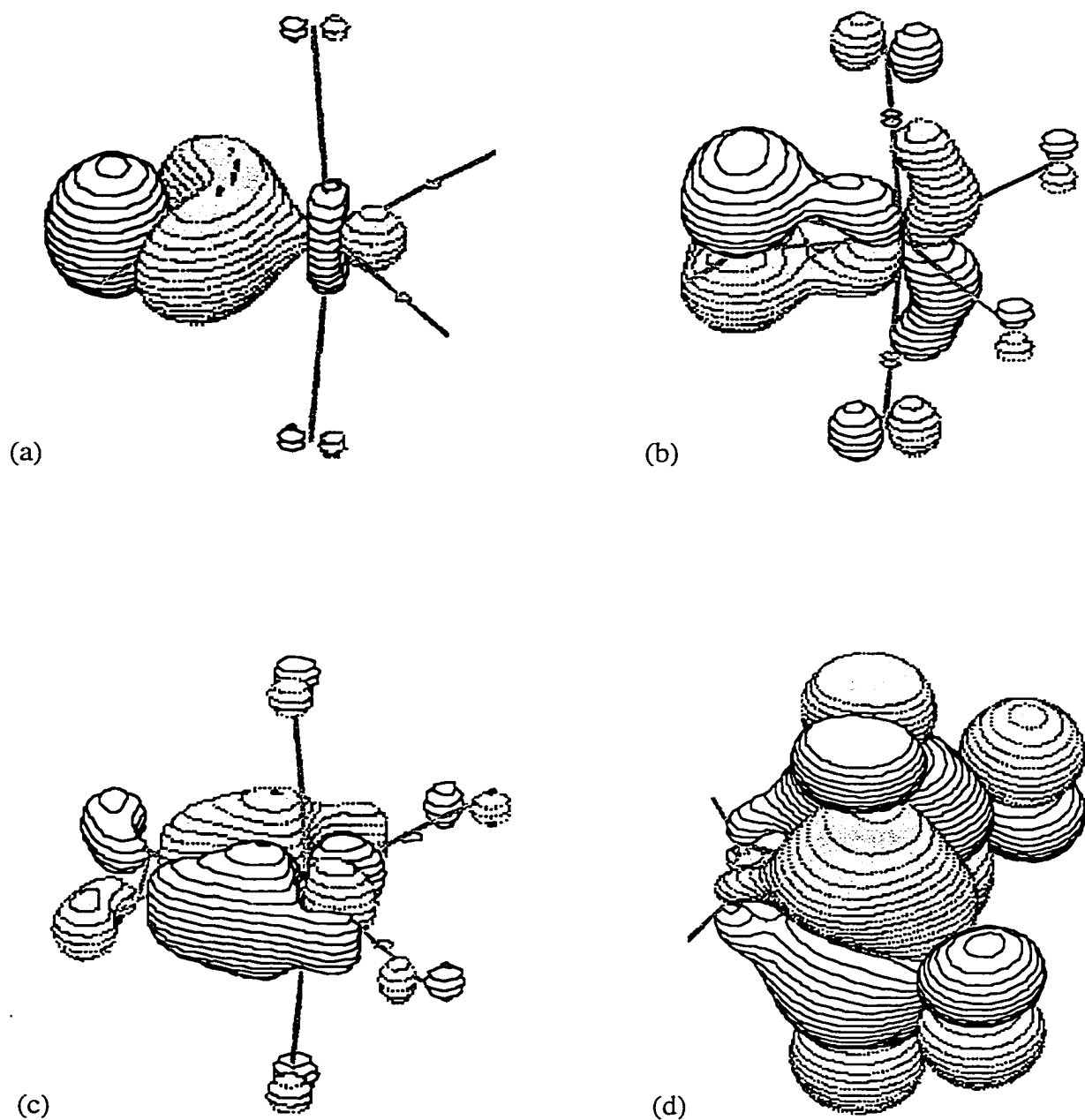


Figure 5.8: The four Dewar-Chatt-Duncanson type metal-acetylene MO interactions of the saturated $M(CO)_4(C_2H_2)$ complex: (a) $C_2H_2 \rightarrow M \pi_{\parallel}-\sigma$ donation, (b) $C_2H_2 \rightarrow M \pi_{\perp}-\pi$ donation, (c) $C_2H_2 \leftarrow M \pi^*_{\parallel}-\pi$ backdonation, (d) $C_2H_2 \leftarrow M \pi^*_{\perp}-\delta$ backdonation.

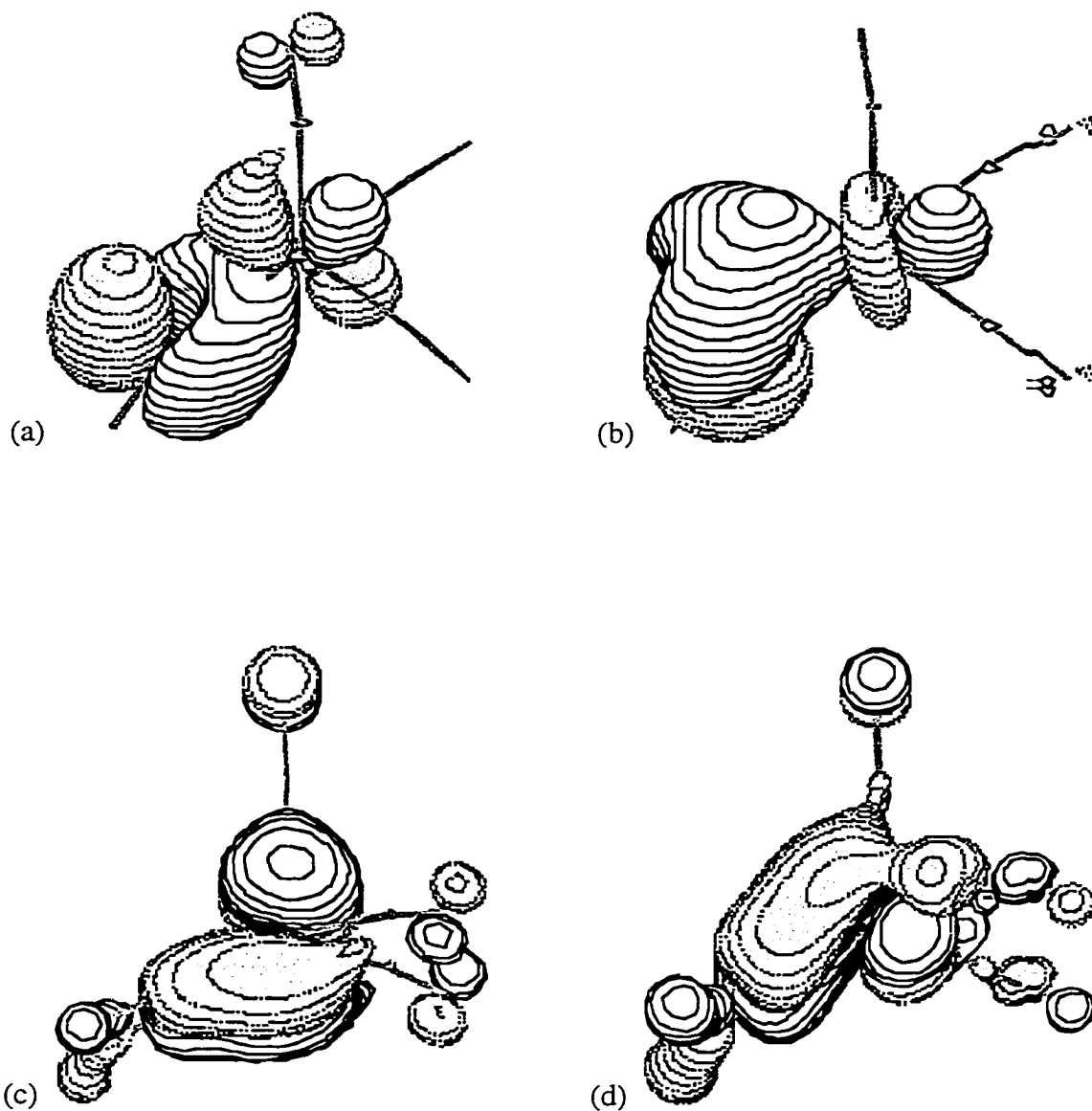


Figure 5.9: The four Dewar-Chatt-Duncanson type metal-acetylene MO interactions of the unsaturated $M(CO)_3(C_2H_2)$ dissociation product. (a) $C_2H_2 \rightarrow M \pi_{\parallel}-\sigma$ donation, (b) $C_2H_2 \rightarrow M \pi_{\perp}-\pi$ donation, (c) $C_2H_2 \leftarrow M \pi^*_{\parallel}-\pi$ backdonation, (d) $C_2H_2 \leftarrow M \pi^*_{\perp}-\delta$ backdonation.

Table 5.8: Charge Decomposition Analysis^{a, b, c} of Metal-Acetylene Bonding in $M(\text{CO})_4(\text{C}_2\text{H}_2)$ and $M(\text{CO})_3(\text{C}_2\text{H}_2)$.

	$\text{Fe}(\text{CO})_4(\text{C}_2\text{H}_2)$	$\text{Fe}(\text{CO})_3(\text{C}_2\text{H}_2)^{\text{d}}$	$\text{Ru}(\text{CO})_4(\text{C}_2\text{H}_2)$	$\text{Ru}(\text{CO})_3(\text{C}_2\text{H}_2)^{\text{d}}$
$q_{\text{di}},$ $i = \pi_{\text{H}} - \sigma_{\text{d}}$	0.25	0.19	0.17	0.11
$q_{\text{di}},$ $i = \pi_{\perp} - \pi_{\text{d}}$	0.02	0.20	0.01	0.14
$q_{\text{bi}},$ $i = \pi^*_{\text{H}} - \pi_{\text{b}}$	0.35	0.20	0.36	0.17
$q_{\text{bi}},$ $i = \pi^*_{\perp} - \delta_{\text{b}}$	0.00	0.27	0.01	0.33

^a Charge Decomposition Analysis scheme of Frenking and co-workers.³³ ^b Results shown are for the charge decomposition analysis of the BLYP/BS2 density. ^c In units of electrons. ^d The orbitals appear to be hybrids in the $M(\text{CO})_3(\text{C}_2\text{H}_2)$ systems.

$\nabla^2\rho(r)$, at the critical points of the electron density topology (i.e. points where the gradient of the electron density, $\nabla\rho(r)$, is zero) yield information regarding the bonding between the atoms in a molecule. Bader's book³⁷ provides a detailed discussion of the theory and its practical applications and shows that: (1) there exists a correlation between the value of $\rho(r)$ at the (3,-1) bond critical points (BCP) of the topology, denoted as $\rho(r_c)$, and the strength of that particular bond; (2) negative values of $\nabla^2\rho(r)$ are indicative of a build-up of electron density, while positive values indicate an area of electron depletion; (3) relatively small, positive values of $\nabla^2\rho(r)$ are typical of closed shell interactions, while values which are large and negative are typical of shared, covalent interactions.

B. Analysis of the Electron Density Topology of $M(\text{CO})_4(\text{C}_2\text{H}_2)$ and $M(\text{CO})_3(\text{C}_2\text{H}_2)$

AIM analysis was employed to locate all of the critical points (r_c) of the electron density in the saturated $M(\text{CO})_4(\text{C}_2\text{H}_2)$ and the formally unsaturated CO dissociated $M(\text{CO})_3(\text{C}_2\text{H}_2)$ complexes as well as the parent pentacarbonyls and their respective CO dissociated intermediates, at the BLYP/BS2//BLYP/BS1 level of theory. The $\rho(r_c)$ and $\nabla^2\rho(r_c)$ values were then used to gauge the changes in the electron density and the metal-ligand bonding which occur upon CO dissociation. The properties of the bond critical points are summarized in Table 5.9. The following discussion will focus on the Fe analogues, however the same discussion is applicable to the heavier Ru congeners.

In the iron carbonyl complexes, $\text{Fe}(\text{CO})_5$ and (1A_1) $\text{Fe}(\text{CO})_4$, (3,-1) bond critical points were located along each of the Fe-C and C-O connections. At each of these BCPs, the values of the Laplacian are indicative of closed-shell type interactions. The dissociation of an equatorial CO in $\text{Fe}(\text{CO})_5$ causes only minor changes in the properties (< 0.01 electron) of the electron density topology. For the alkyne-substituted complexes the electron density topology appears to be more complicated, since not only are (3,-1) BCPs located along each of the Fe-C, C-O and C-C connections, but also a (3,+1) ring critical point (RCP) was located at the centroid of the metal-acetylene cyclopropene-like ring. As in the parent carbonyls, the $\nabla^2\rho(r_c)$ values at the Fe-C and C-O BCPs are indicative of closed-shell interactions. On the other hand, $\nabla^2\rho(r_c)$ values at the C-C and C-H BCPs are negative and relatively large in magnitude and are typical of shared, covalent interactions. CO dissociation from $\text{Fe}(\text{CO})_4(\text{C}_2\text{H}_2)$ results in an increase in the value of $\rho(r_c)$ at the $\text{Fe}-\text{C}_{\text{ax}}$ BCP, while that for the $\text{Fe}-\text{C}_{\text{eq}}$ BCP remains unchanged. The changes in the values of

Table 5.9: Topological Properties at the Bond Critical Points^a of $M(\text{CO})_5$ and $M(\text{CO})_4(\text{C}_2\text{H}_2)$ and their CO dissociated products.^{b,c}

Bond	$\rho(r_c)$	$\nabla^2\rho(r_c)$	$\rho(r_c)$	$\nabla^2\rho(r_c)$
	$\text{Fe}(\text{CO})_5$		$\text{Fe}(\text{CO})_4(^1\text{A}_1)$	
Fe-C _{ax}	0.125	0.621	0.133	0.584
Fe-C _{eq}	0.132	0.567	0.137	0.589
C _{ax} -O _{ax}	0.437	0.518	0.432	0.510
C _{eq} -O _{eq}	0.433	0.503	0.430	0.510
	$\text{Fe}(\text{CO})_4(\text{C}_2\text{H}_2)$		$\text{Fe}(\text{CO})_3(\text{C}_2\text{H}_2)$	
Fe-C _{ax}	0.124	0.612	0.146	0.650
Fe-C _{eq}	0.134	0.601	0.133	0.607
Fe-C _{ac}	0.076	0.187	0.122	0.358
C _{ax} -O _{ax}	0.437	0.514	0.429	0.467
C _{eq} -O _{eq}	0.432	0.479	0.432	0.487
C _{ac} -C _{ac}	0.366	-1.108	0.341	-1.008
C _{ac} -Fe-C _{ac} ^d	0.075		0.115	
	$\text{Ru}(\text{CO})_5$		$\text{Ru}(\text{CO})_4$	
Ru-C _{ax}	0.117	0.460	0.122	0.444
Ru-C _{eq}	0.119	0.425	0.128	0.440
C _{ax} -O _{ax}	0.439	0.545	0.436	0.536
C _{eq} -O _{eq}	0.434	0.523	0.432	0.506
	$\text{Ru}(\text{CO})_4(\text{C}_2\text{H}_2)$		$\text{Ru}(\text{CO})_3(\text{C}_2\text{H}_2)$	
Ru-C _{ax}	0.118	0.459	0.150	0.452
Ru-C _{eq}	0.120	0.445	0.123	0.448
Ru-C _{ac}	0.075	0.216	0.110	0.305
C _{ax} -O _{ax}	0.439	0.540	0.427	0.463
C _{eq} -O _{eq}	0.434	0.509	0.433	0.508
C _{ac} -C _{ac}	0.364	-1.105	0.342	-1.024
C _{ac} -Ru-C _{ac} ^d	0.073		0.103	

^a Electron density topology analysis via Bader's Atoms in Molecules theory.³⁷ ^b All of the data given correspond to the topological properties of (3,-1) bond critical points unless otherwise stated. ^c In atomic units. ^d Corresponds to the topological properties of the (3,+1) ring critical point between the C_2H_2 ligand and the metal atom.

$\rho(r_c)$ at the Fe- C_{ac} and C_{ac} - C_{ac} BCPs are consistent with the structural and CDA findings of an increase in the amount of donation from the acetylene ligand to the metal: $\rho(r_c)$ at the Fe- C_{ac} BCP is increased by 0.03 electrons, while that for the C_{ac} - C_{ac} BCP of the acetylene ligand is decreased by the same amount. Even the increase in the $\rho(r_c)$ value at the ring critical point upon CO dissociation is consistent with an increased amount of bonding between the acetylene ligand and the metal. Interestingly, the AIM analysis shows not only the increased $C_2H_2 \rightarrow M$ donation upon dissociation of CO, but it also indicates that this additional electron density appears to be funneled into the bond between the metal atom and the remaining axial carbonyl. In summary, the AIM results are in full agreement with the structural data and CDA findings, and fully support the rationalization of the decrease in CO BDE values of the alkyne substituted species.

5.3.6 Dependence of the CO BDEs on the Metal Atom

One last item which deserves comment is the marked metal dependence of both the calculated CO BDEs and the experimentally measured ΔH^\ddagger values of the $M(CO)_5$ and $M(CO)_4(C_2H_2)$ systems. The different spin multiplicities of the $M(CO)_4$ ground electronic states make it somewhat difficult to probe the origins of the metal dependence of the parent carbonyls. This is not the case for the alkyne substituted complexes, as CO dissociation leads to singlet ground states for each metal of the triad. Since the calculated CO BDE values were derived from the total energy difference between the reactant and CO dissociation product complexes, the metal dependence must manifest itself as either a ground-state destabilization effect in the reactant complex or as a stabilization effect in the CO dissociation product. The CDA analysis indicates that it is the participation of the π_1 orbital of the alkyne ligand in the $\pi_1 - \pi_d$ interaction which stabilizes the formally unsaturated $M(CO)_3(C_2H_2)$ complex, thereby lowering the CO BDE. The CO BDE dependence on the metal may simply reflect a variation in the amount of $\pi_1 C_2H_2 \rightarrow M$ donation. Hence, the MO energy gap for the interaction between the occupied π_1 orbital of the C_2H_2 ligand and the corresponding unoccupied orbital of correct π symmetry of the $M(CO)_3$ metal fragment, was computed to give an indirect measure of the amount of $C_2H_2 \rightarrow M$ donation. To a first approximation, the smaller the fragment MO energy gap the stronger will be the bonding between the two fragments. Pictorial representations of the occupied π_1 orbital of the acetylene ligand and the unoccupied $M(CO)_3$ metal fragment orbital of correct π symmetry for overlap are available in Appendix C. The geometries of the two fragments were kept at their orientations in the $M(CO)_3(C_2H_2)$ complex. The metal dependence of the $\pi_1 C_2H_2 \rightarrow M$ energy gap in $M(CO)_3(C_2H_2)$, calculated at the

BLYP/BS1//BLYP/BS1 level of theory, is reported at the top of Figure 5.10. The trend in the $\pi_{\perp} \text{C}_2\text{H}_2 \rightarrow \text{M}$ energy gaps down the triad does indeed match that predicted for the CO BDE values and the experimental ΔH^{\ddagger} trends, with Fe predicted to have the smallest gap, Ru the largest and Os an intermediate value. However, upon changing the form of the density functional to B3LYP there is not only an increase in the magnitudes of the MO energy gaps for each metal, but also a significant change in the metal dependence of them. The $\pi_{\perp} \text{C}_2\text{H}_2 \rightarrow \text{M}$ energy gap for Fe is increased relative to the other two congeners, and it is predicted to be the largest of the triad, followed by Ru and Os. Changing from DFT to RHF, yet still employing the same basis set, results in a further increase in the magnitudes of the $\pi_{\perp} \text{C}_2\text{H}_2 \rightarrow \text{M}$ energy gaps for each of the metals as well as a further increase in the gap for Fe relative to that of Ru and Os. It appears that as more Hartree-Fock exchange is incorporated, in going from BLYP to B3LYP to RHF, the magnitude of the $\pi_{\perp} \text{C}_2\text{H}_2 \rightarrow \text{M}$ energy gap for each of the metals is increased and that for iron is increased relative to the heavier congeners. Hence, the metal dependence of the π_{\perp} MO energy gap varies as the method is changed. These results raise doubts regarding the utility of rationalizing chemical phenomena in terms of simple MO energy gap arguments.

5.4 Conclusions

A variety of non-local density functional theory calculations predict a decrease of the first carbonyl dissociation energy of the alkyne-substituted complexes $\text{M}(\text{CO})_4(\text{C}_2\text{H}_2)$ of the iron triad with respect to the parent pentacarbonyl complexes, in full agreement with the results of a recent experimental solution kinetics study. The BLYP optimized geometries of the parent complexes, $\text{M}(\text{CO})_5$ and $\text{M}(\text{CO})_4(\text{C}_2\text{H}_2)$, and the CO dissociated products show good agreement with the available experimental data and with the results of previous theoretical studies. Carbonyl dissociation from $\text{Fe}(\text{CO})_5$ is predicted to be somewhat complicated by the triplet ground state of the dissociation product, however the CO dissociation products of the Ru and Os pentacarbonyls, as well as that of all of the alkyne substituted complexes, are predicted to have singlet ground states.

With the CDA partitioning scheme, it was shown that the lower CO BDEs of the alkyne-substituted species may be attributed to a stabilization of the formally unsaturated $\text{M}(\text{CO})_3(\text{C}_2\text{H}_2)$ via an increased donation from the acetylene ligand to the metal. In the saturated $\text{M}(\text{CO})_4(\text{C}_2\text{H}_2)$ reactant complex the acetylene ligand is a two-electron donor, with only the π_{\perp} orbital donating to the metal; on the other hand, in the CO dissociated

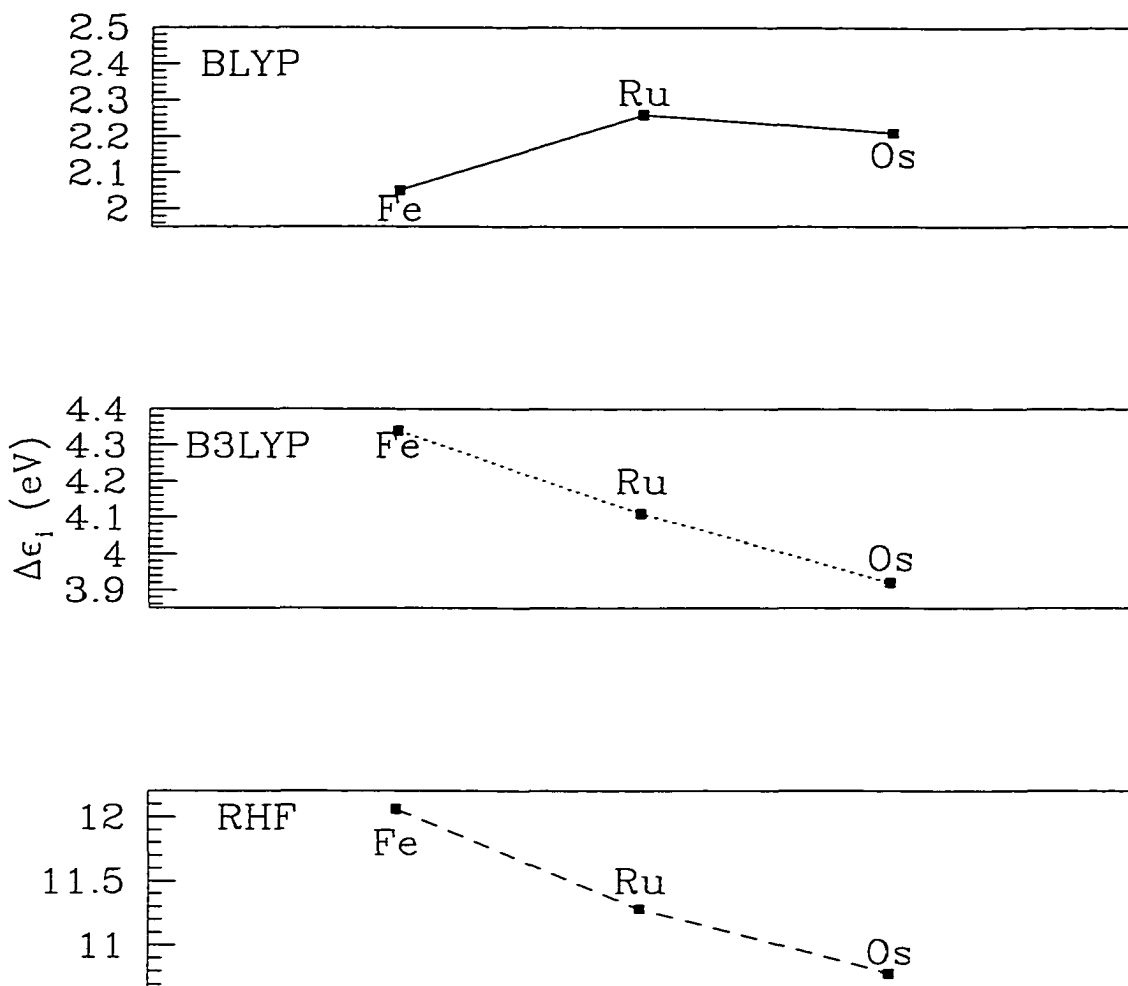


Figure 5.10: The metal dependence of the $\text{C}_2\text{H}_2 \rightarrow \text{M } \pi_1\text{-}\pi_4$ fragment MO energy gap in $\text{M}(\text{CO})_3(\text{C}_2\text{H}_2)$.

product both π orbitals of acetylene donate electron density to the metal, thereby making acetylene formally a four-electron donor and stabilizing the CO dissociated intermediate. The results of the AIM topological analysis of the electron density of the alkyne-complexes are in full agreement with the CDA findings. The values of $\rho(r_c)$ at the M-C_{ac} bond critical points increase while that at the C_{ac}-C_{ac} bond critical point decrease upon removal of an axial carbonyl ligand from the Fe and Ru analogues of M(CO)₄(C₂H₂). Even the increase of $\rho(r_c)$ at the M-acetylene ring critical point is consistent with an increase in the amount of bonding between the acetylene ligand and the metal. Furthermore, the structural changes predicted to occur upon CO dissociation were also in accord with the rationale of an increased donation from the alkyne.

The DFT calculations of the first CO BDEs consistently predict an Fe > Os > Ru metal dependence for the parent pentacarbonyls, and the reverse trend, Fe < Os < Ru, for the alkyne-substituted complexes, in accord with the trends observed experimentally. The different ground states of the M(CO)₄ dissociation products complicated analysis of the metal dependence in the parent pentacarbonyls. Simple MO energy gaps for the critical C₂H₂ → M π - π_d interaction, accredited with stabilization of the unsaturated M(CO)₃(C₂H₂) dissociation product, were computed for each metal of the triad. A correlation was found between the π_1 MO energy gaps and the computed CO BDE values when the BLYP density functional was employed. Iron was found to have the smallest MO energy gap, followed by Os and Ru. Upon increasing the amount of HF exchange from BLYP to B3LYP to RHF, the π_1 MO energy gap for Fe increased with respect to Ru and Os, such that it became the largest of the series, in disagreement with the trend predicted for the CO BDEs.

5.5 References

1. Schutzenberger, P. *Compte Rendus* **1870**, 70, 1134.
2. Mond, L.; Langer, C.; Quincke, F. *J. Chem. Soc.* **1890**, 749.
3. Abel, E. *J. Organomet. Chem.* **1990**, 383, 11.
4. Herrmann, W. A. *J. Organomet. Chem.* **1990**, 383, 21.
5. Werner, H. *Angew. Chem. Int. Ed. Engl.* **1990**, 29, 1077.
6. Collman, J. P.; Hegedus, L. S.; Norton, J. R.; Finke, R. G. *Principles and Applications of Organotransition Metal Chemistry*; University Science Books: Mill Valley, CA, 1987.
7. Atwood, J. D.; Brown, T. L. *J. Am. Chem. Soc.* **1976**, 98, 3160.

8. Cohen, M. A.; Brown, T. L. *Inorg. Chem.* **1976**, *15*, 1417.
9. Cotton, F. A.; Darensbourg, D. J.; Koltzhammer, B. W. S.; Kudaroski, R. *Inorg. Chem.* **1982**, *21*, 1656.
10. Darensbourg, D. J.; Klausmeyer, K. K.; Reibenspies, J. H. *Inorg. Chem.* **1995**, *34*, 4933.
11. Darensbourg, D. J.; Klausmeyer, K. K.; Reibenspies, J. H. *Inorg. Chem.* **1996**, *35*, 1529.
12. Darensbourg, D. J.; Klausmeyer, K. K.; Reibenspies, J. H. *Inorg. Chem.* **1996**, *35*, 1535.
13. Lichtenberger, D. L.; Brown, T. L. *J. Am. Chem. Soc.* **1978**, *100*, 366.
14. Davy, R. D.; Hall, M. B. *Inorg. Chem.* **1989**, *28*, 3524.
15. Caulton, K. G. *New. J. Chem.* **1994**, *18*, 25.
16. Pearson, J.; Cooke, J.; Takats, J.; Jordon, R. B. *J. Am. Chem. Soc.* **1998**, *120*, 1434.
17. Mao, T.; Zhang, Z.; Washington, J.; Takats, J.; Jordon, R. B. *Organometallics* **1999**, *18*, 2331.
18. Marinelli, G.; Streib, W. E.; Huffman, J. C.; Caulton, K. G.; Gagne, M. R.; Takats, J.; Dartiguenave, M.; Chardon, C.; Jackson, S. A.; Eisenstein, O. *Polyhedron* **1990**, *9*, 1867.
19. Crabtree, R. H. *The Organometallic Chemistry of the Transition Metals*; John Wiley and Sons: New York, 1988.
20. Templeton, J. L.; Ward, B. C. *J. Am. Chem. Soc.* **1980**, *102*, 3288.
21. Veillard, A. *Chem. Rev.* **1991**, *91*, 743.
22. Mitchell, S. A.; Blitz, M. A.; Fournier, R. *Can. J. Chem.* **1994**, *72*, 587.
23. Sodupe, M.; Bauschlicher, C. W. J. *J. Phys. Chem.* **1991**, *95*, 8640.
24. Siegbahn, P. E. M. *Theor. Chim. Acta* **1994**, *87*, 277.
25. Sellers, H. J. *J. Phys. Chem.* **1990**, *94*, 8329.
26. Guerts, P.; Burgers, H.; van der Avoird, A. *Chem. Phys.* **1981**, *54*, 397.
27. Wakatsuki, Y.; Koga, N.; Yamazaki, H.; Morokuma, K. *J. Am. Chem. Soc.* **1994**, *116*, 8105.
28. Wakatsuki, Y.; Koga, N.; Werner, H.; Morokuma, K. *J. Am. Chem. Soc.* **1997**, *119*, 360.
29. Stegmann, R.; Neuhaus, A.; Frenking, G. *J. Am. Chem. Soc.* **1993**, *115*, 11930.

30. Pidun, U.; Frenking, G. *J. Organomet. Chem.* **1996**, *525*, 269.
31. Ehlers, A. W.; Dapprich, S.; Vyboishchikov, S. F.; Frenking, G. *Organometallics* **1996**, *15*, 105.
32. Frenking, G.; Pidun, U. *J. Chem. Soc., Dalton Trans.* **1997**, 1653.
33. Dapprich, S.; Frenking, G. *J. Phys. Chem.* **1995**, *99*, 9352.
34. Bader, R. F. W.; Tal, Y.; Anderson, S. G.; Nguyen-Dang, T. T. *Isr. J. Chem.* **1980**, *19*, 8.
35. Bader, R. F. W.; Nguyen-Dang, T. T. *Adv. Quantum Chem.* **1981**, *14*, 63.
36. Bader, R. F. W.; Nguyen-Dang, T. T.; Tal, Y. *Rep. Prog. Phys.* **1981**, *44*, 893.
37. Bader, R. F. W. *Atoms in Molecules: A Quantum Theory*; Clarendon Press: Oxford, U. K., 1990.
38. Stevens, W. J.; Basch, H.; Krauss, M. *J. Chem. Phys.* **1984**, *81*, 6026.
39. Krauss, M.; Stevens, W. J.; Basch, H.; Jasien, P. *Can. J. Chem.* **1992**, *70*, 612.
40. Cundari, T. R.; Stevens, W. J. *J. Chem. Phys.* **1993**, *98*, 5555.
41. Huzinaga, S.; Andzelm, J.; Klobukowski, M.; Radzio-Andzelm, E.; Sakai, Y.; Tatewaki, H. *Gaussian Basis Sets for Molecular Calculations*; Elsevier: Amsterdam, 1984.
42. Ditchfield, R.; Hehre, W. J.; Pople, J. A. *J. Chem. Phys.* **1971**, *54*, 724.
43. Godbout, N.; Salahub, D. R.; Andzelm, J.; Wimmer, E. *Can. J. Chem.* **1992**, *70*, 560.
44. Frisch, M. J.; Trucks, G. W.; Schlegel, H. B.; Gill, P. M. W.; Johnson, B. G.; Robb, M. A.; Cheeseman, J. R.; Keith, T.; Petersson, G. A.; Montgomery, J. A.; Raghavachari, K.; Al-Laham, M. A.; Zakrzewski, V. G.; Ortiz, J. V.; Foresman, J. B.; Cioslowski, J.; Stefanov, B. B.; Nanayakkara, A.; Challacombe, M.; Peng, C. Y.; Ayala, P. Y.; Chen, W.; Wong, M. W.; Andres, J. L.; Replogle, E. S.; Gomperts, R.; Martin, R. L.; Fox, D. J.; Binkley, J. S.; DeFrees, D. J.; Baker, J.; Stewart, J. J. P.; Head-Gordon, M.; Gonzalez, C.; Pople, J. A. *Gaussian 94*; D3 ed.; Gaussian, Inc.: Pittsburgh, PA, 1995.
45. Becke, A. *Phys. Rev. A* **1988**, *38*, 3098.
46. Lee, C.; Yang, W.; Parr, R. G. *Phys. Rev. B* **1988**, *37*, 785.
47. Perdew, J. P. *Phys. Rev. B* **1986**, *33*, 8822.
48. Becke, A. *J. Chem. Phys.* **1993**, *98*, 5648.
49. Perdew, J. P.; Wang, Y. *Phys. Rev. B* **1992**, *45*, 13244.

50. Dapprich, S.; Frenking, G. *CDA*; 2.1 ed.; University of Marburg: Marburg, Germany, 1995.
51. Frisch, M. J.; Trucks, G. W.; Schlegel, H. B.; Gill, P. M. W.; Johnson, B. G.; Wong, M. W.; Foresman, J. B.; Robb, M. A.; Head-Gordon, M.; Replogle, E. S.; Gomperts, R.; Andres, J. L.; Raghavachari, K.; Binkley, J. S.; Gonzalez, C.; Martin, R. L.; Fox, D. J.; DeFrees, D. J.; Baker, J.; Stewart, J. J. P.; Pople, J. A. *Gaussian 92/DFT*; F2 ed.; Gaussian, Inc.: Pittsburgh, PA, 1993.
52. Radius, U.; Bickelhaupt, F. M.; Ehlers, A. W.; Goldberg, N.; Hoffmann, R. *Inorg. Chem.* **1998**, *37*, 1080.
53. Beagley, B.; Schmidling, D. G. *J. Mol. Struct.* **1974**, *22*, 466.
54. Braga, D.; Grepioni, F.; Orpen, A. G. *Organometallics* **1993**, *12*, 1481.
55. Huang, J.; Hedberg, K.; Davis, H. B.; Pomeroy, R. K. *Inorg. Chem.* **1990**, *29*, 3923.
56. Huang, J.; Hedberg, K.; Pomeroy, R. K. *Organometallics* **1988**, *7*, 2049.
57. Li, J.; Schreckenbach, G.; Ziegler, T. *J. Am. Chem. Soc.* **1995**, *117*, 486.
58. Delley, B.; Wrinn, M.; Luthi, H. P. *J. Chem. Phys.* **1994**, *100*, 5785.
59. Ehlers, A. W.; Frenking, G. *Organometallics* **1995**, *14*, 423.
60. Poliakoff, M.; Turner, J. J. *J. Chem. Soc., Dalton Trans.* **1974**, 2276.
61. Poliakoff, M.; Weitz, E. *Acc. Chem. Res.* **1987**, *20*, 408.
62. Barton, T. J.; Grinter, R.; Thomson, A. J.; Davies, B.; PoliakoFF, M. *J. Chem. Soc., Chem. Commun.* **1977**, 841.
63. Barnes, L. A.; Rosi, M.; Bauschlicher, C. W., Jr. *J. Chem. Phys.* **1991**, *94*, 2031.
64. Daniel, C.; Benard, M.; Dedieu, A.; Wiest, R.; Veillard, A. *J. Phys. Chem.* **1984**, *88*, 4805.
65. Bogdan, P. L.; Weitz, E. *J. Am. Chem. Soc.* **1989**, *111*, 3163.
66. Bogdan, P. L.; Weitz, E. *J. Am. Chem. Soc.* **1990**, *112*, 639.
67. Huq, R. A.; Poe, A. J.; Chawla, S. *Inorg. Chim. Acta* **1980**, 3-8, 121.
68. Shen, J.-K.; Gao, Y.-C.; Shi, Q.-Z.; Basolo, F. *Inorg. Chem.* **1989**, *28*, 4304.
69. Kostyk, E.; Welsh, H. L. *Can. J. Phys.* **1980**, *58*, 912.
70. Cooke, J. Ph. D Thesis, University of Alberta, 1998.
71. Espuelas, J.; Esteruelas, M. A.; Lahoz, F. J.; Lopez, A. M.; Oro, L. A.; Valero, C. *J. Organomet. Chem.* **1994**, *468*, 223.
72. Lewis, K. E.; Golden, D. M.; Smith, G. P. *J. Am. Chem. Soc.* **1984**, *106*, 3905.

73. Engelking, P. C.; Lineberger, W. C. *J. Am. Chem. Soc.* **1979**, *101*, 5569.
74. Cotton, F. A.; Wilkinson, G. *Advanced Inorganic Chemistry*; Fifth ed.; John Wiley and Sons: New York, 1988.

Chapter 6

Final Conclusions

The chapters presented in this thesis range from a benchmarking study to the development of new MCP valence basis sets, to two applied organometallic chemistry studies. Although each chapter is a separate entity, independent of the remaining chapters, there is a common theme of critical evaluation of the computational methods which permeates the entire thesis. In all of the chapters of the thesis, a multitude of methods were employed and compared against one another. One must always thoroughly test different computational chemistry methodologies in order to determine which will work best for a particular system of interest. Researchers must be first confident in the numerical results before any confidence can be placed in the conclusions and rationalizations which are drawn from them.

A number of important conclusions can be drawn from the work presented here. The model core potential (MCP) formalism was found to be a very effective approach for modeling simple transition metal complexes, provided that the penultimate ($n-1$) p atomic shell of the metal atom is included in the valence space and treated explicitly in the calculation. The results presented do not show any significant advantage in using the model core potential formalism over the effective core potentials for computing molecular structures, despite the retention of some or all of the proper nodal structure for the valence atomic shells. More computationally efficient MCP valence basis sets, incorporating L-shell structure were successfully derived for the elements of Groups 13 to 18. Use of the new MCP L-shell basis sets in atomic and molecular test calculations showed them to yield results which were not significantly different from the conventional MCP basis sets. Although density functional theory (DFT) is the current method of choice for modeling small to medium sized transition metal complexes^{1,2}, the results of these DFT calculations are strictly tied to the choice of the approximate density functional, as illustrated in the two applied studies presented here. For example, the carbonyl bond dissociation energy for $\text{Os}(\text{CO})_5$ computed at the DFT level was found to be between 29 and 38 kcal/mol, depending on the functional employed. It is actually quite astounding how much molecular properties computed with density functionals can vary, and certainly enforces the need to use a variety of them in order to gain some confidence in the values obtained. The PM3(tm) semiempirical method³ proved to be a useful economical alternative to DFT for predicting molecular structures of transition metal complexes. However, its utility in computing accurate reaction barriers may be suspect. As found by Børve and co-workers⁴, a much more suitable approach to computing reaction energy barriers involves computing the energy of the species using the more accurate DFT method, at the respective PM3(tm) geometries. This hybrid DFT//PM3(tm) approach takes advantage of the accuracy of the

PM3(tm) geometries while employing the more rigorous DFT method for the less expensive single point energy calculations.

From a personal point of view one of the most interesting aspects of the current research was the investigation into the nature of the acetylene-metal interaction in the saturated and unsaturated alkyne complexes. The transformation of numbers into useful chemical concepts which can be understood by a broad range of chemists of varying backgrounds, although not an easy proposition, is where I believe computational chemistry makes its most valued contribution to the chemistry community.

6.1 Further Work

The MCP benchmarking study presented here is still in its infancy and much more work is needed to be fully confident in the performance of the MCP formalism for modeling transition metal compounds. The current study focused on a number of small molecules, some of which are commonly found as ligands in metal complexes, as well as the small MX_4 halogen complexes of the Group 4 metals (Ti, Zr, and Hf). A much larger study encompassing a wider array of metal complexes, containing metals from all of the transition series, with a wide assortment of ligands, coordination geometries, and oxidation states would be extremely useful. A number of previous studies⁵⁻⁹ have tested the reliability of the MCP formalism in studies involving relatively small transition metal complexes, and it would be interesting to extend the studies to larger systems. In order to carry out such a detailed study, analytical gradients and Hessians for the MCPs must be implemented into the GAMESS program^{10,11}, since optimization of geometric structures using the non-gradient Powell method¹² would be too cumbersome. Along with calculations carried out at the Hartree-Fock and post-Hartree-Fock level, calculations should also be carried out at the DFT level, employing a wide assortment of functionals, to gauge the performance of the MCPs in DFT calculations. In addition, it would be very interesting to see how well the newly developed MCP L-shell basis sets performed in these calculations, alongside the conventional MCP basis sets. One of the main problems associated with a study like this is the small amount of experimental data available for comparison purposes.

Another area which would be interesting to investigate further, which arose from the carbonyl scrambling work, would be a comparative study of reaction energy barriers computed using the PM3(tm)//PM3(tm), DFT//PM3(tm), and DFT//DFT approaches. Given the sparse number of studies which have been devoted to evaluating the PM3(tm)

semiempirical method^{4,13-15}, a systematic study of this nature would be beneficial in understanding the strengths and shortcomings of the method.

The results of Chapter 5 pertain to only the first step of the phosphine substitution reactions of the alkyne complexes of the Group 8 metals, the dissociative loss of CO from $M(\text{CO})_4(\text{C}_2\text{H}_2)$. However, kinetics data are available for the remaining steps of the substitution reactions,^{16,17} the successive dissociative loss of CO and the association of a phosphine ligand. Hence, the next logical step would be to continue onward in an effort to map out the entire reaction, predicting which sites are preferred for attack by the incoming phosphine ligands, and whether they are the same sites vacated by the exiting carbonyl or whether some sort of rearrangement must occur. Another interesting aspect for investigation would be to see how the singlet-triplet energy gap of the unsaturated $\text{Fe}(\text{CO})_4$ species is altered when one of the carbonyl ligands is replaced with a phosphine, $\text{Fe}(\text{CO})_3(\text{PH}_3)$.

6.2 Final Comments

The French chemist and physicist Joseph Louis Gay-Lussac prophesized in 1808 that “we are perhaps not far removed from the time when we shall be able to submit the bulk of chemical phenomena to calculation”.¹⁸ Close to two hundred years later, Gay-Lussac’s statements are more true now than ever before. The field of computational chemistry has witnessed a tremendous growth over the last decade or so, but unfortunately it is still not possible to submit all chemical phenomena to computational modeling. However, with the continued advances in computer technology and computational chemistry methodologies, especially for studies of large chemical systems, we are hopefully very near the time when computer modeling will be of assistance to chemists from all fields of chemistry.

6.3 References

1. Ziegler, T. *Chem. Rev.* **1991**, *91*, 651.
2. Ziegler, T. *Can. J. Chem.* **1995**, *73*, 743.
3. *Spartan*; 4.0.3 ed.; Wavefunction, Inc.: Irvine, CA, 1995.
4. Børve, K. J.; Jensen, V. R.; Karlsen, T.; Stovng, J. A.; Swang, O. *J. Mol. Model.* **1997**, *3*, 193.

5. Sakai, Y.; Miyoshi, E. *J. Chem. Phys.* **1987**, *87*, 2885.
6. Miyoshi, E.; Sakai, Y. *J. Comput. Chem.* **1988**, *9*, 719.
7. Miyoshi, E.; Sakai, Y.; Murakami, A.; Iwaki, H.; Terashima, H.; Shoda, T.; Kawaguchi, T. *J. Chem. Phys.* **1988**, *89*, 4193.
8. Jonas, V.; Frenking, G.; Reetz, M. *J. Comput. Chem.* **1992**, *13*, 919.
9. Papai, I.; Goursot, A.; St-Amant, A.; Salahub, D. R. *Theoret. Chim. Acta* **1992**, *84*, 217.
10. Schmidt, M. W.; Baldrige, K. K.; Boaltz, J. A.; Jensen, J. H.; Koseki, S.; Gordon, M. S.; Nguyen, K. A.; Windus, T. L.; Elbert, S. T. *QCPE Bull.* **1990**, *10*, 52.
11. Schmidt, M. W.; Baldrige, K. K.; Boaltz, J. A.; Elbert, S. T.; Gordon, M. S.; Jensen, J. H.; Koseki, S.; Matsunaga, N.; Nguyen, K. A.; Su, S.; Windus, T. L.; Dupuis, M. *J. Comput. Chem.* **1993**, *14*, 1347.
12. Powell, M. J. D. *Comput. J.* **1964**, *7*, 155.
13. Adam, K. R.; Atkinson, I. M.; Lindoy, L. F. *J. Mol. Struct.* **1996**, *384*, 183.
14. Decker, S. A.; Klobukowski, M. *Can. J. Chem.* **1999**, *77*, 65.
15. Cundari, T. R.; Deng, J. *J. Chem. Inf. Comp. Sci.* **1999**, *39*, 376.
16. Pearson, J.; Cooke, J.; Takats, J.; Jordon, R. B. *J. Am. Chem. Soc.* **1998**, *120*, 1434.
17. Mao, T.; Zhang, Z.; Washington, J.; Takats, J.; Jordon, R. B. *Organometallics* **1999**, *18*, 2331.
18. Gay-Lussac, J. L. *Memoires de la Societe d'Arcueil* **1808**, *2*, 207.

Appendix A

Supplementary Material for Chapter 2: Tabulations of Valence Electron Correlation Energies and Molecular Geometries

Table A.1: Valence Electron Correlation Energies (E_{corr} , in E_h) of the Homonuclear Diatomic Molecules.

Molecule	Method	$E_{\text{corr}}(\text{ECP})$	$E_{\text{corr}}(\text{MCP})$	ΔE_{corr}^a
N ₂	MP2	0.3114	0.2960	0.0154
	CISD	0.2857	0.2744	0.0112
P ₂	MP2	0.2287	0.2242	0.0045
	CISD	0.2187	0.2159	0.0028
As ₂	MP2	0.2209	0.2109	0.0100
	CISD	0.2046	0.1952	0.0093
Sb ₂	MP2	0.1988	0.2037	-0.0049
	CISD	0.1826	0.1796	0.0030
F ₂	MP2	0.3632	0.3488	0.0144
	CISD	0.3490	0.3359	0.0131
Cl ₂	MP2	0.2627	0.2735	-0.0107
	CISD	0.2632	0.2706	-0.0073
Br ₂	MP2	0.2329	0.2225	0.0104
	CISD	0.2325	0.2239	0.0086
I ₂	MP2	0.2027	0.1865	0.0161
	CISD	0.2014	0.1883	0.0131

^a Value corresponds to the difference in correlation energies computed from:

$$\Delta E_{\text{corr}} = E_{\text{corr}}(\text{ECP}) - E_{\text{corr}}(\text{MCP}).$$

Table A.2: Valence Electron Correlation Energies (E_{corr} , in E_h) of the Heteronuclear Diatomic Molecules.

Molecule	Method	$E_{\text{corr}}(\text{ECP})$	$E_{\text{corr}}(\text{MCP})$	ΔE_{corr}^a
CO	MP2	0.2791	0.2683	0.0108
	CISD	0.2681	0.2579	0.0101
CS	MP2	0.2389	0.2332	0.0057
	CISD	0.2351	0.2303	0.0048
CSe	MP2	0.2343	0.2249	0.0094
	CISD	0.2270	0.2201	0.0070
CTe	MP2	0.2338	0.2226	0.0112
	CISD	0.2220	0.2126	0.0094
SiO	MP2	0.2663	0.2604	0.0059
	CISD	0.2494	0.2438	0.0056
SiS	MP2	0.2003	0.1981	0.0022
	CISD	0.2027	0.2011	0.0015
SiSe	MP2	0.1900	0.1842	0.0058
	CISD	0.1914	0.1872	0.0042
SiTe	MP2	0.1825	0.1746	0.0079
	CISD	0.1822	0.1757	0.0064
GeO	MP2	0.2745	0.2580	0.0165
	CISD	0.2506	0.2393	0.0113
GeS	MP2	0.1991	0.1944	0.0047
	CISD	0.1992	0.1962	0.0030
GeSe	MP2	0.1877	0.1803	0.0074
	CISD	0.1871	0.1820	0.0051
GeTe	MP2	0.1789	0.1688	0.0101
	CISD	0.1771	0.1695	0.0075
SnO	MP2	0.2809	0.2774	0.0035
	CISD	0.2493	0.2443	0.0050
SnS	MP2	0.1932	0.1902	0.0030
	CISD	0.1921	0.1891	0.0030
SnSe	MP2	0.1802	0.1741	0.0061
	CISD	0.1792	0.1736	0.0056

SnTe	MP2	0.1694	0.1603	0.0091
	CISD	0.1679	0.1597	0.0082
ClF	MP2	0.3095	0.3082	0.0012
	CISD	0.3018	0.2993	0.0025
BrF	MP2	0.2954	0.2842	0.0112
	CISD	0.2865	0.2763	0.0102
IF	MP2	0.2797	0.2673	0.0124
	CISD	0.2699	0.2586	0.0113
BrCl	MP2	0.2478	0.2481	-0.0003
	CISD	0.2478	0.2474	0.0005
ICl	MP2	0.2321	0.2299	0.0022
	CISD	0.2318	0.2295	0.0023
IBr	MP2	0.2175	0.2042	0.0134
	CISD	0.2167	0.2059	0.0108

^a Value corresponds to the difference in correlation energies computed from:
 $\Delta E_{corr} = E_{corr}(ECP) - E_{corr}(MCP)$.

Table A.3: Summary of the Ti-X distances (in Å) and total energies (in a.u.) of the TiX₄ complexes.

Basis Set	RHF		MP2	
	R _e	E	R _e	E
TiF₄				
MCP-SPD				
DZ	1.730	-134.30292	1.742	-135.29458
DZ1f	1.722	-134.32533	1.726	-135.37486
DZ1p	1.734	-134.31084	1.749	-135.32208
DZ1p1f	1.725	-134.33219	1.732	-135.39958
TZ	1.714	-134.37914	1.724	-135.43080
TZ1f	1.704	-134.39648	1.706	-135.50974
TZ1p	1.717	-134.38561	1.730	-135.45603
TZ1p1f	1.707	-134.40265	1.711	-135.53345
ECP1-SPD				
TZ	1.751	-153.17082	1.769	-154.22500
TZ1f	1.744	-153.18150	1.757	-154.30843
ECP2-SPD				
DZ	1.735	-455.59890	1.757	-456.63239
DZ1f	1.727	-455.61270	1.742	-456.71245
TZ	1.728	-455.60986	1.746	-456.68975
TZ1f	1.720	-455.62418	1.729	-456.78362
Expt.				
	1.754		1.754	
TiCl₄				
MCP-SPD				
DZ	2.171	-97.51539	2.168	-98.39732
DZ1f	2.170	-97.52925	2.155	-98.47411
DZ1p	2.178	-97.52081	2.177	-98.41526
DZ1p1f	2.176	-97.53398	2.162	-98.49070
TZ	2.155	-97.57470	2.149	-98.51926
TZ1f	2.152	-97.58260	2.135	-98.59483
TZ1p	2.160	-97.57913	2.155	-98.53594
TZ1p1f	2.157	-97.58687	2.140	-98.61083
ECP1-SPD				
TZ	2.186	-116.46936	2.181	-117.36527
TZ1f	2.184	-116.47338	2.171	-117.44864
ECP2-SPD				
DZ	2.158	-116.61547	2.166	-117.43368
DZ1f	2.154	-116.62154	2.152	-117.51191
TZ	2.154	-116.61927	2.158	-117.48439
TZ1f	2.150	-116.62563	2.141	-117.57544
Expt.				
	2.170		2.170	

TiBr4				
MCP-SPD				
DZ	2.327	-90.53677	2.325	-91.33103
DZ1f	2.327	-90.54922	2.314	-91.40759
DZ1p	2.339	-90.54472	2.336	-91.35312
DZ1plf	2.337	-90.55582	2.321	-91.42761
TZ	2.313	-90.58997	2.305	-91.44739
TZ1f	2.311	-90.59659	2.293	-91.52315
TZ1p	2.321	-90.59600	2.313	-91.46765
TZ1plf	2.318	-90.60231	2.299	-91.54245
ECP1-SPD				
TZ	2.337	-110.29115	2.328	-111.14418
TZ1f	2.335	-110.29407	2.317	-111.22761
ECP2-SPD				
DZ	2.323	-109.46614	2.334	-110.25117
DZ1f	2.320	-109.47059	2.321	-110.32848
TZ	2.320	-109.46861	2.328	-110.30003
TZ1f	2.317	-109.47326	2.312	-110.38967
		Expt.		
	2.339		2.339	
TiI4				
MCP-SPD				
DZ	2.530	-83.40482	2.537	-84.15396
DZ1f	2.533	-83.41618	2.526	-84.23069
DZ1p	2.552	-83.42108	2.551	-84.18055
DZ1plf	2.550	-83.42943	2.535	-84.25359
TZ	2.517	-83.45122	2.513	-84.26376
TZ1f	2.517	-83.45668	2.502	-84.34026
TZ1p	2.533	-83.46316	2.524	-84.28738
TZ1plf	2.532	-83.46810	2.509	-84.36220
ECP1-SPD				
TZ	2.568	-102.53812	2.554	-103.35841
TZ1f	2.567	-102.54024	2.542	-103.44219
ECP2-SPD				
DZ	2.534	-102.32651	2.548	-103.07795
DZ1f	2.532	-102.32980	2.534	-103.15527
TZ	2.533	-102.32813	2.546	-103.12615
TZ1f	2.532	-102.33154	2.529	-103.21541
		Expt.		
	2.546		2.546	

Table A.4: Summary of the Zr-X distances (in Å) and total energies (in a.u.) of the ZrX₄ complexes.

Basis Set	RHF		MP2	
	R _e	E	R _e	E
ZrF₄				
MCP-SPD				
DZ	1.932	-127.06656	1.935	-127.97058
DZ1f	1.907	-127.10142	1.903	-128.05668
DZ1p	1.936	-127.07558	1.941	-127.99511
DZ1p1f	1.910	-127.10833	1.907	-128.07643
TZ	1.913	-127.11435	1.920	-128.07285
TZ1f	1.889	-127.14672	1.886	-128.16095
TZ1p	1.915	-127.12075	1.925	-128.09327
TZ1p1f	1.891	-127.15214	1.890	-128.17794
ECP1-SPD				
TZ	1.917	-142.17659	1.931	-143.13251
TZ1f	1.895	-142.20352	1.902	-143.22381
ECP2-SPD				
DZ	1.918	-444.21298	1.929	-445.16311
DZ1f	1.897	-444.24382	1.901	-445.25906
DZ'	1.928	-444.23198	1.935	-445.20332
DZ'1f	1.921	-444.23677	1.928	-445.21363
TZ	1.908	-444.22232	1.919	-445.22097
TZ1f	1.889	-444.25294	1.891	-445.33206
TZ'	1.921	-444.23751	1.934	-445.26268
TZ'1f	1.901	-444.26168	1.906	-445.35553
Expt.				
	1.90		1.90	
ZrCl₄				
MCP-SPD				
DZ	2.356	-90.31077	2.344	-91.07897
DZ1f	2.347	-90.33125	2.319	-91.15768
DZ1p	2.363	-90.31789	2.352	-91.09756
DZ1p1f	2.352	-90.33705	2.325	-91.17377
TZ	2.349	-90.35014	2.338	-91.17679
TZ1f	2.338	-90.36764	2.312	-91.25661
TZ1p	2.354	-90.35548	2.343	-91.19325
TZ1p1f	2.342	-90.37224	2.316	-91.27136
ECP1-SPD				
TZ	2.353	-105.48785	2.342	-106.26582
TZ1f	2.344	-105.49950	2.320	-106.35052

ECP2-SPD				
DZ	2.348	-105.25477	2.339	-105.96925
DZ1f	2.334	-105.27071	2.313	-106.05875
DZ'	2.359	-105.27504	2.344	-106.01482
DZ' 1f	2.347	-105.28619	2.318	-106.09239
TZ	2.344	-105.25768	2.331	-106.02277
TZ1f	2.330	-105.27386	2.302	-106.12884
TZ'	2.357	-105.27781	2.344	-106.07627
TZ' 1f	2.345	-105.28903	2.319	-106.16479
		Expt.		
	2.32		2.32	
ZrBr4				
MCP-SPD				
DZ	2.505	-83.34098	2.491	-84.01171
DZ1f	2.500	-83.35831	2.471	-84.08884
DZ1p	2.515	-83.34898	2.500	-84.03315
DZ1p1f	2.507	-83.36465	2.477	-84.10741
TZ	2.502	-83.37749	2.488	-84.10753
TZ1f	2.496	-83.39185	2.465	-84.18581
TZ1p	2.508	-83.38314	2.493	-84.12633
TZ1p1f	2.501	-83.39659	2.469	-84.20272
ECP1-SPD				
TZ	2.502	-99.31412	2.488	-100.03918
TZ1f	2.495	-99.32240	2.466	-100.12198
ECP2-SPD				
DZ	2.512	-98.11261	2.500	-98.78110
DZ1f	2.501	-98.12494	2.474	-98.86875
DZ'	2.522	-98.13225	2.502	-98.82667
DZ' 1f	2.513	-98.14060	2.479	-98.90302
TZ	2.507	-98.11485	2.493	-98.83298
TZ1f	2.497	-98.12743	2.465	-98.93733
TZ'	2.521	-98.13482	2.502	-98.88770
TZ' 1f	2.511	-98.14328	2.478	-98.97566
		Expt.		
	2.465		2.465	

ZrI4				
MCP-SPD				
DZ	2.702	-76.21719	2.692	-76.83304
DZ1f	2.703	-76.23192	2.675	-76.90902
DZ1p	2.718	-76.23046	2.701	-76.85597
DZ1p1f	2.714	-76.24178	2.680	-76.92713
TZ	2.702	-76.25112	2.687	-76.92427
TZ1f	2.701	-76.26252	2.668	-77.00147
TZ1p	2.713	-76.25903	2.693	-76.94215
TZ1p1f	2.707	-76.26872	2.670	-77.01650
ECP1-SPD				
TZ	2.729	-91.56775	2.707	-92.24718
TZ1f	2.723	-91.57336	2.686	-92.32860
ECP2-SPD				
DZ	2.723	-90.98025	2.707	-91.60103
DZ1f	2.715	-90.98937	2.684	-91.68661
DZ'	2.732	-90.99877	2.705	-91.64542
DZ'1f	2.725	-91.00450	2.683	-91.72036
TZ	2.720	-90.98192	2.702	-91.65149
TZ1f	2.713	-90.99123	2.676	-91.75348
TZ'	2.730	-91.00098	2.705	-91.70559
TZ'1f	2.723	-91.00681	2.682	-91.79240
Expt.				
	2.660		2.660	

Table A.5: Summary of the Hf-X distances (in Å) and total energies (in a.u.) of the HfX₄ complexes.

Basis Set	RHF		MP2	
	Re	E	Re	E
HfF₄				
MCP-SPD				
DZ	1.909	-127.89448	1.912	-128.77145
DZ1f	1.885	-127.92544	1.880	-128.84628
DZ1p	1.916	-127.90257	1.922	-128.79163
DZ1p1f	1.879	-127.93307	1.875	-128.86433
TZ	1.889	-127.94908	1.895	-128.88336
TZ1f	1.871	-127.98120	1.867	-128.96527
TZ1p	1.895	-127.95500	1.906	-128.90042
TZ1p1f	1.874	-127.98614	1.874	-128.97893
ECP1-SPD				
TZ	1.891	-144.11160	1.906	-145.00264
TZ1f	1.879	-144.14075	1.885	-145.09402
ECP2-SPD				
DZ	1.890	-446.57920	1.902	-447.49988
DZ1f	1.872	-446.61120	1.876	-447.59208
DZ'	1.898	-446.59476	1.907	-447.53538
DZ'1f	1.879	-446.62020	1.881	-447.60869
TZ	1.885	-446.58528	1.895	-447.55893
TZ1f	1.868	-446.61637	1.872	-447.66445
TZ'	1.895	-446.59741	1.908	-447.59550
TZ'1f	1.877	-446.62260	1.881	-447.67738
Expt.				
	1.91		1.91	
HfCl₄				
MCP-SPD				
DZ	2.337	-91.12701	2.322	-91.86906
DZ1f	2.324	-91.14355	2.296	-91.93505
DZ1p	2.347	-91.13414	2.331	-91.88411
DZ1p1f	2.319	-91.15027	2.286	-91.94884
TZ	2.326	-91.17110	2.313	-91.97635
TZ1f	2.320	-91.19122	2.293	-92.04917
TZ1p	2.334	-91.17625	2.324	-91.98922
TZ1p1f	2.325	-91.19544	2.298	-92.06020
ECP1-SPD				
TZ	2.333	-107.41410	2.322	-108.12715
TZ1f	2.327	-107.42932	2.302	-108.21166

ECP2-SPD				
DZ	2.328	-107.60713	2.317	-108.29521
DZ1f	2.315	-107.62504	2.291	-108.38138
DZ'	2.335	-107.62422	2.319	-108.33519
DZ'1f	2.324	-107.63684	2.296	-108.40065
TZ	2.326	-107.60857	2.313	-108.35040
TZ1f	2.313	-107.62654	2.288	-108.45290
TZ'	2.335	-107.62551	2.322	-108.39748
TZ'1f	2.325	-107.63805	2.299	-108.47339
		Expt.		
	2.316		2.316	
HfBr4				
MCP-SPD				
DZ	2.488	-84.15300	2.472	-84.79672
DZ1f	2.481	-84.16612	2.450	-84.86017
DZ1p	2.504	-84.16133	2.486	-84.81441
DZ1p1f	2.484	-84.17400	2.446	-84.87641
TZ	2.480	-84.19370	2.463	-84.90172
TZ1f	2.479	-84.21133	2.446	-84.97313
TZ1p	2.490	-84.19953	2.475	-84.91676
TZ1p1f	2.486	-84.21589	2.452	-84.98593
ECP1-SPD				
TZ	2.484	-101.23976	2.470	-101.89886
TZ1f	2.479	-101.25069	2.450	-101.97928
ECP2-SPD				
DZ	2.495	-100.45995	2.479	-101.10037
DZ1f	2.485	-100.47418	2.455	-101.18408
DZ'	2.501	-100.47664	2.480	-101.14031
DZ'1f	2.493	-100.48635	2.459	-101.20370
TZ	2.494	-100.46123	2.478	-101.15479
TZ1f	2.484	-100.47559	2.452	-101.25549
TZ'	2.502	-100.47814	2.483	-101.20296
TZ'1f	2.494	-100.48782	2.460	-101.27749
		Expt.		
	2.465		2.465	

HfI4				
MCP-SPD				
DZ	2.690	-77.02231	2.675	-77.60892
DZ1f	2.688	-77.03206	2.657	-77.66981
DZ1p	2.722	-77.03733	2.694	-77.63204
DZ1plf	2.701	-77.04635	2.659	-77.69049
TZ	2.683	-77.06070	2.665	-77.70981
TZ1f	2.686	-77.07565	2.651	-77.77970
TZ1p	2.697	-77.06959	2.677	-77.72706
TZ1plf	2.694	-77.08182	2.655	-77.79280
ECP1-SPD				
TZ	2.713	-93.48979	2.693	-94.10121
TZ1f	2.709	-93.49785	2.673	-94.17886
ECP2-SPD				
DZ	2.709	-93.32280	2.690	-93.91316
DZ1f	2.703	-93.33365	2.666	-93.99388
DZ'	2.714	-93.33851	2.687	-93.95195
DZ' 1f	2.708	-93.34538	2.666	-94.01294
TZ	2.709	-93.32391	2.691	-93.96681
TZ1f	2.702	-93.33490	2.664	-94.06457
TZ'	2.714	-93.34001	2.690	-94.01432
TZ' 1f	2.708	-93.34688	2.667	-94.08675
Expt.				
	2.662		2.662	

Table A.6: Summary of the computed geometric parameters for the MX_2Y_2 complexes.^a

Potential	M-X		M-Y	
	RHF	MP2	RHF	MP2
TiCl₂Br₂				
MCP-SPD	2.152	2.149	2.316	2.305
ECP1-SPD	2.186	2.186	2.337	2.325
ECP2-SPD	2.153	2.162	2.322	2.323
TiCl₂I₂				
MCP-SPD	2.150	2.153	2.522	2.508
ECP1-SPD	2.183	2.190	2.570	2.548
ECP2-SPD	2.151	2.167	2.539	2.534
TiBr₂I₂				
MCP-SPD	2.311	2.309	2.519	2.509
ECP1-SPD	2.334	2.332	2.571	2.551
ECP2-SPD	2.318	2.334	2.536	2.539
ZrCl₂Br₂				
MCP-SPD	2.347	2.336	2.505	2.490
ECP1-SPD	2.351	2.341	2.503	2.488
ECP2-SPD	2.340	2.330	2.510	2.496
ZrCl₂I₂				
MCP-SPD	2.346	2.335	2.706	2.689
ECP1-SPD	2.347	2.340	2.735	2.710
ECP2-SPD	2.338	2.329	2.726	2.707
ZrBr₂I₂				
MCP-SPD	2.501	2.487	2.703	2.687
ECP1-SPD	2.407	2.485	2.733	2.709
ECP2-SPD	2.505	2.492	2.723	2.707
HfCl₂Br₂				
MCP-SPD	2.323	2.310	2.484	2.466
ECP1-SPD	2.332	2.321	2.484	2.471
ECP2-SPD	2.323	2.311	2.496	2.480

HfCl₂I₂				
MCP-SPD	2.321	2.308	2.688	2.670
ECP1-SPD	2.328	2.318	2.717	2.697
ECP2-SPD	2.321	2.310	2.715	2.694
HfBr₂I₂				
MCP-SPD	2.478	2.462	2.685	2.667
ECP1-SPD	2.479	2.466	2.716	2.697
ECP2-SPD	2.491	2.475	2.712	2.693

^a The TZ basis set for each pseudopotential was employed in all of the calculations.

Table A.7 : Summary of the X-X bond distances of the dihalides.

Potential	Cl ₂		Br ₂		I ₂	
	RHF	MP2	RHF	MP2	RHF	MP2
MCP	2.015	2.040	2.301	2.324	2.701	2.728
ECP1	2.010	2.038	2.284	2.312	2.675	2.700
ECP2	2.005	2.028	2.315	2.335	2.687	2.708
Expt.	1.987		2.281		2.666	

Appendix B

Supplementary Material for Chapter 3: MCP L-Shell Valence Basis Sets for the Main Group Elements

Table B.1: Optimum MCP-SP L-Shell Basis Sets for the First Row Main Group Elements.

N	α	C_s	C_p	Δ^a
B				
1	33.78671932	-0.05808457	0.00131684	0.41618703E-03
2	4.32145515	-0.24879413	0.05535667	
3	0.89990390	-0.00702982	0.27553693	
4	0.25364584	0.71148422	0.52382464	
5	0.07949164	0.37666488	0.36951606	
C				
1	37.28756443	-0.07863158	0.00447533	0.19828017E-02
2	5.48854614	-0.25023051	0.07271160	
3	1.40333400	-0.01999411	0.26824079	
4	0.42680786	0.69269460	0.50971349	
5	0.12849330	0.41980104	0.37896052	
N				
1	53.45925028	-0.07757986	0.00432313	0.27019110E-02
2	8.11548555	-0.25029454	0.07389636	
3	2.07449391	-0.03670535	0.27646848	
4	0.62126798	0.69509856	0.51470283	
5	0.18206627	0.42755572	0.37021683	
O				
1	72.35429390	-0.07669689	0.00377995	0.35231996E-02
2	11.06193170	-0.25638608	0.07505261	
3	2.76567893	-0.02909782	0.29107800	
4	0.80381210	0.73499973	0.51320225	
5	0.22536525	0.38363212	0.36800102	
F				
1	94.61052745	-0.07593851	0.00347848	0.42623695E-02
2	14.62209357	-0.25943848	0.07678135	
3	3.60048325	-0.03085282	0.30050460	
4	1.02791363	0.75419468	0.51411959	
5	0.27999667	0.36505640	0.36356573	

Ne				
1	160.64134628	-0.05828653	0.00106795	0.17527789E-02
2	21.61536409	-0.27443617	0.07062222	
3	4.67984278	-0.02548416	0.31788223	
4	1.25929417	0.75402723	0.52412743	
5	0.33730191	0.35406004	0.34986959	

^a Values correspond to the sum of the squares of the deviations between the L-shell and reference radial functions evaluated at each radial point in the grid, Equation (3.20).

Table B.2: Optimum MCP-SP L-Shell Basis Sets for the Second Row Main Group Elements.

N	α	C_s	C_p	Δ^a
Al				
1	59.37196043	0.07251255	-0.01081221	0.16200282E-01
2	6.56937230	-0.00794469	-0.10542858	
3	1.56442630	-0.40860578	-0.06246337	
4	0.16567063	0.70854855	0.59117924	
5	0.05208728	0.42890967	0.50769974	
Si				
1	59.95976956	0.06381545	-0.01786194	0.44608725E-01
2	6.28524227	-0.04375645	-0.15721876	
3	1.66596897	-0.46216760	-0.04912570	
4	0.25539492	0.73406876	0.59435329	
5	0.08544019	0.44779459	0.49533583	
P				
1	53.78297465	0.04565604	-0.02100090	0.19307384E-01
2	7.26687095	-0.05289806	-0.14302227	
3	2.05934389	-0.45514342	-0.05376293	
4	0.37271946	0.63041872	0.57769220	
5	0.11407603	0.57405262	0.53253268	
S				
1	39.22730848	0.04599138	-0.04535324	0.15904234E-01
2	6.91483623	-0.11559505	-0.18334703	
3	2.16546416	-0.45780579	-0.01666263	
4	0.46156173	0.72441024	0.60175518	
5	0.13565549	0.51856189	0.50595462	
Cl				
1	37.85013534	0.02437561	-0.06827607	0.59919751E-02
2	7.28626551	-0.11371336	-0.22562148	
3	2.64742215	-0.51284268	0.01141112	
4	0.55734250	0.77832899	0.61041307	
5	0.16244215	0.47547569	0.48718637	

	Ar			
1	43.76207317	0.00342157	-0.09922111	0.43453580E-02
2	8.58356661	-0.06916196	-0.30536230	
3	3.31897011	-0.59229665	0.01379160	
4	0.67940212	0.78141944	0.61701443	
5	0.19728793	0.47625778	0.46124550	

^a Values correspond to the sum of the squares of the deviations between the L-shell and reference radial functions evaluated at each radial point in the grid, Equation (3.20).

Table B.3: Optimum MCP-SP L-Shell Basis Sets for the Third Row Main Group Elements.

N	α	C_s	C_p	Δ^a
Ga				
1	43.63293563	0.00510307	0.04961392	0.14503093E-01
2	8.25275058	0.16740447	-0.05311116	
3	2.09350451	-0.49909315	-0.15455634	
4	0.17079091	0.76668525	0.63975169	
5	0.05171428	0.36085515	0.46767835	
Ge				
1	50.08457824	0.00703801	0.05262546	0.15274757E-01
2	8.04542517	0.22135588	-0.05363663	
3	2.42445596	-0.58518014	-0.18558600	
4	0.24009925	0.67260466	0.62626846	
5	0.07700996	0.47366802	0.47764790	
As				
1	57.33119238	0.00415686	0.10840378	0.15521663E-01
2	11.58377829	0.29184778	-0.03723208	
3	3.05824557	-0.61292415	-0.25198596	
4	0.29517263	0.60581832	0.59421137	
5	0.09830089	0.52716999	0.49920438	
Se				
1	62.37487055	0.00456968	0.09335685	0.10511049E-01
2	10.69373262	0.39157056	-0.03868328	
3	3.43873129	-0.73970720	-0.27882126	
4	0.35743195	0.63380137	0.62275504	
5	0.11458014	0.51888313	0.47773336	
Br				
1	68.00898711	0.00560766	0.10665336	0.66551767E-02
2	10.24444266	0.40398557	-0.03442058	
3	3.65498392	-0.78384656	-0.28485639	
4	0.42276509	0.65991077	0.62462359	
5	0.13300748	0.51745969	0.48460277	

Kr				
1	72.85516559	0.00659348	0.10804412	0.64300715E-02
2	10.48409523	0.47236687	-0.04098390	
3	4.10131202	-0.87520295	-0.32687101	
4	0.48961176	0.66777767	0.64837599	
5	0.15519339	0.51896216	0.45708161	

^a Values correspond to the sum of the squares of the deviations between the L-shell and reference radial functions evaluated at each radial point in the grid, Equation (3.20).

Table B.4: Optimum MCP-SP L-Shell Basis Sets for the Fourth Row Main Group Elements.

N	α	C_s	C_p	Δ^a
In				
1	26.27661760	-0.12750640	0.01568521	0.31851357E-02
2	9.08271886	0.32594138	0.07580539	
3	1.80608718	-0.07082554	-0.20187122	
4	1.23760183	-0.53169639	-0.00618563	
5	0.13600229	0.91206005	0.64845443	
6	0.04021969	0.24915833	0.46267320	
Sn				
1	24.95176834	-0.15043389	0.01462768	0.28062097E-02
2	10.49131963	0.33146528	0.07259711	
3	1.80898242	0.00722958	-0.25936823	
4	1.32519990	-0.63653685	0.03091421	
5	0.17105903	0.92133432	0.69502277	
6	0.05322037	0.27295467	0.41187489	
Sb				
1	25.98329175	-0.24082871	0.01564965	0.41157496E-02
2	11.88756832	0.48210341	0.13329786	
3	2.95537674	0.21688070	-0.08080115	
4	1.75844018	-0.97092198	-0.21780360	
5	0.20857079	0.85837060	0.72005909	
6	0.06745949	0.32535598	0.38798265	
Te				
1	26.78793583	-0.30589894	0.01517883	0.49113110E-02
2	12.94178028	0.57835739	0.15788722	
3	3.15138977	0.35441433	-0.07522202	
4	1.96961270	-1.14900432	-0.25508105	
5	0.24450346	0.86976260	0.72143515	
6	0.07729746	0.32962724	0.39253369	

I				
1	34.65387656	-0.14715104	0.00260817	0.85987614E-03
2	14.22255074	0.15186887	0.16748243	
3	8.42861332	0.36187858	-0.03456884	
4	2.12370539	-0.84792975	-0.36161493	
5	0.68330146	-0.11757362	0.08192655	
6	0.26266413	1.01139218	0.71866422	
7	0.08337510	0.24477909	0.35232439	
Xe				
1	34.39369125	-0.15060049	0.00322150	0.83148630E-03
2	14.85904214	0.23372921	0.13798439	
3	7.33837715	0.27529828	-0.03057592	
4	2.27848797	-0.88375237	-0.36593137	
5	0.68690151	-0.11585304	0.10460091	
6	0.29324405	1.04535856	0.72307198	
7	0.09332746	0.23026933	0.33169991	

^a Values correspond to the sum of the squares of the deviations between the L-shell and reference radial functions evaluated at each radial point in the grid, Equation (3.20).

Table B.5: Optimum MCP-SP L-Shell Basis Sets for the Fifth Row Main Group Elements.

N	α	C_s	C_p	Δ^a
Tl				
1	170.66783496	0.02195753	-0.00250461	0.20466031E-02
2	31.59815730	-0.10731995	-0.02068835	
3	8.08128337	0.20857599	0.10210111	
4	2.75295700	0.18250861	-0.07498218	
5	1.16269592	-0.80276684	-0.19103312	
6	0.14992952	1.02126739	0.55403265	
7	0.04494184	0.19376396	0.57112594	
Pb				
1	167.14380202	0.03374899	-0.00300042	0.25183754E-02
2	34.43843758	-0.14813796	-0.02972776	
3	8.67167765	0.26230812	0.13989692	
4	3.61507485	0.19370804	-0.06569906	
5	1.34132932	-0.86311655	-0.27211317	
6	0.17518741	1.01849589	0.64041541	
7	0.05689278	0.19584036	0.48047142	
Bi				
1	170.20285397	0.04132919	-0.00280881	0.24495888E-02
2	37.07764558	-0.15836596	-0.03267191	
3	9.31127025	0.24855852	0.13993099	
4	3.79961187	0.26287984	-0.05249553	
5	1.47909471	-0.93777490	-0.30349442	
6	0.20199813	1.01947761	0.68334513	
7	0.06870999	0.21037426	0.43664688	

Po				
1	178.92448804	0.05631688	-0.00288437	0.29839554E-02
2	38.29497915	-0.20955639	-0.03996151	
3	10.06662191	0.25317925	0.15985753	
4	4.93357198	0.34400359	-0.03742553	
5	1.64353429	-0.99169351	-0.33505625	
6	0.22714581	0.98548416	0.67666280	
7	0.07551653	0.24545604	0.44940470	
At				
1	179.12012213	0.05994793	-0.00179131	0.20423162E-02
2	41.16324517	-0.21935048	-0.05217571	
3	10.84945164	0.15506488	0.19050010	
4	6.37627828	0.47487430	-0.02506560	
5	1.78924510	-1.05115467	-0.40248432	
6	0.25803856	0.99819288	0.70825314	
7	0.08603474	0.24192774	0.42165782	
Rn				
1	182.29780164	0.06342339	-0.00197120	0.25323715E-02
2	42.34915634	-0.22847354	-0.05142977	
3	11.11943312	0.25056914	0.18947663	
4	5.48557078	0.43572233	-0.02830651	
5	1.89786852	-1.12399993	-0.40619747	
6	0.28875863	1.00570230	0.70901512	
7	0.09745212	0.25801373	0.42586332	

^a Values correspond to the sum of the squares of the deviations between the L-shell and reference radial functions evaluated at each radial point in the grid, Equation (3.20).

Table B.6: Optimum MCP-DSP L-Shell Valence Basis Sets for the Third Row Main Group Elements.

N	α	C_s	C_p	C_d	Δ^a
Ga					
L 7					
1	408.19753787	-0.02822341	0.00016954		0.36548494E-02
2	52.91630124	-0.00671377	0.05909159		
3	16.33638754	0.16476711	-0.00674411		
4	2.53828165	-0.24545077	-0.19467558		
5	1.25486929	-0.25119921	0.04248568		
6	0.17288560	0.83295128	0.56867040		
7	0.05081021	0.32091026	0.53278518		
D 5					
1	55.74442400			0.04435306	
2	14.72136100			0.20816348	
3	4.83822720			0.43011852	
4	1.60624470			0.45518338	
5	0.49300476			0.20447028	
Ge					
L 7					
1	433.95753699	-0.03064237	0.00012487		0.33351300E-02
2	57.90269674	-0.00448577	0.06766028		
3	16.79986773	0.18437122	-0.00543316		
4	2.93909717	-0.26115159	-0.21538174		
5	1.35072018	-0.31338912	0.02205936		
6	0.23516329	0.81418056	0.59534843		
7	0.07215178	0.37701010	0.50464304		
D 5					
1	64.68981000			0.04148314	
2	17.23871600			0.20000632	
3	5.74528800			0.42195557	
4	1.95628290			0.46240145	
5	0.62347294			0.20170133	

As				
L 7				
1	460.44487952	-0.03370940	0.00009123	0.27937971E-02
2	62.86871446	-0.00280279	0.07537570	
3	17.65290331	0.20275973	-0.00411358	
4	3.32503174	-0.27479973	-0.23771802	
5	1.48995464	-0.36513553	0.01027781	
6	0.29824935	0.81064455	0.61394328	
7	0.09407777	0.41041582	0.48682835	
D 5				
1	73.80344300			0.03755337
2	19.80830300			0.18741540
3	6.67302060			0.42092312
4	2.31699190			0.46762162
5	0.75904038			0.19885022
Se				
L 7				
1	491.54168579	-0.03902990	0.00009459	0.31032613E-02
2	67.65456975	-0.00288429	0.08593092	
3	18.93731414	0.22834088	-0.00430574	
4	3.61634776	-0.32180337	-0.27211386	
5	1.60526197	-0.37818560	0.02616637	
6	0.35054699	0.85721022	0.62732701	
7	0.10812514	0.38594947	0.47355996	
D 5				
1	81.06462500			0.03480829
2	21.94419400			0.16160560
3	7.47608730			0.41649021
4	2.64500010			0.48808581
5	0.88935110			0.18939191

Br				
L 7				
1	522.88452126	-0.04249585	0.00008903	0.30171822E-02
2	72.64909317	-0.00190643	0.09207375	
3	19.96019653	0.24489620	-0.00414019	
4	3.94105252	-0.34775849	-0.29534179	
5	1.74752184	-0.39947549	0.03422224	
6	0.40862491	0.88445351	0.64080212	
7	0.12576419	0.37974885	0.45974433	
D 5				
1	87.72113300			0.03587448
2	23.95176900			0.16268664
3	8.24795210			0.41705220
4	2.96786330			0.48689690
5	1.01966970			0.18066116
Kr				
L 7				
1	555.70284866	-0.04427793	0.00007832	0.26614562E-02
2	77.85431432	-0.00107781	0.09703207	
3	21.11100285	0.25776667	-0.00372774	
4	4.29533396	-0.36599551	-0.31562129	
5	1.90278202	-0.42305168	0.04006609	
6	0.47152179	0.90474226	0.65174978	
7	0.14596657	0.37963497	0.44789003	
D 5				
1	93.78921800			0.03586651
2	25.81470500			0.16178387
3	8.98154220			0.41985533
4	3.28364400			0.48497272
5	1.14933390			0.17260299

^a Values correspond to the sum of the squares of the deviations between the L-shell and reference radial functions evaluated at each radial point in the grid, Equation (3.20).

Table B.7: Optimum MCP-DSP L-Shell Valence Basis Sets for the Fourth Row Main Group Elements.

N	α	C_s	C_p	C_d	Δ^a
In					
L 8					
1	1117.0442479	0.01966417	-0.00028469		0.30479805E-02
2	148.55929144	-0.00285849	-0.03092569		
3	40.38091438	-0.12128216	0.01002387		
4	8.96467181	0.30704224	0.11769989		
5	2.48975560	-0.03746868	-0.17385868		
6	1.24029143	-0.55821986	-0.08670284		
7	0.11777285	0.98462483	0.72117514		
8	0.03535615	0.14982680	0.37864443		
D 6					
1	127.85717000			-0.03010810	
2	37.24200300			-0.12608501	
3	14.38783300			-0.16625795	
4	2.67764630			0.38303232	
5	1.04357850			0.54604003	
6	0.35436787			0.24174273	
Sn					
L 8					
1	1167.3462694	0.02208456	-0.00017264		0.31197295E-02
2	163.62294314	-0.00476628	-0.03502374		
3	40.62021102	-0.13892294	0.00742133		
4	10.08103646	0.31944181	0.13574029		
5	2.92536012	0.05074317	-0.15342790		
6	1.36050241	-0.71716513	-0.17314076		
7	0.17891996	0.84811504	0.63833475		
8	0.05803607	0.34734083	0.47128929		

			D 6		
1	184.52791000				-0.01939517
2	50.37842000				-0.10614361
3	17.36772800				-0.20023220
4	2.68458570				0.44852175
5	1.03915190				0.52427474
6	0.36984112				0.18036569
			Sb		
			L 8		
1	1223.3165332	0.02466174	-0.00014483		0.31467307E-02
2	173.64795470	-0.00589779	-0.04030647		
3	41.31296461	-0.15662879	0.00665315		
4	11.04383151	0.34011307	0.14765647		
5	2.96108496	0.08828888	-0.17138489		
6	1.46875022	-0.80252407	-0.19186733		
7	0.22132526	0.83316537	0.65077151		
8	0.07471200	0.39197085	0.46172131		
			D 6		
1	194.91964000				-0.02197811
2	53.28818400				-0.12104670
3	18.44267800				-0.20157712
4	2.91543950				0.45397709
5	1.15571820				0.51750019
6	0.42230671				0.17106669
			Te		
			L 8		
1	1285.2402456	0.02757762	-0.00011136		0.35024665E-02
2	184.11310455	-0.00660271	-0.04350300		
3	42.51564168	-0.17352089	0.00514624		
4	11.98505609	0.36102162	0.15435041		
5	3.04028661	0.14240350	-0.18702045		
6	1.60974691	-0.90606253	-0.20575495		
7	0.25787648	0.87352292	0.66864861		
8	0.08428197	0.37792581	0.45269183		

D 6				
1	205.81944000			-0.02143209
2	56.33698400			-0.10716096
3	19.56532700			-0.19519243
4	3.15080550			0.45564854
5	1.27440720			0.53072132
6	0.47585742			0.14959138
I				
L 8				
1	1348.8247679	0.03138053	-0.00005585	0.37647857E-02
2	197.34423966	-0.00743423	-0.04238793	
3	43.57762384	-0.19705890	0.00115526	
4	13.11442767	0.38714616	0.15807805	
5	3.08331726	0.26028506	-0.18428521	
6	1.82315559	-1.04171680	-0.21193698	
7	0.28993573	0.88312960	0.67350971	
8	0.09687221	0.37543207	0.44675968	
D 6				
1	217.16616000			-0.02146333
2	59.51167400			-0.12562314
3	20.73279000			-0.20961822
4	3.39043700			0.47139139
5	1.39448720			0.51030130
6	0.52917923			0.14675376
Xe				
L 8				
1	1421.7310967	0.03417447	-0.00005590	0.37311468E-02
2	205.53085789	-0.00724663	-0.05379954	
3	46.45617371	-0.20978930	0.00224562	
4	13.69308173	0.40978477	0.18690433	
5	3.52437924	0.22850097	-0.20429699	
6	1.93540698	-1.05885928	-0.24005182	
7	0.33865649	0.88974180	0.68771859	
8	0.11221288	0.39568354	0.44083615	

D 6		
1	228.85114000	-0.02644112
2	62.78869200	-0.14125654
3	21.93966900	-0.21931414
4	3.63546940	0.47109020
5	1.51673200	0.50846285
6	0.58277731	0.13770055

^a Values correspond to the sum of the squares of the deviations between the L-shell and reference radial functions evaluated at each radial point in the grid, Equation (3.20).

Table B.8: Optimum MCP-DSP L-Shell Valence Basis Sets for the Fifth Row Main Group Elements.

N	α	C_s	C_p	C_d	Δ^a
Tl					
L 9					
1	4989.7178509	-0.01461078	0.00007303		0.23407422E-02
2	515.55781201	0.00044629	0.01165427		
3	148.59336424	0.07862011	-0.00394831		
4	35.60660501	-0.20626271	-0.04996985		
5	7.55343203	-1.10537130	2.06197680		
6	7.36964429	1.52165572	-1.96116759		
7	1.32173795	-0.72703451	-0.22953392		
8	0.13811833	0.91147074	0.37858356		
9	0.06527429	0.23167819	0.66562054		
D 7					
1	313.58598000			0.02533901	
2	84.04528200			0.10560821	
3	14.10281600			-0.10409944	
4	8.79926820			-0.22598258	
5	1.66546970			0.49602270	
6	0.65292509			0.49727494	
7	0.23268302			0.17429536	
Pb					
L 9					
1	5189.0091253	-0.01933773	0.00006906		0.20206700E-02
2	541.84252411	0.00179099	0.01478791		
3	146.53024167	0.09484682	-0.00463845		
4	38.54342693	-0.22729470	-0.05770203		
5	7.64348648	-7.06638108	7.02169796		
6	7.58994103	7.53136651	-6.89139258		
7	1.42691801	-0.82254451	-0.30508114		
8	0.17591141	0.94327938	0.61100348		
9	0.05671249	0.24926751	0.50774940		

D 7				
1	323.97353000			0.02747020
2	86.87383800			0.11884049
3	14.67477400			-0.12188661
4	9.20980570			-0.22690564
5	1.78420470			0.50246896
6	0.72224252			0.49116934
7	0.26678258			0.16060479
Bi				
L 9				
1	5405.1166260	-0.02206122	0.00006438	0.18828764E-02
2	569.69063053	0.00265265	0.01749995	
3	146.65763186	0.10825674	-0.00432232	
4	41.08421706	-0.24859384	-0.06796304	
5	8.49626174	-0.12927636	0.42445640	
6	7.23264521	0.63854590	-0.27087520	
7	1.54022153	-0.89078289	-0.35086048	
8	0.20410949	0.94838836	0.65932048	
9	0.06878569	0.26065384	0.45928725	
D 7				
1	334.89629000			-0.02808847
2	89.78876500			-0.12894395
3	14.96327000			0.14948539
4	9.40084710			0.21585541
5	1.90707050			-0.51314762
6	0.78945303			-0.48522582
7	0.29804339			-0.14734203

Po				
L 9				
1	5659.5256214	-0.02680745	0.00005925	0.23565889E-02
2	594.48680667	0.00315385	0.01988035	
3	150.33728987	0.12358667	-0.00412595	
4	42.80086321	-0.27698760	-0.07790592	
5	9.57521304	0.04410002	0.26613072	
6	6.88470658	0.52328840	-0.09012958	
7	1.67415405	-0.96036144	-0.38119489	
8	0.23006375	0.97044852	0.67905941	
9	0.07637472	0.25201950	0.44496157	
D 7				
1	345.97725000			-0.03185123
2	92.79841300			-0.15138881
3	15.29286800			0.19904440
4	9.675039600			0.19124470
5	2.029344600			-0.52252406
6	0.856620200			-0.47192548
7	0.329323960			-0.13954710
At				
L 9				
1	5921.5702326	-0.02828177	0.00005232	0.26926549E-02
2	620.05238021	0.00356703	0.02283430	
3	153.81200691	0.13427029	-0.00381653	
4	44.62883676	-0.29975841	-0.08908173	
5	10.36882026	0.07880791	0.25007826	
6	6.83952899	0.55098133	-0.04658995	
7	1.82274583	-1.03279375	-0.41706638	
8	0.26034788	0.97521671	0.69154870	
9	0.08700788	0.26053218	0.43531823	

D 7				
1	357.27673000		0.03226496	
2	95.85673700		0.16061542	
3	15.63088100		-0.23693505	
4	9.93281670		-0.16990166	
5	2.15430500		0.52786768	
6	0.92420437		0.46940654	
7	0.35987064		0.12680473	
Rn				
L 9				
1	6243.3596693	-0.03140574	0.00005143	0.24772619E-02
2	643.01693253	0.00349505	0.02575367	
3	159.05690083	0.14489645	-0.00360330	
4	46.43177147	-0.31601071	-0.09710743	
5	10.82305508	0.08909346	0.26106672	
6	6.98817009	0.58063273	-0.04315621	
7	1.94852579	-1.09344623	-0.44784934	
8	0.28883710	0.98735530	0.71076732	
9	0.09752337	0.26119389	0.41847338	
D 7				
1	368.73891000		0.03660534	
2	98.94864400		0.17004438	
3	16.21745300		-0.22151728	
4	10.41379300		-0.18034541	
5	2.27025000		0.55053651	
6	0.98664347		0.45217501	
7	0.38808435		0.12182520	

^a Values correspond to the sum of the squares of the deviations between the L-shell and reference radial functions evaluated at each radial point in the grid, Equation (3.20).

Appendix C

Supplementary Material for Chapter 5:

Pictorial Representations of the
 π_{\perp} - π_d Fragment Molecular Orbitals
of $M(\text{CO})_3(\text{C}_2\text{H}_2)$

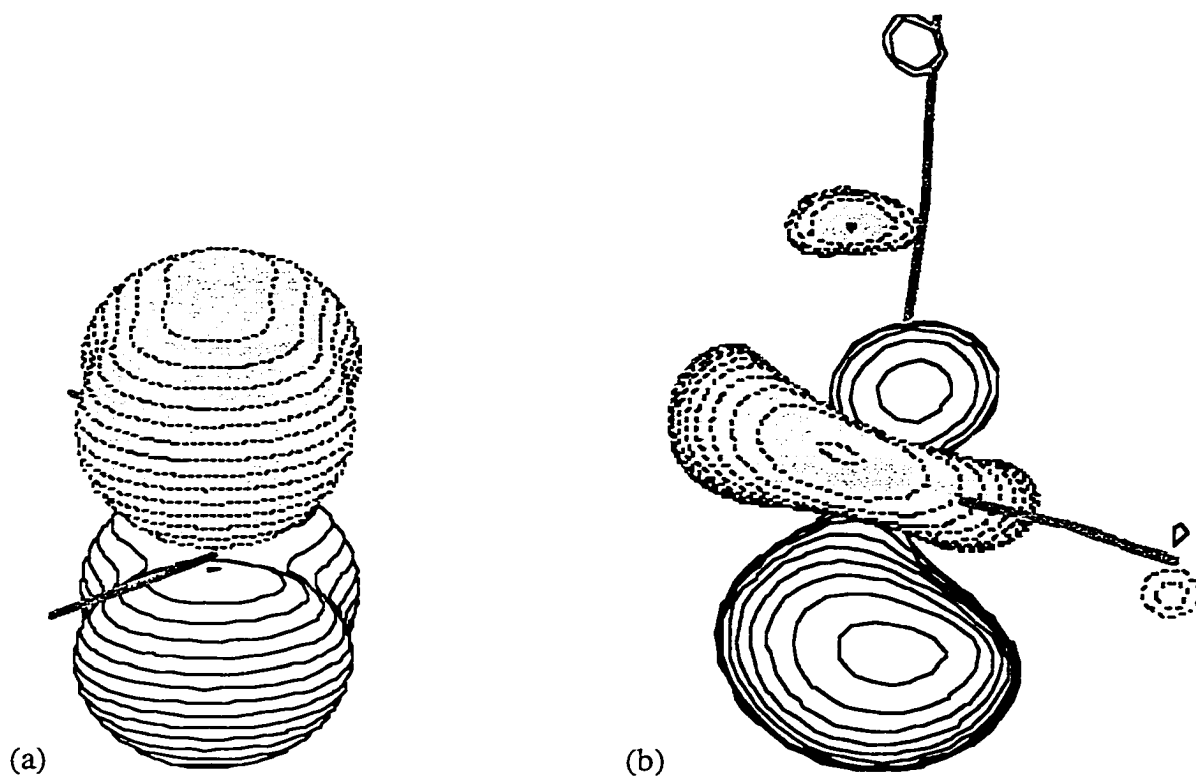


Figure C.1: The MO components of the $C_2H_2 \rightarrow M \pi_1-\pi_d$ interaction in $M(CO)_3(C_2H_2)$: (a) occupied π_1 orbital of C_2H_2 , (b) unoccupied orbital of proper π symmetry of the $M(CO)_3$ fragment.